

## Abstract

PARKER, CHARLES BERNARD. *Size Effects and Reliability Of (Ba,Sr)TiO<sub>3</sub> Thin Films.*  
(Under the direction of Angus I. Kingon)

Thin films of (Ba,Sr)TiO<sub>3</sub> (BST) deposited by Liquid Source MOCVD were investigated. BST is a candidate dielectric for future-generation DRAM and as a tunable dielectric. Two areas of both scientific and commercial interest were investigated. The first area is the effect of decreasing dimension on ferroelectric properties. Several theories of size effects in ferroelectrics were evaluated. The dielectric response of a set of BST films of thicknesses from 15 to 580 nm was measured from 85 to 580 K. These films were extensively characterized and the boundary conditions that often influence size effects measurements were considered, including strain, finite screening length in the electrode, depolarization fields in the ferroelectric, atmospheric effects, control of stoichiometry, and others. The data set was compared to the theoretical predictions and it was determined that Finite Size Scaling provided the best fit to the data. Using this theory, the predicted dielectric response was compared to the requirements of future generations of DRAM and was found to be sufficient, if film strain can be controlled. The second area is reliability. The types of lifetime-limiting electrical failure observed in BST are resistance degradation, time dependant dielectric breakdown (tddb), and noisy breakdown. Previous work on BST reliability has largely focused on resistance degradation at high temperature. This condition is only a small subset of experimental space. This work extends the understanding of BST failure into the low temperature regime and evaluates the effects of both DC and AC stress. It was found that tddb is the dominant failure mode at low temperature and resistance

degradation is the dominant failure modes at high temperature. Synthesizing this work with previous work on resistance degradation allowed a failure framework to be developed. Rigorous extrapolation of resistance degradation and tddb lifetimes was compared to the requirements of future generations of DRAM and was found that while resistance degradation will not limit device lifetimes, tddb will. Refinement of BST processing will be necessary to reduce the defect causing tddb failure.

# SIZE EFFECTS AND RELIABILITY OF (Ba,Sr)TiO<sub>3</sub> THIN FILMS

by

Charles Bernard Parker

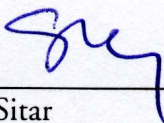
A dissertation submitted to the Graduate Faculty of  
North Carolina State University  
in partial fulfillment of the  
requirements for the Degree of  
Doctor of Philosophy

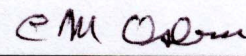
DEPARTMENT OF MATERIALS SCIENCE AND ENGINEERING

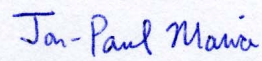
RALEIGH

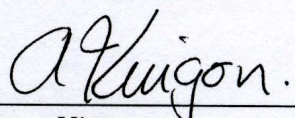
2002

APPROVED BY:

  
\_\_\_\_\_  
Zlatko Sitar

  
\_\_\_\_\_  
Carlton Osburn

  
\_\_\_\_\_  
Jon-Paul Maria

  
\_\_\_\_\_  
Angus Kingon  
Chairman of Advisory Committee

## Dedication

To my wife,

Mary Herring Parker

And my parents,

John and Alison Parker

# Biography

Charles Bernard Parker was born on December 1, 1973 in Asheville, North Carolina. He is the first son of John and Alison Parker. For the last two years of high school, he attended the North Carolina School of Science and Math and was graduated in 1992. The same year he earned the rank of Eagle Scout, partly based on his ability to start fires with everything from a bow and a stick to steel wool and batteries.

He was admitted into the Department of Physics at North Carolina State University and quickly transferred to the Department of Materials Science and Engineering. He received a Bachelors of Science degree in 1996, with minors in English, History, and Economics. His senior design project sought to improve the repeatability of a pressability test for tungsten carbide powder.

He continued at North Carolina State University in the Department of Materials Science and Engineering as a graduate student and research assistant under the supervision of Prof. Angus I. Kingon. In 1999, he changed his degree objective from Masters of Science to Doctor of Philosophy. More importantly, he was fortunate enough to persuade Mary Elizabeth Herring to marry him before she realized how difficult a person he actually is.

His research focused on the properties of high permittivity thin films and their application in future-generation dynamic random access memories.

## Acknowledgements

I would like to thank Prof. Angus Kingon for the opportunity to do the research, for providing a broad perspective of how specific research fits in to the larger body of scientific knowledge, and for the opportunity to interact with the broader scientific community.

I would like to thank Prof. Jon-Paul Maria for his tutelage during the later stages of my Ph.D. work and for invaluable help with the wire bonder.

I would also like to thank the other members of my committee, Profs Carlton Osburn and Zlatko Sitar for their support and participation.

I would like to thank Dr. Stephen Streiffer for training in analytical methods and for advice based on his keen understanding of ferroelectricity and practically everything else.

The other members of the Kingon group who were essential are Cem Basceri and Sandra Lash, for their help in electrical and structural characterization; Prof. Tim Usher, for helping to impedance match the AC testing circuit; and Darin Thomas, for help with the ion beam system.

Finally, I would like to thank my wife for her support, encouragement, understanding, and tolerance; especially when I used every available horizontal surface for organizing papers.

# TABLE OF CONTENTS

LIST OF TABLES .....	IX
LIST OF FIGURES .....	XII
CHAPTER 1: LITERATURE REVIEW .....	1
1.1: FERROELECTRICITY .....	1
1.2: MODELS OF FERROELECTRICITY .....	5
1.2.1: <i>Phenomenological Theory of Ferroelectricity</i> .....	5
1.2.2: <i>Microscopic Theory of Ferroelectricity</i> .....	10
1.3: SIZE EFFECTS .....	16
1.3.1: <i>Dead Layer</i> .....	18
1.3.2: <i>Critical Phenomena and Scaling Theory</i> .....	24
1.3.3: <i>Boundary Conditions</i> .....	46
1.3.3.1: Finite Screening Length .....	46
1.3.3.2: Presence of a Free Surface .....	48
1.3.3.3: Incomplete Depletion and Depolarization Fields .....	49

1.3.3.4: Strain.....	57
1.3.4: LGD Size Effects.....	64
1.3.5: Models of Size Effects in Particles .....	68
1.3.6: Experimental Evidence: Ceramics.....	70
1.3.7: Experimental Evidence: Particles.....	77
1.3.8: Experimental Evidence: Thin Films .....	79
1.4: BARIUM STRONTIUM TITANATE .....	90
1.4.1: Materials Science of BST.....	90
1.4.1.1: Chemistry.....	90
1.4.1.2: Microstructure.....	94
1.4.1.3: Processing.....	95
1.4.1.4: Electrodes .....	96
1.4.2: Electrical Properties.....	98
1.4.3: Applications of BST.....	101
1.5: RELIABILITY .....	104
1.5.1: Statistical Methods .....	104
1.5.2: Reliability of SiO <sub>2</sub> .....	116
1.5.3: Reliability of BST .....	122
1.5.3.1: Resistance Degradation.....	122
1.5.3.2: Time Dependent Dielectric Breakdown.....	132
1.5.3.3: Stress Induced Leakage Currents.....	138
1.5.3.4: AC Stress .....	139
1.6: RESEARCH OBJECTIVES.....	141

<b>CHAPTER 2: EXPERIMENTAL PROCEDURE .....</b>	<b>142</b>
2.1: FILM DEPOSITION .....	142
2.2: ELECTRICAL CHARACTERIZATION .....	147
2.2.1: <i>Capacitance-Voltage and -Frequency</i> .....	148
2.2.2: <i>Current-Voltage and -Time</i> .....	151
2.2.3: <i>AC Stress</i> .....	153
2.3: X-RAY ANALYSIS .....	155
2.4: TEMPERATURE MEASUREMENT .....	156
2.5: FILM LIFT OFF .....	160
<b>CHAPTER 3: SIZE EFFECTS .....</b>	<b>162</b>
3.1: THICKNESS DEPENDENT PROPRTIES .....	162
3.1.1: <i>Temperature dependence of the dielectric response</i> .....	162
3.1.2: <i>Electric field dependence of the dielectric response</i> .....	167
3.1.3: <i>Frequency dependence of the dielectric response</i> .....	172
3.1.4: <i>Hysteresis as a function of temperature</i> .....	175
3.1.5: <i>X-ray estimation of strain</i> .....	176
3.2: MODELING THICKNESS DEPENDANT PROPERTIES WITH THE “DEAD” LAYER CONCEPT .....	188
3.3: MODELING THICKNESS DEPENDANT PROPERTIES WITH THE SCALING LAWS..	197
3.4: CONFOUNDING FACTORS.....	206
3.4.1: <i>Depolarization Fields in the Ferroelectric</i> .....	206
3.4.2: <i>Electrode Effects</i> .....	206
3.4.2.1: <i>Polarization Screening in the Electrode</i> .....	206

3.4.2.2: Perovskite electrodes .....	208
3.4.3: <i>Ferroelectric not Fully Depleted</i> .....	210
3.4.4: <i>Domain Patterns</i> .....	210
3.4.5: <i>Grain Size</i> .....	211
3.5: POLYNOMIAL FIT OF PERMITTIVITY .....	212
3.6: SUMMARY OF SIZE EFFECTS MODELS.....	217
3.7: IMPLICATIONS OF FINITE SIZE SCALING MODEL.....	221
3.8: CONCLUSIONS.....	224
<b>CHAPTER 4: RELIABILITY .....</b>	<b>226</b>
4.1: LOW TEMPERATURE, HIGH FIELD DC FAILURE .....	229
4.1.1: <i>Tddb and Noisy Breakdown</i> .....	231
4.1.2: <i>Stress Induced Leakage Currents</i> .....	238
4.2: HIGH TEMPERATURE, LOW FIELD DC FAILURE .....	245
4.3: HIGH TEMPERATURE, HIGH FIELD .....	246
4.4: AC FAILURE.....	259
4.5: GENERAL FAILURE MODEL .....	268
4.6: FURTHER INVESTIGATION OF TDDB.....	272
4.7: EXTRAPOLATION OF TDDB AND RESISTANCE DEGRADATION LIFETIMES.....	278
4.8: CONCLUSIONS.....	284
<b>CHAPTER 5: FUTURE WORK.....</b>	<b>286</b>
<b>CHAPTER 6: BIBLIOGRAPHY.....</b>	<b>288</b>

# LIST OF TABLES

TABLE 1.1: DEFINITIONS OF SOME CRITICAL EXPONENTS, ADAPTED FROM LINES AND GLASS[36].....	28
TABLE 1.2: TABLE ADAPTED FROM GOLDENFELD [37].....	29
TABLE 1.3: DIFFERENCES BETWEEN BULK AND THIN FILM SOLUBILITIES IN BST.....	92
TABLE 1.4: BOTTOM ELECTRODE EFFECT ON BST PROPERTIES. ADAPTED FROM TSAI AND TSENG[124].....	97
TABLE 1.5: DATA REQUIREMENTS INCREASE FROM LEFT TO RIGHT .....	104
TABLE 1.6: ACCEPTABLE FIT RATES FOR THE YEARS 1992-2001 [128].....	105
TABLE 2.1: PRECURSORS USED IN BST MOCVD .....	143
TABLE 2.2: TYPICAL DEPOSITION CONDITIONS FOR BST FILMS.....	143
TABLE 2.3: COMPOSITIONAL CONTROL AND X-RAY FLUORESCENCE MEASUREMENT PRECISION FOR BST DEPOSITION SYSTEM.....	144
TABLE 3.1: APPROXIMATE POSITIONS FOR $(0\ 0\ \ell)$ FAMILY OF PLANES IN BST.....	178
TABLE 3.2: RESULTS OF X-RAY ESTIMATION OF STRAIN .....	182

TABLE 3.3: MATERIAL PARAMETERS FOR AU AND SrRuO <sub>3</sub> USED IN THE CALCULATION OF THE THIMAS-FERMI SCREENING LENGTH .....	207
TABLE 3.4: R <sup>2</sup> VALUES FOR THE FITTING PARAMETERS. ....	214
TABLE 3.5: PROPERTIES OF 4.5 NM BST FILM BASED ON FINITE SIZE SCALING EXTRAPOLATION. ....	221
TABLE 4.1: WEIBULL PARAMETER ESTIMATES FOR TDDB AND SOFT BREAKDOWN DISTRIBUTIONS.....	233
TABLE 4.2: NONPARAMETRIC TESTS FOR SOFT BREAKDOWN AND TDDB DISTRIBUTIONS .....	234
TABLE 4.3: PERCENTAGE OF FAILURES FROM NOISY BREAKDOWN AND TDDB FOR CAPACITORS OF TWO SIZES .....	237
TABLE 4.4: MEANS OF PRIMARY EXPERIMENTAL VARIABLES. ....	247
TABLE 4.5: PARAMETER ESTIMATES FOR THE EFFECTS IN THE RESISTANCE DEGRADATION MODEL.....	248
TABLE 4.6: WEIBULL PARAMETER ESTIMATES FOR FIGURE 4.34. ....	262
TABLE 4.7: SIGNIFICANCE OF THE DIFFERENCE IN LIFETIME BETWEEN LOW TEMPERATURE AC AND DC TDDB FAILURE USING NONPARAMETRIC TESTS. ....	262
TABLE 4.8: WEIBULL PARAMETER ESTIMATES FOR CURVES SHOWN IN FIGURE 4.43. ....	274
TABLE 4.9: WHOLE MODEL TEST FOR PRE-STRESS LEAKAGE MODEL.....	275
TABLE 4.10: EFFECT LIKELIHOOD RATIO TESTS, INDICATING SIGNIFICANCE, FOR PRE- STRESS LEAKAGE MODEL.....	275
TABLE 4.11: PARAMETER ESTIMATES FOR PRE-STRESS LEAKAGE MODEL. ....	275
TABLE 4.12: WEIBULL PARAMETER ESTIMATES FOR CURVES SHOWN IN FIGURE 4.44. .	276

TABLE 4.13: LOWER AND UPPER CONFIDENCE INTERVALS FOR THE MODEL AND FOR INDIVIDUAL OBSERVATIONS, FOR VARIOUS FIELDS, FOR A 51.0% Ti, 40 NM FILM AT 85 °C. VALUES ARE IN SECONDS. ....	279
TABLE 4.14: EXTRAPOLATED RESISTANCE DEGRADATION LIFETIME FOR A 51.0% Ti, 40 NM FILM AT 85 °C.....	279
TABLE 4.15: WEIBULL PARAMETER ESTIMATES FOR CURVES SHOWN IN FIGURE 4.44. .	280

# LIST OF FIGURES

FIGURE 1.1: ESSENTIAL FEATURES OF FERROELECTRICITY.....	3
FIGURE 1.2: THE PEROVSKITE CRYSTAL STRUCTURE. ....	4
FIGURE 1.3: RELATIONSHIP OF VARIOUS THERMODYNAMIC QUANTITIES, ADAPTED FROM NYE[6].....	6
FIGURE 1.4: EFFECT OF THIN FILM STRESS ON CUBIC MATERIALS.....	9
FIGURE 1.5: THE 3D ISING MODEL, FROM STRUKOV AND LEVANYUK[9] .....	11
FIGURE 1.6: RELATIONSHIPS AMONG THE MODELS OF FERROELECTRICITY.....	17
FIGURE 1.7: THE RELATIONSHIP BETWEEN SOFT MODE AND DIELECTRIC CONSTANT, FROM COWLEY[20].....	18
FIGURE 1.8: SCHEMATIC OF THE DEAD LAYER MODEL. ....	22
FIGURE 1.9: SCHEMATIC OF THE VARIATION OF SPONTANEOUS POLARIZATION AS A FUNCTION OF TEMPERATURE FOR A FERROELECTRIC.....	24
FIGURE 1.10: SCHEMATIC OF LIQUID-GAS PHASE DIAGRAM.....	26
FIGURE 1.11: THE REMNANT MAGNETIZATION AS A FUNCTION OF TEMPERATURE FOR AN ISING FERROMAGNET .....	27

FIGURE 1.12: SPECIFIC HEAT OF 3D ISING MODEL FOR INFINITE AND FINITE SYSTEM SIZE, FROM GOLDENFELD[37]. .....	34
FIGURE 1.13: THE LOGARITHMIC CORRECTIONS TO THE LANDAU COEFFICIENTS IN LiTbF <sub>4</sub> , FROM FROWEIN AND KÖTZLER [38]. .....	35
FIGURE 1.14: THE SHIFT IN THE TRANSITION TEMPERATURE AS A FUNCTION OF CRYSTAL SIZE FOR THE 4D (UPPER CURVE)AND 3D (LOWER CURVE) ISING MODELS FROM BINDER <i>ET AL</i> [53]. .....	38
FIGURE 1.15: MAGNITIZATION PROFILE ACROSS SAMPLES OF DIFFERENT THICKNESSES, WHERE $L$ IS IN UNIT CELLS, FROM BINDER <i>ET AL</i> [53].....	39
FIGURE 1.16: MAGNETIZATION PROFILE AS A FUNCTION OF TEMPERATURE AND POSITION FOR THE HEISENBERG MODEL, UNDER THE ASSUMPTION THAT THE RIGHT HAND SIDE IS PINNED TO THE BULK VALUE OF MAGNETIZATION, FROM BINDER <i>ET AL</i> [53]. .....	40
FIGURE 1.17: MAGNETIC SUSCEPTIBILITY AS A FUNCTION OF $L$ , THE THICKNESS OF UNIT CELLS, AND $H$ , MAGNETIC FIELD, FROM BINDER <i>ET AL</i> [54].....	41
FIGURE 1.18: SCALING PLOT OF MAGNETIC SUSCEPTIBILITY VERSUS CORRECTED FIELD AS A FUNCTION OF $L$ , FROM BINDER <i>ET AL</i> [54].....	42
FIGURE 1.19: POLARIZATION PROFILE ILLUSTRATING THE CONCEPT OF THE EXTRAPOLATION LENGTH AS A FUNCTION OF DISTANCE FROM SURFACE, FROM KRETSCHMER AND BINDER[18]. .....	43
FIGURE 1.20: POLARIZATION PROFILE OF FERROELECTRIC NEGLECTING DEPOLARIZATION FIELDS, FROM KRETSCHMER AND BINDER[18]. .....	44
FIGURE 1.21: POLARIZATION PROFILE CONSIDERING THE EFFECT OF DEPOLARIZATION FIELDS, FROM KRETSCHMER AND BINDER[18].....	45

FIGURE 1.22: THE EFFECT OF FINITE SCREENING LENGTH ON CHARGE DENSITY IN THE ELECTRODE .....	47
FIGURE 1.23: SCHEMATIC OF THE CIRCUIT USED BY BATRA <i>ET AL.</i> TO ANALYSE DEPOLARIZATION FIELDS IN A FERROELECTRIC, FROM BATRA <i>ET AL.</i> [24]. .....	50
FIGURE 1.24: EFFECT OF ELECTROSTATIC BOUNDARY CONDITIONS IN THE BATRA, WURFUL, AND SILVERMAN MODEL. ....	53
FIGURE 1.25: P-E LOOPS OF AN AU/TGS/P-SI DEVICE WITH DIFFERENT LEVELS OF ILLUMINATION, FROM WURFEL <i>ET AL</i> [26]. ....	57
FIGURE 1.26: CALCULATED EFFECT OF STRAIN ON THE PHASE DIAGRAM OF BaTiO <sub>3</sub> , FROM PERTSEV <i>ET AL</i> [57]. ....	59
FIGURE 1.27: THE EFFECT OF 2D COMPRESSIVE STRAIN ON TRANSITION TEMPERATURE IN BaTiO <sub>3</sub> , FROM FORSBERGH[64]. ....	60
FIGURE 1.28: DIELECTRIC RESPONSE AS A FUNCTION OF TEMPERATURE AND PRESSURE FOR CERAMIC SrTiO <sub>3</sub> , FROM SAMARA <i>ET AL</i> [65]. ....	62
FIGURE 1.29: DIELECTRIC CONSTANT OF BaTiO <sub>3</sub> AS A FUNCTION OF TEMPERATURE AND PRESSURE, FROM SAMARA <i>ET AL</i> [65]. ....	62
FIGURE 1.30: DIELECTRIC RESPONSE OF SrTiO <sub>3</sub> ABOUT THE QUANTUM PARAELECTRIC TRANSITION TEMPERATURE, FROM MULLER <i>ET AL</i> [69]. ....	64
FIGURE 1.31: CALCULATION OF CRITICAL SIZE FOR FERROELECTRICITY FOR PbTiO <sub>3</sub> , FROM SHAOPING <i>ET AL</i> [82]. ....	67
FIGURE 1.32: EXTRAPOLATION LENGTH AS A FUNCTION OF TEMPERATURE FOR VARIOUS PARTICLE SIZES, FROM ZHANG <i>ET AL</i> [88]. ....	70

FIGURE 1.33: SHIFT IN TRANSITION TEMPERATURE AS A FUNCTION OF CRYSTAL SIZE, FROM McCAULEY <i>ET AL</i> [13]. .....	72
FIGURE 1.34: VARIATION IN MAXIMUM PERMITTIVITY AS A FUNCTION OF CRYSTAL SIZE, FROM McCAULEY <i>ET AL</i> [13]. .....	72
FIGURE 1.35: CHANGE IN DIFFUSENESS AS A FUNCTION OF CRYSTAL SIZE, FROM McCAULEY <i>ET AL</i> [13]. .....	73
FIGURE 1.36: DIELECTRIC CONSTANT AND LOSS OF CERAMIC $\text{BaTiO}_3$ , FROM FREY AND PAYNE[90]. .....	74
FIGURE 1.37: DIELECTRIC CONSTANT VARIATION AS A FUNCTION OF GRAIN SIZE AND MICROSTRUCTURE FOR $\text{BaTiO}_3$ CERAMICS, FROM FREY AND PAYNE[90]. .....	75
FIGURE 1.38: DIFFUSENESS AS A FUNCTION OF GRAIN SIZE FOR A BST CERAMIC. ADAPTED FROM ZHANG <i>ET AL</i> [92]. .....	76
FIGURE 1.39: SHIFT IN TRANSITION TEMPERATURE AS A FUNCTION OF GRAIN SIZE FOR A BST CERAMIC. ADAPTED FROM ZHANG <i>ET AL</i> [92]. .....	76
FIGURE 1.40: DEGREE OF TETRAGONALITY AS A FUNCTION OF TEMPERATURE FOR DIFFERENT GRAIN SIZES, FROM PARK <i>ET AL</i> [96]. .....	78
FIGURE 1.41: SPECIFIC HEAT AS A FUNCTION OF TEMPERATURE FOR DIFFERENT GRAIN SIZES, FROM PARK <i>ET AL</i> [96]. .....	79
FIGURE 1.42: DIELECTRIC CONSTANT AS A FUNCTION OF TEMPERATURE FOR DIFFERENT GRAIN SIZES, FROM PARK <i>ET AL</i> [96]. .....	79
FIGURE 1.43: VOLTAGE TO REACH A GIVEN POLARIZATION AS A FUNCTION OF THICKNESS, FROM LARSEN <i>ET AL</i> [98]. .....	81

FIGURE 1.44: PERMITTIVITY AS A FUNCTION OF TEMPERATURE FOR DIFFERENT THICKNESSES OF $\text{SrTiO}_3$ , FROM LI <i>ET AL</i> [31].	83
FIGURE 1.45: CALCULATED “BULK” PERMITTIVITY AS A FUNCTION OF THICKNESS FOR DIFFERENT TEMPERATURES FOR $\text{SrTiO}_3$ , FROM LI <i>ET AL</i> [31].	84
FIGURE 1.46: VARIATION OF CAPACITANCE DENSITY OF BST FILMS AS A FUNCTION OF THICKNESS FOR DIFFERENT TEMPERATURES[7].	85
FIGURE 1.47: CAPACITANCE DENSITY OF BST FILMS AS A FUNCTION OF THICKNESS FOR DIFFERENT COMPOSITIONS[7].	86
FIGURE 1.48: CURIE-WEISS CONSTANT AND TEMPERATURE AS A FUNCTION OF THICKNESS FOR 53.0% Ti BST.	87
FIGURE 1.49: THICKNESS SCALED PERMITTIVITY OF BST AS A FUNCTION OF THICKNESS, FROM SINNAMON <i>ET AL</i> [21].	88
FIGURE 1.50: THICKNESS SCALED PERMITTIVITY AS A FUNCTION OF THICKNESS FOR BST, FROM SINNAMON <i>ET AL</i> [21].	89
FIGURE 1.51: CALCULATION OF THICKNESS TO PERMITTIVITY AS A FUNCTION OF THICKNESS FOR THREE SCENARIOS, FROM SINNAMON <i>ET AL</i> [21].	89
FIGURE 1.52: DIELECTRIC SUSCEPTIBILITY OF BST AS A FUNCTION OF TEMPERATURE FOR VARIOUS COMPOSITIONS, FROM BETHE <i>ET AL</i> [106].	91
FIGURE 1.53: EFFECT OF SOME DOPENTS ON THE TRANSITION TEMPERATURE OF CERAMIC BST, FROM HENCB <i>ET AL</i> [110].	92
FIGURE 1.54: DIELECTRIC RESPONSE ABOUT AS A FUNCTION OF Ti STOICHIOMETRY FOR 30 NM MOCVD FILMS, FROM HORIKAWA <i>ET AL</i> [111].	92

FIGURE 1.55: ZERO-BIAS PERMITTIVITY AS A FUNCTION OF COMPOSITION FOR VARIOUS THICKNESSES OF BST[112].	94
FIGURE 1.56: DIELECTRIC LOSS VERSUS TI FOR DIFFERENT THICKNESSES OF BST[112]	94
FIGURE 1.57: J-V CURVES FOR BST/Pt/SiO <sub>2</sub> /Si WITH VARIOUS TOP ELECTRODES, FROM LASH[123].	97
FIGURE 1.58: DIELECTRIC LOSS OF BST/Pt/SiO <sub>2</sub> /Si AS A FUNCTION OF ANNEALING CONDITION FOR VARIOUS TOP ELECTRODES, FROM LASH[123].	98
FIGURE 1.59: CAPACITANCE DENSITY OF BST/Pt/SiO <sub>2</sub> /Si AS A FUNCTION OF ANNEALING CONDITION FOR VARIOUS TOP ELECTRODES, FROM LASH[123].	98
FIGURE 1.60: PERMITTIVITY AND DIELECTRIC LOSS FOR CERAMIC BST. ADAPTED FROM HILTON AND RICKETTS[125].	99
FIGURE 1.61: CHARGING CURRENT FLOWING INTO A 60 NM, 52.0 AT%Ti BST FILM AS A FUNCTION OF TIME, FROM BASCERI[112].	100
FIGURE 1.62: RELATIVE PERMITTIVITY OF A 60 NM, 52.0 AT%Ti BST FILM AS A FUNCTION OF FREQUENCY, FROM BASCERI[112].	101
FIGURE 1.63: DIELECTRIC CONSTANT OF BST AND SiO <sub>2</sub> AS A FUNCTION OF VOLTAGE.	102
FIGURE 1.64: TEM IMAGE OF DRAM CELL USING BST AS THE DIELECTRIC, FROM KOTECKI <i>ET AL</i> [122].	103
FIGURE 1.65: EXTRAPOLATION OF ARRHENIUS-TYPE PROCESS SHOWING THE EFFECT OF SHORT FAILURE TIMES.	107
FIGURE 1.66: RESISTANCE DEGRADATION TIME TO FAILURE FOR 30 NM 51% Ti BST.	109

FIGURE 1.67: RESISTANCE DEGRADATION TIME TO FAILURE FOR 30 NM 51% Ti BST WITH AXES TRANSFORMED.....	110
FIGURE 1.68: MONTE CARLO TIME-TO-FAILURE DATA FROM A LOGNORMAL DISTRIBUTION, UNCENSORED.....	111
FIGURE 1.69: SAME MONTE CARLO AS FIGURE 1.68, SHOWING THE EFFECT OF CENSORING ON THE DISTRIBUTION. ....	111
FIGURE 1.70: WEIBULL PLOT OF DIFFERENT FIT RATES. ADAPTED FROM STATHIS[134]. .....	113
FIGURE 1.71: SCHEMATIC OF GRAPHICAL DETERMINATION OF THE RELIABILITY REQUIREMENTS. ADAPTED FROM HUNTER[129]. ....	114
FIGURE 1.72: WEIBULL PLOT ILLUSTRATING THE EFFECT OF INCREASING STRESS, TYPICALLY ELECTRIC FIELD. ADAPTED FROM HUNTER[129]. ....	114
FIGURE 1.73: WEIBULL PLOT SCHEMATICALLY SHOWING THE EFFECT OF AREA SCALING. ADAPTED FROM STATHIS[134]. ....	115
FIGURE 1.74: DEFECT DENSITY AS A FUNCTION OF INJECTED CHARGE, FOR VARIOUS VOLTAGES. ADAPTED FROM STATHIS[134]. ....	117
FIGURE 1.75: THE PERCOLATION MODEL. ADAPTED FROM DEGRAEVE <i>ET AL</i> [140]....	121
FIGURE 1.76: THE DIFFERENCE BETWEEN SOFT AND HARD BREAKDOWN IN SiO <sub>2</sub> IS THAT IN HARD BREAKDOWN, THE FAILURE AREA PROPAGATES ACROSS THE OXIDE, WHEREAS IN SOFT BREAKDOWN, THERE IS A LOCAL CAPACITIVE DISCHARGE AND INCREASED CURRENT THEREAFTER. ADAPTED FROM SATAKE <i>ET AL</i> [143].....	122
FIGURE 1.77: TYPICAL RESISTANCE DEGRADATION CURVE, SHOWN FOR A BST FILM.[144] .....	123

FIGURE 2.1: SCHEMATIC OF THE LIQUID SOURCE-MOCVD SYSTEM USED TO DEPOSIT THE BST FILMS USED IN THIS STUDY. ....	144
FIGURE 2.2: X-RAY PATTERNS OF A THICKNESS SERIES OF BST FILMS.....	145
FIGURE 2.3: TEM IMAGE OF A (110) BST GRAIN SURROUNDED BY (100) GRAINS IN (A) BRIGHT FIELD AND (B) DARK FIELD. ....	146
FIGURE 2.4: AFM IMAGE OF A 5 X 5 $\mu\text{M}$ PORTION OF A 51.0 AT. % Ti, 30 NM BST FILM ON Pt/SiO <sub>2</sub> /Si. ....	146
FIGURE 2.5: SAMPLE CONFIGURATION USED IN THIS STUDY. ....	148
FIGURE 2.6: CAPACITANCE-VOLTAGE AND PERMITTIVITY-FIELD PLOT OF A 80 NM THICK 51.0% Ti BST FILM. ....	150
FIGURE 2.7: CAPACITANCE-FREQUENCY PLOT OF 580 NM 53% Ti BST FILM. ....	151
FIGURE 2.8: CURRENT-VOLTAGE SCHEMATIC FOR BST, SHOWING THE TWO MAIN LEAKAGE REGIMES. ADAPTED FROM EZHILVALAVAN <i>ET AL</i> [119]. ....	152
FIGURE 2.9: CURRENT-VOLTAGE PLOT FOR A 51 AT. % Ti., 30 NM BST SAMPLE[112]. .....	152
FIGURE 2.10: CURRENT-TIME SCHEMATIC SHOWING THE THREE MAIN REGIMES[112]. .....	153
FIGURE 2.11: SCHEMATIC OF AC DEGRADATION SYSTEM.....	154
FIGURE 2.12: SCREEN CAPTURE FROM XRD SYSTEM .....	155
FIGURE 2.13: SCHEMATIC OF THE TEMPERATURE STAGE. ....	157
FIGURE 2.14: 10 K PER MINUTE TEMPERATURE RAMP SHOWING THE STAGE TEMPERATURE AND SAMPLE SURFACE TEMPERATURE. ....	158

FIGURE 2.15: STEADY-STATE TEMPERATURE CALIBRATION DATA FOR COLD STAGE FROM 85 K TO 580 K. ....	159
FIGURE 2.16: PT/BST/PT FILM AFTER LIFTOFF AND REDEPOSITION ON THE SUBSTRATE. .....	161
FIGURE 2.17: WIRE BOND ATTACHED TO A TOP ELECTRODE ON A LIFTED OFF BST FILM. .....	161
FIGURE 3.1: RELATIVE PERMITTIVITY AS A FUNCTION OF TEMPERATURE FOR VARIOUS THICKNESSES, GIVEN IN NM, ON THE SUBSTRATE. ....	163
FIGURE 3.2 RELATIVE PERMITTIVITY AS A FUNCTION OF TEMPERATURE FOR VARIOUS THICKNESSES, GIVEN IN NM, AFTER BEING LIFTED OFF THE SUBSTRATE. ....	165
FIGURE 3.3: THE DIELECTRIC LOSS TANGENT BST FILMS AS A FUNCTION OF TEMPERATURE, ON THE SUBSTRATE. THICKNESSES ARE GIVEN IN NM.....	165
FIGURE 3.4: THE DIELECTRIC LOSS TANGENT BST FILMS AS A FUNCTION OF TEMPERATURE, AFTER BEING LIFTED OFF THE SUBSTRATE. THICKNESSES ARE GIVEN IN NM. ....	166
FIGURE 3.5: RELATIVE PERMITTIVITY AND DIELECTRIC LOSS TANGENT AS A FUNCTION OF ELECTRIC FIELD FOR A 15 NM BST FILM. ....	168
FIGURE 3.6: RELATIVE PERMITTIVITY AND DIELECTRIC LOSS TANGENT AS A FUNCTION OF ELECTRIC FIELD FOR A 40 NM BST FILM. ....	168
FIGURE 3.7: RELATIVE PERMITTIVITY AND DIELECTRIC LOSS TANGENT AS A FUNCTION OF ELECTRIC FIELD FOR A 67 NM BST FILM. ....	169
FIGURE 3.8: RELATIVE PERMITTIVITY AND DIELECTRIC LOSS TANGENT AS A FUNCTION OF ELECTRIC FIELD FOR A 154 NM BST FILM. ....	169

FIGURE 3.9: RELATIVE PERMITTIVITY AND DIELECTRIC LOSS TANGENT AS A FUNCTION OF ELECTRIC FIELD FOR A 302 NM BST FILM. ....	170
FIGURE 3.10: RELATIVE PERMITTIVITY AND DIELECTRIC LOSS TANGENT AS A FUNCTION OF ELECTRIC FIELD FOR A 581 NM BST FILM. ....	170
FIGURE 3.11: THE RELATIVE PERMITTIVITY AS A FUNCTION OF ELECTRIC FIELD FOR VARIOUS BST FILM THICKNESSES, GIVEN IN NM. ....	171
FIGURE 3.12: THE EFFECT OF FIELD ON THE PERMITTIVITY OF A 581 NM BST FILM AS A FUNCTION OF TEMPERATURE, WITH A 15 NM FILM FOR COMPARISON. ....	172
FIGURE 3.13: DIELECTRIC RESPONSE OF A $\text{Pb}(\text{Li}_{1/4}\text{Fe}_{1/4}\text{W}_{1/2})\text{O}_3$ CERAMIC AS A FUNCTION OF TEMPERATURE FOR VARIOUS FREQUENCIES, FROM LU <i>ET AL</i> [167]. ....	173
FIGURE 3.14: RELATIVE PERMITTIVITY VERSUS TEMPERATURE FOR A 53.1% TI, 40 NM BST FILM FOR A NUMBER OF FREQUENCIES. ....	173
FIGURE 3.15: RELATIVE PERMITTIVITY VERSUS TEMPERATURE FOR A 53.1% TI, 40 NM BST FILM FOR A NUMBER OF FREQUENCIES, ORDINATE SHOWN FROM ORIGIN....	174
FIGURE 3.16: DIELECTRIC LOSS TANGENT VERSUS TEMPERATURE FOR A 53.1% TI, 40 NM BST FILM FOR A NUMBER OF FREQUENCIES. ....	174
FIGURE 3.17: RELATIVE PERMITTIVITY AS A FUNCTION OF ELECTRIC FIELD, AT 85 AND 300 K, FOR A 581 NM BST FILM. ....	175
FIGURE 3.18: DIELECTRIC LOSS TANGENT AS A FUNCTION OF ELECTRIC FIELD, AT 85 AND 300 K, FOR A 581 NM BST FILM. ....	176
FIGURE 3.19: (001) PEAK OF A 40 NM BST FILM BOTH ON THE SUBSTRATE AND LIFTED OFF. ....	178
FIGURE 3.20: (002) PEAK OF A 40 NM BST FILM BOTH ON THE SUBSTRATE AND LIFTED OFF. ....	179

FIGURE 3.21: (003) PEAK OF A 40 NM BST FILM BOTH ON THE SUBSTRATE AND LIFTED OFF. ....	179
FIGURE 3.22: (004) PEAK OF A 40 NM BST FILM BOTH ON THE SUBSTRATE AND LIFTED OFF. ....	180
FIGURE 3.23: LATTICE PARAMETER VERSUS THE NELSON-RILEY FUNCTION FOR A 40 NM FILM, BOTH ON AND LIFTED OFF THE SUBSTRATE. ....	180
FIGURE 3.24: LATTICE PARAMETER VERSUS THE NELSON-RILEY FUNCTION FOR A 150 NM FILM, BOTH ON AND LIFTED OFF THE SUBSTRATE. ....	181
FIGURE 3.25: LATTICE PARAMETER VERSUS THE NELSON-RILEY FUNCTION FOR A 580 NM FILM, BOTH ON AND LIFTED OFF THE SUBSTRATE. ....	181
FIGURE 3.26: MAXIMUM PERMITTIVITY ON AND LIFTED OFF THE SUBSTRATE. ....	183
FIGURE 3.27: TRANSITION TEMPERATURE ON AND LIFTED OFF THE SUBSTRATE.....	183
FIGURE 3.28: DIFFUSENESS ON AND LIFTED OFF THE SUBSTRATE. ....	184
FIGURE 3.29: THE RELATIVE PERMITTIVITY OF A 15 NM, 53.1% Ti BST FILM, BEFORE AND AFTER REMOVAL FROM SUBSTRATE.....	184
FIGURE 3.30: THE RELATIVE PERMITTIVITY OF A 40 NM, 53.1% Ti BST FILM, BEFORE AND AFTER REMOVAL FROM SUBSTRATE.....	185
FIGURE 3.31: THE RELATIVE PERMITTIVITY OF A 67 NM, 53.1% Ti BST FILM, BEFORE AND AFTER REMOVAL FROM SUBSTRATE.....	185
FIGURE 3.32: THE RELATIVE PERMITTIVITY OF A 154 NM, 53.1% BST FILM, BEFORE AND AFTER REMOVAL FROM SUBSTRATE.....	186
FIGURE 3.33: THE RELATIVE PERMITTIVITY OF A 302 NM, 53.1% Ti BST FILM, BEFORE AND AFTER REMOVAL FROM SUBSTRATE.....	186

FIGURE 3.34: THE RELATIVE PERMITTIVITY OF A 581 NM, 53.1% Ti BST FILM, BEFORE AND AFTER REMOVAL FROM SUBSTRATE.....	187
FIGURE 3.35: SCHEMATIC OF CAPACITOR CIRCUIT WITH DEAD LAYER APPROXIMATION, COMPOSED OF BULK AND INTERFACE CAPACITORS, DEPENDENCIES OF COMPONENTS ARE DETAILED. THE EQUIVALENT CIRCUIT IS SHOWN ON THE RIGHT. ....	188
FIGURE 3.36: DEAD LAYER TREATMENT OF INVERSE CAPACITANCE DENSITY AS A FUNCTION OF THICKNESS.....	189
FIGURE 3.37: SLOPES CALCULATED FROM THE DEAD LAYER TREATMENT AS A FUNCTION OF TEMPERATURE. ....	191
FIGURE 3.38: INTERCEPTS CALCULATED FROM THE DEAD LAYER TREATMENT AS A FUNCTION OF TEMPERATURE.....	191
FIGURE 3.39: "BULK" RELATIVE PERMITTIVITIES CALCULATED FROM THE DEAD LAYER TREATMENT.....	192
FIGURE 3.40: CURIE-WEISS PLOT OF INVERSE PERMITTIVITY AS A FUNCTION OF TEMPERATURE, FOR VARIOUS THICKNESSES, BST FILMS ON THE SUBSTRATE.....	193
FIGURE 3.41: CURIE-WEISS PLOT OF INVERSE PERMITTIVITY AS A FUNCTION OF TEMPERATURE, FOR VARIOUS THICKNESSES, BST FILMS LIFTED OFF THE SUBSTRATE. ....	194
FIGURE 3.42: CURIE TEMPERATURES FROM THE CURIE-WEISS PLOTS SHOWN IN FIGURE 3.40 AND FIGURE 3.41, AS A FUNCTION OF INVERSE THICKNESS.....	194
FIGURE 3.43: CURIE CONSTANTS AND TEMPERATURES FROM THE CURIE-WEISS PLOTS SHOWN IN FIGURE 3.40 AND FIGURE 3.41, AS A FUNCTION OF THICKNESS.....	195

FIGURE 3.44: THE DEAD LAYER PLOT CHOOSES ONE TEMPERATURE FOR THE ANALYSIS, AS SHOWN IN PART A WITH THE MEASURED PERMITTIVITIES. BUT THE CURVES WOULD REQUIRE THE FORM IN PART B FOR THE ANALYSIS TO YIELD THE PROFFERED INTERPRETATION.....	196
FIGURE 3.45: LOG-LOG PLOT OF TRANSITION DIFFUSENESS AS A FUNCTION OF THICKNESSES, GIVEN IN NUMBER OF UNIT CELLS. ....	199
FIGURE 3.46: TRANSITION DIFFUSENESS AS A FUNCTION OF THICKNESSES, GIVEN IN NUMBER OF UNIT CELLS. ....	200
FIGURE 3.47: LOG-LOG PLOT OF MAXIMUM PERMITTIVITY AS A FUNCTION OF THICKNESSES, GIVEN IN NUMBER OF UNIT CELLS. ....	201
FIGURE 3.48: LOG-LOG PLOT OF MAXIMUM PERMITTIVITY AS A FUNCTION OF THICKNESSES, GIVEN IN NM. ....	202
FIGURE 3.49: LOG-LOG PLOT OF TRANSITION TEMPERATURE SHIFT AS A FUNCTION OF THICKNESSES, GIVEN IN NUMBER OF UNIT CELLS. ....	203
FIGURE 3.50: TRANSITION TEMPERATURE SHIFT AS A FUNCTION OF THICKNESSES, GIVEN IN NM.....	203
FIGURE 3.51: (A) MAGNETIC SUSCEPTIBILITY AS A FUNCTION OF FIELD FOR VARIOUS THICKNESSES, GIVEN IN NUMBER OF UNIT CELLS, FROM BINDER AND HOHENBURG[53] (B) RELATIVE PERMITTIVITY AS A FUNCTION OF ELECTRIC FIELD FOR A NUMBER OF THICKNESSES, GIVEN IN NM.....	205
FIGURE 3.52: VARIATION OF THE SOFT MODE IN $\text{SrTiO}_3$ FOR VARIOUS TEMPERATURES, FROM COWLEY[20]. ....	209
FIGURE 3.53: THE RELATIVE PERMITTIVITY AS A FUNCTION OF ELECTRIC FIELD FOR VARIOUS BST FILMS USED IN THIS STUDY; THICKNESSES GIVEN IN NM. ....	212

FIGURE 3.54: THE RELATIVE PERMITTIVITY AS A FUNCTION OF ELECTRIC FIELD FOR VARIOUS BST FILMS; THICKNESSES GIVEN IN NM.....	213
FIGURE 3.55: LINEAR TERMS OF POLYNOMIAL FIT TO ELECTRIC FIELD-PERMITTIVITY CURVES, AS A FUNCTION OF THICKNESS.....	214
FIGURE 3.56: MEAN TERMS OF POLYNOMIAL FIT TO ELECTRIC FIELD-PERMITTIVITY CURVES, AS A FUNCTION OF THICKNESS.....	215
FIGURE 3.57: QUADRATIC TERMS OF POLYNOMIAL FIT TO ELECTRIC FIELD- PERMITTIVITY CURVES, AS A FUNCTION OF THICKNESS. ....	215
FIGURE 3.58: THIRD-ORDER TERMS OF POLYNOMIAL FIT TO ELECTRIC FIELD- PERMITTIVITY CURVES, AS A FUNCTION OF THICKNESS. ....	216
FIGURE 3.59: SCHEMATIC OF A BST DRAM CELL.....	222
FIGURE 3.60: CURVES OF CAPACITANCE DENSITY VERSUS DRAM CELL HEIGHT FOR VARIOUS DESIGN RULES, ADAPTED FROM SUMMERFELT[173]. ....	223
FIGURE 3.61: SCHEMATIC OF CONFORMAL BST ON Pt BOTTOM ELECTRODES SHOWING GEOMETRIC LIMITATIONS OF THE PLUG TYPE CAPACITOR. ADAPTED FROM SUMMERFELT[173]. ....	223
FIGURE 4.1: MOST INVESTIGATIONS OF FAILURE IN BST HAVE BEEN CONDUCTED IN QUADRANT I, WHERE RESISTANCE DEGRADATION DOMINATES. THIS DISSERTATION WILL EXTEND THE INVESTIGATION OF FAILURE TO II AND IV.....	227
FIGURE 4.2: TYPICAL TDDB FAILURE, SHOWN FOR A 51% Ti, 40 NM BST SAMPLE STRESSED AT 1250 kV/cm AT 25 °C. ....	230
FIGURE 4.3: TYPICAL NOISY BREAKDOWN FAILURE, SHOWN FOR A 51% Ti, 40 NM BST SAMPLE STRESSED AT 1250 kV/cm AT 25 °C.....	230

FIGURE 4.4: TYPICAL RESISTANCE DEGRADATION FAILURE, SHOWN FOR A 51% Ti, 40 NM BST SAMPLE STRESSED AT 1250 kV/cm AT 25 °C.....	231
FIGURE 4.5: WEIBULL PLOT OF TDDB AND NOISY BREAKDOWN FAILURES TOGETHER FOR 51.0% Ti, 40NM, 1250 kV/cm DC STRESS. ....	232
FIGURE 4.6: WEIBULL PLOTS OF TDDB AND NOISY BREAKDOWN FAILURES FOR 51.0% Ti, 40NM, 1250 kV/cm DC STRESS. ....	233
FIGURE 4.7: TOP ELECTRODE OF A CAPACITOR THAT FAILED FROM TDDB. THE AREAS OF FAILURE CAN BE SEEN AS DARK CIRCLES IN THE IMAGE. ....	235
FIGURE 4.8: SCRATCH MADE BY PROBE ON THE TOP ELECTRODE OF A SAMPLE THAT FAILED FROM NOISY BREAKDOWN. ....	235
FIGURE 4.9: SCRATCH MADE BY PROBE ON THE TOP ELECTRODE AND A NEARBY HOLE IN THE ELECTRODE OF A SAMPLE THAT FAILED FROM TDDB. ....	236
FIGURE 4.10: TOP ELECTRODE OF A CAPACITOR THAT FAILED FROM TDDB SHOWING CATASTROPHIC FAILURE.....	236
FIGURE 4.11: CHARGING AND DISCHARGING MEASUREMENTS SHOWING SEPARATION OF POLARIZATION AND TRUE LEAKAGE CURRENTS FOR A 52.0 AT% Ti 60 NM BST FILM AT 25 °C. ADAPTED FROM KINGON <i>ET AL</i> [174].....	239
FIGURE 4.12: CURRENT-TIME OF A 52.0 AT% Ti. 90 NM FILM AT 25 °C, FOR VARIOUS STRESS TIMES. ....	240
FIGURE 4.13: DISCHARGE CURRENT-TIME DATA FOR A 51.0 AT% Ti, 40NM BST FILM, LINES INDICATE POWER-LAW FIT.....	242
FIGURE 4.14: LOG CURRENT VERSUS VOLTAGE FOR A 51.0 AT% Ti, 40NM BST FILM, FOR VARIOUS STRESS CYCLES. ....	243

FIGURE 4.15: CURRENT VERSUS VOLTAGE FOR A 51.0 AT% TI, 40NM BST FILM, FOR VARIOUS STRESS CYCLES. ....	244
FIGURE 4.16: SCHEMATIC OF A LEVERAGE PLOT. ....	249
FIGURE 4.17: WHOLE MODEL LEVERAGE PLOT FOR RESISTANCE DEGRADATION MODEL. .....	249
FIGURE 4.18: PLOT OF MODEL RESIDUALS FOR THE RESISTANCE DEGRADATION MODEL. .....	250
FIGURE 4.19: TIME TO BREAKDOWN AS A FUNCTION OF FIELD WITH MEASURED AND PREDICTED VALUES. ....	251
FIGURE 4.20: LEVERAGE PLOT FOR FIELD. ....	252
FIGURE 4.21: LEVERAGE PLOT FOR THICKNESS. ....	252
FIGURE 4.22: LEVERAGE PLOT FOR INTERACTION OF FIELD AND THICKNESS. ....	253
FIGURE 4.23: LEVERAGE PLOT FOR TEMPERATURE, ON AN AHRRENIUS SCALE. ....	253
FIGURE 4.24: LEVERAGE PLOT FOR THE INTERACTION OF FIELD AND TEMPERATURE. ....	254
FIGURE 4.25: LEVERAGE PLOT FOR THE INTERACTION OF THICKNESS AND TEMPERATURE. ....	254
FIGURE 4.26: LEVERAGE PLOT FOR COMPOSITION. ....	255
FIGURE 4.27: LEVERAGE PLOT FOR THE INTERACTION OF FIELD AND COMPOSITION. ....	255
FIGURE 4.28: LEVERAGE PLOT FOR THE INTERACTION OF THICKNESS AND COMPOSITION. ....	256
FIGURE 4.29: LEVERAGE PLOT FOR THE INTERACTION OF TEMPERATURE AND COMPOSITION. ....	256
FIGURE 4.30: LEVERAGE PLOT FOR SECOND ORDER THICKNESS EFFECT. ....	257
FIGURE 4.31: LEVERAGE PLOT FOR SECOND ORDER COMPOSITION EFFECT. ....	257

FIGURE 4.32: LOG CURRENT VERSUS TIME FOR A SEVERAL 51.0 AT% Ti 40 NM BST FILMS, STRESSED AT 1 KHZ FOR 10 <sup>9</sup> CYCLES AT VARIOUS STRESS LEVELS. ....	260
FIGURE 4.33: LOG CURRENT VERSUS TIME FOR A 51.0 AT% Ti, 40 NM SAMPLE STRESSED AT 10 V <sub>PP</sub> AND 1 MHZ. ....	261
FIGURE 4.34: WEIBULL PLOT OF AC FAILURE TIMES AND DC TDDDB FAILURE TIMES. ..	261
FIGURE 4.35: TIME TO FAILURE FOR 51.0 AT% Ti, 40 NM SAMPLES AS A FUNCTIONS OF FREQUENCY. ....	263
FIGURE 4.36: TIME TO FAILURE OF VARIOUS COMPOSITIONS OF 40 NM BST FILMS....	264
FIGURE 4.37: LOG CURRENT DENSITY VERSUS TIME FOR A 52.0 % Ti, 40 NM BST SAMPLE, FOR VARIOUS STRESS CONDITIONS. ....	265
FIGURE 4.38: LOG CURRENT DENSITY VERSUS TIME FOR A 52.0 % Ti, 40 NM BST SAMPLE, STRESSED AT ±3 V AND 1 KHZ, FOR VARIOUS NUMBERS OF CYCLES. ....	265
FIGURE 4.39: CURRENT DENSITY VERSUS TIME FOR A 40NM, 51.0% Ti SAMPLE STRESSED OF ±3V AT 1 KHZ. ....	266
FIGURE 4.40: CURRENT DENSITY VERSUS VOLTAGE FOR A 40NM, 51.0% Ti SAMPLE BEFORE AND AFTER STRESS. ....	267
FIGURE 4.41: TWO SCHEMAS FOR CLASSIFICATION OF BST FAILURE MODES (A) ATTRIBUTES SOFT BREAKDOWN TO INTERFACIAL CONTAMINATION AND (B) ATTRIBUTES SOFT BREAKDOWN TO THE SAME MECHANISM, EXPRESSED IN A DIFFERENT MODE. ....	268
FIGURE 4.42: DARK FIELD IMAGE OF Pt/BST/Pt. ....	273
FIGURE 4.43: WEIBULL PLOT FOR THREE CAPACITOR SIZES: THE RED LINE INDICATES 50 μm <sup>2</sup> CAPACITORS, THE GREEN LINE 200 μm <sup>2</sup> , AND THE BLUE 500 μm <sup>2</sup> . ....	274

FIGURE 4.44: WEIBULL PLOT FOR STRESS VOLTAGES: THE RED LINE INDICATES 7 V STRESS, THE GREEN LINE 8 V STRESS, AND THE BLUE LINE 9 V STRESS..... 276

FIGURE 4.45: WEIBULL PLOT OF THE THREE VOLTAGES, TESTED AT 25 °C, THEIR ASSOCIATED LINES OF FIT, AND THE EXTRAPOLATED FAILURE DISTRIBUTIONS FOR VARIOUS VOLTAGES. .... 280

FIGURE 4.46: WEIBULL PLOT OF THE THREE VOLTAGES, AT 80 °C, EXTRAPOLATED USING THE RESINGER TEMPERATURE DATA, THEIR ASSOCIATED LINES OF FIT, AND THE EXTRAPOLATED FAILURE DISTRIBUTIONS FOR VARIOUS VOLTAGES. .... 281

FIGURE 4.47: WEIBULL PLOT SHOWING EXTRAPOLATED BST FAILURE DISTRIBUTIONS AS WELL AS THE 10 FIT LINES FOR THE DEVICE AND TESTED AREA..... 282

# Chapter 1: LITERATURE REVIEW

## 1.1: Ferroelectricity

A ferroelectric is a material that exhibits a switchable, spontaneous polarization under equilibrium conditions below some temperature. The first observation of ferroelectricity was made in 1921 by Valasek[1]. He noted that Rochelle salt exhibited dielectric hysteresis in certain crystallographic directions. Valasek compared the phenomena with ferromagnetism, from which ferroelectricity gets its name by analogy. Three things were noted. First, the measured electric polarization depends on the previously applied field in much the same way that iron shows hysteresis in a plot of induction vs. field (**B** vs. **H**). Second, there is a transition temperature,  $T_C$ , above which there is no dielectric anomaly. And third, there is a large dielectric and piezoelectric response near and below  $T_C$ .

Above the transition temperature or Curie temperature, a ferroelectric material is paraelectric. Near the Curie temperature, ferroelectrics display anomalous behavior in their dielectric, elastic, optical, and thermal properties. The exact nature of the anomalies

depend on the order of the transformation. The crystal structure in the paraelectric phase is centrosymmetric. At the phase transition it changes to a more general structure, loses symmetry, and becomes ferroelectric[2].

Ferroelectric properties arise from the crystallographic changes at the transition temperature; chief among these properties is the spontaneous polarization. The spontaneous polarization is linked to high permittivity, pyroelectricity, piezoelectricity (electromechanical response), and non-linear electrical properties. These properties show a temperature dependence of the same form as the polarization. Figure 1.1 illustrates the relationship between ferroelectricity and crystal structure.

Of the 32 point groups, 21 are non-centrosymmetric. A non-centrosymmetric point group has at least one unique direction. A unique direction cannot be made to coincide with another by a symmetry operation. Of these non-centrosymmetric point groups, 10 have only one unique axis that is crystallographically different at one end than the other end. These ten are known as polar crystals. All the potential ferroelectric materials belong to this class. The paraelectric-ferroelectric transformation of a material can be of either first or second order and either of the displacive or order-disorder type. If the transformation is displacive, it is referred to as a normal ferroelectric, or if order-disorder, as a relaxor ferroelectric[3].

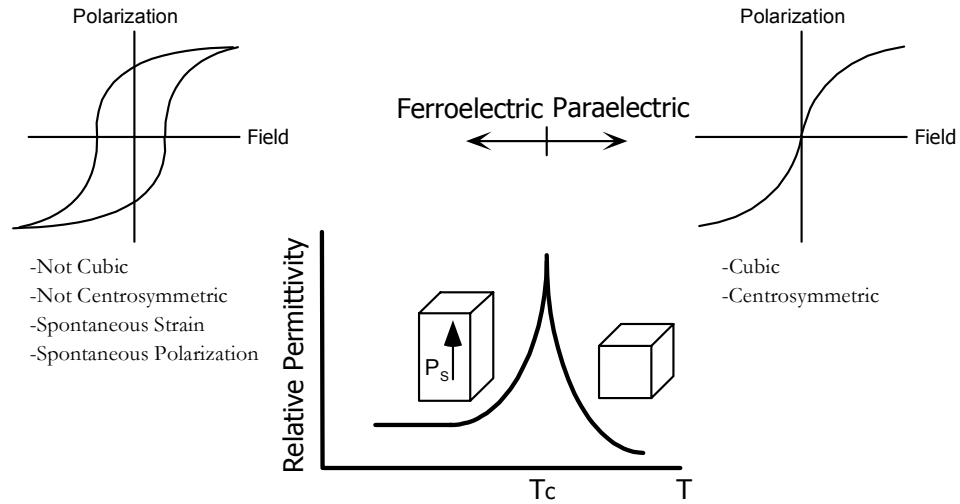


Figure 1.1: Essential Features of Ferroelectricity.

The hallmark of ferroelectricity is a reduction in crystal symmetry as the crystal undergoes the phase transformation.

There are several descriptive metrics used to characterize ferroelectrics. The Curie-Weiss plot is the most common, for historical reasons. It is a plot of inverse permittivity versus temperature, as seen in Figure 1.60. The two coefficients are the slope, or Curie-Weiss constant, and the intercept, or Curie-Weiss temperature. The equation for the Curie-Weiss fit is

$$\frac{1}{\epsilon(T)} = \frac{(T - T_C)}{C'}$$

It should be noted that the Curie temperature is the temperature of the ferroelectric-paraelectric phase transition and the Curie-Weiss temperature is the extrapolated intercept of the linear portion of the Curie-Weiss plot. These two temperatures are not necessarily the same, although they can be.

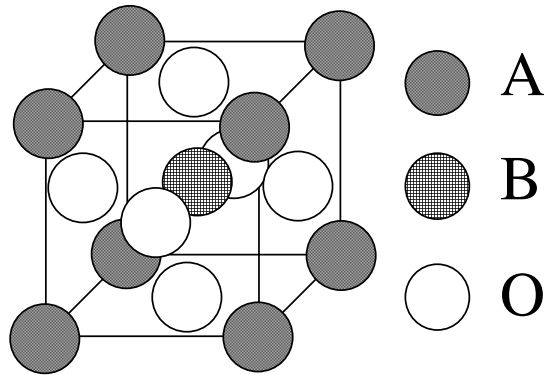


Figure 1.2: The perovskite crystal structure.

The ferroelectric crystal structure of interest is perovskite, shown schematically in Figure 1.2. Named after the mineral  $\text{CaTiO}_3$ , or perovskite, it is of the form  $\text{ABO}_3$ . A is a 1+, 2+, or 3+ metal and B is a 5+, 4+, or 3+ element. The three oxygen atoms provide a charge of 6-. It is cubic in the paraelectric phase and non-cubic in the ferroelectric phase. The spontaneous polarization is typically considered as being linked to a distortion of the  $\text{BO}_6^{4-}$  octahedron. The displacements that occur at the phase transition are relatively small. The ferroelectric phase transformation has relatively shallow minima. The energy barrier is small enough to be accessible by the switching of an applied electric field. There are relationships between the phase transition, crystal symmetry, and dielectric properties. The dielectric properties are thus dependent on the temperature, stress and strain, applied field, composition, and size of the ferroelectric, as explained in the next section.

## 1.2: Models of Ferroelectricity

Two main classes of models are used to describe ferroelectrics: phenomenological models and statistical models. Phenomenological models are based on phenomenological thermodynamics. They model macroscopic behavior well, *e.g.*, effects of crystal symmetry under equilibrium conditions. Descriptions neither require nor provide understanding of microscopic mechanisms. Microscopic models are based on statistical thermodynamics. Model parameters have physical meaning, accounting for the dipoles and interactions of dipoles. However, the model parameters are unmeasurable.

Landau theory is a microscopic theory. Landau-Ginzburg theory is the phenomenological form of Landau theory. The phenomenological approach to ferroelectricity was developed by Devonshire, based upon the Landau-Ginzburg phase transformation theory, and originally dealt with the case of  $\text{BaTiO}_3$ [4], but was later extended to ferroelectrics generally[5]. It is referred to as LGD theory.

### 1.2.1: Phenomenological Theory of Ferroelectricity

The discussion of the phenomenological theory is divided into two portions. The first is the thermodynamic theory of crystals and the second is the thermodynamic theory of ferroelectric phase transformations.

The thermodynamic theory of crystals models the relationships between the thermal, electrical, and mechanical properties of a crystal. The classic graphical representation of these relationships is presented in Figure 1.3, adapted from Nye[6]. Examination of the figure makes clear the importance of the various couplings. For

instance, to know the permittivity, it is necessary to know the temperature, polarization, electric field, and stress or strain. These relationships are combined with the requirements of crystal symmetry to describe the system.

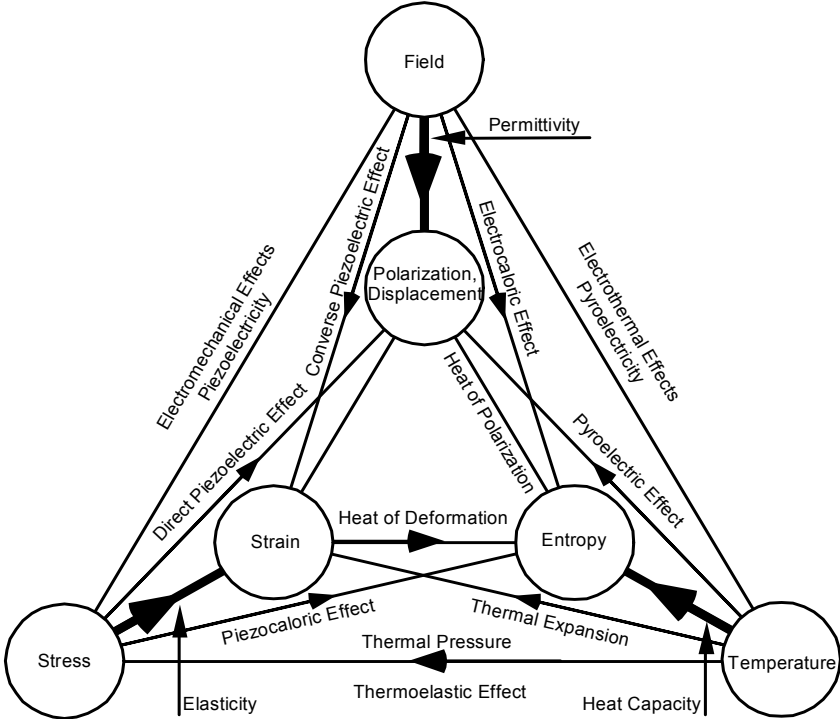


Figure 1.3: Relationship of various thermodynamic quantities, adapted from Nye[6]  
 The independent experimental variables, on the outer triangle, are shown in their relationship to the dependent experimental variables, on the inner triangle.

The LGD approach makes several assumptions. It assumes that the stress  $\mathbf{X}_{ij}$ , strain  $\mathbf{x}_{ij}$ , electric field  $E$ , polarization  $P$ , temperature  $T$ , and entropy,  $S$ , are sufficient to describe a dielectric system.  $E$  and  $P$  are vectors,  $\mathbf{X}_{ij}$  and  $\mathbf{x}_{ij}$  are second rank tensors, and  $T$  and  $S$  are scalars. Depending upon the symmetry of the crystal, the system can be determined with as few as 10 variables. There are several ways that the free energy function can be constructed. Specific experimental systems are chosen to simplify the analysis. It is easier to vary stress and field, so it is logical to have stress and field as independent variables and strain and polarization as dependent variables.

To give an example of this descriptive flexibility, consider the Helmholtz free energy

$$A = U - TS$$

and the Elastic Gibbs function

$$G = H - TS$$

along with their differential relations

$$dA = -SdT - X_{ij}dx_{ij} + E_i dP_i$$

and

$$dG = -SdT + x_{ij}dX_{ij} + E_i dP_i.$$

Examination of these two differential relationships suggests several things. First, at a constant temperature, there should be a direct relationship between the stress and strain and the electric field and polarization, as illustrated in Figure 1.3. Second, at constant stress and constant temperature, the elastic Gibbs function varies as a function of polarization only, likewise the Helmholtz free energy varies as a function of polarization only for constant strain and temperature.

To evaluate the thermodynamic function, LGD theory uses a power series expansion of the free energy in the independent variables near the paraelectric-ferroelectric transition temperature. This approach allows use of the same descriptive equation above and below the transition temperature.

As mentioned above, the appropriate free energy terms depend on the experimental system. Typically the elastic Gibbs function is chosen, with polarization as

the order parameter. For the case where the stresses are zero, the polarization vector is only along one crystal direction, and the non-polar phase is centrosymmetrical, the free energy is[5]

$$G(\Theta, P) = G_o(\Theta) + \frac{1}{2}\beta(\Theta)P^2 + \frac{1}{4}\xi(\Theta)P^4 + \frac{1}{6}\zeta(\Theta)P^6.$$

where  $\Theta$  is temperature and  $P$  is polarization. The series expansions are by nature an approximation, so the number of terms included is governed by standard considerations of explanatory power versus the number of model parameters.

A stable state corresponds to a minimum in the free energy. Both  $\xi(\Theta)$  and  $\zeta(\Theta)$  are weak functions of temperature and are typically assumed to be temperature independent. Solving for  $P_s \neq 0$  shows that for  $\xi > 0$  a second-order phase transformation is preferred and for  $\xi < 0$  a first-order transformation is preferred.

More useful relations are obtained when the derivative of free energy with respect to polarization is taken. Typically, the form is terminated after the cubic term. This is partly because the higher order terms are less significant to the overall equation of fit and partly because it is impossible to find a closed form of polarization as a function of field above third order. The third order equation is

$$\frac{\partial \tilde{G}}{\partial P} = E_{app} \approx 2\alpha_1 P + 4\alpha_{11} P^3$$

The relationships of the LGD theory allow not only the acquisition of physical quantities that are experimentally inaccessible, but also allows quantitative prediction of the interaction of the variables in the equation of state, such as the effects of strain on the transition temperature.

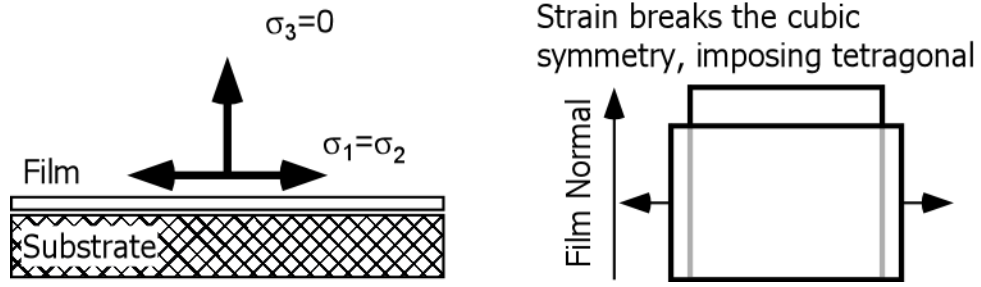


Figure 1.4: Effect of thin film stress on cubic materials

Perovskites are cubic above the transition temperature. The tensile strain arises from mismatch of the thermal expansion coefficients between the substrate and the film.

The case of thin film perovskites is different from bulk perovskites in several ways. First, instead of being under conditions of constant stress, films are typically under conditions of constant strain. This leads to minimization not of the Gibbs free energy, but rather of the Helmholtz free energy. Films are under a biaxial strain because of growth stresses and the thermal expansion differences of the film, electrodes, and substrate. The formula for a {100}-oriented film under equibiaxial strain has been previously derived and is [7]

$$\frac{\partial \Delta A}{\partial P} = E = \alpha_1 P + \alpha_{11} P^3 + \alpha_{111} P^5 - 2g_{11} x_3 P - 4g_{12} x_1 P$$

where  $A$  is the Helmholtz free energy,  $E$  is the electric field across the film, and  $P$  is the polarization normal to the substrate[7].  $\alpha_1$ ,  $\alpha_{11}$ , and  $\alpha_{111}$  are the dielectric stiffnesses,  $g_{11}$  and  $g_{12}$  are elements of the electrostrictive tensor.  $x_1$  is the in-plane principal strain and  $x_3$  is the principal strain normal to the surface. Since the film is relatively cubic and under equibiaxial strain from the substrate,  $x_1$  and  $x_3$  can be related from the elastic tensor as

$$x_3 = \frac{-2C_{12}x_1}{C_{11}}$$

where  $C_{11}$  and  $C_{12}$  are the appropriate stiffnesses. Grouping terms yields

$$E = \left[ \alpha_1 + \left( \frac{4g_{11}C_{12}}{C_{11}} - 4g_{12} \right) x_1 \right] P + \alpha_{11} P^3 + \alpha_{111} P^5,$$

which can be used to calculate the effect of strain on the dielectric response.

The equation was simplified further by Streiffer *et al.*[8] by substituting empirical parameters for thermodynamic parameters, indicated by the prime, and dropping the fifth order term, yielding

$$E_{app} = 2\alpha' P + 4\alpha' P^3$$

The cubic dielectric stiffness was found to be relatively temperature and thickness independent. However, the linear term can be decomposed into a thickness dependent term and a temperature dependent term, making the final form of the relationship

$$E_{app} = 2 \left( \frac{\beta}{t} + \gamma(T) \right) P + 4\alpha' P^3$$

### 1.2.2: Microscopic Theory of Ferroelectricity

Microscopic, or statistical, models of ferroelectricity deal with the atoms and the forces between the atoms directly, rather than in a continuum as the phenomenological models do. Ideally, the models would be able to calculate the structure and properties of a crystal if the chemical composition is known. Practically, the models are developed and tested with data from known ferroelectrics. The Hamiltonian is constructed to capture the desired features of the ferroelectric system. There are a large number of models, but the discussion will be limited to the one most commonly used to describe ferroelectrics, the 3D Ising model[9].

The Ising model treats materials as a lattice of spins. A simple cubic Ising lattice is illustrated in Figure 1.5. The number and values of allowed spins vary, but for ferroelectrics it is sufficient to have two spins, up or down, with values of  $\pm 1$ . Interactions between the spins and interactions with the boundary conditions are of four types: applied external field, long-range interactions with distant units, long-range interactions with nearby units, and short range interactions with nearby units. The interactions are calculated on a spin-to-spin-basis, so the model is not necessarily mean field. Once the Hamiltonian is defined, the thermodynamic potential can be calculated. Ising models are typically presented in the following form

$$U(\sigma) = -\frac{1}{2} \sum_{RR'} J(R-R') \sigma_R \sigma_{R'}$$

where the spins are given by  $\sigma$ , the positions of the spins by  $R$ , and the interactions by  $J$ . The 2D Ising model is attractive because it is analytically solvable for thermodynamic functions. The 3D Ising model must be numerically approximated.

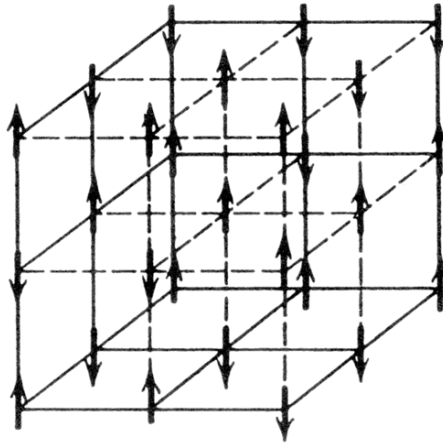


Figure 1.5: The 3D Ising model, from Strukov and Levanyuk[9]

A general model, the Ising model approximates a material as a lattice of spins. Ising models can be used to model many materials besides ferroelectrics and ferromagnets.

There are many applications of the 3D Ising model to ferroelectrics exist, so one particular variant will be presented: the four-spin transverse Ising model for first order ferroelectrics[10, 11]. The Hamiltonian is

$$H = -\sum_i \Omega_i S_i^x - \frac{1}{2} \sum_{ij} J_{ij} S_i^z S_j^z - \frac{1}{4} \sum_{ijkl} J_{ijkl} S_i^z S_j^z S_k^z S_l^z$$

where the tunneling frequency is  $\Omega$ ,  $S_i^x$  is the x-component of the spin at lattice site  $i$  and  $S_i^z$  the corresponding z-component.  $J_{ij}$  is the two-spin and  $J_{ijkl}$  the four-spin interaction constant. The average, or mean-field, spin of the system is

$$S_i = \left( \langle S_i^x \rangle^2 + \langle S_i^y \rangle^2 + \langle S_i^z \rangle^2 \right)^{1/2}$$

so that the entropy of the system can be written

$$\phi = -k_B \sum_i \left[ 2S_i \tanh^{-1}(2S_i) + \frac{1}{2} \ln(1 - 4S_i^2) \right]$$

allowing the construction of the free energy of the system

$$F = -\sum_i \Omega_i S_i^x - \frac{1}{2} \sum_{ij} J_{ij} S_i^z S_j^z - \frac{1}{4} \sum_{ijkl} J_{ijkl} S_i^z S_j^z S_k^z S_l^z + k_B T \sum_i \left[ 2S_i \tanh^{-1}(2S_i) + \frac{1}{2} \ln(1 - 4S_i^2) \right]$$

The free energy can then be simplified in the thin film approximation, *i.e.*,

$$\frac{\partial F}{\partial \langle S_i^y \rangle} = 0$$

and

$$\frac{\partial F}{\partial \langle S_i^x \rangle} = 0$$

so that the microscopic equation in the thin film approximation is

$$\begin{aligned}
F = & \sum_i \frac{\Omega_i \langle S_i^z \rangle^2}{\tanh\left(\frac{\Omega_i}{2k_B T}\right)} - \frac{1}{2} \sum_{ij} J_{ij} S_i^z S_j^z - \frac{1}{4} \sum_{ijkl} J_{ijkl} S_i^z S_j^z S_k^z S_l^z \\
& + \sum_i \frac{\Omega_i \langle S_i^z \rangle^4}{\tanh^3\left(\frac{\Omega_i}{2k_B T}\right)} \left( \frac{\sinh\left(\frac{\Omega_i}{k_B T}\right)}{\left(\frac{\Omega_i}{k_B T}\right)} - 1 \right) + \sum_i \frac{\Omega_i \langle S_i^z \rangle^6}{\tanh^5\left(\frac{\Omega_i}{2k_B T}\right)} \\
& \left( 1 - \frac{\sinh\left(\frac{\Omega_i}{k_B T}\right)}{\left(\frac{\Omega_i}{k_B T}\right)} - \frac{4 \sinh^3\left(\frac{\Omega_i}{2k_B T}\right) \cosh\left(\frac{\Omega_i}{2k_B T}\right)}{\left(\frac{3\Omega_i}{k_B T}\right)} \right)
\end{aligned}$$

If the spins change slowly as a function of position, which is a reasonable assumption for the mean-field case, the summation can be approximated by the volume integral

$$\sum_i \rightarrow \frac{1}{a_3} \int dx dy dz$$

The parameters of the microscopic model must be adapted to the phenomenological form to be experimentally measurable, so the parameters are divided into surface and bulk terms. In the 3D Ising model, there are different components for the surface and interface terms, *e.g.*, for the two spin interaction, the surface term is  $J_s$ , the bulk term is  $J_b$ , and there is a function that models the decay of the surface term into the bulk value as a function of distance from the surface. This function can be approximated as the extrapolation length,  $\delta$ . Much is said later about the extrapolation length in the scaling section, suffice it to say that the extrapolation length accounts for the presence of a surface.

The integrated microscopic model yields the phenomenological model in the LGD form, given as

$$F = \int \left[ \frac{1}{2} AP^2 + \frac{1}{2} BP^4 + \frac{1}{2} CP^6 + \frac{1}{2} D(\nabla P)^2 \right] dv + \int D \left( \frac{P^2}{2\delta} + \frac{P^4}{4\delta_4} + \frac{P^6}{6\delta_6} \right) ds$$

where the various parameters are expressed in terms of the microscopic model

$$A = \frac{a^3}{4\mu^2} \left( \frac{2\Omega}{\sinh(1/2)\beta\Omega} - 6J \right)$$

$$B = \frac{a^9}{16\mu^4} \left[ \frac{4\Omega}{\tanh^3(1/2)\beta\Omega} \left( \frac{\sinh \beta\Omega}{\beta\Omega} - 1 \right) - n_0 J_{40} \right]$$

$$C = \frac{a^{15}}{64\mu^6} \frac{2\Omega}{\tanh^5(1/2)\beta\Omega} \left( 1 - \frac{\sinh \beta\Omega}{\beta\Omega} + \frac{4 \sinh^3(1/2)\beta\Omega \cosh(1/2)\beta\Omega}{3\beta\Omega} \right)$$

$$D = \frac{a^5}{4\mu^2} J$$

$$\delta^{-1} = \frac{1}{a} \left[ \frac{5J - 4J_s}{J} + \frac{2}{J} \left( \frac{\Omega_s}{\tanh(1/2)\beta\Omega} - \frac{\Omega}{\tanh(1/2)\beta\Omega} \right) \right]$$

$$\delta_4^{-1} = \frac{a^6}{4\mu^2} \left\{ \frac{n_{40}J_{40} - n_4J_4 - n_{4s}J_{4s}}{J} + \frac{1}{J} \left[ \frac{4\Omega_s}{\tanh^3(1/2)\beta\Omega} \left( \frac{\sinh \beta\Omega_s}{\beta\Omega_s} - 1 \right) - \frac{4\Omega}{\tanh^3(1/2)\beta\Omega} \left( \frac{\sinh \beta\Omega}{\beta\Omega} - 1 \right) \right] \right\}$$

$$\delta_6^{-1} = \frac{a^{12}}{16\mu^6} \left\{ \left[ \frac{2\Omega_s}{\tanh^5(1/2)\beta\Omega_s} \left( 1 - \frac{\sinh \beta\Omega_s}{\beta\Omega_s} + \frac{4 \sinh^3(1/2)\beta\Omega_s \cosh(1/2)\beta\Omega_s}{3\beta\Omega_s} \right) \right] - \left[ \frac{2\Omega}{\tanh^5(1/2)\beta\Omega} \left( 1 - \frac{\sinh \beta\Omega}{\beta\Omega} + \frac{4 \sinh^3(1/2)\beta\Omega \cosh(1/2)\beta\Omega}{3\beta\Omega} \right) \right] \right\},$$

The above shows that it is possible to express experimentally measurable properties of ferroelectrics in terms of atomic interactions. Among the reasons that the Ising and other microscopic models are interesting is that it is possible in some cases to represent the ferroelectric in terms of a few parameters, where many more would be required in the phenomenological case. Note the relative simplicity of the Hamiltonian compared to the final equation. The main theoretical uses of the microscopic models are thus their ability to be quickly developed for a particular problem to test theoretical insights[12].

### 1.3: Size Effects

Central to understanding size effects is the proper segmentation of the topic. Much of the size effects body of work consists of *ad hoc* empirical adjustments. The effects of reduced dimension can be grouped into three categories. The first is size effects that correspond to material property changes due to dimensional scaling alone and can only be treated theoretically or computationally, these are hereafter known as finite size effects. The second is experimentally observable size effects, which incorporate pure size effects and also consider the complexity of real systems, in the current case this corresponds to electrical property changes in thin films, such as depolarization fields in the dielectric and polarization screening in the electrode. The major boundary conditions include effects of depolarization fields in the ferroelectric, domain patterns, incomplete depletion, strain, and polarization screening in the electrodes. The third is processing artifacts resulting from limitations in film, small particle, or ceramic processing technology. These artifacts arise from preparing ferroelectric crystals with arbitrarily small dimension. These can be minimized through careful procedures and characterization, see, *e.g.*, McCauley *et al.*[13]. In the case of thin films, these artifacts include changes in composition or crystallographic texture, or the presence of interfacial contamination.

The most complete model for finite size effects would start with a model Hamiltonian, derive a phenomenological form or perhaps two, one for static dielectric behavior and another for dynamic dielectric behavior, apply the corrections for the sample particulars, and produce a testable equation. Figure 1.6 shows this progression from left to right. This is currently impossible and the different approaches taken to explain size effects tend to be incomplete and fragmentary. Size effects are treated in two ways: explanations and models. Explanations provide a fundamental understanding of size

effects. Models seek to mathematically describe size effects but provide no physical origin. Explanations are the focus, as they provide fundamental insight, but to understand experimental results, models must sometimes be considered.

Finite size effects are most often explained using one of two models: the dead layer model[14, 15], which is based on the Thomas theory of ferroelectricity, and the Binder approach to finite size scaling[12, 16-19], which is based on the transverse Ising model. Both consider the effect of a free surface on the dipole-dipole interactions that give rise to ferroelectricity and the resultant effect on permittivity. The main idea of both explanations is that for unit cells near to the surface of a ferroelectric crystal, there are fewer neighboring dipoles and a consequent hardening of the soft mode. This mode hardening reduces the magnitude of the ferroelectric dipole and the dielectric susceptibility. Ferroelectric crystals of all sizes can be described as having an interior component and a surface component. Only when the crystal size becomes small enough does the relative volume fraction of the surface component become important, and a relationship between size and thermodynamic properties such as permittivity, for example, become discernible.

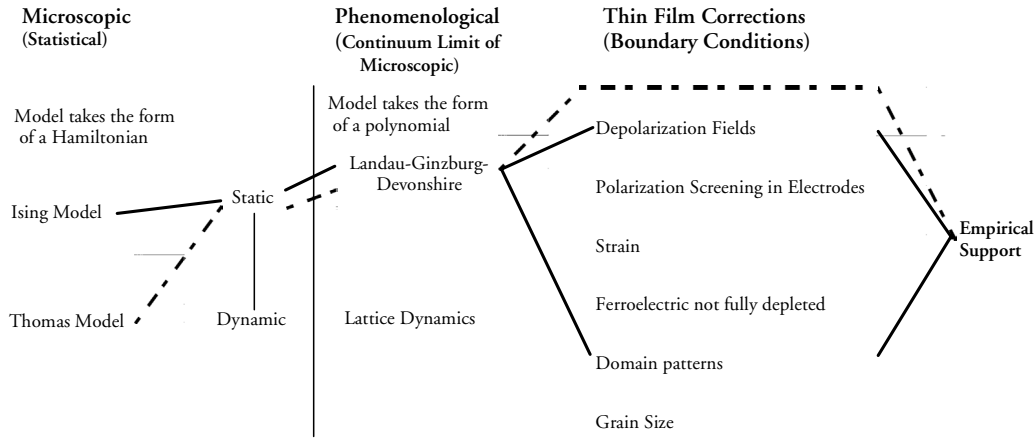


Figure 1.6: Relationships among the models of ferroelectricity. The ideal model would start on the left with atomic interactions and derive a testable phenomenological equation. The dead layer is shown as a dashed line and the Binder approach as a solid line. The approach taken in this work is that size effects are separate from the sample corrections.

### 1.3.1: Dead Layer

The first explanation of finite size effects is the dead layer model[14, 15]. It posits a “dielectrically dead layer” at the surface of the ferroelectric capacitor. The dead layer theory is an extension of the Thomas theory of ferroelectricity, which models the ferroelectric as a lattice of dipoles, each with a vibrational degree of freedom that is represented as an oscillator that represents the polarization. The cooperative nature of ferroelectricity is represented as interaction between the dipoles. Note that a dipole may not physically correspond to the motion of one ion, but may be the correlated motion of several ions. At long ranges, the interaction of the dipoles is purely electrostatic. At short ranges, the dipole motion has an anharmonicity to account for the ferroelectric polarization and an intercell interaction to account for the correlated motion of dipoles.

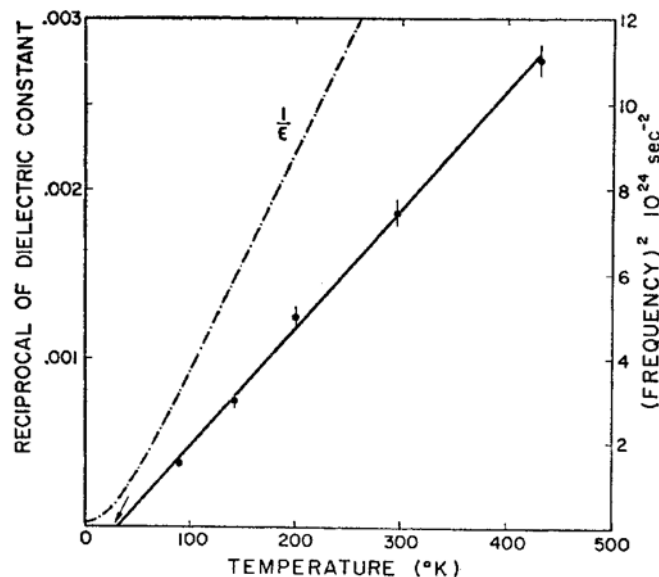


Figure 1.7: The relationship between soft mode and dielectric constant, from Cowley[20].

The soft mode frequency is a function of the restoring force of the ions. A larger restoring force leads to a higher frequency. The dielectric constant is one less than the dielectric susceptibility, which is also known as the dielectric compliance. As the crystal approaches the transition temperature it becomes softer, mechanically and electrically.

The intercell interaction incorporates phonon dispersion and other aspects of lattice dynamics in addition to the purely electrostatic. It also allows for the observed softening of the ferroelectric vibrational mode as the transition temperature is approached. The soft mode causes the polarization “catastrophe” at the transition temperature. This relationship between the soft mode and the dielectric constant, illustrated in Figure 1.7, is the principal insight of the lattice dynamical theory of ferroelectricity. The figure was taken from the most complete treatment of lattice dynamics of strontium titanate, by Cowley[20]. The functional form of the permittivity above  $T_0$  follows the Curie-Weiss law.

The derivation of the dead layer equations is not presented. The most important relations are given along with the significant physical insights. Consider a film with surface normals along the  $x$ -direction. The Thomas theory Hamiltonian takes the following form:

$$H = \sum_l (V(p_l) - Ep_l) - \frac{1}{2} \sum_{l \neq l'} v_{ll'} p_l p_{l'}$$

where

$$V(p_l) = \frac{1}{2} w_0^2 p_l^2 + \frac{1}{2} u p_l^4$$

$p_l$  is the polarization,  $V(p_l)$  is the local dipole potential,  $E$  is the internal electrostatic field,  $v_{ll'}$  is the dipole-dipole interaction,  $w_0$  is the stiffness of the harmonic oscillator,  $u$  is the anharmonic strength, and  $m$  and  $q$  are the mass and charge of the dipole, respectively.

The oscillator stiffness,  $w_0^2$ , is related to the Einstein frequency,  $\omega_0^2$ , by the following relation

$$w_0^2 = m \omega_0^2 / q^2$$

where  $m$  is the mass and  $q$  is the charge of the dipole. The other variables are defined as above. When the system is treated in mean field approximation, as denoted by brackets, the LGD form emerges from the Thomas theory. To third order, the equation is

$$E = A(T)\langle p \rangle + B(T)\langle p \rangle^3$$

where the linear and quadratic coefficients are

$$A(T) = \frac{1}{\chi^{(0)}} - V_0,$$

where  $\chi^{(0)}$  is the noninteracting susceptibility and  $V_0$  is the mean field local potential and

$$B(T) = \frac{\left(\frac{1}{T}\right)^3}{\chi^{(0)4}} \left[ \frac{\langle p^2 \rangle_0^2}{2} - \frac{\langle p^4 \rangle_0}{6} \right].$$

This result is significant because the LGD equations are presented in a form where the parameters have microscopic meaning, as before in the case of the Ising model.

Modifying the result for thin films requires modeling the polarization of the film as a function of position from the surface. The physical sense of the dead layer model is captured in Figure 1.8. A sub-polarized surface layer acts as if it is “dielectrically dead.” The bulk of the film acts as a bulk ferroelectric. As thickness decreases, there is a lower overall permittivity and a lower Curie-Weiss temperature. Dead layer theory predicts a linear relationship of thickness vs. inverse permittivity

$$\epsilon_{eff} = \frac{T_1}{T + \left(\frac{2\delta}{d\epsilon_0}\right)T_1 - T_C},$$

where  $T_1$  is a model parameter. The decrease in the Curie-Weiss temperature is

$$T_C^{eff} = T_C - \frac{2\delta}{d\epsilon_0} \approx T_C - \frac{T_0}{d\lambda}.$$

Two parameters to note for the comparison to the Binder approach are the correlation length and the dead layer thickness. The correlation length is discussed in detail in the scaling section and is given as

$$\eta = \frac{\lambda}{w} \sqrt{\frac{V_0}{T_0} (T - T_C) + \frac{4\pi}{v_c \epsilon_0}}$$

where  $\lambda'$  is the range parameter for the interaction between the dipoles, given by  $v(x)$ , and the other terms are as defined previously. Zhou and Newns draw attention to the behavior of the correlation length, noting that it does not diverge at temperature approaches the transition temperature.

The dead layer thickness is

$$\delta = \frac{1}{\lambda} \left( \sqrt{1 + \frac{v_c w_0^2 \epsilon_0}{4\pi}} - 1 \right)$$

and is related to  $\lambda$  and  $\eta$  by the following relation

$$\delta = \frac{1}{\lambda} - \frac{1}{\eta}.$$

The final form of the dead layer equation is

$$\frac{1}{C} = \frac{4\pi}{A} \left( \frac{d - 2\delta}{\epsilon_b} - \frac{2\delta}{\epsilon_0} \right),$$

where  $d$  is film thickness,  $C$  is the capacitance,  $A$  is the area of the capacitor,  $\epsilon_b$  is the bulk permittivity, and  $\epsilon_0$  is the dead layer permittivity, and  $\delta$  the dead layer thickness.

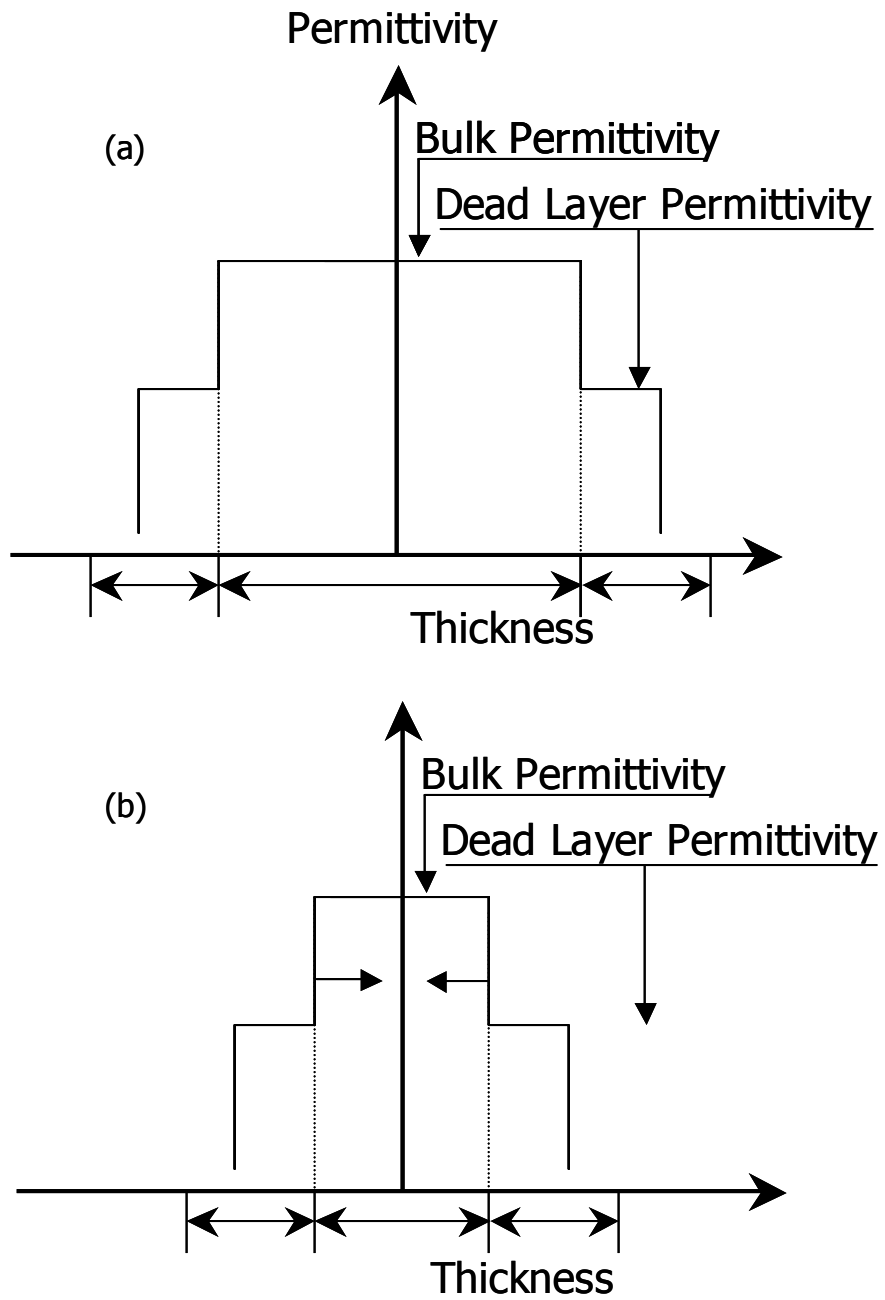


Figure 1.8: Schematic of the dead layer model.

(a) shows the dead layer at the surfaces of the film (b) shows the effect of a decrease in thickness: the two components do not change, but the ratio of components changes.

The dead layer model is used by Zhou and Newns to estimate some of the physical parameters of STO. The empirical successes are as follows. First, it observes a linear relationship of the first term of the LGD expansion. Second, the estimate for the charge to mass ratio of the dipoles is a reasonable value:  $4.7 \cdot 10^{-11} \text{ (A}\cdot\text{s)}^2 \text{ K g}^{-1}$  predicted, versus  $1.3 \cdot 10^{-11} \text{ (A}\cdot\text{s)}^2 \text{ K g}^{-1}$  calculated, based on a guess of the nature of the actual dipoles in the system. Third, the Einstein vibration frequency is of the right order of magnitude. However, the dead layer model does not provide an explanation for a change in the Curie constant or diffuseness of transition with decreasing film thickness and there are many model parameters.

Sinnamon *et al.* have summarized the possible physical origins of the dead layer, apart from the symmetry arguments of the soft mode[21]. Those proposed origins not dealt with in the boundary conditions section are discussed briefly. First, a low dielectric constant space charge region at the interface could lower the near-surface permittivity[22]. However Batra *et al.* show that the influence of such a space charge region is an insufficient explanation[23-26]. Second, there could be an increase in oxygen vacancy concentration near the film surface. Electrodes such as Pt can accommodate a large amount of oxygen, leaving the dielectric oxygen-deficient. This could directly cause the dead layer, or effect the creation of surface states that serve as the origin of the dead layer[27]. However, this effect should be mitigated by an O<sub>2</sub> anneal, and there is little difference in film properties between an O<sub>2</sub> and an N<sub>2</sub> anneal[28]. Finally, interdiffusion between the dielectric and electrode are another possible origin, but the data are inconclusive[29, 30].

Evidence for the hardening of the soft mode in thinner ferroelectric films is given by Xi *et al.*[31]. Far-infrared ellipsometry and low frequency dielectric measurements were made on SrTiO<sub>3</sub> thin films. The results show that the bulk relationship between the

optical-phonon eigenfrequencies and the dielectric constant, the LST relation, central to the lattice dynamical model of ferroelectricity is maintained in thin films[31].

### 1.3.2: Critical Phenomena and Scaling Theory

The Binder approach to finite size scaling is the second major theoretical approach to size effects. It has two portions: the correct electrostatic boundary conditions and the application of finite size scaling theory to correct the phenomenological model. To understand how the approach differs from the dead layer model, some background is needed. This section introduces scaling theory, how scaling was explained by the renormalization group, and finally the renormalization group approach to finite size scaling.

For a material with a phase transition, many of the thermodynamic properties can be expressed in terms of an order parameter, such as temperature or electric field. Consider the temperature dependence of spontaneous polarization in a ferroelectric, shown in Figure 1.9. In this case, temperature is the order parameter and spontaneous polarization is the thermodynamic property.

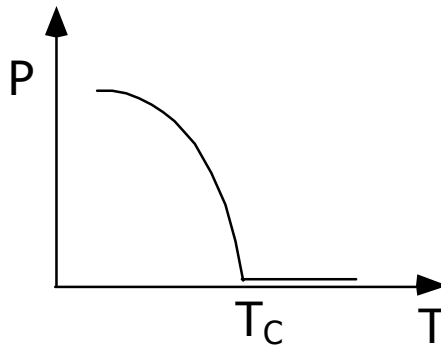


Figure 1.9: Schematic of the variation of spontaneous polarization as a function of temperature for a ferroelectric.

Above  $T_C$ , the spontaneous polarization is zero; below  $T_C$ , it increases monotonically.

These relationships can be described by power laws. The exponent of the power law is called a critical exponent. In this case, the power law would be as follows

$$P \propto |T_c - T|^\beta .$$

For each material, many power laws can be constructed. For the case of the ferroelectric crystal, some of these power laws are

$c_p(T)$	Heat Capacity
$c/a(T)$	Spontaneous Strain
$\chi(T)$	Dielectric Susceptibility

The dependence of these properties on the order parameter are all expressed by power laws, each with a specific critical exponent. Scaling theory can be used to relate these critical exponent values. These relationships are empirical and determined through observation, but hold for an extraordinary number and variety of material systems: superfluids, ferromagnets, ideal gases, ferroelectrics, etc. That these relationships hold across so many material systems indicates a fundamental physical link. Those systems with similar power law exponents are said to belong to the same universality class. Three examples are given from the universality class that includes ferroelectrics: liquid-gas, ferromagnet-paramagnet, and ferroelectric-paraelectric.

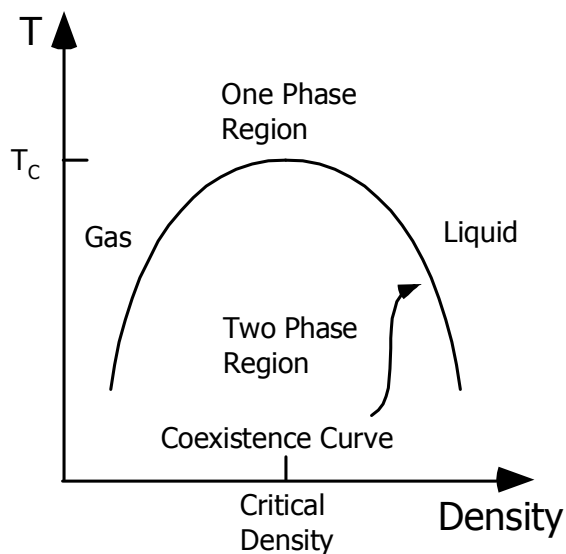


Figure 1.10: Schematic of liquid-gas phase diagram.

The first system is liquid-gas, where the order parameter is density and the thermodynamic property is temperature. A portion of the phase diagram for a class of chemicals is shown in Figure 1.10. The plot of temperature versus pressure shows what combinations of temperature and pressure that yield a gas, a liquid, or a combination of gas and liquid. It is possible to go from a liquid to a gas by increasing the temperature, changing the pressure, and then decreasing the temperature. The curve shows the limiting combination of temperature and density for a two phase system. For many compounds, the liquid-gas coexistence curve not only follows a similar form, but the model parameters of the parabolic curve are similar. The curve follows the form

$$|\rho_+ - \rho_-| \propto |T - T_C|^x,$$

where  $\rho$  is density and  $T$  is temperature. The value of the critical exponent,  $x$ , for sulphurhexafluoride is experimentally found to be  $0.327 \pm 0.006$ [32] and the value  $^3\text{He}$  is  $0.321$ [33].

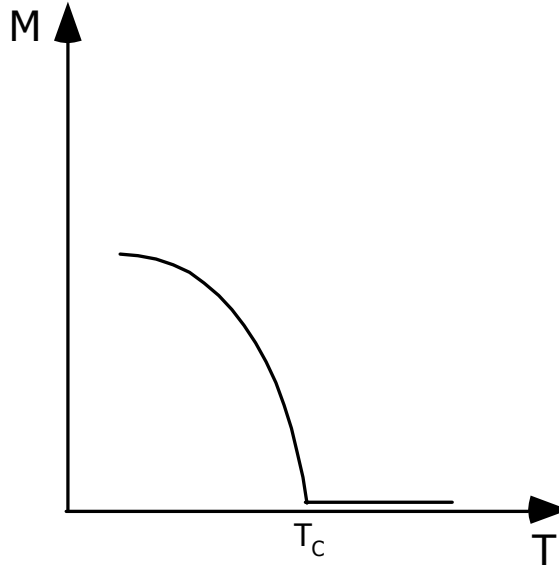


Figure 1.11: The remnant magnetization as a function of temperature for an Ising ferromagnet  
The magnetization is zero below the critical temperature and increases monotonically below it.

The second example is of Ising ferromagnets and antiferromagnets. Magnets can be thought of as a lattice of dipoles, or spins, that can exchange energy. Above the Curie temperature,  $T_C$ , the spins have no tendency to orient in any direction and the material is paramagnetic. Below  $T_C$ , the spins tend to align in the same direction; there is a net magnetization that rises continuously as the temperature decreases below  $T_C$ . The material below  $T_C$  is ferromagnetic. There are similar materials, called antiferromagnets, where the spins align opposite to one another below  $T_C$ . The curve of the magnetization for the antiferromagnet  $\text{DyAlO}_3$ [34] is experimentally found to be

$$M \propto (T_C - T)^{0.311 \pm 0.005}$$

Ferroelectrics, as discussed previously, have a temperature below which there is a net polarization. The curve is similar to the ferromagnetic case.  $\text{Pb}(\text{Zr}_{0.9}, \text{Ti}_{0.1})\text{O}_3$  has a  $T_C$  of 289 °C and the curve was experimentally found to be[35]

$$P_s \propto (T_C - T)^{0.33}.$$

The three cases illustrate that systems that are chemically different can have some aspects of the thermodynamics that are similar, as expressed by the critical exponents. The feature that the above systems share is the lack of a latent heat of transformation. There are many critical exponents. The definitions of some of the more common exponents are given in Table 1.1.

Table 1.1: Definitions of some critical exponents, adapted from Lines and Glass[36]

Property	Definition	Exponent
Specific heat ( $T > T_c$ )	$\sim (T - T_c)^{-\alpha}$	$\alpha$
Order parameter ( $T < T_c$ )	$\sim (T_c - T)^\beta$	$\beta$
Susceptibility ( $T > T_c$ )	$\sim (T - T_c)^{-\gamma}$	$\gamma$
Order parameter at $T_c$ as a function of field, $h$	$\sim h^{1/\delta}$	$\delta$
Correlation length	$\sim (T - T_c)^{-\nu}$	$\nu$
Pair correlation function	$\sim  r - r' ^{-(d-2+\eta)}$	$\eta$

As mentioned above, the exponents are related through scaling laws. An arbitrary number of scaling laws can be constructed, some are as follows[36]

$$\alpha + 2\beta + \gamma = 2$$

$$\alpha + 2\beta + \gamma = 2$$

$$\beta\delta = \beta + \gamma$$

$$(2 - \eta)\nu = \gamma$$

The values of these exponents “near” critical values of thermodynamic variables, such as temperature and pressure, are part of the evidence for the breakdown of mean field theories, as mean field theories predict rational fractions for critical exponents and rational fractions are not observed. Table 1.2 lists the values of several of the different scaling law parameters[37].

Table 1.2: Table adapted from Goldenfeld [37]

The values of the critical exponents are difficult to measure empirically, as discussed by Frowein *et al.*[38] and Goldenfeld [37], thus a range of values is given.

Exponent	Landau	d=2 Ising	d=3 Ising	Empirical
$\alpha$	0	0	0.110	0.110-0.116
$\beta$	1/2	1/8	0.325	0.316-0.327
$\gamma$	1	7/4	1.2405	1.23-1.25
$\delta$	3	15	4.82	4.6-4.9
$\nu$	1/2	1	0.630	0.615-0.635
$\eta$	0	1/4	0.032	0.016-0.06

The history of critical phenomena and scaling theory is presented below is largely adapted from an overview of the renormalization group by Goldenfeld[37]. It was observed that the equations of state of many of the classical theories of phase transformations, such as the Van der Waals theory of gasses and the Weiss theory of superconductors actually looked very similar near their respective phase transitions. This underlying similarity was utilized by Landau to formulate his theory of phase transitions, which is the most elegant and general of the classical approaches. It describes systems with an order parameter that is zero above some temperature and increases monotonically and continuously below that temperature[39]. The classical theories, including Landau's, are mean field theories. Mean field theories assume an average value of some variable, such as polarization or magnetization, and fluctuations of the order parameter are ignored. The fluctuations of the order parameter are the random deviations from an average value in a small region of the system. Near the critical point, the fluctuations cannot be ignored because the free energy cost to create a fluctuation decreases. Ultimately, it is a fluctuation propagating through the system that causes the phase transition. Landau theory can be used to estimate the importance of the fluctuations and even derive a relation as to when it is invalid, known as the Ginzburg criterion[36].

The failure of Landau theory became clear when the measured values of the critical exponents were decidedly non-Landau. Many scaling laws were developed for

various physical system and the similarity of many of the critical exponents were noted, but there was no understanding as to why the scaling laws should hold until an explanation was advanced by Kadanoff. His explanation was that near the transition, the system “looks the same on all length scales,” which is not entirely correct. The fundamental physical insight was not given a rigorous formulation until 1971 when Wilson presented the idea of the renormalization group, for which he received the Nobel Prize for Physics in 1982[40, 41]. The renormalization group approach gave insight into the origin of the scaling laws, provided values for some of the critical exponents, and allowed calculation of the effect of finite size on physical properties near the phase transition[37].

The renormalization group is a method that makes tractable systems with a large number of degrees of freedom. The fundamental insight of the renormalization group is that microscopic details that act over a range smaller than the correlation length can be neglected[36]. The correlation length, or  $\xi$ , is the distance over which some physical quantity, such as the order parameter, can change. Far away from the transition temperature, fluctuations around the mean value for some property are small. All values are near the average value.

Consider a gas, where density is the order parameter. There are density variations even at thermal equilibrium. Some regions will have higher or lower density than the average density. There are even regions of near-liquid density. Far away from the phase transition, a distribution of droplet sizes exists, but most are near the average size. This average size is representative of the correlation length. The correlation length increases as the phase transition temperature is approached and at that temperature, for an infinite system,  $\xi$  diverges to infinity[37].

The way that the approach to the transition temperature is accomplished mathematically is by integrating out the variables that have a wavelength shorter than the correlation length. It is possible to write an effective Hamiltonian that neglects wavevectors shorter than some cut-off length,  $\Lambda$ . This is given as

$$\exp\left\{\frac{-H(\Lambda)}{kT}\right\} \equiv \prod_{i,q>\Lambda} \int \exp\left\{\frac{-H(\Lambda)}{kT}\right\} d\phi_{iq}$$

where the integral is evaluated over all microscopic variables whose wavelength,  $q$ , is larger than  $\Lambda$ .  $\Lambda$  is taken to be slightly larger than the reciprocal correlation length  $\xi^{-1}$ . The new Hamiltonian is actually more complicated than the original, but recall that as the critical temperature is approached, the correlation length increases, so that closer to the transition, additional transformations can be performed and more degrees of freedom eliminated. Each renormalization decreases the value of the cutoff,  $\Lambda$ , by  $s$ , so that there is a transformation  $\tau$  that is applied repeatedly to define new Hamiltonians:

$$\begin{aligned} \tau H(\Lambda) &= H\left(\frac{\Lambda}{s}\right) \\ \tau H\left(\frac{\Lambda}{s}\right) &= H\left(\frac{\Lambda}{s^2}\right) \\ \tau H\left(\frac{\Lambda}{s^2}\right) &= H\left(\frac{\Lambda}{s^3}\right) \\ &\textit{et cetera} \end{aligned}$$

In the limit, this set of operations, or renormalization group, results in a Hamiltonian satisfying

$$\tau H^* = H^*$$

so that the types of critical behavior, the universality classes mentioned earlier, are determined by the form of  $\tau$ [36].

Goldenfeld suggests that there are two main classes of models in physics. The first is the traditional model, which seeks to faithfully describe the physical system to the last detail. New experimental results are incorporated by adjusting or adding parameters. The second type of model seeks to construct a minimal model that describes the essential aspects of the system, typically without regard to microscopic detail. The measurable quantities typically take the form of dimensionless numbers or universal functions. This type of model is exemplified by the classical BCS theory. It presents various dimensionless ratios and functions for all weak-coupling superconductors. All the microscopic effects are put into as few parameters as possible[37]. The second type of model is how scaling theory fits into the overall theoretical framework. The specifics of a material's phase diagram, thermodynamics, interatomic potentials, and electrostatic boundary conditions are modeled by the Ising model, Potts model, Heisenberg model, *et cetera*. But the critical phenomena only depend on the symmetry of the order parameter, the dimensionality of the system, and the nature of the critical point, not the coupling constants, lattice types, or other microscopic considerations[37].

The renormalization group approach can be used to describe processes that are intrinsically quantum mechanical in nature, such as ferroelectrics and ferromagnets. For second order transitions, it is always valid, and for first order transitions, no counterexample has yet been produced. This is because  $\xi$  is much larger than the sizes where quantum mechanics must be invoked[37].

According to statistical thermodynamics, only infinite systems, or systems at zero Kelvin, theoretically exhibit phase transformations [12]. Renormalization group methods provide insight into the effect of finite size on phase transformations within the context of scaling theory. This topic is known as finite size scaling. Consider a system with dimension  $L$  and volume of  $L^d$ , given as

$$f_s([K], L^{-1}) = \ell^{-d} f_s([K'], \ell L^{-1})$$

The free energy density,  $f_s$ , is a function of the coupling constants,  $K$ , and the inverse size of the system,  $L^{-1}$ . On the right hand side of the equation, the form arises because a renormalization group transformation reduces the effective size of the system by  $\ell$ . And since the renormalization group is a local operation, the total size of the system does not affect the operation. An example of finite size scaling is outlined for the specific heat. Consider the specific heat of a system, given as

$$c(t, L^{-1}) = |t|^{-\alpha} F_f^\pm(L^{-1}t^{-\nu})$$

where the complexity of the system is collected into  $F$  to allow the general scaling behavior to be described and  $t$  is the reduced temperature, defined as

$$t \equiv \left( \frac{T - T_C}{T_C} \right)$$

by introducing a new scaling function,  $D(x)$ , that has a maximum at  $x_0$

$$c(t, L^{-1}) = |t|^{-\alpha} (L^{-1}t^{-\nu})^{-\alpha/\nu} D^\pm(tL^{1/\nu})$$

the scaling behavior is

$$c(t, L^{-1}) = L^{\alpha/\nu} D^\pm(tL^{1/\nu})$$

The shift in  $T_C$  near for a non-infinite system is given as

$$t_L = \frac{x_0}{L^{1/\nu}} \propto L^{-1/\nu}$$

and the decrease in maximum height of the specific heat is

$$c(t, L^{-1}) = L^{\alpha/\nu} D(x_0) \propto L^{\alpha/\nu}$$

These results are shown graphically in Figure 1.12[37].

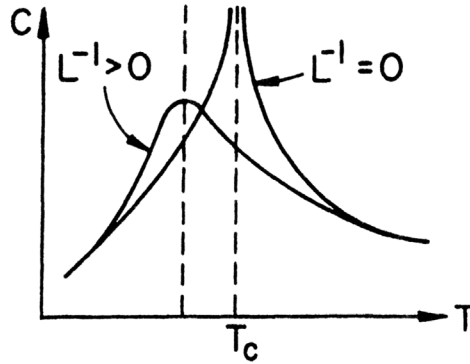


Figure 1.12: Specific heat of 3D Ising model for infinite and finite system size, from Goldenfeld[37].

Much of the early work applying the renormalization group approach to ferroelectricity and ferromagnetism was done by Aharony, [42, 43], Aharony and Fisher[44-48], and Fisher [49].

Although the ideas of the critical phenomena and scaling theory are well established, direct observation of logarithmic corrections of LGD exponents in ferroelectrics is difficult for two reasons. First, cases that are analytically treatable are not often experimentally measurable, for instance, systems with dimensionality above 3 are correct in the mean-field theory approximation. Second, the cases that are measurable are only measurable with great difficulty. One example of the difficulties in measuring the small corrections is given by Frowein and Kötzer[38]. They measured the field and temperature and field dependence of the magnetization of two ferromagnets,  $\text{LiTbF}_4$  and Dy-ethylsulfate. The data was compared to the predicted logarithmic corrections to the equation of state,

$$h = \frac{\left(\frac{T}{T_c}\right)}{\hat{\Gamma}} m + \frac{1}{\hat{\Gamma} \hat{B}^2} m^3$$

which is practically identical to the LGD equation of state, where

$$\hat{\Gamma} = \frac{\Gamma \ln^{(\frac{1}{3})} \left( \frac{\partial m}{\partial h} \right)_T}{\chi_0}$$

and

$$\hat{B} = \frac{B \ln^{(\frac{1}{3})} \left( \frac{\partial m}{\partial h} \right)_T}{\chi_0}$$

The temperatures were measured to within 0.1 mK and the magnetization was detected with a superconducting quantum-interference device. The logarithmic corrections to Landau theory were observed, as can be seen in Figure 1.13.

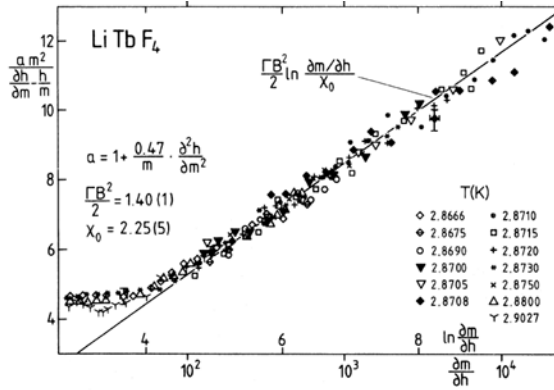


Figure 1.13: The logarithmic corrections to the Landau coefficients in  $\text{LiTbF}_4$ , from Frowein and Kötztler [38].

Turning to the Binder approach itself, four main methods were used to understand the effects of finite size on phase transformations. First, for some cases it is possible to calculate the partition function of the Hamiltonian directly[50]. However, the cases that are directly calculable are limited. Second, the renormalization group methods allowed estimation for many additional cases. This approach was discussed earlier. Third, the 2D and 3D Ising model can be approximated as a series expansion, via Landau theory[17]. Much of the early work was done in this way. Finally, increases in computer power have allowed Monte Carlo methods to be employed[51].

The effect of finite size is that the phase transition is rounded, shifted, and reduced in magnitude. As the system decreases in size, the anomaly smoothly shifts to lower temperatures and disappears. The broadening, or rounding, of thermodynamic property anomalies should follow this form

$$\Delta T_{\text{rounding}} \propto N^{\frac{-\theta}{D}}$$

where  $\theta$  is the rounding exponent,  $D$  is the dimensionality of the system, and  $N$  is the number of units cells. The shift in  $T_c$  follows the equation

$$T_c(N) - T_c(\infty) \approx N^{\frac{-\gamma}{D}}$$

where  $\gamma$  is the shift exponent. Finally, the reduction in the magnitude of the properties, such as maximum permittivity, follows

$$K_{\text{Max}} = L^{\nu}$$

where  $\gamma$  is the dielectric constant critical exponent,  $\nu$  is the correlation length critical exponent, and  $L$  is the linear dimension of crystal, typically in unit cells[12].

First, the statistical treatment will be presented, followed by the phenomenological treatment. It should be noted that the finite size scaling arguments were formulated in a similar fashion by Fisher, whose notation is different[49]. The results are fundamentally the same and the Binder approach was developed further over the next two decades. Most of the work done using the statistical treatment is for ferromagnetic materials, which are similar to ferroelectrics in many respects, and for the aspects discussed, the similarity holds.

The essential insight of the Binder approach is that there are surface critical exponents and bulk critical exponents. Surfaces affect the thermodynamics in two ways. First, it is necessary to include a term that accounts for the differences in specific heat, polarization, *etc.*, as the ratio of surface to bulk atoms changes. Second, the translational invariance is broken, so that a property with a local effect would have a value different than the bulk value at the surface. There would also be local effects that only happen at the surface. The difference between a surface effect and the value of a local effect at a surface is like the difference between a bulk interface free energy, such as a grain boundary, and a surface free energy[17]. The effects of the surface can be treated by a single parameter,  $\lambda$ , the extrapolation length. For example, for the case of the surface magnetization,

$$m_s = \frac{\lambda}{\xi} m_b$$

where  $m_s$  is the surface magnetization,  $\xi$  is the correlation length, and  $m_b$  is the bulk magnetization. The decay from surface to bulk exponents was found to be approximately exponential in form[17].

The Ising model was employed to investigate the effect of temperature and field on magnetization profiles. The mathematics for the Ising treatment are involved and less relevant to the case of size effects in BST than the phenomenological treatment. The overview of the treatment is that it investigates the implications of the addition of a surface term to the Ising Hamiltonian,

$$H = -J \sum_{\substack{NN \\ Bulk}} \sigma_i \sigma_j - J_s \sum_{\substack{NN \\ Surf}} \sigma_i \sigma_j ,$$

where  $\sigma$  is  $\pm 1$ ,  $J_s$  is the nearest-neighbor, or  $NN$ , interaction in the surface, and  $J$  is the interaction in all other pairs[52]. The major results can be summarized in five figures. The first is the prediction of a power-law form of the  $T_c$  shift with decreasing size, in this case,  $L$  unit cells. Figure 1.14 shows this relationship. The line of larger slope was computed for the 4D Ising model and the line of smaller slope for the 3D Ising model. The 3D Ising model predicts a value of 1.5 for  $\nu$ . Additionally, the curves intersect the origin, which is the expected behavior for finite size scaling[53].

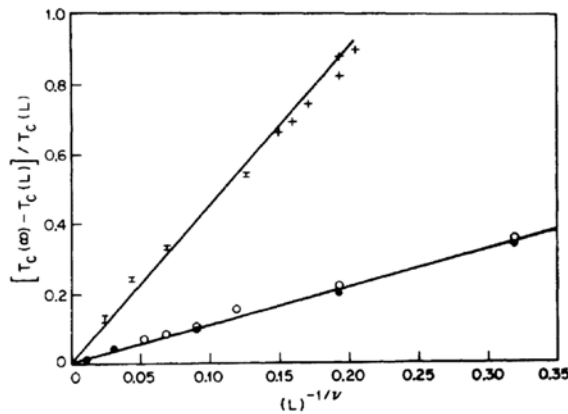


Figure 1.14: The shift in the transition temperature as a function of crystal size for the 4D (upper curve) and 3D (lower curve) Ising models from Binder *et al*[53].

The second figure, Figure 1.15, plots the magnetization profile as a function of position, with the centerline being the center of the film. Various thicknesses are plotted, with the number of unit cells ranging from 5 to 20. All but the thinnest film reaches the bulk value for that temperature in the interior. Note also that the magnetization decreases near the surface, but does not drop in a stepwise fashion, but rather in a smooth curve, unlike the approximation made in the dead layer theory.

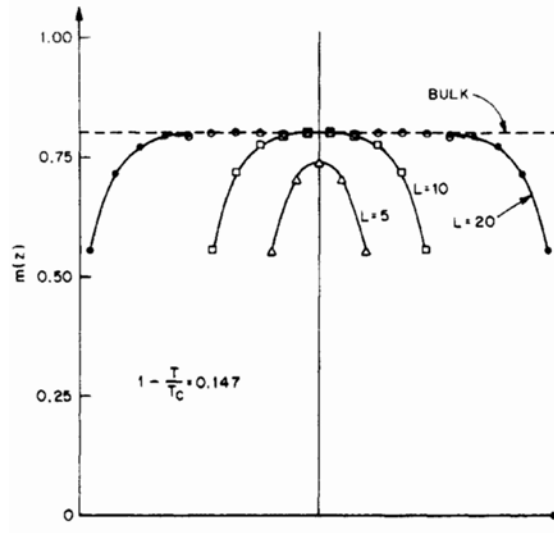


Figure 1.15: Magnetization profile across samples of different thicknesses, where  $L$  is in unit cells, from Binder *et al* [53].

The third plot is somewhat more complicated. The calculations of the magnetization in Figure 1.16 were done using the Heisenberg model under the assumption that the right hand side is pinned to the bulk magnetization and the left side is a free surface. As the quantity  $1 - (T/T_c)$  decreases, the temperature approaches the transition temperature. The dashed line is the bulk magnetization at that temperature. Closer to the transition temperature, the effect of the surface becomes more important. This behavior is consistent with the understanding of materials with a cooperative phenomenon. Further from the transition, the cooperative effect is smaller and the individual ionic contributions are more important. Closer to the transition, the cooperative effects are more important and the surface affects the properties farther into the material[53].

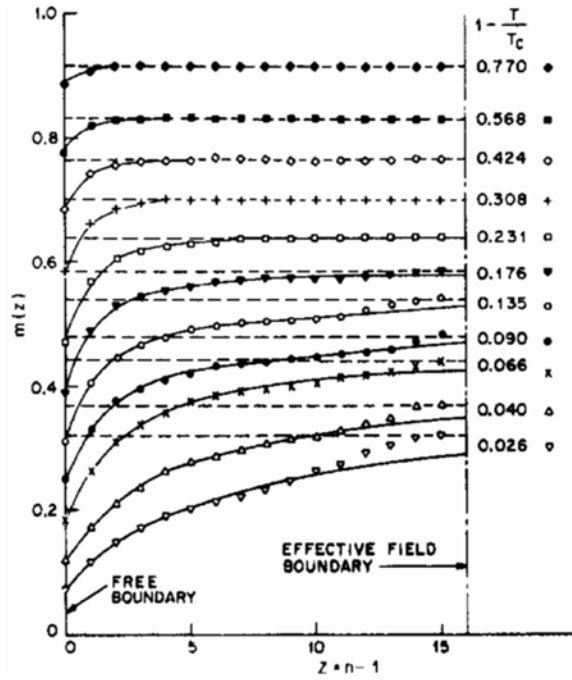


Figure 1.16: Magnetization profile as a function of temperature and position for the Heisenberg model, under the assumption that the right hand side is pinned to the bulk value of magnetization, from Binder *et al* [53].

The fourth plot, Figure 1.17, shows the magnetic susceptibility as a function of field for different thicknesses[54]. Again,  $L$  is the thickness of the film in number of unit cells. This behavior is quite close to the behavior that is found in BST as a function of thickness: the zero-field behavior shows the largest difference between the thicknesses and the films converge at high fields.

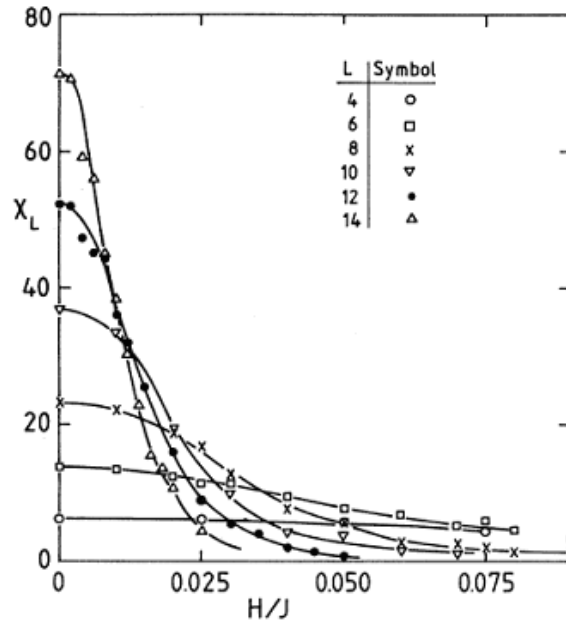


Figure 1.17: Magnetic susceptibility as a function of  $L$ , the thickness of unit cells, and  $H$ , magnetic field, from Binder *et al* [54].

The final figure, Figure 1.18, replots the data from Figure 1.17, only scaled. Data collapse is the hallmark of scaling theory. Data plotted with the correct axes should collapse into a single curve as a function of size. When the data from Figure 1.17 is adjusted by the appropriate power law relation, all the curves show the same behavior regardless of thickness. The power law dependence and data collapse can be used as a test of scaling.

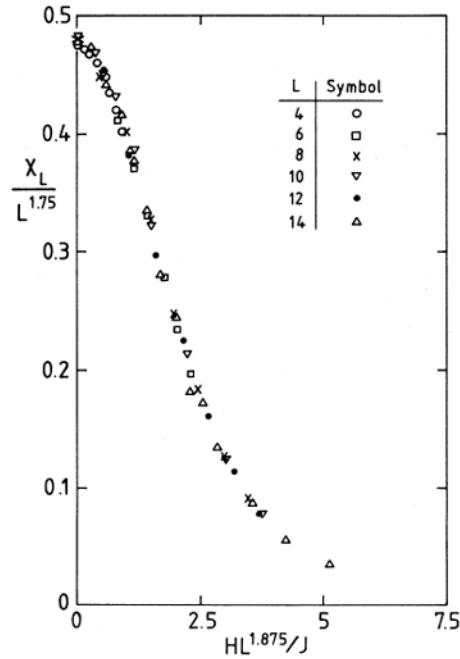


Figure 1.18: Scaling plot of magnetic susceptibility versus corrected field as a function of  $L$ , from Binder *et al* [54].

The phenomenological treatment of size effects in ferroelectrics consists of three parts: the logarithmic corrections to the LGD equation derived from finite size scaling studies of the 3D Ising model, the ferroelectric domain structure, and the depolarization fields that result from incomplete polarization screening at the ferroelectric surface. The last two are boundary conditions. Binder incorporates the treatment of Batra *et al.* [23-26] into the evaluation of depolarization fields and considers the case of a monodomain sample. The extrapolation length that was developed in the work on Ising models is applied to ferroelectrics. Figure 1.19 shows the polarization as a function of position, with 0 being the surface of the ferroelectric. The correlation length,  $\xi$ , is marked at the value of the correlation length measured from the surface.  $P_\infty$  is the bulk polarization and  $P_i$  the surface polarization. The change in properties with decreasing thickness can be explained by the extrapolation length,  $\lambda$ . All the terms, *i.e.*,  $P_\infty$ ,  $P_i$ ,  $\xi$ , and  $\lambda$  are temperature dependent[18].

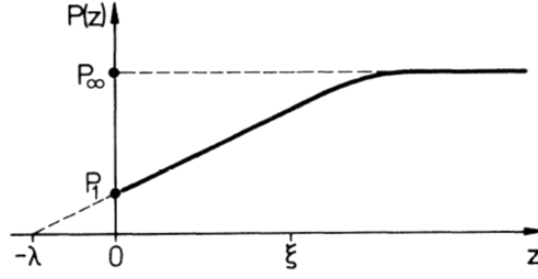


Figure 1.19: Polarization profile illustrating the concept of the extrapolation length as a function of distance from surface, from Kretschmer and Binder[18].

The standard LGD equation is expanded with the addition of the extrapolation length.

$$F = \int_V dV \left[ \frac{1}{2} A P^2(\vec{r}) + \frac{1}{4} B P^4(\vec{r}) - \frac{1}{2} C (\nabla P)^2 - \frac{1}{2} \vec{E}_a(\vec{r}) P^2(\vec{r}) \right] + \int_S \frac{1}{2} C \lambda^{-1} [P^2(x, y, z = 0^+) + P^2(x, y, z = L^-)] dx dy$$

where

$$A = 2a'(T - T_C),$$

$$B = 2a' \left( \frac{T_C}{P_0^2} \right),$$

$$P_0 = P(T = 0),$$

$$C = 2a' T_C a_0^2,$$

$$\text{and } a' = \frac{2\pi}{C'}.$$

$C'$  is the Curie constant of the material and  $a_0$  is a fitting parameter approximately the magnitude of the lattice parameter. The first two terms in the volume integration are the standard LGD terms. Polarization gradients are thermodynamically unfavorable, this is reflected in the third term. The final volume term corrects the polarization distribution

due to the presence of depolarization fields, hence the presence of the  $1/2$ . The size correction is proportional to the surface, rather than the volume, so a second integration is required[18].

For a film of infinite thickness, the result reduces to the bulk case,

$$\frac{A}{C}P_{\infty} + \frac{B}{C}P_{\infty}^3 = \frac{E_{Ext}}{C}$$

*i.e.*, there is no polarization distribution in the ferroelectric. The integration is carried out for a film of thickness  $L$ . There are two results. The first neglects the presence of depolarization fields. The resultant polarization profile is given as

$$P(z) = \frac{(P_1 - P_{\infty}) \cosh\left[\frac{\left(z - \frac{L}{2}\right)}{\xi_b}\right]}{\cosh\left(\frac{L}{2\xi_b}\right)} + P_{\infty},$$

where polarization is a function of position,  $z$ .  $P_1$  is the surface polarization and  $P_{\infty}$  is the bulk polarization. This is shown in Figure 1.20. The polarization is close to the bulk polarization at the center of the film and is reduced to  $P_1$  at the surface, over a range of  $\xi_b$ .

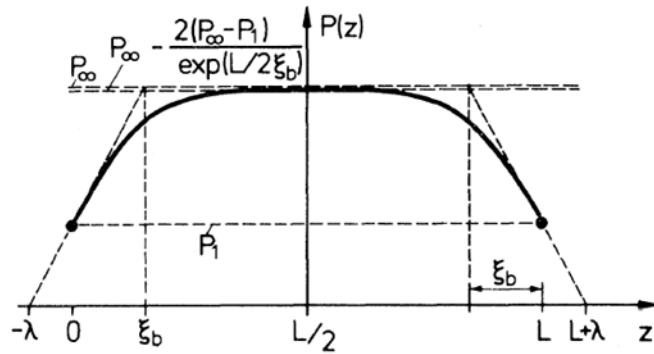


Figure 1.20: Polarization profile of ferroelectric neglecting depolarization fields, from Kretschmer and Binder[18].

Note that the polarization is close to the bulk polarization near the center of the ferroelectric.

The second case corresponds to depolarization fields being taken into account. In this case, the bulk correlation length is transformed to  $\kappa$ . The main difference is that the length  $\kappa^{-1}$  does not diverge at the transition temperature and is adjusted by the magnitude of the depolarization field. This yields a polarization at the center of the ferroelectric of magnitude

$$P\left(\frac{L}{2}\right) \approx P_{\infty} - \frac{(P_{\infty} - P_1)}{1 + \frac{L\kappa A}{8\pi}}$$

and  $P_1$  of magnitude

$$P_1 = \frac{\kappa\lambda P_{\infty} \tanh\left(\frac{\kappa L}{2}\right)}{1 + \left(\kappa\lambda + \frac{8\pi}{L\kappa A}\right) \tanh\left(\frac{\kappa L}{2}\right)}$$

both shown in Figure 1.21. The depolarization fields have three main effects. First, the interior polarization no longer reaches  $P_{\infty}$ . Second, the surface effects that would otherwise occur are diminished. Third, the surface critical exponents are much closer to, and may be equal to, the bulk critical exponents[18].

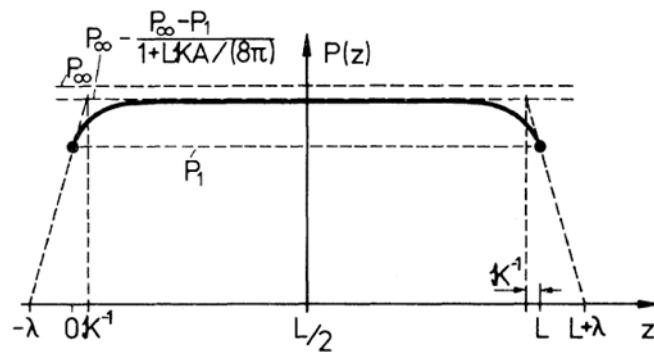


Figure 1.21: Polarization profile considering the effect of depolarization fields, from Kretschmer and Binder[18].

### 1.3.3: Boundary Conditions

The other component of intrinsic size effects is boundary conditions. Boundary conditions that influence high-k capacitors generally are finite screening length in the electrode[55], effect of the presence of a free surface on the dipoles directly[56], and free charge carriers, or incomplete depletion, in the dielectric. The most important boundary conditions for ferroelectric capacitors are depolarization fields in the ferroelectric[23-26], strain[8, 57, 58], electrode material, and ferroelectric domain structure.

#### *1.3.3.1: Finite Screening Length*

The finite-screening length effect is a relaxation of the assumption that the electrodes are atomically smooth and perfect conductors. When a voltage is applied to a perfect electrode, the displacement charge occurs in a plane at the electrode-dielectric interface. In real electrodes, the displacement charge is screened over some thickness of the electrode. The screening length is shown schematically in Figure 1.22. The reason for the distribution of the charge density in the real metal is that screening depends on the effective static dielectric constant of the conduction electrons. For bulk metals, the conduction electrons are free to move throughout the material, so the effective dielectric constant is infinite. This is not the case for thin films, where the dielectric constant is more influenced by the polarizability of the metal atoms composing the lattice, *i.e.*, the electrons bound to the ionic core. Black *et al.* use the Thomas-Fermi method, which allows calculation of the potential throughout a free electron gas from knowledge of the electron density[55].

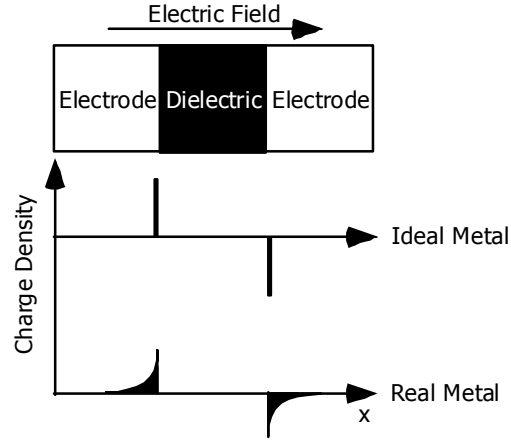


Figure 1.22: The effect of finite screening length on charge density in the electrode  
 The schematic of the electrode-dielectric-electrode system indicates the direction of the electric field. The middle portion of the figure shows the sheet of charge at the surface of the electrode. The bottom portion of the figure illustrates the effect of finite screening length.

The derived equation modeling the effect of finite-screening length is

$$\frac{1}{C_{eff}} = \frac{1}{\epsilon_0} \left\{ \frac{t}{\epsilon_d} + \frac{2\ell_{TF}}{\sqrt{\epsilon_m}} \right\} = \frac{1}{C_{dielectric}} + \frac{1}{C_{interface}}$$

where  $\epsilon_0$  is the permittivity of free space,  $\epsilon_d$  is the permittivity of the dielectric,  $\ell_{TF}$  is the Thomas-Fermi screening length,  $t$  is the thickness of the dielectric, and  $\epsilon_m$  is the permittivity of the metal. Black *et al.* use data for Cu to apply the model. For Cu the value of  $\ell_{TF}$  is approximately 0.055 nm,  $\epsilon_m$  about 5, and  $C_{interface}$  about 180 fF/ $\mu\text{m}$ . For the case of a capacitor with a dielectric constant of 800, the effect of the screening length is to reduce the total capacitance by almost 50%[55]. Black *et al.* assume values for SRO and apply the model again, then take the Cu result as indicative of Pt. They are able to explain the differences in films that have Pt electrodes from films that have SRO electrodes by noting that SrRuO<sub>3</sub> has a higher permittivity and thus a shorter  $\ell_{TF}$ .

The analysis of Black *et al.* indicates that the electrode effect may be significant. However, some of the assumptions in the Black model have enough uncertainty that the conclusions are of limited utility. Further consideration of the Thomas-Fermi screening

length brings additional insight into a critical assumption in the paper, that the permittivity of SrRuO<sub>3</sub> is at least 10 times that of Pt; about 100 for SRO and Pt about 8. From Kittel[59],  $k_s^{-1}$  is the Thomas-Fermi screening length and

$$k_s^2 = \frac{6\pi N_0 e^2}{\mathcal{E}_F}$$

where  $N_0$  is the density of states,  $e$  is the electron charge, and  $\mathcal{E}_F$  is the Fermi level, in eV. Thus,

$$\ell_{TF} \propto \sqrt{\frac{\mathcal{E}_F}{N_0}},$$

so as the ratio of Fermi level to density of states increases, the  $\ell_{TF}$  should decrease and the electrode permittivity should increase. The density of states of Pt is orders of magnitude larger than the density of states of SrRuO<sub>3</sub>. The Fermi level for Pt is larger than for SrRuO<sub>3</sub>, Cu has a Fermi level of 7, but this does not offset  $N_0$ , suggesting that Pt should have a larger  $\ell_{TF}$  and thus a larger permittivity.

Several questions remain. First, the model does not account for the temperature dependence of the permittivity and thus variable interfacial capacitance. Also, since the screening occurs over a small distance, the surface atoms, and not the average for the crystal, are central to the calculation of  $\ell_{TF}$ . The electrodes certainly influence the overall capacitance of the capacitor stack, through polarization screening, but the magnitude is uncertain.

### 1.3.3.2: Presence of a Free Surface

Natori *et al.* examined the effects of film thickness on the permittivity of a thin film capacitor by applying Lorentz's local field theory. The method is computationally

involved, so only the range of conditions investigated and the major results are discussed. The capacitor was modeled as a lattice of dipoles, specifically an infinite plate of a varying number of dipole layers. A series of thicknesses were calculated, from 10 to 500 dipole layers. The polarizability of the dipoles was adjusted to yield bulk dielectric constants from 10 to 1000. The results are as follows. First, the decrease in permittivity near the interface is more marked for higher permittivity materials. Second, the larger the effective dielectric constant of the capacitor, the more pronounced the thickness effect. For a bulk permittivity of 10, the drop of permittivity in a capacitor of 500 dipole layers versus 10 dipole layers is 4%; for a bulk permittivity of 1000 the drop is 82%[56]. The results are important because this behavior is due entirely to the polarizability of the dipoles and not the cooperative interaction of ferroelectricity. The ferroelectric interaction would act as a superposition with the direct dipole effect.

### *1.3.3.3: Incomplete Depletion and Depolarization Fields*

When the ferroelectric phase transition occurs, an electric field is generated from the displacements of ions resulting from a change in crystal symmetry. This field must be compensated. The compensation can be in the film or on the electrode. Most charge is compensated in the electrode, because the ferroelectric typically has much less available free charge. For the thin film case, the polarization cannot be fully compensated by free charge in the electrode. Ferroelectricity is different from other cooperative phenomena in that there is an accompanying field with the polarization. Superconductivity, for instance, can be affected by a magnetic field, but does not itself generate one. Ferroelectricity can be thought of as two distinct interactions, a microscopic interaction that creates the polarization and an opposing depolarization field that reduces the polarization. These two interactions have different size dependencies[26]. The example given by Batra *et al.* is for the analytically tractable case of a slightly conductive ferroelectric film with the

electrodes shorted. Watanabe also treated the problem of depolarization fields in ferroelectrics[60-62]. The method employed by Watanabe makes more use of band structure, but the results are similar to those of Batra *et al.*

The work of Batra *et al.* suggest that the incomplete polarization affects the stability of the ferroelectric phase and is manifested as transition temperature and spontaneous polarization values below the bulk values. The reason that the film is chosen to be slightly conducting is to account for the presence of defects in the film[24].

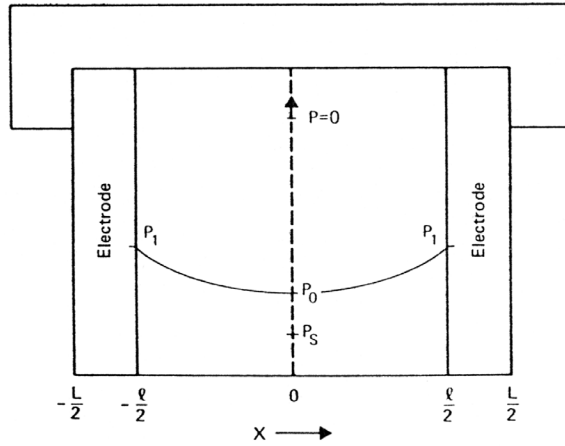


Figure 1.23: Schematic of the circuit used by Batra *et al.* to analyse depolarization fields in a ferroelectric, from Batra *et al.* [24].

The case of metallic electrodes with spatially inhomogeneous charge distribution in the electrode is presented in Figure 1.23. The compensating charge is in both the electrode and the film, with the internal space charge causing the variation of the polarization in the film. The interface values are denoted by  $P_1$ , the center of the film by  $P_0$ , and the bulk value by  $P_s$ ; all are negative in this construction. The field, polarization, and space charge density are related by the following equations.

The first is the LGD expansion to third order:

$$E(x) = aP(x) + \zeta P^3(x)$$

where  $a$  is the Curie-Weiss law, in the following form

$$a \equiv \left( \frac{4\pi}{C} \right) (T - T_0);$$

where  $C$  is the Curie constant; and  $T_0$  the bulk transition temperature. The second equation approximately expresses the equilibrium condition that the current is zero, assuming that  $\rho \ll qn_p$ ,

$$E(x) = -4\pi\lambda_f^2 \frac{d\rho(x)}{dx}$$

where the screening length is given in terms of the background carrier density,  $n_p$  as

$$\lambda_f = \sqrt{\frac{kT}{4\pi q^2 n_p}}.$$

The final equation is Poisson's equation

$$\frac{dE(x)}{dx} + 4\pi \frac{dP(x)}{dx} = -4\pi\rho(x).$$

These can be used to solve for the field in the ferroelectric, considering the screening length approximation,

$$E_e(x) = -4\pi\rho_0 \cdot \exp\left[-\frac{1}{\lambda_e} \left( |x| - \frac{l}{2} \right)\right]$$

where  $x$  is less than  $-l/2$ ,  $\rho_0$  is the total charge in each electrode, and the screening length is

$$\lambda_e = \sqrt{\frac{kT}{4\pi q^2 n_e}}$$

and is based on Boltzmann statistics.

If the field, polarization, and space charge are approximated to third order, the above set of equations can be solved analytically in the following six equations

$$\frac{P(x)}{P_s} = 1 - \frac{2\lambda_e(\varepsilon_f - 1)}{\Phi l} \left[ 1 + \frac{1}{2\varepsilon_f} \left( \frac{x}{\lambda_f} \right)^2 \right]$$

$$E(x) = -\frac{8\pi P_s \lambda_e}{\Phi l} \left[ 1 + \frac{1}{2\varepsilon_f} \left( \frac{x}{\lambda_f} \right)^2 \right]$$

$$\rho(x) = \frac{2P_s \lambda_e}{\Phi l \lambda_f} \left[ \frac{x}{\lambda_f} + \frac{1}{6\varepsilon_f} \left( \frac{x}{\lambda_f} \right)^3 \right]$$

$$\rho_0 = -\frac{P_s}{\Phi} \left[ 1 + \frac{1}{24\varepsilon_f} \left( \frac{l}{\lambda_f} \right)^2 \right]$$

where

$$\Phi \equiv 1 + \frac{2\lambda_e \varepsilon_f}{l} + \frac{\lambda_e l}{4\lambda_e^2} + \frac{1}{24\varepsilon_f} \left( \frac{l}{\lambda_f} \right)$$

and

$$\varepsilon_f = 1 - \frac{2\pi}{a} \cong \frac{C}{2(T_0 - T)}$$

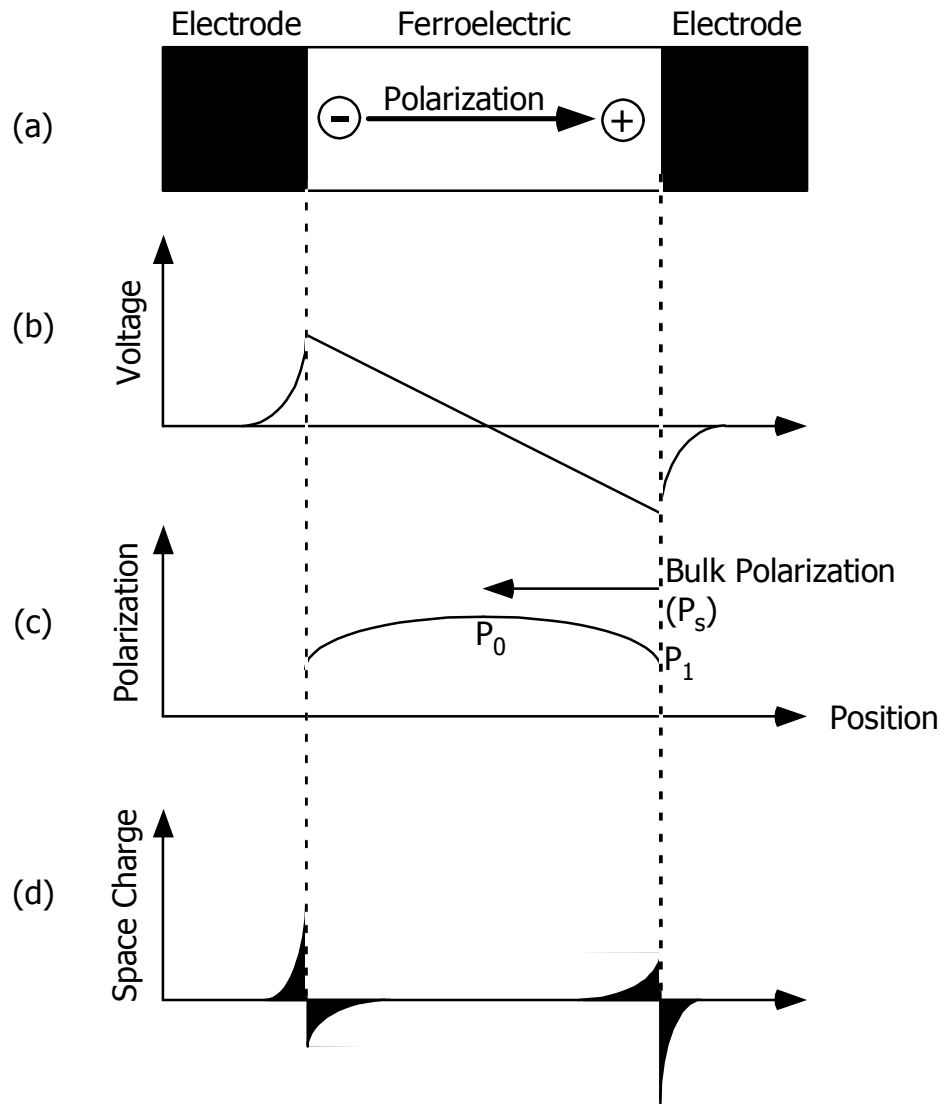


Figure 1.24: Effect of electrostatic boundary conditions in the Batra, Wurful, and Silverman model. The sections illustrate the various quantities in the system (a) shows the sense of polarization (b) shows the voltage profile (c) shows the voltage profile, and (d) shows the space charge profile

A schematic of the main parameters can be seen in Figure 1.24. Part (a) of the figure shows the sense of the ferroelectric polarization in the film. The voltage, shown in part (b), has a nonlinear form in the electrodes because of the finite screening length, but is approximately linear in the ferroelectric, because the ferroelectric is a relatively good insulator. The polarization in part (c) is similar to Figure 1.23: there is a reduction near the surface due to the depolarization fields and overall in the ferroelectric, the polarization is below the bulk value. The space charge in part (d) assumes steady-state conditions.

The space charge is approximately the same magnitude as the screening length in the electrode. In the ferroelectric, the space charge occupies a much larger fraction of the ferroelectric film thickness length, again because the ferroelectric is a relatively good insulator and there are few delocalized electrons.

Several physical insights can be gained from examining 4 special cases of the set of equations. The first case is that the film thickness approaches infinity ( $l \rightarrow \infty$ ). This is the bulk case and the bulk results are obtained. The polarization becomes uniform at the bulk value,  $P_s$ . The field in the ferroelectric goes to zero and the internal space charge,  $\rho(x)$ , becomes uniform.

Second, the screening length in the ferroelectric is infinite ( $\lambda_f \rightarrow \infty$ ). In this case, the polarization and field in the ferroelectric are uniform and the compensation charge resides entirely in the electrodes. Below the critical thickness

$$l_c = \frac{2\lambda_e C}{(T_0 - T)}$$

the ferroelectric state becomes unstable.

Third, the screening length in the electrode approaches infinity ( $\lambda_e \rightarrow \infty$ ). In this case, the surface polarization,  $P_s$ , is zero.  $P_0$  decreases with decreasing  $l$  and below the critical thickness

$$l_c = \frac{2\lambda_f (2C)^{0.5}}{(T_0 - T)^{0.5}}$$

the ferroelectric state becomes unstable.

Fourth, the screening length in the electrode approaches zero ( $\lambda_e \rightarrow 0$ ). The depolarization field would be zero and the polarization would be the bulk polarization. However, there would still be a distribution of space charge within the ferroelectric[25].

Extending this to semiconductor electrodes requires calculation of the band bending in the electrodes,

$$V_b = \frac{kT}{q} \ln \left( \frac{2\pi\rho_0^2}{\epsilon_e n_i(T)kT} \right)$$

where  $n_i$  is the intrinsic carrier concentration,  $\epsilon_e$  is the dielectric constant of the electrode, and  $\rho_0$  is the charge per unit area on the surface of the electrode[24].

The effect of depolarization fields on the thermodynamic stability of the ferroelectric phase was estimated for the case of triglycine sulphate (TGS) with semiconducting electrodes. There are shifts in transition temperature,

$$\Delta T_0 \approx \frac{2\lambda_e C}{\epsilon_e l}$$

the spontaneous polarization,

$$P_s(l, T) \cong \left( \frac{4\pi}{C\xi} \right)^{\frac{1}{2}} \left[ T_0 - T - \frac{2\lambda_e C}{\epsilon_e l} \right]^{\frac{1}{2}}$$

and the average magnitude of the depolarization field in the ferroelectric,

$$E_f \cong - \left( \frac{64\pi^3}{C\xi} \right)^{\frac{1}{2}} \left[ T_0 - T - \frac{2\lambda_e C}{\epsilon_e l} \right]^{\frac{1}{2}} \left( \frac{2\lambda_e}{\epsilon_e l} \right)$$

The calculation yielded a thickness of 0.41  $\mu\text{m}$  for the minimum thickness for ferroelectricity, with the value for metal electrodes being about 4 nm. A shorter screening length corresponds to a smaller depolarization field. These values are quite reasonable.

The most significant evidence for the effect of depolarization fields is given by Wurfel and Batra using an Au/TGS/p-Si device. The number of majority carriers in the Si bottom electrode could be affected by changing the intensity of light on the sample. P-E loops were taken at different illumination levels. The effects of the illumination level can be seen in Figure 1.25. At higher illumination levels, more charge is available to compensate the ferroelectric polarization. Positive polarization in the figure means that polarization vector is toward the Si electrode. The sense of the vector is from negative to positive, so negative charge is required at the interface to compensate. Negative charge in this case has two sources: accumulation of minority carriers and depletion of majority carriers. Negative polarization is not affected strongly; it is compensated by majority carrier accumulation. The loops were traced at 100 Hz, so minority carriers are not a concern; thermal generation is too slow. Thus the change of intensity has the effect of changing the depolarization field in the TGS, without the experimental difficulties of changing the film thickness, such as varying structural defects and domain structure[26].

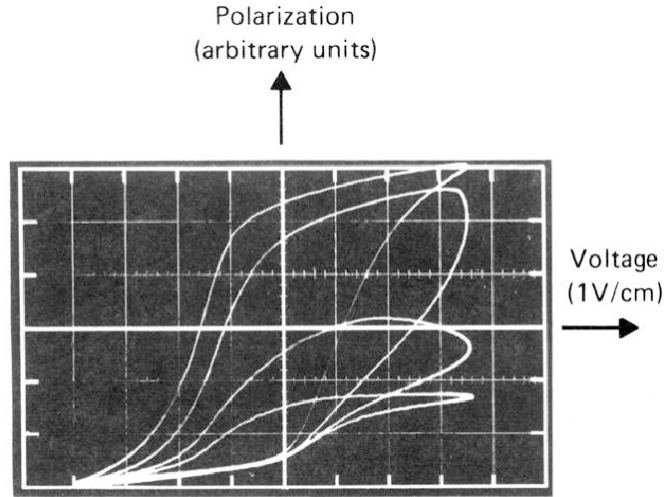


Figure 1.25: P-E loops of an Au/TGS/p-Si device with different levels of illumination, from Wurfel *et al*[26].

The negative side is not affected by illumination level, but the positive polarization was controlled by the number of compensating charge carriers, which was increased by increasing the illumination level.

Certainly thin ferroelectric films are incompletely compensated, but the total effect of depolarization fields is difficult to quantify. In the paraelectric phase, depolarization fields have less significance than in the ferroelectric phase. Additionally, compensation is good for metal electrodes.

#### 1.3.3.4: Strain

The LGD treatment describes a coupling between strain and polarization[5]. The treatment of strain or stress effects has three parts: modification of LGD theory, insight from scaling theory, and experimental measurements. The thin film conditions are different than the bulk conditions and recent theoretical work has extended LGD theory to the thin film case[57, 58, 63]. Consider a film with the *c*-axis normal to the substrate with no shear stresses acting at the surface of the film. In the Voigt notation, this corresponds to  $\sigma_3=\sigma_4=\sigma_5=0$ . Thus the free energy functional for a film under plane, biaxial stress (a Legendre transformation of elastic Gibbs function  $G$ ) is

$$\tilde{G}(\vec{P}, u_m, T) = G + u_1 \sigma_1 + u_2 \sigma_2 + u_6 \sigma_6$$

where  $P$  is polarization,  $u$  is strain, and  $\sigma$  is stress. The full expansion of the functional is cumbersome and not presented.

Thin films can accommodate strains that would not be possible in bulk materials. Strain distorts the material and modifies the stability of the ferroelectric phase with respect to the cubic phase, forcing the unit cell to become tetragonal. This is reflected as a shift in the Curie-Weiss temperature. A film in compression would tend to transform to a lower temperature with the spontaneous polarization occurring out of the plane, because the strain helps to overcoming the free energy barrier. Similarly, a film in tension would tend to transform at a lower temperature with a spontaneous polarization in the plane of the film.

The main insight of the work of Pertsev *et al.* is that because of the constraint imposed by the substrate, different orientations of the polarization with respect to the substrate must be considered as separate ferroelectric phases, so there are 5 low temperature phases for BaTiO<sub>3</sub>, rather than 3. The phase with the highest transition temperature is the most stable and therefore is the one to which the prototype will transform. A modified phase diagram for BaTiO<sub>3</sub> is presented below in Figure 1.26. The principle polarizations are  $P_1$ ,  $P_2$ , and  $P_3$ , with  $P_3$  normal to the film surface. There are four ferroelectric phases on the phase diagram: (i) the  $c$  phase,  $P_3 \neq 0$ ,  $P_1 = P_2 = 0$ , (ii) the  $r$  phase,  $P_3 \neq 0$ ,  $P_1 = P_2 \neq 0$ , (iii) the  $aa$  phase,  $P_3 = 0$ ,  $P_1 = P_2 \neq 0$ , and the  $ac$  phase,  $P_3 \neq 0$ ,  $P_1 \neq 0$ ,  $P_2 = 0$ .

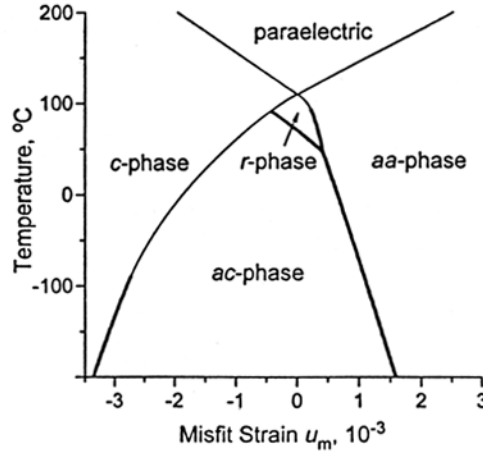


Figure 1.26: Calculated effect of strain on the phase diagram of BaTiO<sub>3</sub>, from Pertsev *et al*[57]. Phase diagram for BaTiO<sub>3</sub>. Note that the calculated Curie temperature at zero strain matches the observed bulk value.

The transition temperature of the out-of-plane phase is given by

$$T_3 = T_0 + 2C\epsilon_0 \frac{2Q_{12}}{s_{11} + s_{12}} u_m$$

where  $T_0$  is the Curie-Weiss temperature,  $C$  is the Curie-Weiss constant,  $\epsilon_0$  is the dielectric constant of free space,  $Q$  is the electrostrictive tensor, and  $s$  is the compliance tensor. The transition temperature of the in-plane phase is given by

$$T_1 = T_0 + 2C\epsilon_0 \frac{Q_{11} + Q_{12}}{s_{11} + s_{12}} u_m.$$

The best estimation of the effect of 2D strain were made by Forsbergh using a single crystal of BaTiO<sub>3</sub> in a pressure apparatus that applied force to the edges, but not the face, and used a polarized-light microscope to detect the transition, obviating the need for electrical fixturing[64]. The transition temperature increases with the square of the pressure. The thermal hysteresis also increases with increasing pressure. Though the data shows only compression, the expectation of Forsbergh is that tension will show the opposite trend. The cubic-tetragonal transformation is shown in Figure 1.27. The

increase in transition temperature is consistent in sign and reasonably close in magnitude with the calculations of Pertsev *et al.*, discussed above.

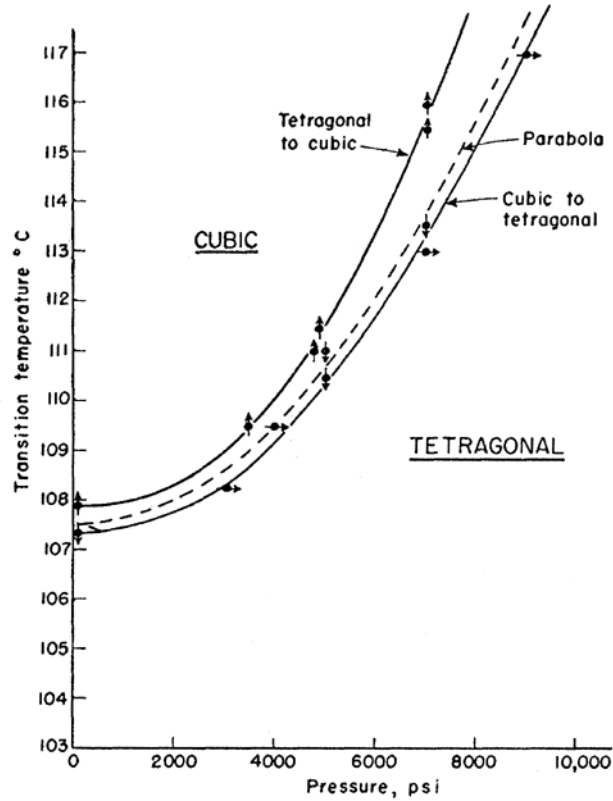


Figure 1.27: The effect of 2D compressive strain on transition temperature in  $\text{BaTiO}_3$ , from Forsbergh[64].

Samara conducted a series of experiments on ceramic  $\text{BaTiO}_3$  and  $\text{SrTiO}_3$  measuring the dielectric response as a function of temperature and pressure[65]. Recall that the phenomenological treatment observes correlations among the thermodynamic variables. From the perspective of the ferroelectric, increasing pressure, substituting a smaller Sr atom for a larger Ba atom, and lowering the temperature make the unit cell smaller. The effect of all 3 changes is to lower the transition temperature. Samara's work with  $\text{SrTiO}_3$  shows how substitutable these effects are. Figure 1.28 shows the permittivity of single crystal  $\text{SrTiO}_3$  as a function of temperature and pressure. Both sets of curves are

similar in form. Additionally, since the change in permittivity is approximately the same form, it is possible to construct a relation of the Curie-Weiss form for pressure,

$$\epsilon = \frac{C^p}{(p - p_0)}$$

in analogy to the Curie-Weiss law,

$$\epsilon = \frac{C^t}{(T - T_C)}$$

Ceramic BaTiO<sub>3</sub> samples were investigated as a function of pressure and temperature. Figure 1.29 shows the effect of pressure on BaTiO<sub>3</sub>. As pressure is increased, the same three effects that occur with thickness are observed: the transition shifts to a lower temperature, the transition becomes more diffuse, and the magnitude of the transition decreases. To the ferroelectric, pressure has an effect similar to sample size.

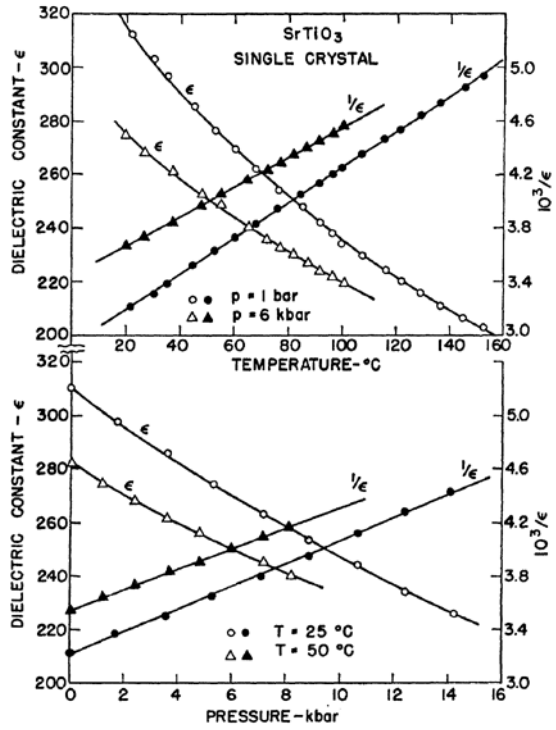


Figure 1.28: Dielectric response as a function of temperature and pressure for ceramic SrTiO<sub>3</sub>, from Samara *et al*[65].

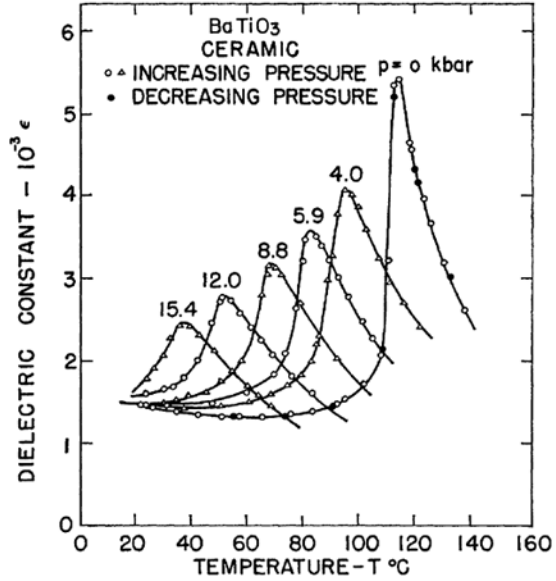


Figure 1.29: Dielectric constant of BaTiO<sub>3</sub> as a function of temperature and pressure, from Samara *et al* [65].

The effect of pressure is similar to the effects of finite size: decreasing transition temperature, decreasing maximum permittivity, and increasing diffuseness as a function of pressure.

The relationship between pressure and sample size has been noted by several groups[66, 67]. The correlations between the exponents have been investigated by Uchino and Nomura. The data was fit to the generalized Curie-Weiss law,

$$\left( \frac{1}{\epsilon} - \frac{1}{\epsilon_{\max}} \right) = C(T - T_c)^\gamma$$

which is used to model diffuse phase transitions, with  $\gamma$  varying between 1 and 2, and the pressure analog

$$\left( \frac{1}{\epsilon} - \frac{1}{\epsilon_{\max}} \right) = C^*(p - p_c)^{\gamma^*}.$$

The results suggested that the critical exponents  $\gamma$  and  $\gamma^*$  are close. For  $\text{Pb}(\text{Mg}_{1/3}\text{Nb}_{2/3})\text{O}_3$ , the value of  $\gamma$  is 1.64 and the value of  $\gamma^*$  is 1.66, which is within experimental resolution. It was suggested that there was some correlation, or common cause. However, no general explanation for the similarity between the effects of finite size and pressure for ferroelectrics has been advanced.

An explanation specific to BST was suggested by Roth *et al*[68].  $\text{SrTiO}_3$  is a quantum paraelectric. Recall that the failure of Landau theory is that it can not account for thermodynamic fluctuations that become more likely as the phase transition temperature is approached. The fluctuations are responsible for the transition. At low temperatures, there is a quantum mechanical stabilization of the soft mode, preventing  $\text{SrTiO}_3$  from becoming ferroelectric. The incipient nature of the phase transition is shown in Figure 1.30. Below about 4 K, the cooperative effects are stabilized, so the permittivity cannot increase[69].

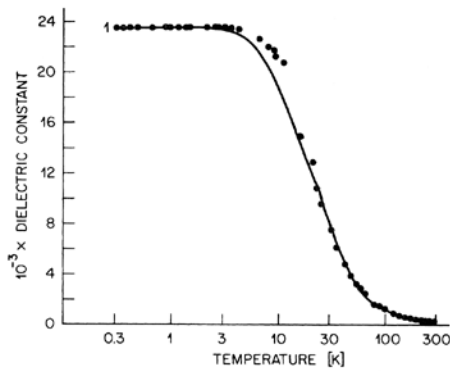


Figure 1.30: Dielectric response of SrTiO<sub>3</sub> about the quantum paraelectric transition temperature, from Muller *et al.*[69].

The quantum stabilization of the phase results in a constant dielectric response below the stabilization temperature

Roth *et al.* added enough Ba to raise the ferroelectric transition temperature to 60 K. Hydrostatic stresses of up to 0.7 GPa were applied and the dielectric response observed.  $\gamma$  varies from 1, which is classical Curie-Weiss behavior, to 2, the derived quantum stabilized limit. At high temperatures,  $\gamma$  converges to 1 for all measured pressures. Near the ferroelectric transition temperature,  $\gamma$  was highly pressure dependent. As the critical pressure for disappearance of ferroelectricity is approached, the diffuseness increases and diverges at the critical pressure. It was found that pressure affects the ferroelectric phase transition by quantum mechanical stabilization. The theory suggests that pressure, temperature, and composition can have similar effects from the perspective of the ferroelectric[68].

#### 1.3.4: LGD Size Effects

Most size effects models are corrections to the LGD model. Many attempts have been made to extend LGD theory to the case of thin film or otherwise constrained geometries[70-81]. The approach taken by Cross *et al.* is typical and rigorous and thus will be discussed in more detail[82, 83]. The minimum dimension for ferroelectricity is

calculated based on two observations. First, the surface of the ferroelectric crystal is different than the interior. The symmetry that is expressed in the soft mode behavior is altered. This surface contribution can be represented as a surface tension that is proportional to the surface area. Smaller ferroelectric systems have a much higher proportion of surface area. Second, the correlation lengths, which are a measure of the cooperative effect in ferroelectrics, are not isotropic. Along the polar direction, the forces are much stronger and longer-ranged than normal to the polar direction.

The LGD model includes polarization gradient terms. These terms can be neglected for large systems, but not small systems. The free energy of the crystal, neglecting depolarization fields, is

$$\Phi = \int_V \left\{ \frac{A}{2} P^2 + \frac{B}{4} P^4 + \frac{C}{6} P^6 + \frac{D_{11}}{2} (\nabla_z) P^2 + \frac{D_{44}}{2} (\nabla_x) P^2 + \frac{D_{44}}{2} (\nabla_y) P^2 \right\} dV + \int_{s_1} \frac{D_{11} \delta_3^{-1}}{2} P^2 dx dy + \int_{s_2} \frac{D_{44} \delta_1^{-1}}{2} P^2 dz dy + \int_{s_3} \frac{D_{44} \delta_1^{-1}}{2} P^2 dz dy$$

where

$$A = A_0 (T - T_{c0})$$

and  $T_{c0}$  is the Curie temperature of the bulk crystal;  $A_0$ ,  $B$ , and  $C$  are the standard LGD coefficients;  $S_1$ ,  $S_2$ , and  $S_3$  are the six surface planes of the surface of the crystal;  $\delta$  is the extrapolation length; and  $D_{11}$  and  $D_{44}$  are the normalized coefficients of the gradient term along the various directions in the crystal. The condition for the equilibrium free energy is

$$D_{44} (\nabla_x^2 + \nabla_y^2) P + D_{11} \nabla_z^2 P = AP + BP^3 + CP^5$$

with the boundary condition given as

$$|\nabla_i \pm \delta_i^{-1}|P|_{x_i \pm \frac{a_i}{2}} = 0 (i=1,2,3)$$

where  $x_i$  is  $x, y, z$  and  $a_i$  is  $A_0, B_0, C_0$ . The approximation

$$(D_{44}(\nabla_x^2 + \nabla_y^2)P + D_{11}\nabla_z^2P) - (A + BP_0^2 + CP_0^4)P \approx 0$$

where  $P_0$  is  $P(0,0,0)$  in the crystal, makes the above equations analytically solvable and should be valid for small crystals near the transition. This approximation yields approximate solutions for a first order transition and exact solutions for a second order transition.

For a first order transition,

$$P_0 = \pm \left\{ -\frac{B}{2C} \left[ 1 + \sqrt{1 - \frac{4A_0C}{B^2}(T - T_c)} \right] \right\}^{\frac{1}{2}}$$

and

$$T_c = T_{c0} + \frac{3B^2}{16A_0C} - \left\{ \frac{2D_{44}}{A_0\delta_1} \left( \frac{1}{a_0} + \frac{1}{b_0} \right) + \frac{2D_{11}}{A_0c_0\delta_3} \right\}.$$

For a second order transition,

$$P_0 = \pm \left\{ -\frac{B}{2C} \left[ 1 - \sqrt{1 - \frac{4A_0C}{B^2}(T - T_c)} \right] \right\}^{\frac{1}{2}}$$

and

$$T_c = T_{c0} - \left\{ \frac{2D_{44}}{A_0\delta_1} \left( \frac{1}{a_0} + \frac{1}{b_0} \right) + \frac{2D_{11}}{A_0c_0\delta_3} \right\}.$$

It is assumed that all  $\delta_s$  are positive. Using the equations for  $T_c$  it is possible to evaluate the minimum crystal size for ferroelectricity. These critical sizes were calculated for several perovskites, only the curves for  $\text{PbTiO}_3$  will be presented. As can be seen from Figure 1.31, the critical size for  $\text{PbTiO}_3$  is about 4 nm. The result agrees reasonably well with several empirical estimates of the critical size of particles, especially that of Ishikawa, *et al.*[84], discussed later. The results from the model can be used to estimate a critical volume. Assuming a cubic ferroelectric, the predicted critical volume is in the range of  $10^3$  to  $10^4$  nm<sup>3</sup>.

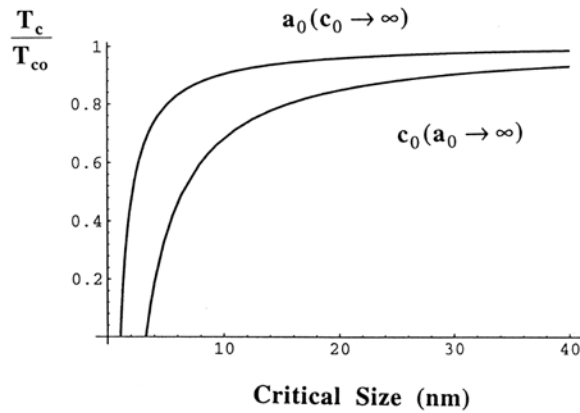


Figure 1.31: Calculation of critical size for ferroelectricity for  $\text{PbTiO}_3$ , from Shaoping *et al.*[82]. The ratio of the transition temperature of the modeled ferroelectric to a bulk ferroelectric is plotted as a function of critical size, with  $c$  being the film normal direction.

Several points about the nature of size effects can be made. First, the critical size is strongly affected by the shape of the ferroelectric, as the magnitude of the cooperative effects depend on the crystallographic orientation of the material. Second, although phenomenological theory is useful over a wide range, it does require corrections that are ultimately non-mean field in origin, namely the extrapolation length,  $\delta$ . It should be noted that the diffuseness of the transition is not explained by the theory and is attributed by Cross *et al.* to other origins, such as processing difficulties[82].

### 1.3.5: Models of Size Effects in Particles

Size effects in particles are typically described using the LGD model, but particles are a special case that warrants special mention. It is attractive to consider size effects in particles, as spherical particles do not require calculation of asymmetric correlation lengths and other difficulties associated with thin film geometries. Several groups have attempted to theoretically account for the effect of size on small particles of ferroelectric material[85, 86]. The most complete treatment was given by Jiang and Bursill[87]. Their model uses two corrections to the LGD theory. The first is the extrapolation length developed by Binder *et al.* and discussed previously. The second is LGD coefficients that vary as a function of size. The model provides an explanation for the  $c/a$  ratio, latent heat, dielectric response, and  $T_c$  shift of the particles. However, it is not greatly different from the previous LGD treatments and does not give any physical insight. It will be discussed because the relations derived are often used to predict the minimum size for ferroelectricity not only in particles, but also ceramics and thin films.

The equation of state is the LGD equation, given as

$$G = \frac{1}{2}\alpha(T, d)P^2 + \frac{1}{4}\beta(d)P^4 + \frac{1}{4}\gamma P^6$$

where

$$\alpha(T, d) = \alpha_0(T - T_{0\infty}) + \frac{A}{d - D_s}$$

and

$$\beta(d) = \beta_\infty \exp\left(-\frac{B}{d}\right).$$

$\gamma$  is assumed to be size independent. The adjustments are empirical fits to the size data for  $\text{PbTiO}_3$  powder.  $\beta_\infty$  is the bulk value for  $\beta$ .  $d$  is the particle size and  $A$ ,  $B$ , and  $D_s$  are fitting coefficients.

The spontaneous polarization is

$$P_s^2 = \frac{-\beta(d) + \sqrt{\beta(d)^2 - 4\alpha(T, d)\gamma}}{2\gamma}$$

The shift in  $T_c$  as a function of  $d$  is

$$T_c = T_{0\infty} - \frac{A}{d - D_s\alpha_0} + \frac{3\beta(d)^2}{16\alpha_0\gamma}$$

and the spontaneous polarization at  $T_c$  is

$$P^2 = \frac{3\beta(d)}{4\gamma}$$

What distinguishes the treatment of Jiang and Bursill's approach is the extension of the model into portions of LGD theory normally neglected. The predicted  $c/a$  ratio is given as

$$\frac{c}{a_d} = \frac{c}{a_\infty} - \left[ \frac{c}{a_\infty} - 1 \right] \exp(-C(d - D_c))$$

where  $C$  is a fitting parameter and  $D_c$  is the critical particle size, so when  $d=D_c$ ,  $c/a$  is 1 [87].

Zhang *et al.* calculated the average extrapolation length in ferroelectric particles of various sizes as a function of temperature. It was assumed that isotropic, ferroelectric particles of  $\text{BaTiO}_3$  were embedded in a non-ferroelectric matrix. The results are shown in Figure 1.32. Several concepts about the nature of the correlation length in

ferroelectrics are illustrated. First, in part b of the figure, the length decreases as a function of particle size, since the dipoles near the surface do not have the same effective extrapolation length. This causes the average value to decrease as the fraction of near-surface volume increases. Second, correlation length is correlated to  $T_c$ .  $T_c$  decreases with decreasing size and so does  $\xi$ . In part a of the figure, the maximum correlation length is related to the size of the ferroelectric. Once the correlation length is about the size of the particle, it can not increase more[88].

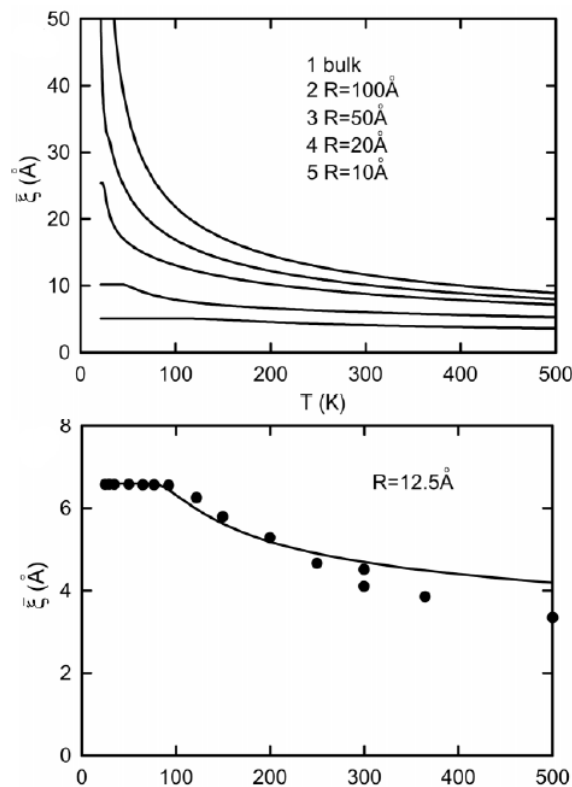


Figure 1.32: Extrapolation length as a function of temperature for various particle sizes, from Zhang *et al*[88].

### 1.3.6: Experimental Evidence: Ceramics

Experimental studies of size effects are difficult. Not only are there many confounding factors, such as, depolarization, strain, and others mentioned previously, but

size effects themselves are often subtle and smaller in magnitude than the experimental control of composition, temperature, or measurements such as particle size, that are necessary for the investigation of size effects. Attempts to calculate a minimum size for ferroelectricity, as discussed above, are especially difficult to translate into experimental measurements. Most of the predictions of minimum size are based on experimental extrapolation. Not measuring ferroelectricity can be due to many reasons, only one of which is a sample smaller than the minimum size.

McCauley *et al.* investigated size effects in glass ceramics. Barium carbonate, silica, alumina, and titania were combined in a powder. This powder was melted and poured onto an aluminum slab quickly cooling it to prevent devitrification. The amorphous samples were annealed for different times at the same temperature, so crystal size was carefully controlled. The results were analyzed in terms of scaling theory. Recall that the four general predictions of scaling theory are a reduction in  $T_C$ , a reduction in  $T_{\max}$ , an increase in the diffuseness of the transition, and that these relationships should be linearized by a log-log treatment. Figure 1.33 shows the decrease of  $T_C$  with a decreasing number of unit cells,  $N$ . Figure 1.34 shows the relationship between the maximum permittivity and number of unit cells,  $N$ . Finally, the equation describing permittivity-temperature behavior of relaxor ferroelectrics was employed,

$$\frac{1}{\epsilon} = \frac{1}{\epsilon_{\max}} + \frac{(T - T_{\max})^2}{2\epsilon_{\max}\delta^2}$$

to generate a diffuseness parameter,  $\delta$ . This relationship is shown as a function of the number of unit cells,  $N$ , in Figure 1.35[13, 89].

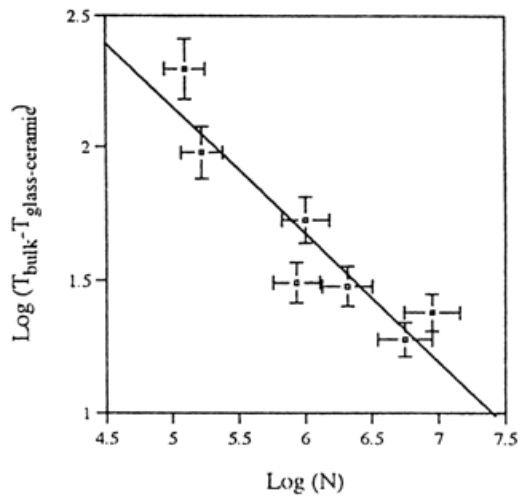


Figure 1.33: Shift in transition temperature as a function of crystal size, from McCauley *et al*[13].

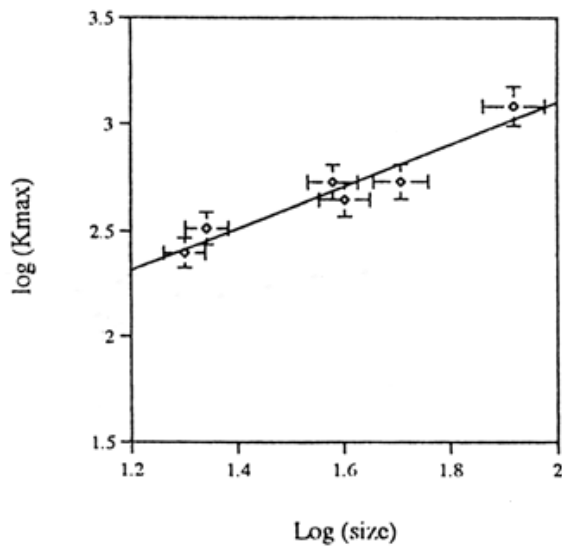


Figure 1.34: Variation in maximum permittivity as a function of crystal size, from McCauley *et al*[13].

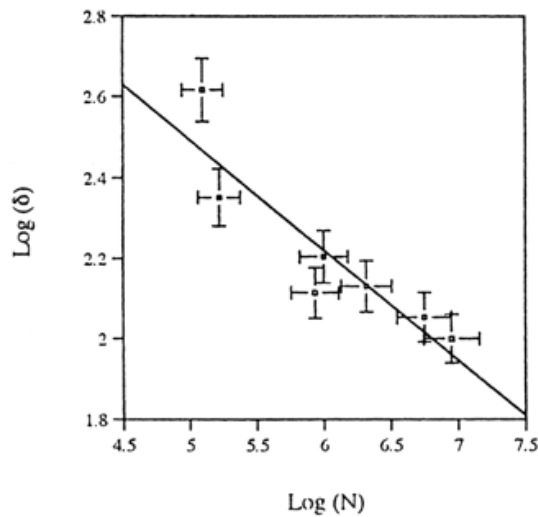


Figure 1.35: Change in diffuseness as a function of crystal size, from McCauley *et al*[13].

Another study by Frey *et al.* examined the role of surface area, including grain boundaries, on the permittivity of BaTiO<sub>3</sub> ceramics[90]. The BaTiO<sub>3</sub> powder was prepared via a chemical route that was designed to produce powders substantially free of hydroxyl defects[91]. The resultant powders were pressed into pellets in a hot press at 8 GPa for 30 min at 700 °C. Greater than 98% theoretical density was achieved. Subsequent annealing was used to control grain size. Temperature sweeps were from higher to lower temperature. The relative permittivity and dielectric loss tangent are showed as a function of temperature in Figure 1.36. The data do not vary smoothly, as McCauley *et al.s'* data do. The data illustrates one of the difficulties of size effects investigations: the microstructure of the grains change as a function of thickness. Below about 0.5 μm, the twins common in BaTiO<sub>3</sub> ceramic grains become less stable and are thus less common. The change in microstructure is apparent in this case, but is often more subtle and acts as an uncontrolled confounding factor.

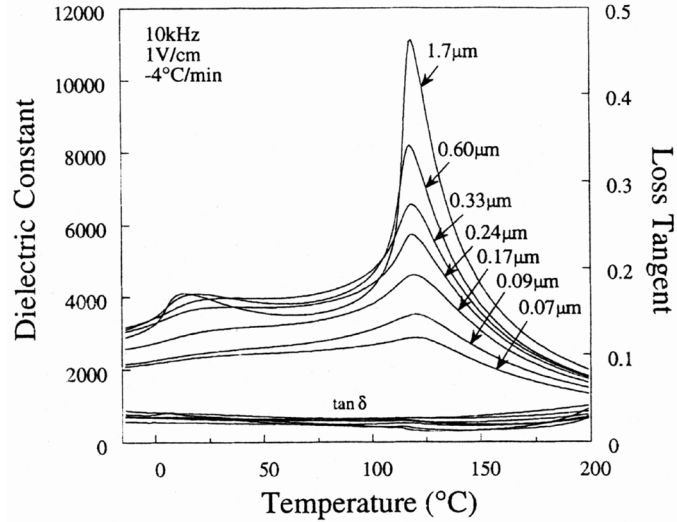


Figure 1.36: Dielectric constant and loss of ceramic BaTiO<sub>3</sub>, from Frey and Payne[90].

Figure 1.37 shows the maximum dielectric constant as a function of grain size. The data was interpreted by a model with a grain boundary exhibiting a temperature-independent reduced permittivity and a grain interior that behaves as a single crystal ferroelectric. All grain sizes contain combinations of these two components. The result of an applied field is series-connected capacitors. This is essentially a phenomenological dead layer model formulated for a ceramic. The dielectric response of the blocking-layer model is

$$\frac{1}{\bar{K}'} = \frac{v_1}{K_1'} + \frac{g v_2}{K_2'}$$

where  $\bar{K}'$  is the apparent dielectric constant,  $v_i$  is the fraction of the phase,  $K_i'$  is the dielectric constant of that portion of the grain, and  $g$  is a geometric factor, based on the morphology of the grains, about 1/3 for the case presented. The model fit gives a thickness to the blocking layer of 0.8 nm and a dielectric constant of 130.

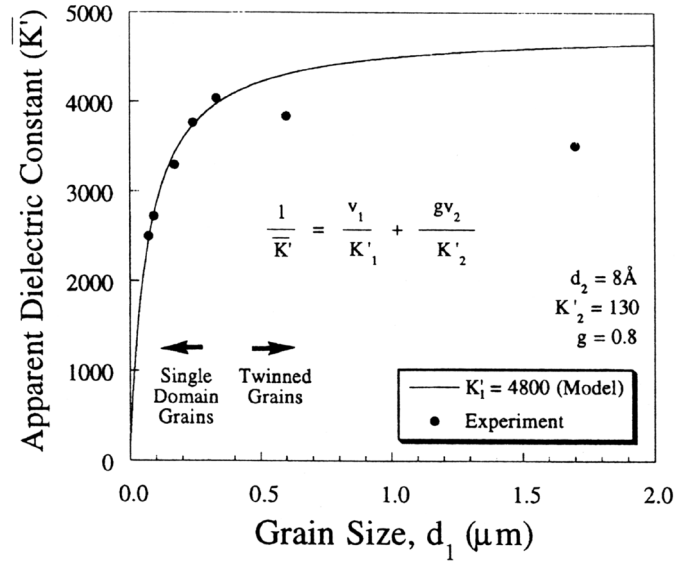


Figure 1.37: Dielectric constant variation as a function of grain size and microstructure for BaTiO<sub>3</sub> ceramics, from Frey and Payne[90].

Zhang *et al.* studied BST ceramics derived from a sol-gel process. The Ba/Sr ratio varies from 1/3 to all Sr. The study suffers from not having as careful composition control of the (Ba + Sr)/Ti ratio. It varies from 1.00/1.02 to 1.00/1.95[92]. Additionally, the grain size was modified by changing the sintering temperature, rather than the sintering time, which may affect the quality of the data, since different temperatures may result in coarsening processes and thus in different morphologies. The dielectric response was measured from 10 K to 400 K. Using data extracted from the paper, the trends expected from finite size are observed. The diffuseness data is shown in Figure 1.38. The expected power law relation is observed. However, the  $T_c$  data do not follow the pattern as well, as can be seen in Figure 1.39[92]. One possibility is that since the measurement of  $T_c$ , being one temperature, is less precise than the diffuseness, which is a fitting parameter over a large range of data.

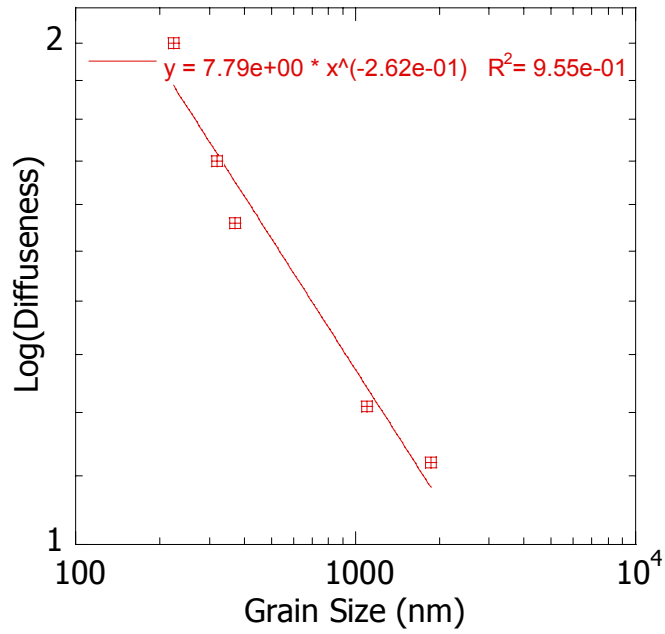


Figure 1.38: Diffuseness as a function of grain size for a BST ceramic. Adapted from Zhang *et al*[92].

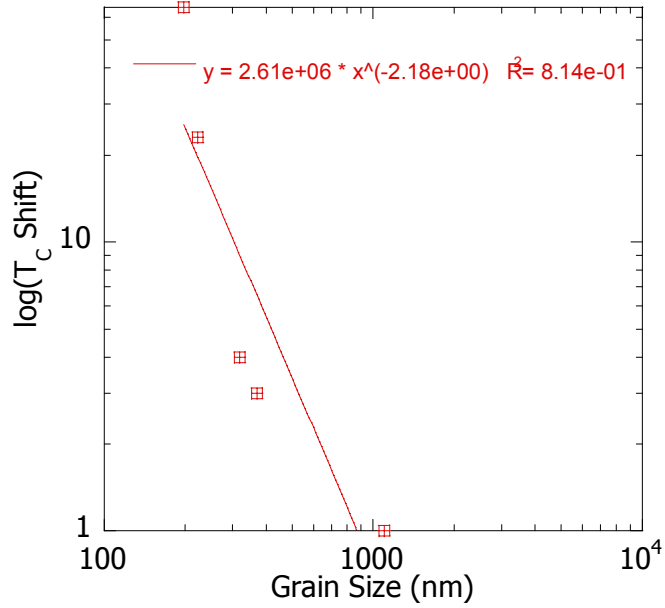


Figure 1.39: Shift in transition temperature as a function of grain size for a BST ceramic. Adapted from Zhang *et al*[92].

### 1.3.7: Experimental Evidence: Particles

Investigating size effects with particles has advantages over ceramics in that the stress state is easier to understand. It is also easier to control the composition and homogeneity than for thin films and ceramics. However, there are problems unique to particles, especially the difficulty of making electrical measurements. Many groups have investigated finite size effects in particles[84, 93-95], so the focus will be on a representative sample.

Zhong *et al.* used a sol-gel process to create particles of  $\text{PbTiO}_3$  with a narrow distribution. The particles were characterized by Raman spectroscopy, x-ray diffraction, and differential scanning calorimetry. Particle sizes were controlled by adjusting the calcining time and temperature. Scherrer's equation was used to determine the size. Scherrer's equation is

$$D = \frac{K\lambda}{(B \cos(\theta))}$$

where  $D$  is the grain size,  $\lambda$  is the wavelength,  $\theta$  is the diffraction angle,  $B$  is the integrated peak width, and  $K$  is a constant that is crystal-dependent. The calculated size was verified with TEM.

Three factors were measured as a function of particle size. The first is tetragonality, or  $c/a$  ratio, which decreased from 1.065 for the 200 nm particles to 1.059 for the 22 nm particles. The Raman shift decreased from 85  $\text{cm}^{-1}$  in the 200 nm particles to 71  $\text{cm}^{-1}$  for the 22 nm particles. This suggests that the soft mode frequency decreases with decreasing particle size. Finally, the specific heat displayed the three expected finite-size scaling relations, decreased magnitude, decreased maximum

temperature, and increased diffuseness with decreasing size. However, the data are only good in a qualitative sense, as the error of the DSC measurements is at least 5 K[92].

Park *et al.* attempt to make quasi-particle electrical measurements of  $\text{Pb}(\text{Sc}_{1/2}\text{Ta}_{1/2})\text{O}_3$  by using sol-gel derived particles and lightly sintering the aggregates so that they achieve between 50-70% theoretical density. A coating of hydrated manganese nitrate was used to minimize the effects of internal stress and depolarization fields. Particle sizes were controlled by adjusting the pH and pressure during the precursor reaction. Three methods were used to characterize the particle sizes, calculating both mean and standard deviation: a commercial laser-scattering particle size analyzer, XRD patterns, and SEM of the fracture surface.  $T_C$  was measured three ways: XRD, electrically, and DSC. The study finds that  $c/a$  ratio, specific heat, and dielectric response display the expected finite-size scaling behavior. The XRD, specific heat, and dielectric data are summarized in Figure 1.40, Figure 1.41, and Figure 1.42 respectively[96]. Not all particle sizes are shown for all the characterization methods.

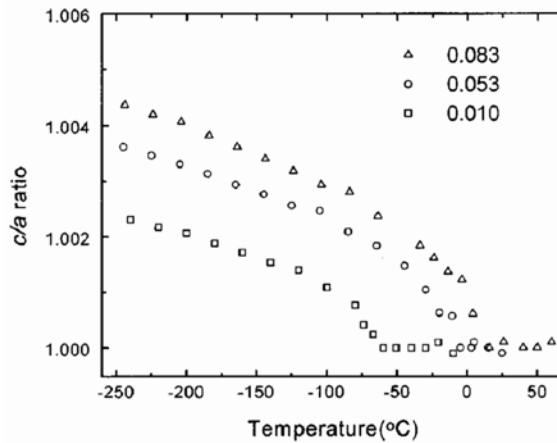


Figure 1.40: Degree of tetragonality as a function of temperature for different grain sizes, from Park *et al.*[96].

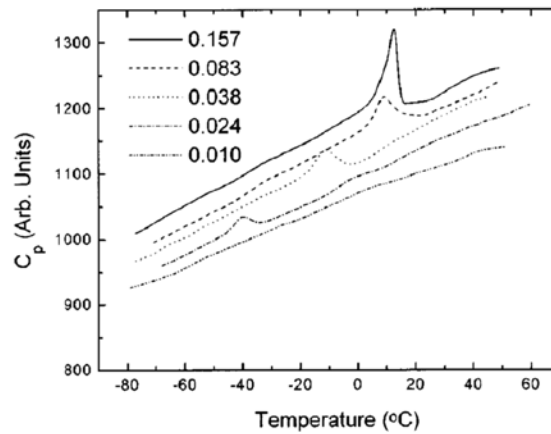


Figure 1.41: Specific heat as a function of temperature for different grain sizes, from Park *et al*[96].

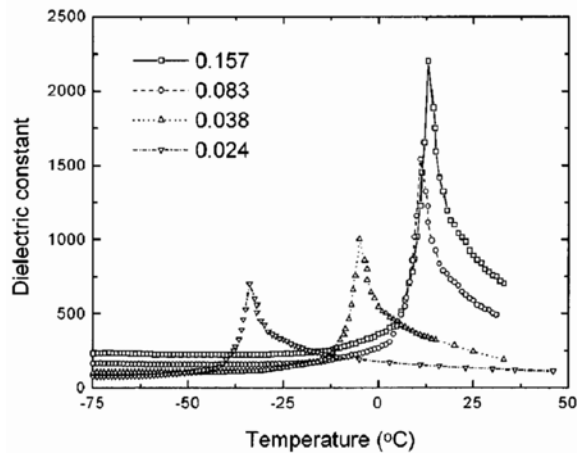


Figure 1.42: Dielectric constant as a function of temperature for different grain sizes, from Park *et al*[96].

### 1.3.8: Experimental Evidence: Thin Films

The work on size effects in ferroelectric thin films is largely confined to the BST systems, including the end members  $\text{BaTiO}_3$  and  $\text{SrTiO}_3$ . A single investigation of PZT is included, as it is the best investigation of PZT, which is an important ferroelectric system. The analysis of size effects in PZT is a precursor to the dead layer theory. The balance of the subsection discusses the BST system.

Size effects in thin films are often referred to as thickness effects. For many films, the grains are columnar. Volume is thus linearly dependent with thickness, so it is a distinction without much difference. Once possible physical origin of thickness effects in ferroelectrics is that the nucleation composition may be different than the growth composition, *i.e.*, slightly Ti-rich, as is the case for BST, or there may actually be a series capacitor configuration from an interfacial layer between the dielectric and the electrode. Earlier work on BST occasionally showed amorphous interfacial layers. Paek *et al.* deposited BST via RF Magnetron sputtering onto Pt/Ti/SiO<sub>2</sub>/Si at 550°C. The large columnar grains typical of (100) BST were observed, but a small semi-crystalline layer at the BST-Pt interface was also observed by TEM. For the thickness series investigated, there was a roughly linear relationship between film thickness and interfacial layer thickness. At 50 nm, the amorphous layer was 11 nm thick. For a 300 nm film, the amorphous layer was 9.5 nm thick[97].

Prior to the dead layer model's formulation by Zhou and Newns, Larsen *et al.* suggested a blocking layer model, which is to say a surface layer with different properties[98]. The effect was investigated with PbZr<sub>0.51</sub>Ti<sub>0.49</sub>O<sub>3</sub> deposited on Pt/Ti/SiO<sub>2</sub>/Si via MOCVD, with top electrodes deposited by sputtering. The dielectric response was measured in three ways: a Sawyer-Tower circuit, for measuring ferroelectric hysteresis; capacitance; and pulse testing, to measure the suitability for use in ferroelectric memories. The capacitance curves were used to generate the standard inverse capacitance density versus thickness plot. The interfacial capacitance was calculated to be 4.1 nF. The coercive field was measured with the Sawyer-Tower circuit. The coercive field scales linearly with field as

$$V_C = V_0 + E_C d .$$

The intercept of coercive voltage versus thickness is 0.2 V.

Finally, the pulse switching response was measured as a function of the pulse voltage. Two 100 ns pulses of the same sign are separated by 10  $\mu$ s. Then there is a 20 ms delay followed by two pulses of the opposite sign. This is repeated over a range of voltages. From this test, it is possible to calculate the switched polarization, the non-switched polarization, and the remnant polarization for each voltage. If the data are plotted as in Figure 1.43, *i.e.*, the voltage to reach a given polarization as a function of thickness, the intercept can be interpreted via the following equation

$$V_p = E_{PZT}d + \frac{d_{bl}}{\epsilon_0\epsilon_{bl}}P$$

where the *bl* subscript denotes the blocking layer terms. The following dead layer assumptions are made in the analysis. First, there is a series connection of 2 dielectrics, neither having a thickness dependence. Second, the blocking layer was assumed to not have a field dependence and is non-ferroelectric. It should be noted that the intercept should be constant as a function of charge if the theory is correct.

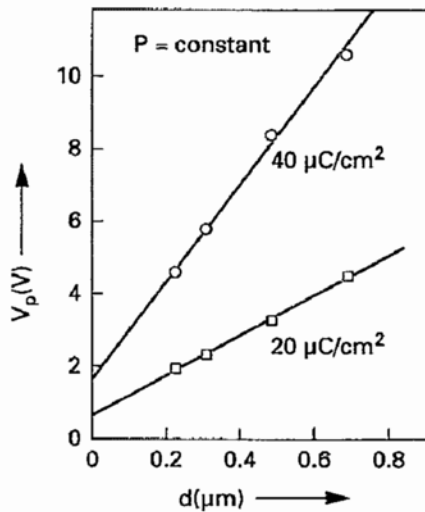


Figure 1.43: Voltage to reach a given polarization as a function of thickness, from Larsen *et al*[98].

The resultant capacitance densities, given as  $\epsilon_{bt}/d_{bt}$  with units of  $\text{nm}^{-1}$ , are calculated for the three methods: for the capacitance, 23; for the hysteresis, 20; and for the pulse, 28[98].

Li *et al.* deposited  $(\text{Ba}_{0.5}\text{Sr}_{0.5})\text{TiO}_3$  on to MgO substrates, via PLD. This results in a compressive stress in the BST upon cooling. Scans of the (001) peaks were taken in order to calculate the out-of-plane lattice constant and thus the stress in the film. The lattice constant increased from about 0.3940 nm for a 14 nm film to 0.3952 nm for a 500 nm film. The LGD relationship between stress and permittivity is such that BST films under compressive stress should display a higher dielectric constant. The magnitude of the effect is not well known. The data of Li *et al.* are remarkable in that the permittivity of the 14 nm thick capacitor is 2350 and the permittivity of the 500nm thick capacitor is 1700. The data provide some confirmation of the Pertsev calculations. However, temperature data is not presented, so the data's utility is limited, as the difference could be caused by a transition temperature shift. Additionally, no theory of size effects is used to treat the data and the capacitors are interdigitated, so the permittivity calculations are nontrivial.

Tsai and Cowley machined a sample of poled  $\text{BaTiO}_3$  into a wedge for observation in TEM. The domain structure was visible in the microscope. EELS was employed to measure the thickness of the sample. It was hypothesized that there was a non-ferroelectric surface layer in which relaxation occurred, so that near the edge, there would be a region where the sample was too thin for ferroelectricity to be stable, as evidenced by the lack of a domain structure. The thickness of the surface layer was measured to be 10 nm, putting the minimum thickness for ferroelectricity at 20 nm[99].

Many groups investigated thickness effects in the context of the dead layer model, but must do not take temperature-dielectric response data[100-102]. An exception to this is the work that Li *et al.* did in investigating thickness effects on a series of SrTiO<sub>3</sub> films. The films were deposited by PLD on to SrRuO<sub>3</sub> electrode, with a LaAlO<sub>3</sub> substrate. The films' thicknesses ranged from 25 nm to 2.5 μm. The dielectric response was measured from 4 K to 300 K. The permittivity data are summarized in Figure 1.44. The data follow the expected form. The data are analyzed using the dead layer equation. This is used to extract the bulk component of the permittivity. Figure 1.45 shows that the “bulk” permittivities are not constant as a function of film thickness. This result is inconsistent with the dead layer model. Additionally, considering the inverse permittivity versus inverse thickness plot that is inset in Figure 1.45, it is apparent that the dead layer either has variable thickness or permittivity as a function of temperature. Both are inconsistent with the dead layer model[31].

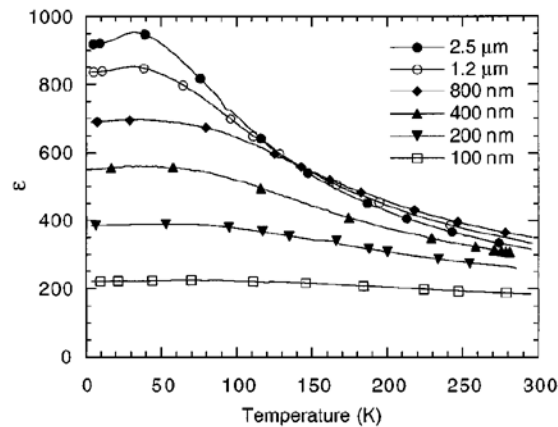


Figure 1.44: Permittivity as a function of temperature for different thicknesses of SrTiO<sub>3</sub>, from Li *et al.*[31].

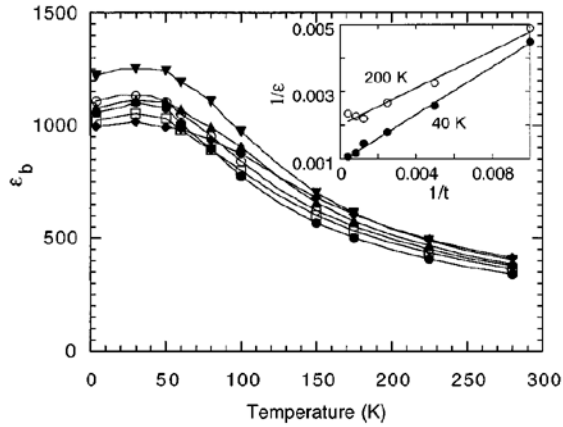


Figure 1.45: Calculated “bulk” permittivity as a function of thickness for different temperatures for  $\text{SrTiO}_3$ , from Li *et al.*[31].

Turning to the investigation of thickness effects in BST thin films, it is important to reiterate that it is a straightforward process to incorrectly measure and interpret thickness effects; experimental artifacts must be carefully controlled. While many groups have used the dead layer model to understand thickness effects in BST[21, 28, 31, 80, 100, 103, 104], few papers provide insight beyond the work of Li *et al.* [28]. This work will not be discussed in detail.

An investigation by Horikawa *et al.* demonstrate the difficulties of measuring size effects in thin film BST[105]. Films were grown by rf-sputtering from a  $(\text{Ba}_{0.65}\text{Sr}_{0.35})\text{TiO}_3$  ceramic target with the substrate from 500 to 700 °C, with the composition verified by XRF. Film thicknesses were measured by SEM and grain size was measured by x-ray using Scherrer’s formula. The x-ray estimates were verified with TEM on some samples. It was found that the dielectric response was a stronger function of grain size than of film thickness. Additionally, the deposition temperature affected the grain size. Deposition at higher temperatures is expected to produce films with better crystallinity. Thinner films were weakly affected by the deposition temperature, but as film thickness increased, the difference between the lower and higher temperature dielectric constants became larger. Additionally, the temperature data follow the expected trend with grain size, with  $T_c$

decreasing as grain size decreases[105]. This is consistent with finite size scaling model, as grain size and not film thickness should be the relevant quantity.

A study of thickness effects of BST films was performed by Basceri *et al.* [7] and continued by Streiffer *et al.*[8]. The samples used in the work are an MIM structure: Pt/BST/Pt/SiO<sub>2</sub>/Si. The (100) fiber-textured BST films were deposited at 640 °C onto Pt-coated Si wafers by liquid-source chemical vapor deposition, with thicknesses from 24 to 160 nm. The Ba to Sr ratio was 70/30. The (Ba+Sr)/Ti ratio was varied from 49/51 (51.0%Ti) to 46.5/53.5 (53.5% Ti). The compositions and thicknesses were established to approximately ±0.3 at.% and ±5.0%, respectively, by standards-based x-ray fluorescence. Capacitors were defined by evaporating Pt through a shadow mask at 315 °C.

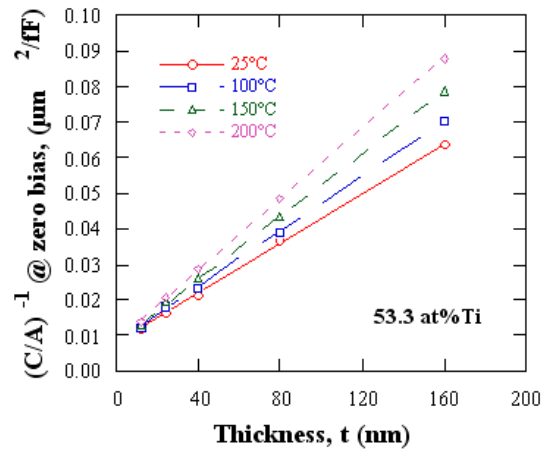


Figure 1.46: Variation of capacitance density of BST films as a function of thickness for different temperatures[7].

Plots of inverse capacitance density and thickness are shown as a function of temperature in Figure 1.46 and as a function of composition in Figure 1.47. The extrapolated interfacial capacitance is noted to be independent of temperature and composition, within the experimental resolution. The dead layer model segments the apparent capacitance as

$$\frac{A}{C_{app}} = \frac{A}{C_i} + \frac{A}{C_B} = \frac{t_i}{\epsilon_i \epsilon_0} + \frac{(t-t_i)}{\epsilon_B \epsilon_0}$$

where the subscript  $B$  denotes the “bulk” of the film and  $i$  denotes the interfacial layer. Figure 1.46 shows the correct relationship for the dead layer as a function of temperature. The interfacial component is temperature independent within the measurement resolution and the bulk component is temperature dependent. Likewise, Figure 1.47 shows the correct behavior as a function of composition. If there is an interfacial layer caused by contamination or a change in the soft mode near that interface, the layer should be much less sensitive to composition than the bulk of the film, which is closer to being an ideal ferroelectric. It was noted by Basceri *et al.*[7] that since ferroelectricity is a cooperative phenomena, the permittivity of the films could be a function of film thickness, irrespective of the interfacial layer[7].

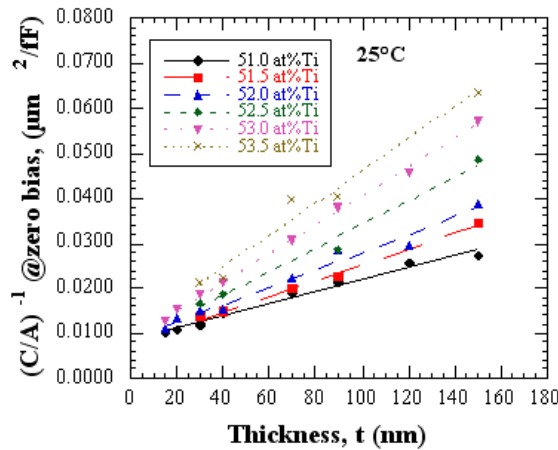


Figure 1.47: Capacitance density of BST films as a function of thickness for different compositions[7].

Streiffer *et al.* continue the analysis by calculating the Curie-Weiss constants and Curie-Weiss temperatures for the materials. It is a consequence of the dead layer model that the Curie-Weiss constants should be thickness independent and the Curie-Weiss temperatures should be a strong function of thickness. This data is plotted in Figure 1.48. Several possibilities were advanced for the thickness dependence of the permittivity,

divided into two categories: intrinsic and extrinsic. The extrinsic effects could be some combination of the following: contamination of the interface by hydrocarbons or other chemicals, a change in the composition in the near-interface region, and/or a change in the grain size in the near-interface region. The extrinsic effects could be some combination of the following: incomplete polarization screening by the electrode; the dead layer effect, or other interfacial discontinuity; and/or electrode-film band offsets that give rise to surface states and fields near the interface[8]. The overall conclusion of the work is that the thickness effects are likely caused by some combination of the above. The experimental data is generally corroborative with a dead layer explanation.

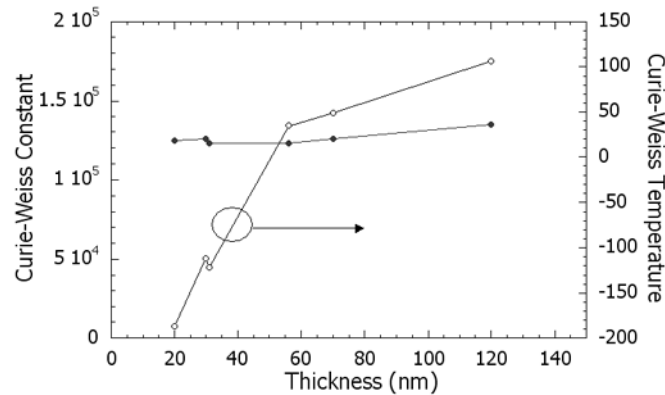


Figure 1.48: Curie-Weiss constant and Temperature as a function of thickness for 53.0% Ti BST.

Sinnamon *et al.* examined a thickness series of  $(\text{Ba}_{0.5}\text{Sr}_{0.5})\text{TiO}_3$  deposited by PLD on  $\text{SrTiO}_3$ , with thicknesses from 7.5nm to 950 nm[21]. Au top electrodes were formed by thermal evaporation. The data were taken at 400 °C to lessen the effect of  $T_c$  shifts resulting from the “Curie anomaly suppression.” The permittivity and  $\tan(\delta)$  are plotted in Figure 1.49. Several important experimental variables were not controlled for, including strain and grain size. However, the treatment gives some insight into the logical consequences of the dead layer theory.

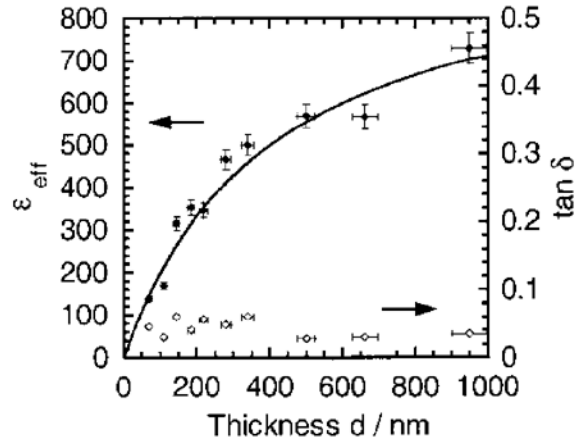


Figure 1.49: Thickness scaled permittivity of BST as a function of thickness, from Sinnamon *et al*[21].

Figure 1.50 shows the ratio of thickness to permittivity versus thickness for the films measured in the study. The dead layer thickness is not calculable, only the ratio of thickness to permittivity is known. Using the standard dead layer equation, the permittivity as a function of thickness is calculated for three scenarios. The first is that the dead layer model's two component assumption is strictly correct. The material is composed of a bulk and dead layer component, assumed to be 3.75 nm for the purposes of the illustration. This results in a step function permittivity profile for the film. The result is that below twice the dead layer thickness,  $d/e$ , there is an anomaly the permittivity, the falloff with thickness is much more severe. Both the assumed permittivity profile and the resultant  $d/e$  plot is shown in case (i) in Figure 1.51. The second case is for the more physically realistic case of a parabolic decrease in permittivity within the dead layer thickness. This also results in a permittivity anomaly in the  $d/e$  plot, as shown in case (ii) in Figure 1.51. The final assumption is that the dead layer has no thickness, but is only an interface component. This corresponds to (iii) in Figure 1.51 and is the best fit to the data. The conclusion is that the dead layer model is at best an incomplete model, as one of the necessary consequences, *i.e.*, the form of the rolloff in the permittivity for very thin films has not been observed[21].

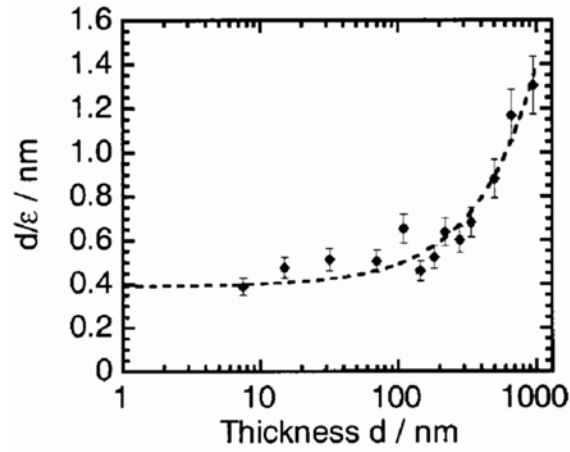


Figure 1.50: Thickness scaled permittivity as a function of thickness for BST, from Sinnamon *et al*[21].

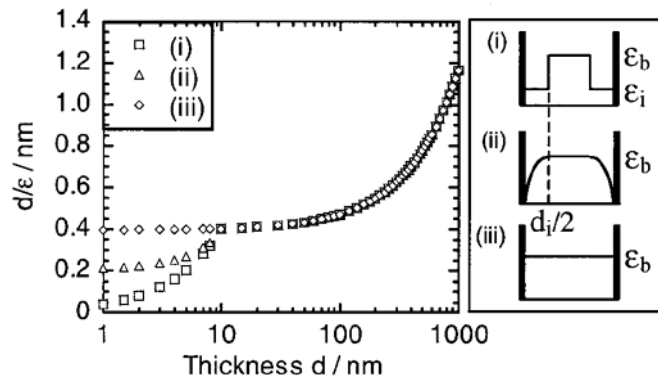


Figure 1.51: Calculation of thickness to permittivity as a function of thickness for three scenarios, from Sinnamon *et al*[21].

## 1.4: Barium Strontium Titanate

This section is divided into three subsections. The first is an introduction to the chemistry and deposition of barium strontium titanate. The second discusses the application of BST to DRAM. The third subsection is an overview of the electrical properties of BST.

### 1.4.1: Materials Science of BST

#### *1.4.1.1: Chemistry*

BST belongs to the perovskite class. It is made up of the end members strontium titanate,  $\text{SrTiO}_3$ , and barium titanate,  $\text{BaTiO}_3$ .  $\text{SrTiO}_3$  has a permittivity maximum at 20K, for  $\text{BaTiO}_3$  the value is 395 K. In principle,  $\text{SrTiO}_3$  and  $\text{BaTiO}_3$  are completely soluble. It is possible to tune the temperature of maximum permittivity by adjusting the ratio of the end members, as can be seen in Figure 1.52. Each mol% of Sr addition to  $\text{BaTiO}_3$  causes a drop in the transition temperature of 3.4 °C. For 70/30 Ba/Sr the transition temperature is about 300 K[106]. The Ba/Sr ratio is the first of two compositional variables. The second is the (Ba+Sr)/Ti ratio, which is more important to the electrical properties. Since BST belongs to the perovskite class, there are many possible dopents. The effects of some of these on the transition temperature are shown in Figure 1.53.

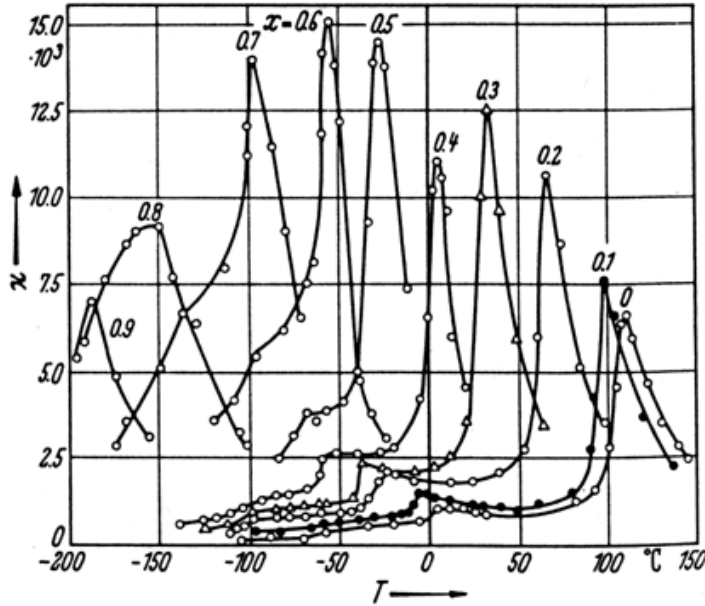


Figure 1.52: Dielectric susceptibility of BST as a function of temperature for various compositions, from Bethe *et al*[106].

The bulk properties of BST are well understood, but the thin film properties are different and less understood. For example, the bulk solubilities are much smaller than the thin film solubilities, as shown in Table 1.3. Stemmer *et al.* performed high-spatial resolution electron energy loss spectroscopy to examine the local atomic environment at both the grain interior and grain boundary for films of 51 at% Ti and 53.5 at% Ti. It was found that the Ti/O ratio was about the same in the grain and at the grain boundary for the lower % Ti film. In the higher % Ti film, the grain boundary had a higher Ti/O ratio than the grain interior. Amorphous grain boundary regions were noted in the higher % Ti film. Some excess Ti is accommodated by the grain, additional Ti is accommodated at the grain boundary, and in the case of great excess, some amorphous titania is deposited between the grains[107].

Table 1.3: Differences between bulk and thin film solubilities in BST

	Bulk[108]	Thin Film[109]
(Ba+Sr)/Ti Upper Limit	<1.001	>1.20
(Ba+Sr)/Ti Lower Limit	>0.999	<0.75

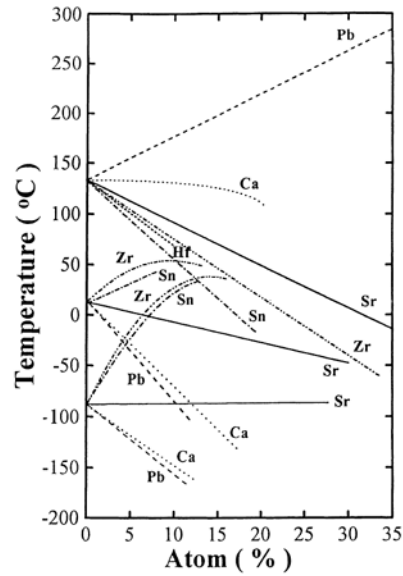


Figure 1.53: Effect of some dopants on the transition temperature of ceramic BST, from Hench *et al*[110].

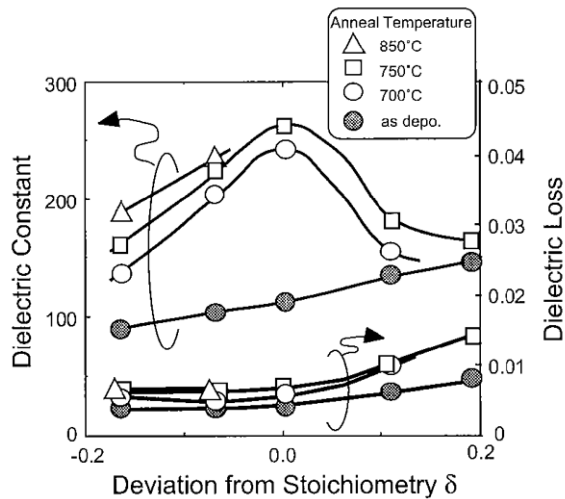


Figure 1.54: Dielectric response about as a function of Ti stoichiometry for 30 nm MOCVD films, from Horikawa *et al*[111].

$\delta < 0$  indicates Ti excess.

Horikawa *et al.* of Mitsubishi examined the effect of (Ba+Sr)/Ti stoichiometry on the dielectric response of BST films[111]. The dielectric constant and dielectric loss

tangent can be seen in Figure 1.54. The dielectric constant decreases on either side of stoichiometry. The films were grown via a two-stage liquid source MOCVD on Pt/SiO<sub>2</sub>/Si. A seed layer was grown at a higher temperature and then the balance of the film was deposited at a lower temperature, followed by a crystallization anneal. The top electrodes were defined by shadow mask

Three results can be seen in Figure 1.54. First, the dielectric constant decreases on either side of stoichiometry. Second, for Ti excess ( $\delta < 0$ ), the dielectric loss tangent is relatively constant as a function of titanium. For  $\delta > 0$  the dielectric loss tangent increases further from stoichiometry. Third, increasing the anneal temperatures increases the dielectric constant, but has a marginal effect on the loss. Similar results were found by Yamamichi *et al.* with sputtered films of BST as a function of Ti nonstoichiometry[109].

Basceri conducted an extensive study on the effects of excess Ti on dielectric properties. Figure 1.55 shows the relationship of zero-bias permittivity and Ti. The convention for the composition is (Ba,Sr)+Ti equals 100, so that 51% Ti is (49)/(51). The data show that the further from stoichiometry a sample is, the lower the permittivity. Additionally, the effect of composition is reduced as the films become thinner.

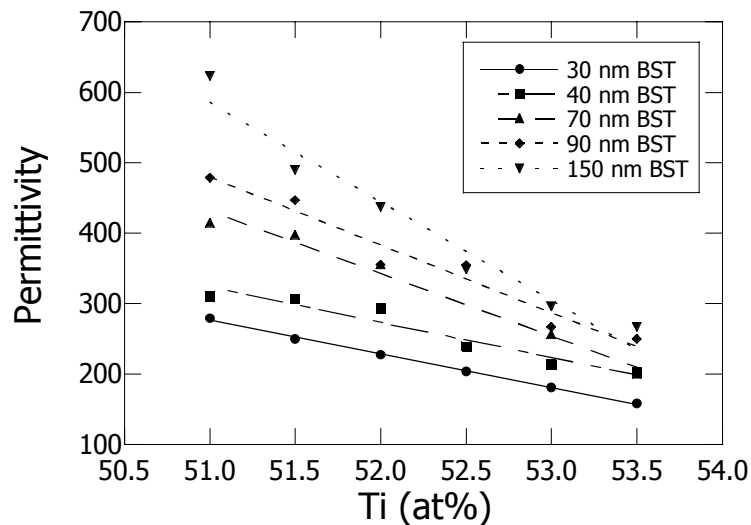


Figure 1.55: Zero-bias permittivity as a function of composition for various thicknesses of BST[112].

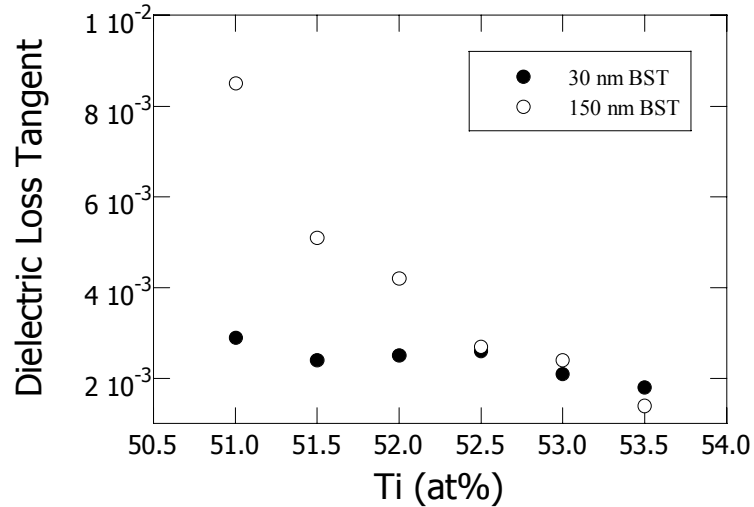


Figure 1.56: Dielectric loss versus Ti for different thicknesses of BST[112]

#### 1.4.1.2: Microstructure

The temperature at which BST crystallizes from an amorphous film was measured by Noh *et al.* using synchrotron radiation[113]. An amorphous, 550 nm BST film was sputtered on to single crystal MgO (001) and heated. A metastable intermediate phase was nucleated in the range of 500-600 °C, which preceded the nucleation of the perovskite phase at about 700 °C.

There are two main orientations of BST: [100] and [110]. The [100] orientation of BST is the more desirable of the two, as the dielectric loss tends to be lower and the film smoother. Two processing parameters are believed to have the strongest effect. The first is the deposition temperature and the second is the substrate. A study by Lee, *et al.* found the [110] component to be reduced by higher deposition temperatures[114]. BST films were sputtered on to Pt/SiO<sub>2</sub>/Si from 500 to 650 °C. 500 °C deposition produced films with a majority [111] component and of poor crystallinity. By 600 °C, the films

were more crystalline, with a majority component of [110] and a minor component of [100] and improved crystallinity, and at 650 °C, the films had a major [100] component and a small [110] component.

Undoubtedly the grain size has an effect on the dielectric properties, but it is difficult to adjust the grain size without simultaneously changing the other properties. An example is provided by Lee *et al*[115]. It was found that rf-sputtering of BST led to a microstructure where the grain size, measured by surface morphology, increased as a function of film thickness. The reason for this relationship is not given. It might be that the growth orientation is different than the nucleation orientation, or that grain coarsening occurs from the longer time at elevated temperatures. It is then impossible to extract the grain size effect, as the grains would have different shape and size distributions based on the cause of the coarsening.

#### 1.4.1.3: Processing

Thin films of polycrystalline BST are highly sensitive to the deposition conditions. While there are several deposition methods for BST, such as rf-sputtering[116], chemical solution deposition[117], and pulsed laser ablation[118]. The currently preferred method is MOCVD. MOCVD films tend to have the best electrical properties. MOCVD can produce deposition rates acceptable for commercial use and can deposit on complex geometries, which is essential as DRAM capacitor structures have high aspect ratios. Additionally, MOCVD films have good thickness and composition uniformity, good crystallinity, and high density[119].

There are three main drawbacks of MOCVD. The first is that the deposition temperatures must be high enough to crack the metallorganic bond. Lower deposition temperatures is one advantage of sputtering, both DC and rf, but it is more difficult to

maintain the desired chemistry at high deposition rates[119]. One alternative, demonstrated by Yamamichi *et al.*, is electron cyclotron resonance plasma MOCVD. This allows processing at 450 °C, which is compatible with processing limits of a RuO/Ru/TiN/TiSi bottom electrode and barrier layer[120]. The second drawback of MOCVD is that the standard source materials deteriorate over time and the third is the low vapor pressure accorded by the sources. The last two drawbacks were solved by researchers at Mitsubishi by using liquid precursors that were injected into the reactor[121]. The organometallic precursors, such as metal-tetramethylheptanedionates, are dissolved in a high vapor pressure solvent such as tetrahydrofuran, and delivered to a vaporizer in controlled quantities. This technique is important since it enables excellent run-to-run stoichiometric uniformity across an 8-inch wafer.

#### 1.4.1.4: Electrodes

Electrodes are important because they affect the dielectric properties directly, both electrodes affect the band gap alignment; the bottom electrode provides the growth surface for the BST; and either electrode may react or interdiffuse with BST. The main candidates are noble metals such as Pt, Ir, and Ru and conducting oxides such as SrRuO<sub>3</sub>, Ir/IrO<sub>2</sub>, and Ru/RuO<sub>2</sub>. The metals tend to have lower leakage, perhaps because of a larger potential barrier. While Pt is the reference electrode, there are several problems with Pt: poor adhesion to SiO<sub>2</sub> and Si, hillock formation, and high oxygen diffusivity.

The electrodes are typically combined with an oxygen diffusion barrier between the electrode and plug. The barrier should prevent plug oxidation, prevent the electrode from reacting with the plug, and remain reasonably conductive[122].

Salient characteristics of common BST bottom electrodes are presented in Table 1.4. The effects of top electrodes are summarized in Figure 1.57 through Figure 1.59.

The top electrodes have a more limited effect on the capacitor structure. Pt, Ir, IrO<sub>2</sub>, Ir/IrO<sub>2</sub> top electrodes were deposited on 50 nm of 51 at.% Ti BST/Pt/SiO<sub>2</sub>/Si by Lash to optimize annealing conditions for the top electrode material. Temperature, annealing atmosphere, and top electrode type were investigated[123].

Table 1.4: Bottom Electrode Effect on BST properties. Adapted from Tsai and Tseng[124].

Property	Electrode					
	Pt	Ir	IrO <sub>2</sub> /Ir	Ru	RuO <sub>2</sub> /Ru	
Dielectric Constant	As deposited	219	309	234	548	322
	After 700 °C O <sub>2</sub> Anneal	503	593	501	325	433
Dielectric Loss	0.014	0.046	.016	.32	.017	
Leakage Current (*10 <sup>-8</sup> A/cm <sup>2</sup> w/100kV/cm bias)	2.2	4.9	2.5	39.4	3.5	
Work Function (eV)	5.6	5.32		4.8		
Breakdown Field (MV/cm)	3.84	3.68	3.49	1.94	1.84	
Surface Roughness (nm)	1.9	1.27	2.25	4.40	4.12	
H <sub>2</sub> Damage Endurance (%drop in dielectric constant)	16	12	13	29	14	
Stability in O <sub>2</sub> ambient to 700 °C	Yes	Yes	Yes	No	Yes	

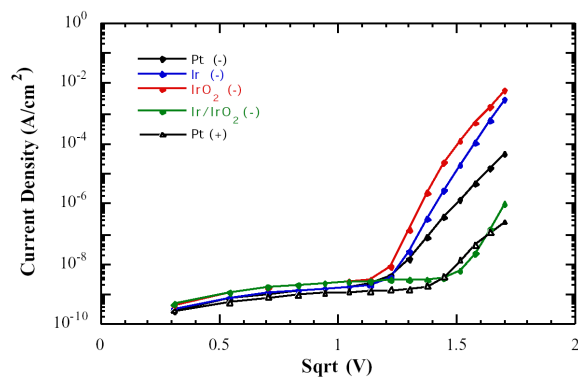


Figure 1.57: J-V curves for BST/Pt/SiO<sub>2</sub>/Si with various top electrodes, from Lash[123].

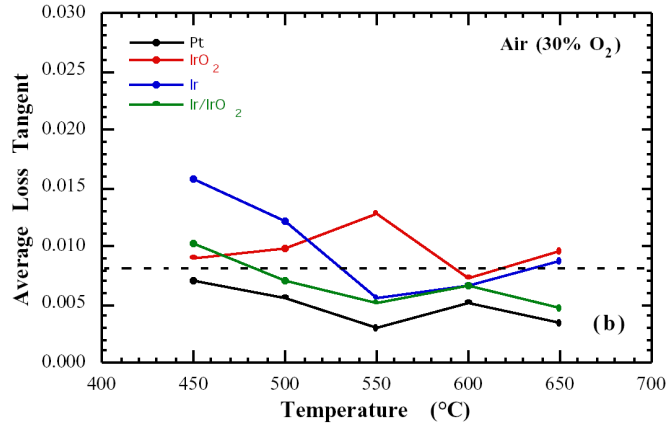


Figure 1.58: Dielectric loss of BST/Pt/SiO<sub>2</sub>/Si as a function of annealing condition for various top electrodes, from Lash[123].

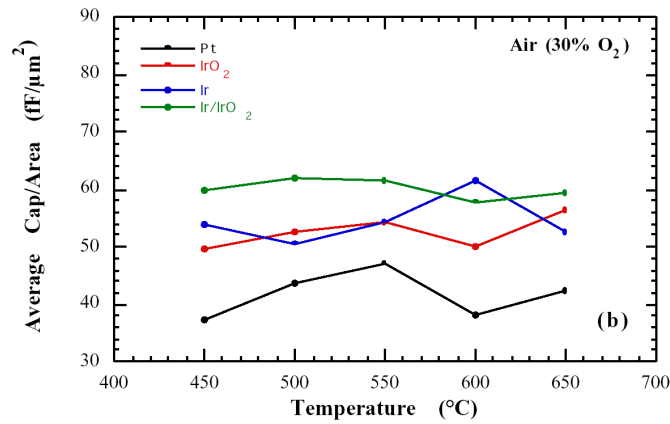


Figure 1.59: Capacitance density of BST/Pt/SiO<sub>2</sub>/Si as a function of annealing condition for various top electrodes, from Lash[123].

### 1.4.2: Electrical Properties

The four aspects of the electrical properties that are most important are: (1) temperature and (2) voltage dependence of the permittivity and the dielectric relaxation as a function of (3) time and (4) frequency. The focus of this subsection is on the properties that differ from the conventional oxide or oxynitride dielectrics.

The temperature dependence of the permittivity is much stronger in ceramic rather than thin film BST, as will be discussed in the chapter on size effects. Figure 1.60 shows the curve for the permittivity of ceramic  $(\text{Ba}_{0.7}\text{Sr}_{0.3})\text{TiO}_3$ . The permittivity decreases by more than 80% over 150 K. This dependence must be taken into account when considering BST for an application such as use as a DRAM capacitor[119].

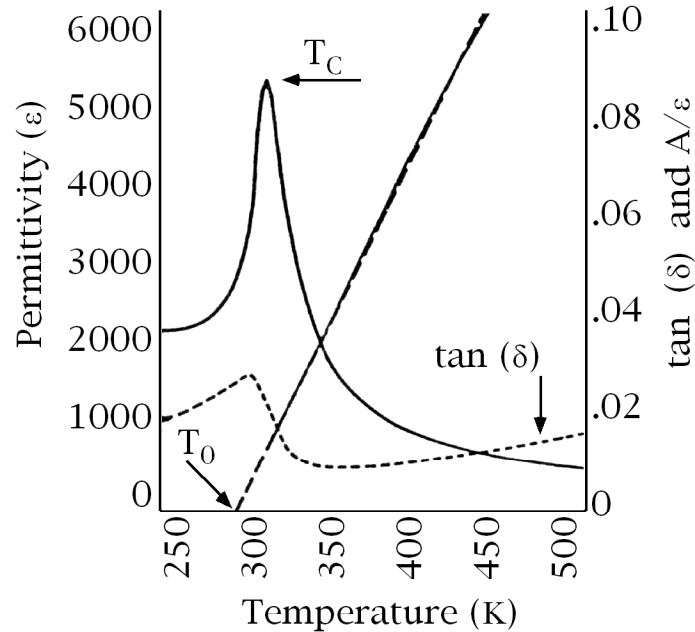


Figure 1.60: Permittivity and dielectric loss for ceramic BST. Adapted from Hilton and Ricketts[125]. Noted on the plot are the Curie-Weiss temperature,  $T_0$ , and the transition temperature,  $T_c$ .

The field dependence of the permittivity is shown in Figure 1.63. The small signal permittivity is the value often reported, but a bias across the capacitor, such as the write bias, causes the permittivity to drop. The accessible permittivity is typically 5% less than that calculated from the zero-field permittivity.

The frequency dependence is significant because a capacitor can conceivably see any frequency, from DC to the operating frequency, during normal operation of a DRAM cell[126]. The polarization of BST has faster and slower components. They follow a power law dependence of in both the time and frequency domains. This correspondence

is known as the Curie- von Schweidler law, which simply states that the dielectric relaxation should be characterized by an exponent in both the time,

$$J_p(t) = J_0 t^{-n}$$

and frequency,

$$C_t - C_\infty = C_0 f^{n-1}$$

domains and that the exponent should be the same in both cases[122]. This behavior is shown by Basceri in a 60 nm, 52.0 at% Ti Pt/BST/Pt/ZrO<sub>2</sub>/SiO<sub>2</sub>/Si sample as a function of time for both current and permittivity in Figure 1.61 and Figure 1.62, respectively[112].

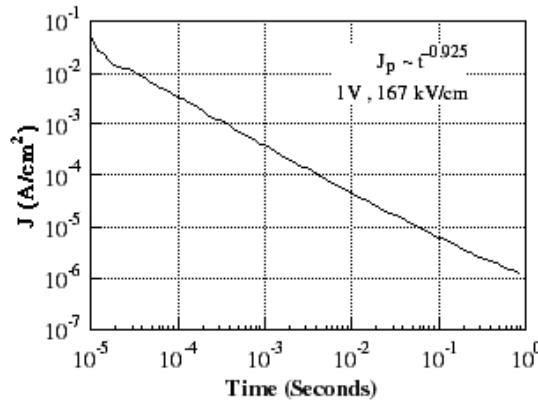


Figure 1.61: Charging current flowing into a 60 nm, 52.0 at%Ti BST film as a function of time, from Basceri[112].

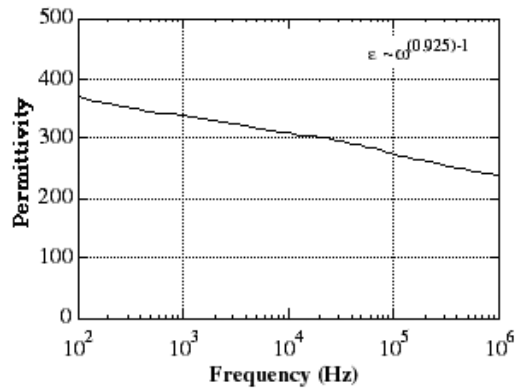


Figure 1.62: Relative permittivity of a 60 nm, 52.0 at%Ti BST film as a function of frequency, from Basceri[112].

### 1.4.3: Applications of BST

The primary application for thin film BST is as the capacitor dielectric in DRAM. The area of the capacitor decreases with each generation, but the required charge for successful read-out does not. The minimum charge is derived from the requirements of the sense amplifiers, circuit parasitics, and the  $\alpha$ -particle emissions from naturally occurring trace radioactive impurities in packaging materials or from cosmic rays. The requirement translates to *circa* 25-30 fF/cell. This means that higher capacitance densities are required for each generation. There are three main avenues for increasing capacitance density. First, the cell geometry can be made more complex, which adds process steps and thus increases cost. Second, the dielectric can be made thinner, which can cause reliability and deposition problems. Third, a higher permittivity dielectric can be used[122].

BST has dielectric behavior greatly different from SiO<sub>2</sub>. The three significant differences are as follows. First, the dielectric constant is a function of applied voltage. This can be seen in Figure 1.63 and is evident in the LGD treatment. Second, BST has a crystalline microstructure, as can be seen in Figure 4.42, whereas SiO<sub>2</sub> is amorphous, so there are grain boundaries and other microstructural considerations. Finally, BST is a

three component oxide and  $\text{SiO}_2$  is a single component oxide, so the overall complexity of the system is much higher.

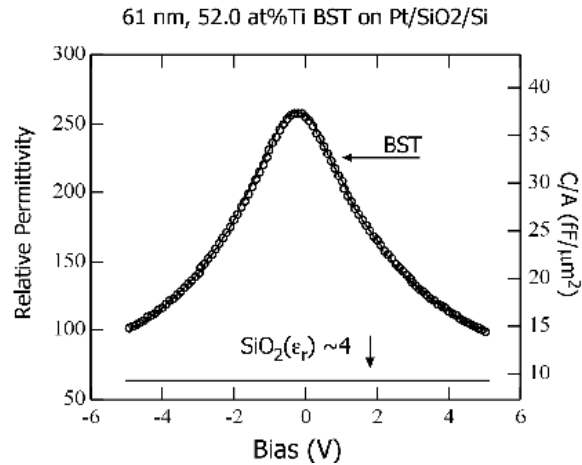


Figure 1.63: Dielectric constant of BST and  $\text{SiO}_2$  as a function of voltage.

The requirements of BST for use in DRAM were discussed by Ezhilvalavan and Tseng. The requirements include an  $\text{SiO}_2$  equivalent thickness of less than 2 Å; a leakage current density of less than  $10^{-7}$  A (although  $10^{-8}$  A is closer to the current requirement); and a 10 year lifetime at 85 °C of  $10^{15}$  cycles at 1.6V and a frequency of 100 MHz[119]. Additionally, 90% of the written charge should be available for readout. This translates to a dielectric loss of less than 0.008, as calculated by Lash[123].

Kotecki *et al.* at IBM have fabricated a stacked BST capacitor with a minimum feature size of 0.2  $\mu\text{m}$ . The bottom Pt electrode is 250 nm, the TaSiN diffusion barrier is 75 nm, and the BST is 27 nm[122]. A TEM image of the cell can be seen in Figure 1.64.

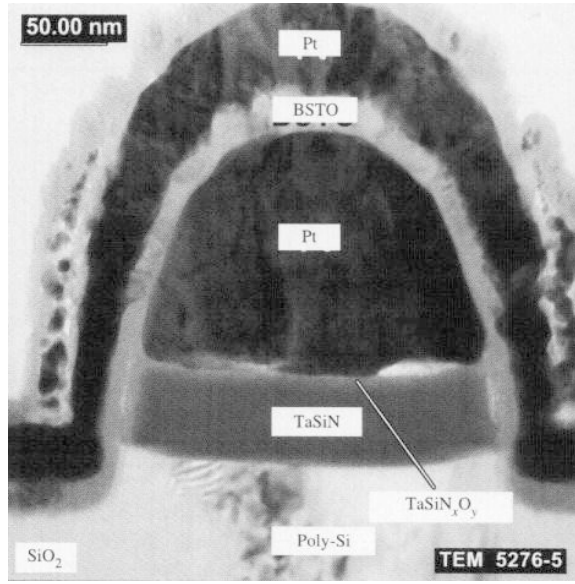


Figure 1.64: TEM image of DRAM cell using BST as the dielectric, from Kotecki *et al*[122].

BST is different from  $\text{SiO}_2$  in that the dielectric properties are a strong function of temperature, chemistry, thickness, and strain. The microstructure must be carefully controlled to optimize the dielectric properties. The electrodes and barrier layer systems add to integration complexity.

## 1.5: Reliability

The review of reliability first discusses some of the statistical methods used. Then the case of SiO<sub>2</sub> is reviewed for concepts and procedures that can be transferred to BST. Finally, the BST reliability literature is reviewed.

### 1.5.1: Statistical Methods

Modeling reliability requires thorough understanding of the statistics used to analyze the data, for two reasons. First, the amount of data needed is often large and is either slow or expensive to obtain. Second, it is easy to infer too much from the large extrapolations that are typically required for reliability estimation. The amount of data needed depends upon the underlying distribution of the data and the type of reliability information desired, as shown in Table 1.5. The most data intensive case is modeling a non-normal distribution with competing failure modes as stress conditions change. A model for this case for SiO<sub>2</sub> is implemented by Degraeve *et al*[127].

Table 1.5: Data requirements increase from left to right

Median failure time (50% Failed)	→	Estimation of entire distribution
Normal or lognormal data with constant variance	→	Strongly non-normal data (Weibull, gamma), or distribution a function of stress parameters
One failure mode	→	Multiple, competing failure modes

Failure is a device property being beyond an acceptable limit. The property may change beyond that limit or may have started beyond that limit. Failure criteria are application specific. The failure criteria for DRAM capacitors include leakage current less than  $10^{-7}$  A/cm<sup>2</sup> and a  $\tan(\delta)$  less than 0.008. Failure does not necessarily occur at dielectric breakdown. Breakdown is a catastrophic change in the film conduction mechanism and is one type of failure. Thus, time to failure,  $t_f$ , may not be the same as time to breakdown,  $t_{BD}$ . Reliability is quality over time. A definition of reliability should include time, temperature, operating voltage, percent failed, and active oxide area. One definition that encompasses the necessary components is given by Degraeve *et al.*, “Fewer than 0.01% failures are allowed after 10 years on an effective gate oxide area of 0.1cm<sup>2</sup> at operating voltage and temperature[127].”

The two most common are failures in time (rate), or FIT, and average failure rate, or AFR. Reliability goals from the ITRS roadmap are expressed as FIT rate. The values from several past years are shown in Table 1.6. A FIT is a device failure in a billion device hours, *e.g.*, 10,000 devices tested for 1,000 hours is  $10^6$  device hours. If one failure occurred, the FIT rate would be  $(1/10^6)*10^9$ , or 100 FIT.

Table 1.6: Acceptable FIT rates for the years 1992-2001 [128]

1992	100 FIT
1992-1995	10 FIT
1995-1998	1 FIT
1998-2001	0.1 FIT

Closely related to FIT is AFR. AFR is calculated from the hazard function. The hazard function is the instantaneous probability of failure at time  $t$ , essentially the ratio of the probability distribution function and the unfailed percentage of devices, given as

$$h(t) = \frac{f(t)}{1 - F(t)}$$

The average failure rate of survivors over some time is the integral of the hazard function, given as

$$AFR(t_1, t_2) = \frac{1}{t_2 - t_1} \int_{t_1}^{t_2} h(t) dt = \frac{-\ln(1 - F(t_2)) + \ln(1 - F(t_1))}{t_2 - t_1}.$$

where  $t$  is time,  $h(t)$  is the hazard function, and  $F$  is the cumulative distribution function of the failure distribution. The units of AFR is  $\text{hr}^{-1}$ , so 1 FIT is  $10^{-9} \text{ hr}^{-1}$  [129].

The group of methods used to analyze reliability data, *i.e.* survival statistics, are distinctive in two main ways. First, the distributions of device lifetimes are often strongly skewed and are described by distributions such as the exponential, Weibull, and lognormal. Second, the data are often censored. A large portion of reliability data can be understood with four statistical concepts: distribution estimation, maximum likelihood, censoring, and Weibull plots.

Accurately predicting the reliability of a statistical process requires not only the prediction of median lifetime, but also the prediction of the entire failure distribution. The low  $t_{\text{BD}}$  tail negatively affects reliability, leading to an overestimation of reliability and operating lifetime. This can be seen in Figure 1.65. The first 1% of failures practically controls reliability. The distribution depends on many variables: stress field, temperature, processing, *et cetera*. Until it is shown otherwise, it must be assumed that the distribution changes with stress conditions. Investigation of the distribution of tddb of BST under AC stress by Reisinger, *et al.* found that the intercept, slope, and overall shape of the distribution do indeed change as a function of stress frequency [126].

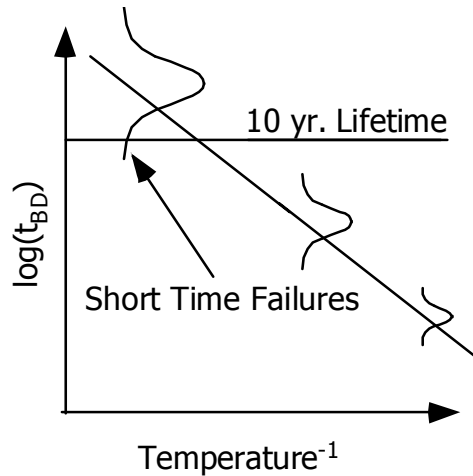


Figure 1.65: Extrapolation of Arrhenius-type process showing the effect of short failure times.

Consequently, it is necessary to model the effects of changing various conditions, such as the stress field or temperature, on the failure distributions. The standard statistical analyses are based on error or failure distributions that are either normal or lognormal and are not suitable for modeling other distributions, such as the Weibull distribution. For instance, if it were desired to construct an Arrhenius plot with observed lifetime data that is modeled by a Weibull failure distribution, a version of the Arrhenius relationship specifically derived for the Weibull distribution must be used[130].

Once the appropriate model is derived, a proper method must be used to estimate the model parameters. There are two major estimation methods used: maximum likelihood and a special case of maximum likelihood, least squares.

Least squares parameter estimation is more commonly used, because of the ease of computation. It minimizes the sum of the squared distances from the predicted value to the measured data. Consider a one variable, two parameter linear model

$$y = \beta_0 + \beta_1 \cdot x + \varepsilon .$$

The predicted response,  $y$ , is a function of the intercept,  $\beta_0$ , the product of the explanatory variable  $x$  and the linear coefficient  $\beta_1$ , and the random errors,  $\varepsilon$ . These

random errors capture the variation that is not explained by the model. The random errors have four main requirements that limit the cases where least squares analysis can be applied. The assumptions are these. The  $\epsilon$ 's must be independent, identically distributed, normally distributed with the mean at zero, and have constant variance. For this case, with uncensored data, maximum likelihood parameters and least squares parameters yield the same values. The greater the violation of the assumptions, the less accurate the least squares fit. For other common lifetime distributions, such as the Weibull and exponential, the resultant parameters are biased. Additionally, confidence intervals cannot be reliably calculated [131]

Another drawback of least squares is that the data must be uncensored, *i.e.*, all the failure tests must be run to completion. Since reliability experiments often seek to characterize the early failures, it is useful to use an estimation method that allows the censoring of data.

Maximum likelihood estimation is more robust than least squares and can accommodate censored data. Additionally, there is no need to know the cumulative distribution function. While the computation of MLE parameters is computationally intensive, the concept is fairly straightforward. The MLE takes the probability function of the data, *i.e.* how likely observations in the sample are, and an assumed model and finds the parameter values from which the observed samples is most likely to have been generated[130].

Also important is understanding the effect transformed axes have on confidence intervals. Most predictions of lifetime for BST are based on large extrapolations of data taken at high temperature and field, as in the analysis for both resistance degradation by Basceri *et al.*[112] and tddb by Yamamichi *et al.*[132]. Typically, these extrapolations are

fit using transformed axes, for example, an Arrhenius plot is the natural log of the dependant variable as a function of inverse temperature. Estimating model parameters of the transformed data and then transforming back to the original space is not the same as fitting the parameters in the original model. There are three points that are important to note about transformed models. First, the resultant parameter estimates will likely be different than those that would be found by fitting least squares to the data directly. Also, the resulting  $R^2$  value from the transformed data does not refer to the explanation of variation in the untransformed data. The most important consideration is the effect that the re-transformation has upon confidence intervals. An example is given for a loglinear model, as can be seen in Figure 1.66. The data from Figure 1.66 was taken from Basceri *et al*[112]. The model would be extrapolated back to 80 °C, corresponding to a  $1000/T$  value of 2.832. The confidence intervals seem quite reasonable in Figure 1.66, but upon re-transformation the interval estimates become quite large, as can be seen in Figure 1.67.

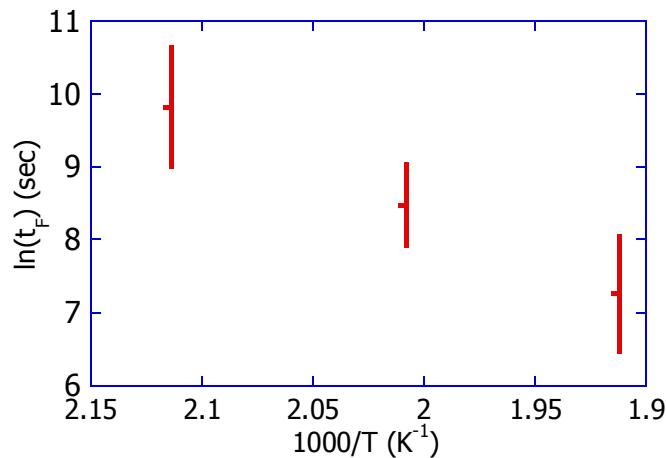


Figure 1.66: Resistance degradation time to failure for 30 nm 51% Ti BST.  
 The estimate is indicated by the horizontal bar in each interval. The interval indicates 95% model confidence.

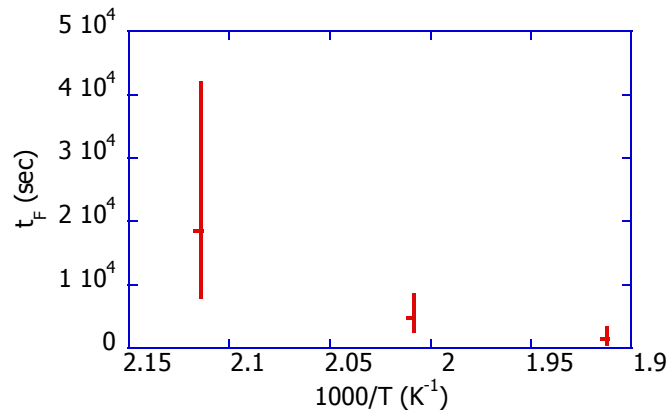


Figure 1.67: Resistance degradation time to failure for 30 nm 51% Ti BST with axes transformed. The estimate is indicated by the horizontal bar in each interval. The interval indicates 95% model confidence.

There are three kinds of censoring: right, left, and interval. In right censoring the exact failure time is unknown, it is greater than some specified value, *e.g.*, a test that stops after 8 hours, with some samples still surviving. Left censoring occurs when the failure time is only known to be before a certain time. Interval censoring occurs when samples are examined for failure multiple times and it is only known that it failed between observations. Censored observations cannot be ignored without biasing the analysis. A censored sample can provide useful lifetime information that cannot be utilized with least squares estimation. Furthermore, maximum likelihood methods are needed to determine model parameters. An example of censoring is presented in Figure 1.68 and Figure 1.69. In the former, the Monte Carlo data taken from a lognormal distribution is presented. In the latter, the distribution is capped at a value, as would be the case for right censoring.

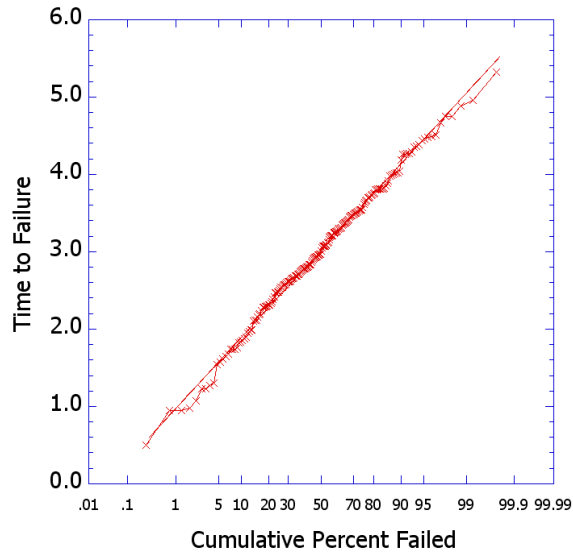


Figure 1.68: Monte Carlo time-to-failure data from a lognormal distribution, uncensored.

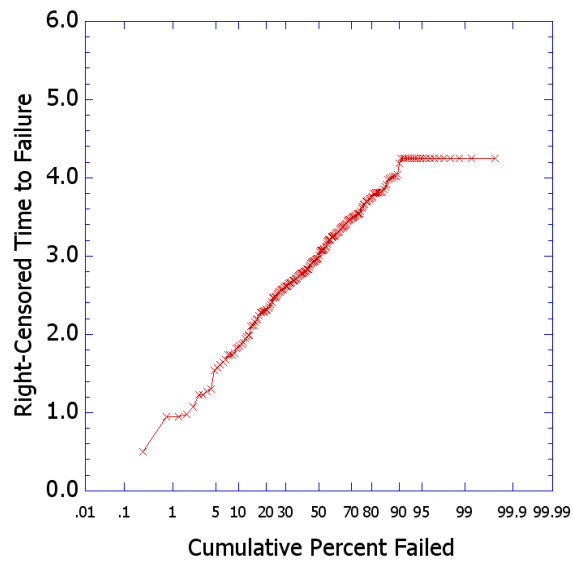


Figure 1.69: Same Monte Carlo as Figure 1.68, showing the effect of censoring on the distribution. The effect of the censoring can be seen on the cdf. After some time, the test is stopped.

The Weibull distribution is used to model  $\text{SiO}_2$  breakdown and other “weakest link” systems, where defects are randomly distributed and the weakest defect causes failure of the entire system, in this case a weak point in the capacitor causes failure of the entire device. The Weibull probability distribution function (pdf) is given as

$$f(x; \alpha, \beta) = \frac{\alpha}{\beta} x^{\alpha-1} e^{-\left(\frac{x}{\beta}\right)^\alpha}$$

The cumulative distribution function (cdf) is given as

$$F(x) = 1 - \exp\left[-\left(\frac{x}{\alpha}\right)^\beta\right],$$

where  $F$  is the cumulative failure probability by time  $x$ ;  $\alpha$  is the characteristic value, *i.e.* the value of  $x$  at 63.2 percent failed, when

$$F(x) = 1 - \left(\frac{1}{e}\right)$$

and  $\beta$  is the Weibull slope, indicating the spread of the failure times.  $\beta$  is called the shape parameter[133]. Plotting

$$W \equiv \ln[-\ln(1 - F)]$$

versus  $\ln(x)$  gives a line of slope  $\beta$ [134].

In addition to describing the failure distribution the Weibull plots have many useful features,. First, the average failure rate requirement is a line with slope 1 and an intercept of 1/FIT. Plotting failure requirements on a Weibull plot shows reliability for the entire failure distribution. Weibull plots show graphically if reliability is adequate. If the CDF is above the AFR line, reliability is inadequate. This is shown schematically in Figure 1.70.

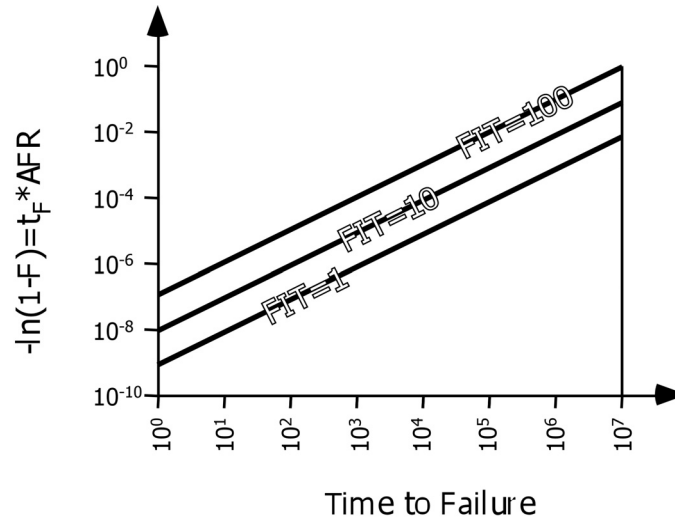


Figure 1.70: Weibull plot of different FIT rates. Adapted from Stathis[134].

The first 1% of failures control reliability, so the entire distribution must be extrapolated. This was done above, with the curves showing the Weibull distribution functions. Reliability is discussed in terms of FIT, or failures in time, again as discussed in the literature review. The current value of FIT allowed in a chip 1, which is to say that fewer than 1 failure should occur in 1 billion device hours. This can be translated into an average failure rate. On a Weibull plot, the average failure rate is a line of slope 1 and a y-intercept at  $1/\text{FIT}$ , giving it units of  $\text{hr}^{-1}$ . The 1 and 10 FIT lines were calculated. The reliability is sufficient if the entire Weibull distribution falls below the required FIT line. This is illustrated in Figure 1.71. The right bound of the forbidden region is 10 years, or about  $10^5$  on the Weibull plot. The upper bounds is the FIT line. If the Weibull distribution does not fall inside this region, then the reliability is sufficient.

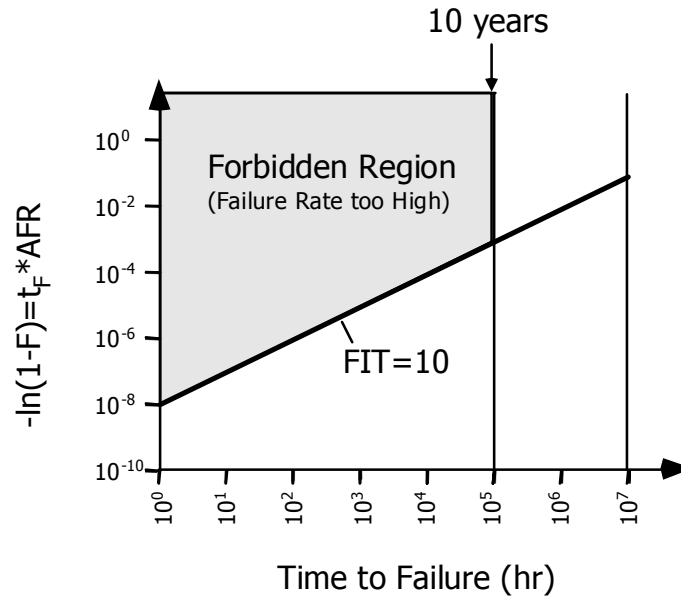


Figure 1.71: Schematic of graphical determination of the reliability requirements. Adapted from Hunter[129].

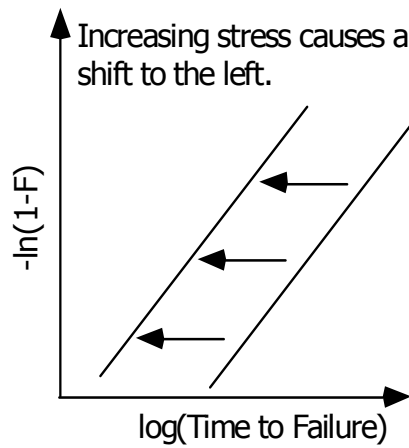


Figure 1.72: Weibull plot illustrating the effect of increasing stress, typically electric field. Adapted from Hunter[129].

Second, increasing the field causes a shift to the left. The magnitude of the shift varies based on the physical system. This effect is shown schematically in Figure 1.72.

Third, scaling the area results in vertical shift of the line. If the probability of one device failing is  $p$ , then the probability of  $N$  identical, independent units failing is

$$F=1-(1-p)^N$$

so that

$$\ln[-\ln(1-F)]=\ln N-\ln[-\ln(1-p)].$$

This means that increasing the area by a factor  $N$  shifts the curve on the Weibull plot upward by the factor  $\ln(N)$ [134]. There are several things that also scale with  $N$  elements: area,  $N=A_N/A_i$ ; perimeter,  $N=P_N/P_i$ ; and number of corners,  $N=N_{c1}/N_{c2}$ [129].

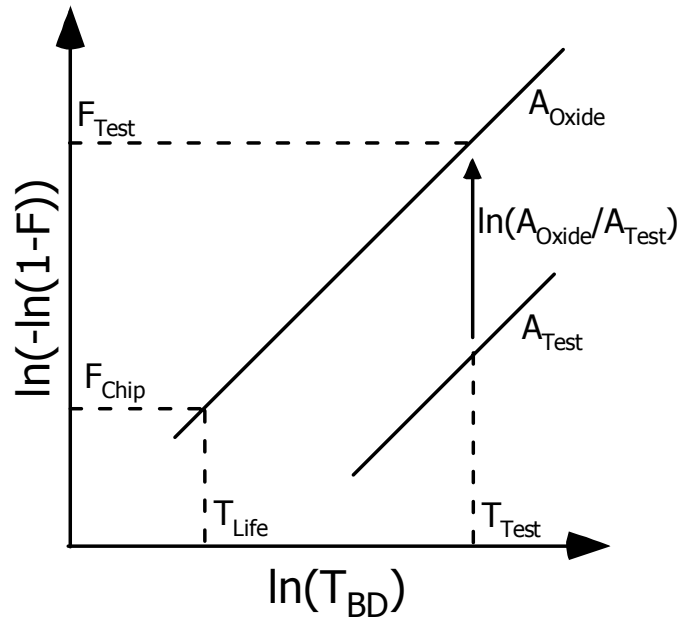


Figure 1.73: Weibull plot schematically showing the effect of area scaling. Adapted from Stathis[134].

A modified form of the area scaling equation is given by Stathis as

$$\frac{T_{Life}}{T_{Test}} = \left( \frac{A_{Test}}{A_{Oxide}} \right)^{\frac{1}{\beta}} \left( \frac{\ln(1-F_{Chip})}{\ln(1-F_{Test})} \right)^{\frac{1}{\beta}} \approx \left( \frac{A_{Test} F_{Chip}}{A_{Oxide} F_{Test}} \right)^{\frac{1}{\beta}}$$

For a desired failure rate  $F_{Chip}$ , for the oxide area  $A_{Oxide}$ , there is an equivalent higher failure rate  $F_{Test}$  that occurs in time  $T_{Test}$ , with area  $A_{Test}$ . The  $\beta$  value used should be that of the projected operating voltage. Use of this equation is illustrated in Figure 1.73. Scaling the

area tested to the active oxide area and desired failure rate of the device results in a shift of the line[134].

### 1.5.2: Reliability of SiO<sub>2</sub>

BST and SiO<sub>2</sub> are both used as thin film dielectrics that fail from weakest-link mechanisms. The understanding of failure modes and mechanisms, nomenclature, and analysis techniques, developed for SiO<sub>2</sub> over the past 40 years, can be applied to BST. The two dissimilarities that should be noted are as follows. First, BST is crystalline and SiO<sub>2</sub> is amorphous, so there are microstructural differences. A result of the microstructural differences is that BST interfaces are substantially rougher than SiO<sub>2</sub> interfaces and therefore localized field concentration effects are larger. Second, BST is a three component oxide and SiO<sub>2</sub> is a single component oxide, so the chemistry is much more complex.

There are two main types of test acceleration. The first is applied stress, either current or voltage. The second is elevated temperature. SiO<sub>2</sub> failure proceeds faster at higher temperature. There are other considerations of secondary importance, such as the effects of stress applied as a duty cycle. The two main types of electrical stress are constant current and constant voltage. The gate is under voltage stress, rather than current stress, thus constant voltage stress is more frequently used. Also, the construction of a model for the acceleration factors is more straightforward for voltage stress[135].

Constant current stress is typically used to calculate charge-to-breakdown and the trap generation rate. There is a critical trap density that leads to failure, as can be seen in Figure 1.74. Trap generation rate is important because the critical density decreases with increasing voltage, as the discharge can occur over a larger distance of the dielectric. It

was demonstrated that this method of testing is more dependent on the specifics of the MOS processing and test conditions and is thus less comparable as a metric of reliability. If the processing conditions affect the Weibull slope, which is especially the case for thin oxides, *i.e.*, less than 3 nm, the constant current charge-to breakdown is meaningless[136].

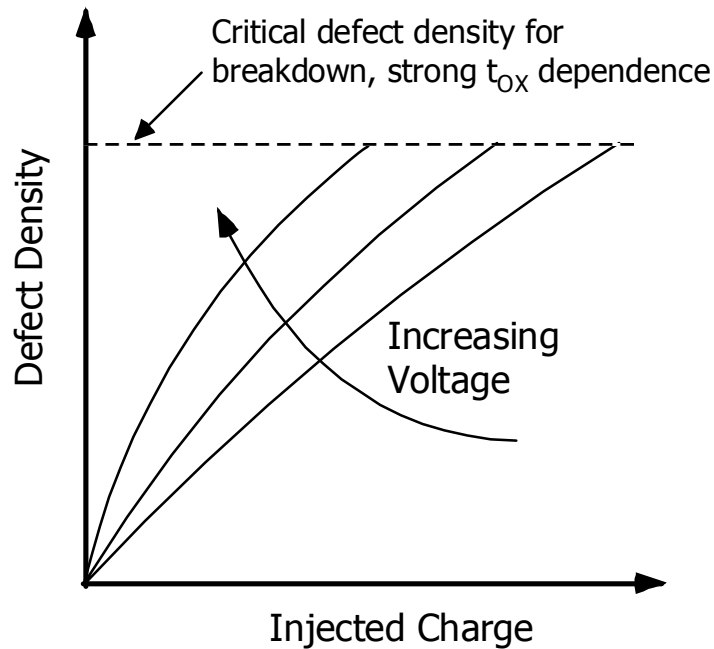


Figure 1.74: Defect density as a function of injected charge, for various voltages. Adapted from Stathis[134].

SiO<sub>2</sub> failure is broadly divided into two categories: extrinsic and intrinsic. Extrinsic failure is due to a “killer” defect, typically from the fabrication process. The defects are scattered along the surface of the wafer, so the probability of a killer defect being present in a device increases with device size. Thus, the probability of the device experiencing extrinsic failure scales with oxide area. Extrinsic failures occur at short times. Intrinsic failure occurs at long times and is a materials property: the true dielectric strength. For high quality SiO<sub>2</sub>, the failure rate does not scale with oxide area. Such measurements are typically taken to be intrinsic [135], although careful measurements of

the area suggests an area dependence that does change with oxide area, but the variation is less than the wafer-level parameter scatter and related uncertainties[137].

A confounding factor is that at any given condition a sample of failures may not be due to one type of defect, but a number of defects with different distributions. Different defects operate under different stress conditions, especially “latent” defects with an upper field threshold causing them to be absent from severe stress conditions. Latent defects limit the usefulness of certain types of extrapolations[135].

The four main steps of dielectric breakdown are as follows. First, defects appear and form chains from low field leakage. Second, there is conversion from planar to local injection. Third, there is a sudden, irreversible change in the conduction mechanism. Fourth, thermal damage at the breakdown spot spreads laterally across the oxide[138]. Traps created by electrons flowing across the oxide are the main cause of oxide damage. Correspondingly, major changes in trap creation occur for oxide thicknesses below 3 nm, when the conduction mechanism changes from Fowler-Nordheim to direct quantum-mechanical tunneling.

Soft breakdown begins in the same manner as dielectric breakdown. During the stress, localized failure occurs (step 3), perhaps leading to local capacitive discharge. However, there is no lateral propagation. This failure may occur several times before  $t_{ddb}$  for a given film. Soft breakdown is seen more commonly in ultra-thin, *i.e.*, less than 5 nm, oxide films[139].

While there is no consensus on the microscopic mechanism of breakdown, three explanations for defect generation in  $\text{SiO}_2$  are featured most prominently in the literature: the hydrogen model, the anode hole injection model, and the thermochemical model. In the hydrogen model, it is hypothesized that hydrogen creates defects. Exposing  $\text{SiO}_2$  to

atomic hydrogen radicals produces electrically active defects that are similar to those produced by electrical stress. These defects are paramagnetic interface defects (Si dangling bonds at the Si/SiO<sub>2</sub> interface), diamagnetic interface defects (fast and slow interface states), and bulk electron traps. There is good agreement between the desorption rate of hydrogen as a function of incident electron energy and the voltage dependence of the trap generation process. However, there does not appear to be any isotope effect on the breakdown process, while there is a large effect on the desorption rate for hydrogen versus deuterium, so this model's validity is questionable[134].

The second model is the anode hole injection model. It suggests that the cause of failure is the injection of holes from the anode contact. There has been significant theoretical work supporting the process of injection by surface plasmon excitations that decay into electron-hole pairs at the Si gate. Empirical support comes mainly in the constant hole fluence to breakdown as a function of the oxide field, with  $Q_p$  approximately 0.1 C/cm<sup>2</sup>. Also, the expected dependence on anode material is observed. This model is also known as the inverse exponential model. The form of the equation is

$$t_{BD} = t_0 \cdot \exp\left(\frac{-\text{Constant}}{E_{OX}}\right).$$

This functional form originates in the Fowler-Nordheim current, so the model might not hold in this form for very thin oxides. It yields an infinite time to failure at zero field, which is physically correct. The proposed mechanism has some difficulties. First, it can explain the relationship between  $E_{ox}$  and  $t_{BD}$  at high fields, but not at low fields. Second, it fails to quantitatively account for the defect generation rate: the hole current at low voltages, *i.e.* between 2-3 V, is approximately 12 orders of magnitude below the electron current. The measurements of holes through an SiO<sub>2</sub> layer shows that the holes generate

traps at approximately the same rate as do electrons; not nearly enough defects are generated by anode hole injection to cause failure[134].

The thermochemical model is also known as the exponential model. The form is

$$t_{BD} = t_0 \cdot \exp(-\beta \cdot E_{OX})$$

The largest support for the exponential model is empirical: the breakdown data follow an exponential dependence on field. A 3-year experiment with oxide fields as low as 5.3 MV/cm on 9 nm films agreed well with the thermochemical model. The model posits that defect generation is due to the applied field. Current through the oxide is secondary in importance. The applied field interacts with oxygen vacancies, which correspond to weak Si-Si bonds, in SiO<sub>2</sub>. The activation energy for bond breakage is lowered by the dipolar energy, yielding a quantitative prediction that agrees well with experiment. However, measurements made of Fowler-Nordheim stress with varyingly doped anodes showed that time to breakdown correlates with electron energy, rather than with oxide field. The model may be correct, but the mechanism is highly doubtful[134].

A relatively recent model, formulated by Degraeve *et al.*, does not propose a mechanism, but is good as predictive model[127]. The critical defect density model, or percolation model, proposes that damage builds up to a critical level and a new conduction path forms. This process is illustrated in Figure 1.75. It links electron trap generation and anode hole injection. In the early 1990s, it was noted that the charge to breakdown is inversely related to the initial rate of defect generation. As thinner films were tested, it was found that the number of defects required for failure decreased. Traps were generated in SiO<sub>2</sub> by both Fowler-Nordheim and substrate hot electron injection. The neutral electron trap density was measured periodically as a function of the injected electron fluence, in order to measure the critical trap density. The model predicted several

important characteristics of thin oxide breakdown: the decrease in hole fluence at breakdown, the dependence of the Weibull slope on oxide thickness, and the re-emergence of an oxide area effect on the failure distribution[140]. Thinner oxide requires fewer defects in the chain to bridge the electrodes, until the oxide is so thin that only one defect is needed[141].

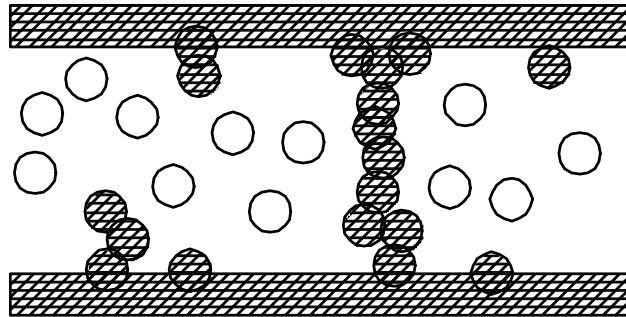


Figure 1.75: The percolation model. Adapted from Degraeve *et al*[140].  
Traps form randomly and eventually create a conductive path through the oxide.

The percolation model gives insight into the statistical relationship between as to the natures of soft-, or quasi-breakdown and hard breakdown. Empirical support came from the work of Sune, *et al*[142]. They examined the breakdown statistics of hard and soft breakdowns in  $\text{SiO}_2$  and found that hard breakdown and the first soft breakdown event have indistinguishable failure statistics, while having very different J-V behavior[142]. As shown in Figure 1.76, the difference is in the area of the failure[143]. After a conductive path is created, the charge built up on the capacitor rushes through the path. For hard breakdown, the area propagates across the oxide. Soft breakdown only occurs at that path, so leakage increases, but catastrophic failure does not occur.

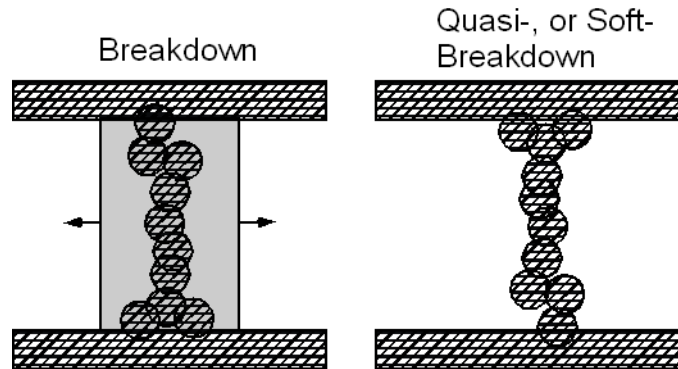


Figure 1.76: The difference between soft and hard breakdown in  $\text{SiO}_2$  is that in hard breakdown, the failure area propagates across the oxide, whereas in soft breakdown, there is a local capacitive discharge and increased current thereafter. Adapted from Satake *et al*[143].

### 1.5.3: Reliability of BST

The main area of reliability research in the perovskite materials has been in the areas of fatigue and imprint, both of which are important in applications that use the ferroelectric properties, such as nonvolatile memory, but these two failure mechanisms are less important for applications such as DRAM, where the material is used in a paraelectric phase. The focus of this section is on the failure modes that are likely to operate in DRAM and related paraelectric applications. The four failure mechanisms that are of interest are resistance degradation, time dependent dielectric breakdown, stress induced leakage current, and soft breakdown.

#### 1.5.3.1: *Resistance Degradation*

Resistance degradation is the regular increase of leakage current under elevated temperature and dc field stresses. A typical example of resistance degradation is given in Figure 1.77. While there are likely lower stress limits for the other types of failure, there is not a lower stress limit for resistance degradation. The discussion of resistance degradation is divided into 2 parts. The first examines resistance degradation in single

crystals and ceramics. The second extends the bulk models into the behavior of thin films.

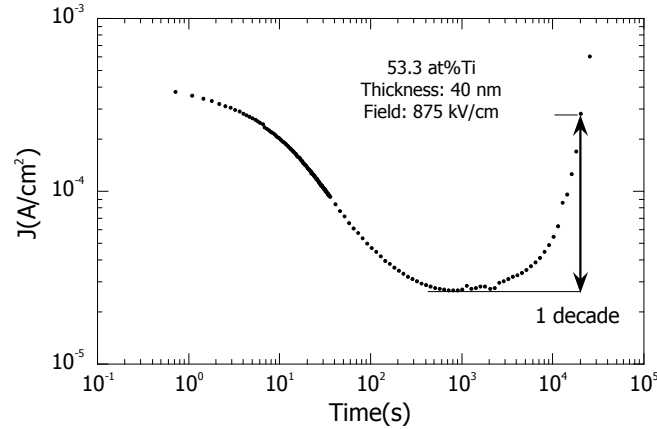


Figure 1.77: Typical resistance degradation curve, shown for a BST film.[144]

The definition of time to failure for resistance degradation is given as the time for the current to rise 1 decade (10x) over the minimum current. This formulation is attractive because the basic curve shape is common to many systems and sample geometries.

While perhaps not unique to perovskites, resistance degradation is certainly most investigated for this class of materials. A decrease of electrical resistance under temperature and electric field stresses was first observed in (Be,Ba)TiO<sub>3</sub> by Bunting *et al.* in 1951[145]. There are two models for resistance degradation in bulk dielectrics, grain boundary and reduction.

The grain boundary model proposes that the applied dc field leads to the degradation of the grain boundaries. In ceramics, the grain boundaries have a higher resistivity than the grain interior. The Maxwell-Wagner polarization causes high fields across the grains that lead either to the emission of trapped charge carriers or to a local dielectric breakdown process[146].

The reduction model assumes that the oxygen vacancies present in relatively large quantities in undoped bulk materials are the main component of the degradation process. These oxygen vacancies are positively charged with respect to the lattice and thus undergo electromigration under the influence of a dc field. The oxygen vacancies accumulate at the cathode, where they are compensated by electrons ejected from the cathode. A reaction at the anode leads to the injection of additional oxygen vacancies, which leads to the reduction of the ceramic and a concomitant decrease in resistivity[146].

The most complete investigation into resistance degradation in bulk single crystals and ceramics was conducted by Waser *et al.* Their model of the degradation process will be presented and then followed with evidence from the study[147-149].

The distribution of oxygen vacancies is homogeneous before the application of dc voltage. During the voltage and temperature stress, the oxygen vacancies diffuse toward the cathode. However, ionic transfer is blocked at the grain boundaries. This leads to the region near the anode becoming more p-type and the region near the cathode more n-type, becoming effectively a forward-biased p-n junction, leading to an increase in current. The difference from the reduction model is that no net reduction occurs in the grain, simply a segregation of defects.

Waser *et al.* used fuse-grown single crystals of SrTiO<sub>3</sub> to examine the effects of doping, temperature, and field strength on resistance degradation lifetime. Much of the work was on SrTiO<sub>3</sub>, which is an end member of the BST solid solution, as the analysis is not complicated by ferroelectric behavior. The investigation found that the resistance degradation lifetime followed an Arrhenius relationship with temperature,

$$t_{rd} = t_0 \exp\left[\frac{Q_T(V)}{kT}\right].$$

An Arrhenius relationship is expected if the origin of the degradation is diffusional. Doping affects the  $Q_T$  term, effectively changing the activation energy of the resistance degradation lifetime, depending on whether the dopant is an acceptor or a donor. Donor doping tends to increase the lifetime and acceptor doping tends to decrease it, presumably by affecting the number of oxygen vacancies.

The field dependence of the resistance degradation lifetime is related to the drift velocity of the oxygen vacancies,

$$v_{V_o} = \mu_{V_o} E$$

where  $\mu_{V_o}$  is the mobility of oxygen vacancies and  $E$  is the electric field. An inverse relationship between lifetime and electric field is expected, however the data suggest a power-law relationship.

Electrocoloration experiments were conducted on Fe-doped SrTiO<sub>3</sub>, which changes color according to the valence of the Fe. While not direct evidence, it is reasonably strong support of the proposed process. The Fe added to the SrTiO<sub>3</sub> consists mostly of Fe<sup>3+</sup>, only a small amount of the Fe exists as Fe<sup>4+</sup>. Fe<sup>3+</sup> is colorless and Fe<sup>4+</sup> is deep red. An oxygen vacancy can reduce 2 Fe<sup>3+</sup> to Fe<sup>4+</sup>. As the bias is applied to the sample, the area that loses oxygen vacancies becomes darker (anode) and the area that gains oxygen vacancies becomes lighter (cathode). Three main results were observed. First, the rate, temperature dependence, and field dependence of the color generation and motion agreed well with estimates of the diffusivity of oxygen vacancies.

Second, the grain boundaries blocked the motion of oxygen vacancies, as the experiments noted that the degradation time is not strongly affected by the oxygen partial pressure. The electrocoloration experiments were conducted in both an oxidizing and a

reducing environment and no significant solid/gas interface transfer reaction occurred. Third, the degradation is reversible if the sample is reverse-biased, or if the sample is annealed at high temperatures in an oxidizing environment.

More direct evidence of the motion of oxygen vacancies was obtained by Warren *et al.* They examined the motion of oxygen vacancies within the oxygen octahedra of ceramic  $\text{BaTiO}_3$  by using electron paramagnetic resonance (EPR). Oxygen vacancy motion was detected by changes in the alignment of Fe-oxygen vacancy defect dipoles created by dc electrical field/heat combinations. Resistance degradation occurred concomitantly with the detected oxygen vacancy motion. While the motion was only measured in the local octahedra, it is an important observation that lends support to the electromigration of oxygen vacancies over the length of the grain[150].

Turning to thin film studies, Numata *et al.* examined resistance degradation in both  $\text{SrTiO}_3$  and  $(\text{Ba}_x\text{Sr}_{1-x})\text{TiO}_3$  and compared the results to those of Waser *et al.* The structure tested was  $\text{Au}/((\text{Ba,Sr})\text{TiO}_3 \text{ or } \text{SrTiO}_3)/\text{Pt}/\text{Ti}/\text{SiO}_2$ . Both the films exhibited resistance degradation of similar form. The temperature dependence of the resistance degradation lifetime followed an Arrhenius relationship. When compared to the Waser data, the values were larger by orders of magnitude. This suggests that some aspect of the mechanism may be different in thin film versus bulk. However, it is possible that the poor lifetimes reported by Waser were sample specific and thus not generalizable[151].

The other finding was that resistance degradation occurred for positive bias, but not for negative bias. Although not mentioned in the paper, it is known that Pt has a much greater oxygen solubility than Au, which may explain the asymmetry in the results. Finally, it was suggested that increasing Ti nonstoichiometry increased lifetime, but since no effort in controlling chemistry was reported, this result is of limited utility [151].

Grossmann *et al.* examined the differences in resistance degradation between thin film and bulk BST. Samples of BST deposited via CSD on Pt/SiO<sub>2</sub>/Si with Pt top electrodes were exposed to pressures of O<sub>2</sub> from 10<sup>-5</sup> bar to 1 bar with a small bias (0.05 V) applied. The steady-state leakage increased at higher pO<sub>2</sub>. When the sample was driven to failure, there was no observed differences between the high and low pO<sub>2</sub> cases in either lifetime or shape of the J-t curves. This result makes an argument based solely on oxidation and reduction unlikely. A second experiment was performed with ITO top electrodes. The samples were illuminated with a slightly greater-than-bandgap light during testing. The presence or absence of the light did not influence the degradation rate, though a constant photocurrent was observed. Thus, the resistance degradation of the films is not solely caused by motion of charge carriers[152].

The most comprehensive study of resistance degradation in thin films was conducted by Basceri *et al.*[112, 144, 153]. The effect of dc field, applied voltage polarity, temperature, film thickness, and (Ba+Sr)/Ti ratio were examined. The general trends were these. Resistance degradation is thermally activated and voltage/field dependent. The temperature dependence is Arrhenius. The field dependence is not clear. The most likely candidates are power law voltage dependence and exponential or inverse exponential voltage dependence. While the films had larger values for the calculated exponents than were found for bulk materials, the differences in degradation behavior are differences of degree rather than of kind.

All methods of extrapolation yielded a median lifetime greater than the currently requirement of 10 years at the DRAM operating conditions of 1.6 V and 80 °C. The final equation incorporating the field and temperature effects is

$$t_d = t_0 (V^{-n}) \exp \left[ \frac{Q_T (V)}{kT} \right]$$

where  $t_d$  is the failure time,  $V$  is in volts,  $Q_T$  is the activation energy in eV, and  $n$  is the power law exponent, a fitting parameter. Thickness and composition changes cause changes in the activation energy.

Thicker films have shorter lifetimes than thinner films, perhaps due to some microstructural difference. When the Arrhenius temperature dependence of the degradation is calculated, the activation energy decreases as film thickness increases. Films that have relatively symmetric leakage current have similarly symmetric resistance degradation lifetimes, so if electrode effects are eliminated, resistance degradation is polarity independent. This suggests that the defects that cause degradation are distributed homogeneously throughout the film.

Stoichiometry has a more complicated effect than the monotonic influence of thickness. The resistance degradation lifetime increases as the Ti content is increased from 50.5 to 52.0 at.% Ti, and then decreases as at. % Ti increases.

Zafar *et al.* examined resistance degradation in  $\text{Ba}_{0.5}\text{Sr}_{0.5}\text{TiO}_3$  films deposited by sputtering, thicknesses of either 100 nm or 40 nm and evaporated Pt electrodes. To characterize the role of oxygen vacancies in thin film BST, J-t plots were analyzed as a function of applied field at 190 °C. This temperature was chosen as a compromise between decreasing the influence of the relaxation currents and shortening the lifetime too much from resistance degradation. The theory of space-charge-limited transients suggests that a peak in the J-t curve upon application of a voltage step is due to a reservoir of charge carriers near the injecting electrode. This peak was attributed to either a number of oxygen vacancies being present in the sample upon deposition or oxygen ions moving into the electrode when the field is applied. The peak positions are related to the drift mobility of the injected charge via the Einstein equation

$$\tau = \frac{(0.78t^2)}{(\mu V_{app})}$$

where  $\tau$  is the peak position in seconds,  $t$  is the thickness of the sample in cm and  $\mu$  is the drift mobility. The value obtained for thin films,  $2 \cdot 10^{-12} \text{ cm}^2/\text{V s}$ , is assumed to be due to oxygen vacancies. When the value is used to calculate the diffusivity via the Einstein equation and then applied to the diffusion equation, it yields a value for the activation energy comparable to that found in bulk. The values were 1.1 eV and 0.9-1.1 eV, for the bulk and thin film, respectively. This result suggests that the mechanism of resistance degradation is not fundamentally different than in thin films and bulk BST[154].

A model for the prediction of resistance degradation lifetime was suggested by Zafer *et al.* based on a modified testing procedure. The method of Waser *et al.*, discussed previously, is to drive the capacitor to failure at high field and elevated temperature, then extrapolate back to operating conditions. An alternate method makes use of the two competing forces: diffusion and electric field. At a given field, the driving force causes motion of the oxygen vacancies until the concentration gradient is large enough that it matches the magnitude of the electric field. BST was measured at 1 V from 125 °C to 270 °C. Two main changes were observed in the electrical properties before and after resistance degradation. First, the Schottky barrier height at the cathode decreases during degradation and reaches a final, lower value at steady state. The value of the final shift was about 0.17 eV, regardless of the time required to reach the final value. The second change was a positive offset of about 0.5 V in the maximum of the C-V curve. The C-V curve for BST ideally has a maximum value at 0 V[155].

The time to reach the maximum current, the value of the current, and the shift in barrier height are used to construct the model. There are two equations in the model.

The first models the barrier height at the cathode, which is attributed to the motion of oxygen vacancies, as a function of time,

$$\delta\phi(t) = \Delta\phi_{\max} \left\{ 1.0 - \exp\left[-\left(\frac{t}{\tau}\right)^\beta\right] \right\}$$

where  $\Delta\phi_{\max}$  is the maximum decrease in barrier height,  $\beta$  is a fitting constant, and  $\tau$  is the characteristic value that has an Arrhenius relationship. The second describes the current as a function of time, based on the temperature dependence of the change in barrier height.

$$J(t) = J_{\text{init}} \exp\left[\frac{\delta\phi(t)}{kT}\right]$$

where  $J_{\text{init}}$  is the initial current,  $k$  is Boltzmann's constant, and  $T$  is temperature in Kelvin. This model has an advantage over the more common time to breakdown model because the actual current is predicted. It is the absolute current that determines the failure of BST in an application such as a DRAM capacitor, not the time to a 10x increase of current. A limitation of the model is that the measurement of  $J_{\text{init}}$  is assumed to be at steady-state leakage rather than relaxation plus leakage. This condition is not met at low temperatures, so another method must be employed to determine the steady-state leakage.[155].

Baumert *et al.* examined films of SrTiO<sub>3</sub> and (Ba<sub>0.5</sub>Sr<sub>0.5</sub>)TiO<sub>3</sub> by sputtering. The structures were Pt/Film/Pt/SiO<sub>2</sub>/Si. A 10 nm amorphous layer occurred at the film-Pt bottom electrode for the SrTiO<sub>3</sub>, but not for the (Ba<sub>0.5</sub>Sr<sub>0.5</sub>)TiO<sub>3</sub>. Resistance degradation experiments were carried out on a 97.2 nm film at 125, 150, and 175 °C and 3, 4, 5, and 7 V. The failure criterion chosen was the Waser definition. The activation energies

calculated were in the range of 0.67 to 0.92 eV. The temperature and voltage acceleration was modeled via 2 Arrhenius relationships:

$$t_{ch} = t_T \exp\left[\frac{Q_T}{kT}\right]$$

and

$$t_{ch} = t_V \exp\left[\frac{Q_V}{V}\right]$$

where  $t_{ch}$  is the characteristic time,  $t_T$  and  $t_V$  the temperature and voltage acceleration constants,  $Q_T$  and  $Q_V$  the activation energies,  $T$  temperature in Kelvin, and  $V$  volts. While the failure definition was the same as Waser's, the equation used to model the failure was not. Waser *et al.* used a power law, derived from basic considerations of charge and nonstoichiometry, whereas Baumert *et al.* used an exponential relationship[116]. The data fit reasonably well, suggesting that it is not clear which form of field acceleration should be used.

The effect of bottom electrodes on resistance degradation was investigated by Tsai and Tseng. Three different metals were investigated: Pt, Ir, and Ru. BST was deposited by rf magnetron sputtering, with the stoichiometry  $(\text{Ba}_{0.47}, \text{Sr}_{0.53})_{0.5}\text{Ti}_{0.5}\text{O}_3$ . Top Pt electrodes were deposited by shadow mask, and ellipsometry was used to determine film thickness. The breakdown data presented did not appear to be resistance degradation, but rather tddb. Nevertheless, there were two important results[156].

The first is that the electric field dependence of time to breakdown is not strongly dependent on the electrode material. This is expected if resistance degradation is due to the motion of oxygen vacancies within the grain. The Pt and Ir electrodes were

significantly smoother than the Ru electrodes, so morphology likely plays a role in lifetime. In addition, Ru freely interdiffuses with Ti, affecting the chemistry of the film.

The second thing to note is that is that the resulting time to failure was modeled empirically using an exponential function given as

$$t_B = \alpha \cdot \exp[-\beta E]$$

where  $t_B$  is the time to failure and  $\alpha$  and  $\beta$  are fitting parameters. This equation, as for the Baumert data, fits the field dependence reasonably well. The values of  $\beta$  have units of cm/MV. The values of  $\beta$  for the films are Pt, 2.33; Ir, 2.37; and Ru 8.9. Again, the differences in the morphology of the bottom electrodes and not the material, *per se*, is the likely origin of the difference[156].

#### 1.5.3.2: Time Dependent Dielectric Breakdown

One of the more rigorous investigations of failure in BST was conducted by Reisinger *et al.* Several notes were made regarding the reliability requirements of the BST capacitors, two of the more salient were

“(1) The lifetime until the intrinsic mode breakdown, extrapolated from the tddb tests to operating conditions has to *significantly exceed* 10 years (emphasis added.)

(2) After screening A-mode breakdown by a burn-in there is only one defect allowed to cause a failure on a total area of at least 2000cm<sup>2</sup>[126]

The films were deposited via the ATMI process[157] that was used for the films in this dissertation, so the results have particular relevance. At each experimental condition, 25 data points were collected, which is sufficient to calculate Weibull statistics if the distribution is known.

The examination of dielectric breakdown was divided into three sections. The first is the effect of AC stress on  $t_{BD}$ , discussed in the ac stress section starting on page 139. The second is the effect of temperature on DC failure. And the third was the area extrapolation for the tddb failures to actual device conditions.

The effects of elevated temperature were unexpected. Whereas for  $\text{SiO}_2$ , there is a monotonic decrease in lifetime with increasing temperatures, for BST it was found that  $t_{BD}$  increases by 2 orders of magnitude from 22 °C to 85 °C and then slowly declines to the 22 °C value again at about 175 °C. The worst-case scenario occurred at 22 °C.

The extrapolation back to operating conditions was accomplished using the following assumptions. The required maximum failure rate was taken to be 10 FIT. The area calculation assumed 20 fF per cell for  $10^9$  cells,  $t_{ox}$  was measured to be 0.6 nm, so the resulting active oxide area is about 2 cm<sup>2</sup> per Gb device.[126]. The result of the extrapolation suggested that the BST is sufficiently reliable for  $\pm 1\text{V}$  operation, but not for  $\pm 2\text{V}$  operation[126].

Scott *et al.* considered the origin of dielectric breakdown, or tddb, in perovskites in general and BST in particular. BST films of compositions from Ba 70-80 at.% Ti were deposited via CSD. The breakdown behavior of the films was examined as a function of thickness, temperature, voltage ramp rate, electrode material, and electrode area.

The leakage current increases nonlinearly with an applied voltage ramp. Breakdown occurred at approximately the same current, 10-100  $\mu\text{A}/\text{cm}^2$ . It was suggested that failure occurred at a specific current or conductivity threshold. This sort of breakdown might be by thermal runaway, so the fundamental mechanism for breakdown likely changes as the conductivity mechanism changes[158].

The proposed mechanism for failure is avalanche breakdown. The original equation was proposed by von Hippel:

$$eE_B\lambda = ch\nu$$

where  $e$  is the charge on the electron,  $\lambda$  is the electron mean free path in the dielectric,  $h\nu$  is the energy to ionize a constituent element, such as  $\text{Ti}^{3+}$  to  $\text{Ti}^{4+}$ . The equation was adjusted by the work function mismatch between the perovskite and electrode. An example is given of how the electrode material might affect breakdown in PZT.  $h\nu$  in PZT is  $1.05 \pm 0.04$  eV. This is the energy for oxygen vacancy motion. The work function of Au is 4.82 eV, Pt 6.0 eV, and PZT 4.0 eV. A capacitor with gold electrodes would degrade under a 2 V bias, but one with Pt electrodes should not, because of the work function mismatch.

The dependence of breakdown voltage on electrode material would suggest that the breakdown field is thickness independent. To test this hypothesis, BST films with Pt electrodes were driven to failure with a voltage ramp. The conclusion from the result is that breakdown field is independent of thickness from 60 to 260 nm. This result is similar to PZT under the same stress conditions, suggesting that the electrode material may influence the breakdown via the modified von Hippel theory. But of the eight thicknesses measured, only 2 of the 8 error bars overlap the grand mean and several of the thicknesses' error bars do not overlap at all. Based on the data, it is not reasonable to conclude that breakdown is thickness independent.

The possibility that breakdown is electrical, rather than thermal, was investigated by looking for correlations between electrode work function and breakdown field. The following electrode compositions were examined: Pt/Ti, Pt/Cr, Au/Cr, and W. The result is that breakdown correlates with work function, but not with thermal conductivity.

Larger work functions lead to lower leakage current at a given field, resulting in higher breakdown fields. But the preceding is not a valid argument for an electrode effect on breakdown via thermal runaway. The thermal conductivity of the electrode has little to do with thermal breakdown, since failure would occur in the film. The heating from a sudden change in conduction mechanism and the resultant capacitive discharge would be quick enough that the thermal conductivity of the electrode is not as relevant, so comparing the field dependence to the steady-state leakage current is not likely to be useful.

Finally, the effect of electrode size was investigated by examining capacitors ranging in area from  $2 \cdot 10^3$  to  $1.6 \cdot 10^4 \mu\text{m}^2$ . There is a slight trend toward shorter lifetimes with larger capacitors, but the trend is not significant[158].

Huang *et al.* investigated time dependent dielectric breakdown in BST. 70/30 Ba/Sr BST films were deposited by CSD on Pt/Ti/SiO<sub>2</sub>/Si. Au top electrodes were patterned by lift-off. A distinction is made by the authors between low field leakage and high field leakage. While Huang *et al.* do not explicitly state a conduction mechanism, it is known that the BST system has a double Schottky barrier[112], resulting in a different voltage dependence above and below the Schottky barrier height. It is necessary to distinguish these two regimes for purposes of extrapolating the stress field back to operating conditions. In the two most common forms of the extrapolation, field plotted as the ordinate as field or inverse field.  $\text{Log}(t_{BD})$  is plotted on the abscissa. Much debate has occurred in the SiO<sub>2</sub> community about the proper form of the equation[135], as the two forms yield very different lifetime prediction. Both estimates were made for the films studied. The field extrapolation yields a lifetime of 31.6 years at 3.3 V, versus a lifetime of  $3.16 \cdot 10^{24}$  years for the inverse field extrapolation.

Huang *et al.* suggest that the extrapolation be done in the following manner. The current-field relationship of BST is

$$J \propto E^m$$

with different values of  $m$  for high and low field. If the field scaling is modeled as an exponential, the form will be

$$t_{BD} \propto \frac{1}{J} \propto E^{-m}$$

Thus, the field scaling is related to the slope of the current-field curve. The high-field data taken by Huang *et al.* yield similar values of  $m$  for the high-field case, 16.38 for the slope of the  $\log(t_{BD})$ - $\log(E)$  line and 16.5 for the slope of the  $\log(J)$ - $\log(E)$  line. The extrapolation line is constructed in a stepwise fashion. The slope of the low-field portion of the extrapolation is assumed to be the same as the slope of the current-field curve, about 1. The result of the extrapolation is a lifetime of 31,700 years.

It should be noted that the data are not statistically significant. Not only are the extrapolations and the error bars are large, the similarity of the two terms is likely coincidental. Even if it is not, a similarity between the leakage mechanism and lifetime at high field does not necessarily extend to low field, where the leakage mechanism is known to be different. If the failure mechanism changes as a function of field, then a stepwise function might be appropriate, but no such change is proposed. Additionally, data for the value of  $m$  at lower fields are not presented[159].

An important study by Tsai *et al.* compares the lifetime of BST deposited on several bottom electrode materials: Pt, Ir, IrO<sub>2</sub>/Ir, Ru, and RuO<sub>2</sub>/Ru. AFM measurements of the rms roughness were made. It was found that the Pt, Ir, and IrO<sub>2</sub>/Ir bottom electrodes had very similar roughnesses, about 1.5 nm. The BST deposited on

these electrodes had slightly larger roughnesses. However, the Ru and RuO<sub>2</sub>/Ru electrodes had an rms roughness of 3 nm and the deposited BST films had an rms roughness of 4 nm. When these samples were tested under constant current stress to find time to breakdown, the Pt, Ir, and IrO<sub>2</sub>/Ir bottom electrode samples broke down in the range of 3-4 V, but the Ru and RuO<sub>2</sub>/Ru bottom electrode samples broke down about 2 V, suggesting that there is a correlation between failure and interfacial roughness. This relationship might have been due to the increased field concentration effects of the rougher films. Also, corresponding to the work of Scott *et al*, the tddb lifetime of the BST occurred in the following order, based on top electrode type: Pt, Ir, Ir/IrO<sub>2</sub>, Ru, the same order as the work function of the metals[160].

The effect of interfacial roughness and grain size on lifetime has been investigated by Noma and Ueda. BST was deposited by MOD on Pt/Ti/GaAs, with Pt top electrodes deposited by e-beam evaporation. Different average grain sizes were obtained by altering the annealing profile. Two samples with different mean grain sizes were examined via deep level transient spectroscopy (DLTS). Understanding DLTS is much more straightforward in structures without grain boundaries and other aspects of the more complex BST system so while quantitative understanding is difficult, trends are accessible. Capacitors were then stressed at three fields to find time to failure and characterize the trap states. The activation energy of the traps was determined by an Arrhenius plot to be 0.75 eV. Some capacitors were stopped during the testing and DLTS measurements taken again. It was determined that the activation energy did not change significantly, but that the capture cross-section of the traps increased dramatically during the stress. This provides direct evidence for a single trap in tddb failure. The trap generation rate increases with increasing voltage. Additionally, the DLTS measurements show that the

sample with a 50 nm grain size had a larger capture cross-section than the 80 nm grain size sample so the trap is likely an interfacial trap, rather than in the grains[161].

Twenty capacitors were stressed at three voltages and 125 °C for several hours. The failure times of the failed samples were used to construct Weibull plots. Although the data are biased estimates of mean time to failure, the trend is accessible. The resulting  $t_{BD}$  measurements showed between a 1.5 and 2 orders of magnitude lifetime increase in the larger grain size sample. The data suggests that capture cross section, grain size, and lifetime are related. The conclusion from the study is that the tddb defect is interfacial in nature and is a single defect, not a distribution of defects[161].

#### 1.5.3.3: Stress Induced Leakage Currents

Yamamichi *et al.* examined the reliability of BST at a function of thickness and composition, specifically examining SILC and tddb failure. BST of thicknesses from 50 to 160 nm was sputtered on Pd/R-plane sapphire. (Ba+Sr)/Ti ratios were varied from 0.94 to 1.10. Au top electrodes were deposited via dc magnetron sputtering. Charge to breakdown ( $Q_{BD}$ ) was calculated by integrating the leakage current from  $t=0$  to  $t=t_{BD}$ . This is an overestimation of  $Q_{BD}$ , because dielectric relaxation of BST has a relaxation current component.

The tddb results for (Ba+Sr)/Ti=1.05 were plotted as Log(tddb) vs.  $E$ ,  $1/E$ , and  $V$ . The results suggested that the electric field is more appropriate than voltage in lifetime prediction. As at.% Ti increased, the lifetime at a given stress field increased also. Current density vs. field plots were used to correlate the leakage to the tddb lifetime. Higher leakage was correlated to a lower lifetime, when the leakage is related to a change in stoichiometry, but not when the change is due to other factors. The slopes of the tddb

vs.  $E$  curves did not change as a function of composition, so it was suggested by the authors that the failure mechanism is the same.

The SILC were not calculated correctly, as the relaxation currents must be extracted from the leakage current. The quantity calculated is still useful, as the allowable time between DRAM refreshes depends on current components. A figure was constructed of  $\Delta Q_{loss}$ , the difference in charge lost from the capacitor in 10 sec before and after the application of a stress, versus  $Q_{stress}$ , the calculated charge from the charge-to-breakdown measurement. These plots were constructed for two thicknesses, 50 and 130 nm, and two compositions, 1.05 and 0.94. The films with Ti excess showed a much smaller  $\Delta Q_{loss}$ . This is an important result. The effect of thickness was that thicker films could accept a smaller  $Q_{stress}$  than the thinner films, but the finding was again due to the incorrect calculation of  $Q_{BD}$ [132, 162].

#### 1.5.3.4: AC Stress

Few investigations of the effect of AC stress on perovskites have been conducted. Chen *et al.* examined the influence of duty cycle and AC stress on time to failure of SrTiO<sub>3</sub>[163]. The films were sputtered at 550 °C on Ir/SiO<sub>2</sub>/Si. Pt top electrodes were patterned by sputtering. A number of samples were driven to failure by constant voltage stressing. For the balance of the tested samples, the stress was interrupted a number of times. Under both positive and negative bias, the time to failure increased as the number of interruptions increased. *E.g.*, three interruptions yielded a five-fold increase for positive voltage, from 200 to 1000 seconds, and a two-fold increase for negative voltage, from 60 to 140 seconds. Next, the on-time of the duty cycle was varied from 0.8 msec to 0.5 msec. The time to failure decreased from 3100 seconds to 200 seconds, respectively.

A 50% duty cycle stress was applied at frequencies from 100 Hz to 1 MHz. The time to failure increased from 125 to 1350 seconds, respectively.

The explanation for the dependence on stress frequency was the trapping and detrapping of defects. When the stress is interrupted, the trapped holes and trapped electrons detrapp. The traps must be re-filled when stress recommences before the damage process can continue. Hole trapping at the cathode is believed to be the origin of failure for  $\text{SiO}_2$ , which is why  $\text{SiO}_2$  manifests a longer lifetime under AC stress than DC stress. A similar process may be operative with  $\text{SrTiO}_3$  and other perovskites[163].

The work by Resinger *et al.* investigated the effect of AC stress on BST lifetime. AC stress was applied as a  $14 V_{pp}$  square wave, with cycle times expressed as a pulse width. It was found that for DC stress and for short pulse widths (less than 6 msec), the  $t_{BD}$  was similar, with the characteristic lifetime of 5000 sec, but at 20 msec cycle time, the characteristic lifetime was 150 sec. This difference was attributed to the occupation of traps near the cathode. Trapping impedes current through the film and thus should improve lifetime. *I.e.* part of the charges are trapped during one pulse and detrapped during the next pulse of opposite sign. However, AC stress prevents occupation of traps if the AC period is shorter than the trapping times. So time to failure decreases from DC stress to 6 msec, then abruptly increases back to the DC failure time. At a cycle time of 6 msec, the distribution splits between the two failure modes. The test was stopped several times for some samples and leakage characteristics measured, but SILC was never observed[126].

## 1.6: Research Objectives

The research objectives are divided into two groups. The first relates to size effects. The thickness series provided by ATMI will be used to evaluate the two competing size effects explanations and determine which provides the best fit to the data over the widest experimental range. These two explanations are the Binder approach to finite size scaling and the dead layer model. The analysis will also consider for the boundary conditions and many experimental artifacts that have prevented discernment of the better model to date. This effort includes direct measurement of the strain effect on the dielectric properties.

The results of the experimental work will be used with the better model to evaluate the suitability of BST as the capacitor dielectric in DRAM to the end of the ITRS roadmap.

The second portion will develop a framework for BST failure. Using a consistent set of films, the various failure modes will be evaluated as a function of stress, temperature, composition, and film thickness. These results will be combined with the previous results of Basceri *et al.*[112, 144, 153] and given a more rigorous statistical treatment to determine and characterize the defect that is most likely to limit device lifetime.

The results of the reliability evaluation will be used to determine if the reliability is sufficient for use as a DRAM capacitor or for use as a tunable dielectric.

# Chapter 2: EXPERIMENTAL PROCEDURE

## 2.1: Film Deposition

The BST films used in this study were deposited by Advanced Technology Materials, Inc. on Pt/SiO<sub>2</sub>/Si. BST film thicknesses ranged from 15 to 580 nm. A schematic of the MOCVD system is shown in Figure 2.1. The particular features of the system include a temperature-controlled gas mixing manifold, temperature controlled walls, a shower-head injector, and load-lock wafer loading. The liquid delivery system mixes, meters, and transports the precursors, listed in Table 2.1, at room temperature and high pressure to a heated zone, where they are flash vaporized and mixed with a carrier gas (Ar). The liquid source system was designed to work with low vapor pressure precursors and produce a temperature controlled, low pressure stream of gas. It has the advantage of only heating the precursors as needed, preventing the precursor degradation that often occurs in the MOCVD of BST. The gas stream is then combined with oxidizer gases, O<sub>2</sub> and N<sub>2</sub>O, and finally passes through a showerhead injector into the deposition chamber.

Table 2.1: Precursors used in BST MOCVD

Film Component	Precursor
Barium	bis(2,2,6,6-tetramethyl-3,5-heptanedionate)tetraglyme
Strontium	bis(2,2,6,6-tetramethyl-3,5-heptanedionate)tetraglyme
Titanium	bis(isopropoxy)bis(2,2,6,6-tetramethyl-3,5-heptanedionate)titanium

Common deposition conditions are listed in Table 2.2. The Ba/Sr ratio was chosen to be 70/30 to provide a permittivity maximum at approximately 300 K. The (Ba+Sr)/Ti ratio is the main microstructural variable. It affects how the films nucleate, the permittivity and tunability, the leakage characteristics, and has a storage effect on resistance degradation lifetime. The nucleation behavior is better for excess Ti, but the permittivity decreases, so the range of 49.5/50.5 to 46.5/53.5 was chosen as the range of investigation.

The film compositions were determined by a standards-based wavelength dispersive x-ray fluorescence spectroscopy technique. The deposition tool is stable, no systematic composition drift was observed during the deposition of 1300 wafers of 30 nm thick BST films [164]. The films produced are uniform, with a variation of electrical properties of less than 3% across a 6 inch wafer. Compositional control of Ba, Sr, and Ti and the corresponding x-ray fluorescence measurement precision are given in Table 2.3. The standard deviation of measured thickness was 2.4%.

Table 2.2: Typical deposition conditions for BST films

Substrate Temperature	640 °C
Flow Rate	0.07 cc/min
Deposition Pressure	700 mtorr
Oxidizers	500 sccm O <sub>2</sub> & 500 sccm N <sub>2</sub> O
Ba/Sr Ratio	70/30
(Ba+Sr)/Ti (A:B) ratio	~50/50-47/53
Nominal Deposition Rate	0.09 nm/sec

Table 2.3: Compositional control and x-ray fluorescence measurement precision for BST deposition system

Element	Deposition Precision (Atomic % ( $\sigma$ ))	Measurement Precision (Atomic % ( $\sigma$ ))
Barium	0.44	0.31
Strontium	0.39	0.10
Titanium	0.36	0.22

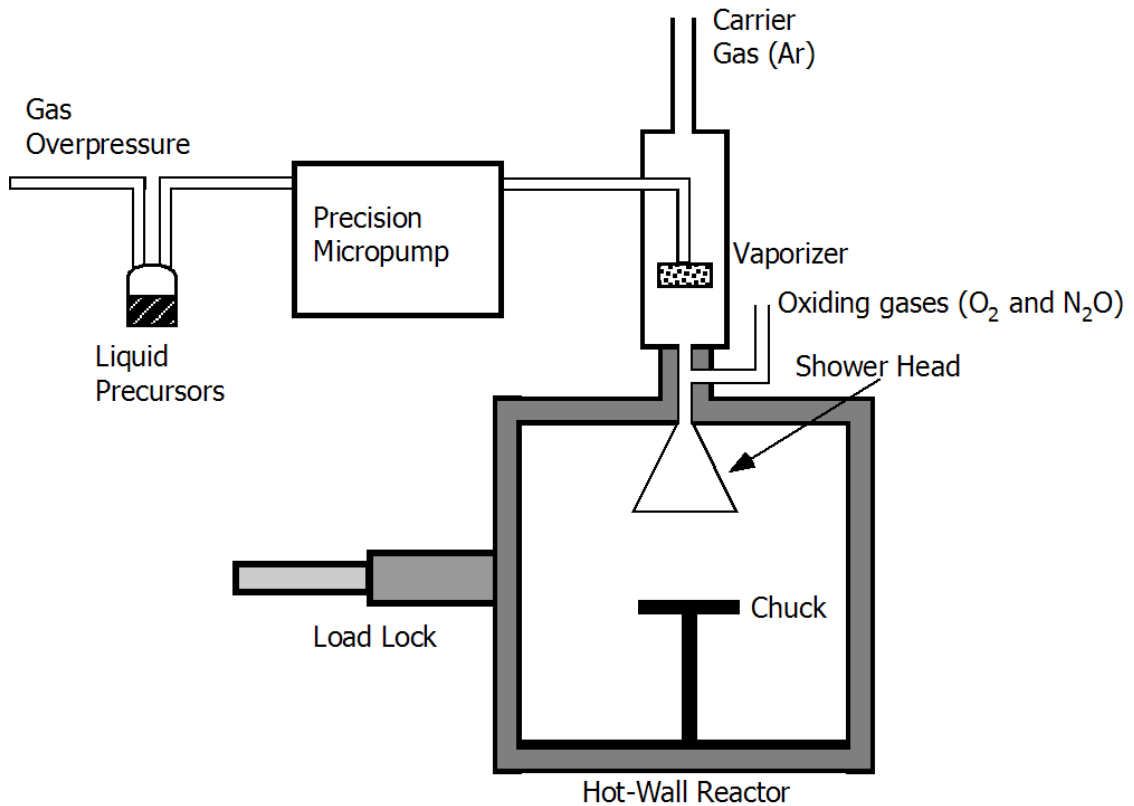


Figure 2.1: Schematic of the Liquid Source-MOCVD system used to deposit the BST films used in this study.

The films had a columnar microstructure and were strongly (100) textured, with a minor (110) component. The (110) component appears randomly. There is not a strong thickness, composition, or deposition temperature dependence. A thickness series of 51.0 at. % Ti films deposited by IBM, using the same deposition method, shows no thickness dependence of the (110) component, as can be seen in Figure 2.2. As mentioned previously, the (110) component is less desirable for two reasons. The grains are not as

smooth as the (100) component and the dielectric constant is lower. A bright field/dark field image of a (110) grain with (100) grains on either side can be seen in Figure 2.3. Finally, Figure 2.4 shows an AFM height image showing the surface of a typical BST film. The 30 nm BST film has an rms roughness of 1.3 nm. The image was collected in tapping mode.

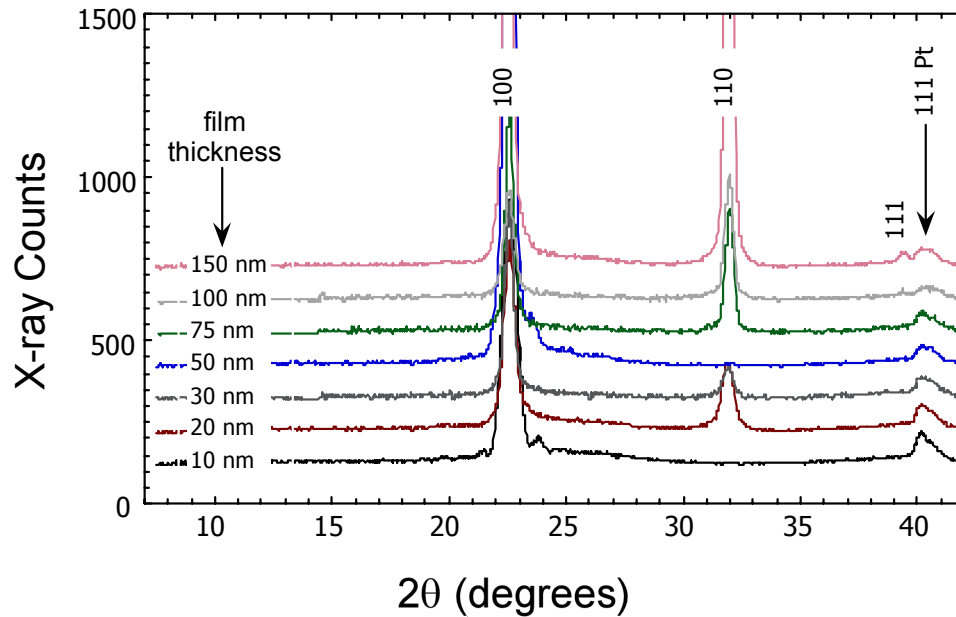


Figure 2.2: X-ray patterns of a thickness series of BST films.

The (110) component shows no thickness dependence.

The 100 nm thick, (111) fiber-textured Pt bottom electrodes were prepared by sputtering at 315 °C on 500 nm of thermal SiO<sub>2</sub>. Capacitors were defined by magnetron sputtering 100 nm of Pt through a shadow mask at room temperature. A top electrode anneal at 550 °C for 30 min. in air is necessary to obtain low leakage currents and dielectric loss. This anneal was repeated if the capacitor's properties worsened due to environmental exposure. Contact sizes were measured optically.

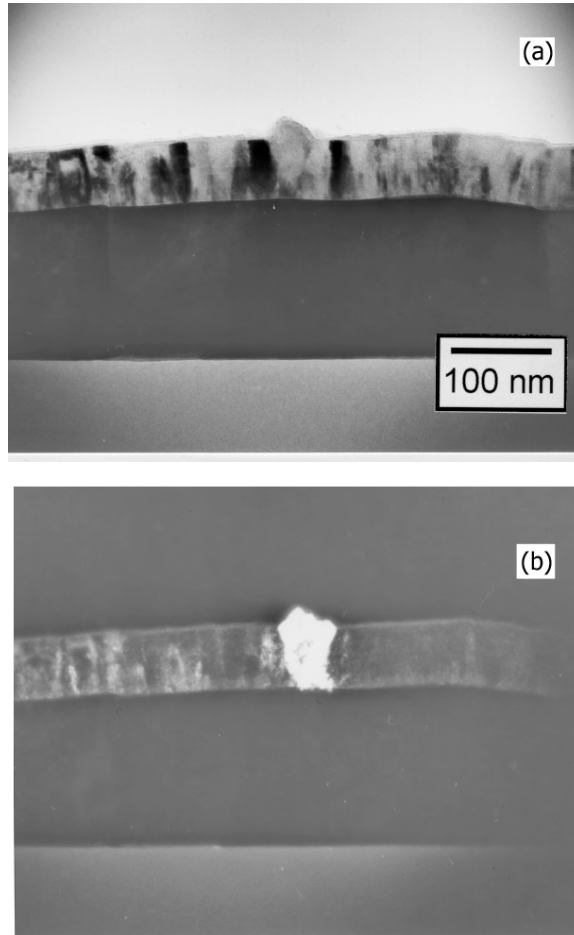


Figure 2.3: TEM image of a (110) BST grain surrounded by (100) grains in (a) bright field and (b) dark field.

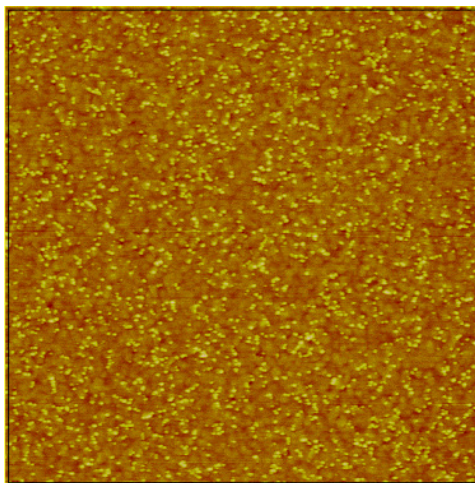


Figure 2.4: AFM image of a 5 x 5  $\mu\text{m}$  portion of a 51.0 at. % Ti, 30 nm BST film on Pt/SiO<sub>2</sub>/Si.

## 2.2: Electrical Characterization

The electrical characterization of the samples in the study was carried out by several methods. The impedance measurements were performed with an HP 4192A impedance analyzer. Current measurements were usually with a Keithley 617 picoammeter. If the measured current exceeds 1 mA a Keithley 2400 sourcemeter was used. Two systems were used to further the capabilities of the above instruments. The first is an MMR Joule-Thompson refrigerator system, which enables temperature measurements from 85 to 580 K. The second is a circuit that utilizes solid-state relays to enable AC measurements. These systems are discussed further in this section. The sample configuration used in this study is shown in Figure 2.5. It indicates the electric field convention used in this study. Contact with the bottom electrode was made by etching the BST with hydrofluoric acid. However, HF damages the BST in an area around the area of application, so when the sample is too small for HF, an adjacent capacitor is shorted to serve as the bottom electrode.

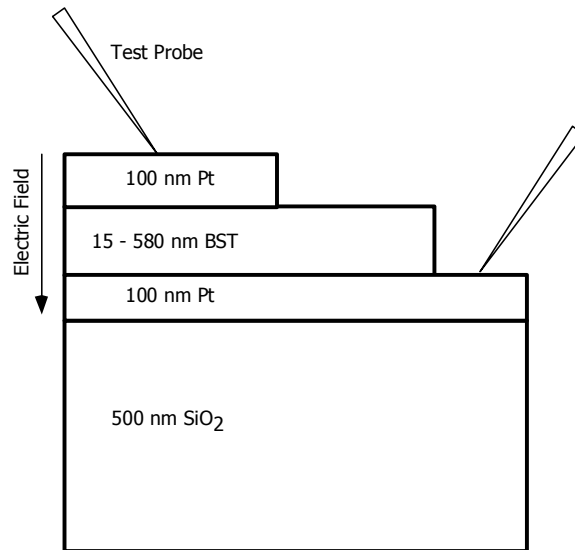


Figure 2.5: Sample configuration used in this study.

The field convention used in this study is as follows. Positive bias corresponds to the direction of the electric field shown. Negative bias is the opposite.

### 2.2.1: Capacitance-Voltage and -Frequency

The HP 4192A can generate frequencies in the range of 5 Hz to 13 MHz, using an auto-balancing bridge. The four terminal pair configuration is used. Four coaxial cables are used. The outer two send the sense signal. The inner two measure the voltage. The coaxial cables isolate the voltage sensing cables from the sense signal, resulting in a large range of measurable impedances. Additional fixturing is necessary, so for the two test configurations used in this study, an open/short calibration[165] was performed as a function of frequency to determine the range of test frequencies accessible. The calibration was to ensure that the device under test was measured accurately. If necessary, the impedances from the device under test and the test fixture were deconvolved.

The open/short calibration assumes that the test fixture residuals can be modeled as a residual impedance in series with the device and a stray admittance in parallel with the device. The open calibration is performed by making a frequency sweep with the test

fixtures the same distance apart as during measurement. The admittance is measured, composed of a real and imaginary part,

$$Y = G + j\omega C$$

The short calibration is performed by making a frequency sweep with the test fixture shorted. The residual impedance is measured, again composed of a real and imaginary part,

$$Z_s = R_s + j\omega L_s$$

Thus, for each frequency, the following equation can be solved

$$Z_{device} = \frac{(Z_{measured} - Z_s)}{1 - (Z_{measured} - Z_s)Y}$$

The capacitance-tan ( $\delta$ ) spot measurements were performed at a frequency of 4 kHz. The HP 4192A consists of a number of measurement circuits. Near the center of the circuit, in frequency space, the measurement is the most accurate. When this is combined with the different impedances of the two test fixtures and capacitance densities to be measured, 4 kHz best satisfied the competing requirements. The sense voltage was adjusted to provide a common measurement field of approximately 6.5 kV/cm to the capacitors, *i.e.*, for the 581 nm sample, 0.377 V and for the 154nm sample, 0.1 V.

Figure 2.6 shows a typical C-V curve. It is more useful as permittivity-field, which is shown on the other axes. Note that due to the sense voltage, the measured permittivity is lower by about 3-5% from the true zero-bias permittivity.

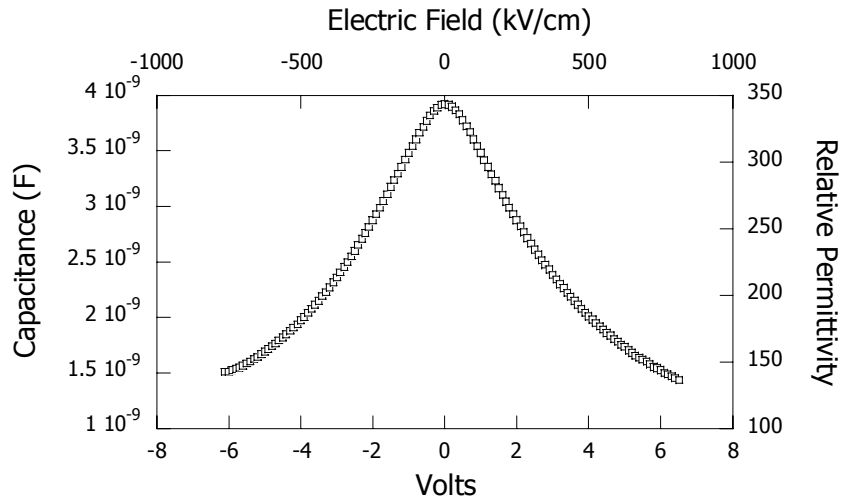


Figure 2.6: Capacitance-Voltage and Permittivity-Field plot of a 80 nm thick 51.0% Ti BST film.

Capacitance-frequency curves are typically plotted on a log scale, because the Curie-von Schweidler model predicts a power law relationship, which is linearized by a log-log treatment. A typical C-f plot is shown in Figure 2.7. Several test artifacts are highlighted. The low frequency resolution of the impedance analyzer, less than about 1 kHz, is not as good as above it. Near the edge of a measurement circuit, the measurement is significantly less accurate, as can be seen from the discontinuity at about 25 kHz. And although not a test artifact, closer to the RC resonance the measured permittivity depends strongly on the capacitance and test frequency and so is not as good for comparing the permittivity of wide thicknesses of films. When the test fixtures and other measurement artifacts are accounted for, BST films display a relatively smooth C-f curve, as was shown previously in Figure 1.62.

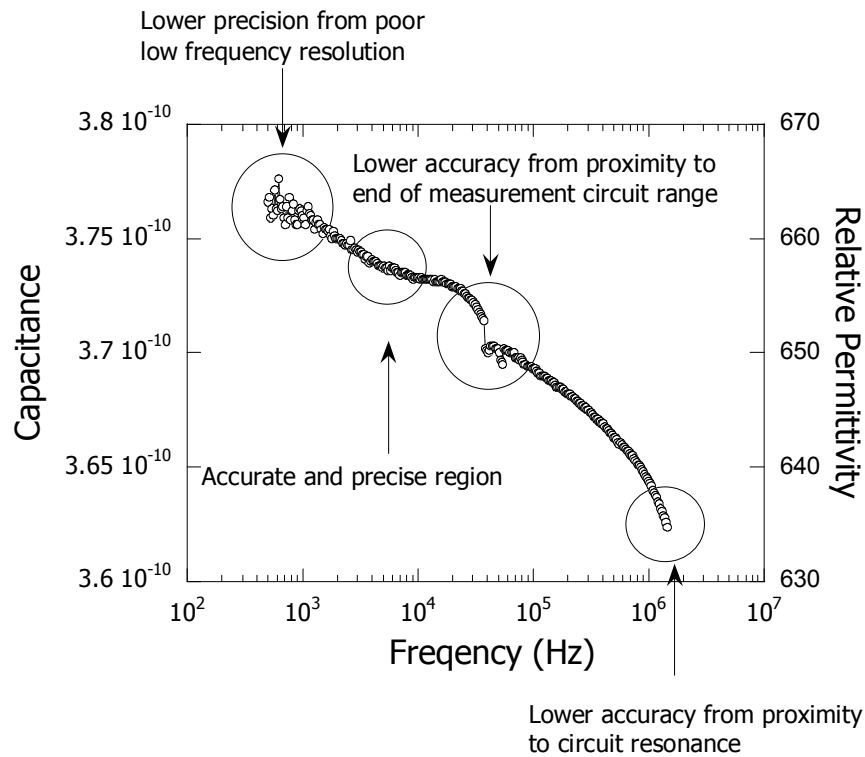


Figure 2.7: Capacitance-frequency plot of 580 nm 53% Ti BST film.

Various measurement artifacts are noted.

### 2.2.2: Current-Voltage and -Time

The Keithley 617 is accurate to within 100 aA, with the proper test fixtures. These measurements are DC, so the issues of test frequency are not important. The test configuration is designed to minimize stray electromagnetic radiation through proper grounding and shielding. Additionally, the probe station is lightproof, to ensure that optically generated electron-hole pairs do not influence the measurement of leakage current. A schematic of a typical J-V plot is shown in Figure 2.8. In the sub-threshold regime, dielectric relaxation dominates. Typically, this regime is from 0-2 V. It is the most important to understand, as DRAM devices will likely operate in this voltage range. At larger voltages Schottky emission dominates and BST capacitors display the characteristic  $\log(\text{current})$  versus  $\sqrt{\text{voltage}}$  relationship.

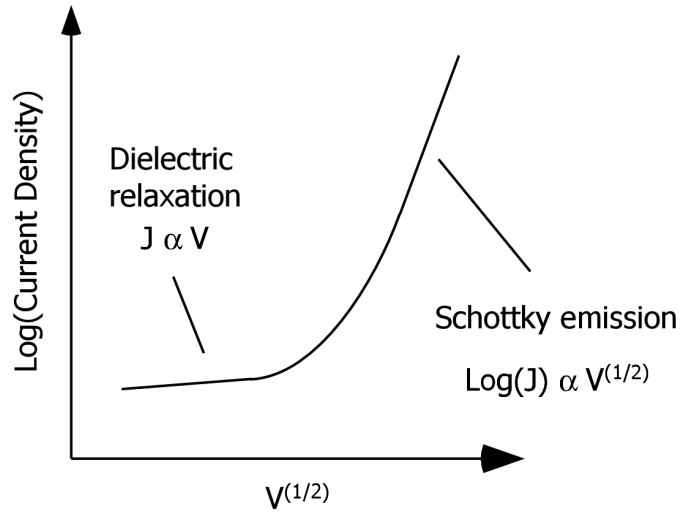


Figure 2.8: Current-Voltage schematic for BST, showing the two main leakage regimes. Adapted from Ezhilvalavan *et al*[119].

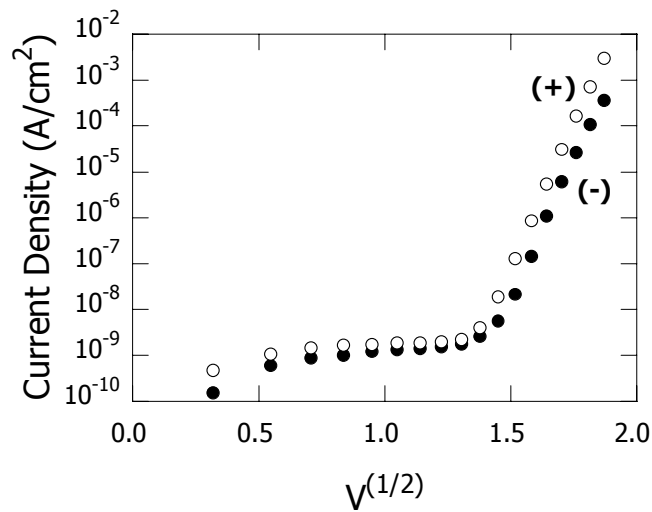


Figure 2.9: Current-Voltage plot for a 51 at. % Ti., 30 nm BST sample[112].

Current-time behavior can be roughly divided into three regimes, as illustrated by Figure 2.10. The first is dielectric relaxation, which was discussed previously. The second is steady state leakage. Here, the leakage current is relatively constant, the majority of the relaxation having occurred. Finally, the sample begins to degrade, undergoing one of the failure mechanisms discussed in Chapter 4.

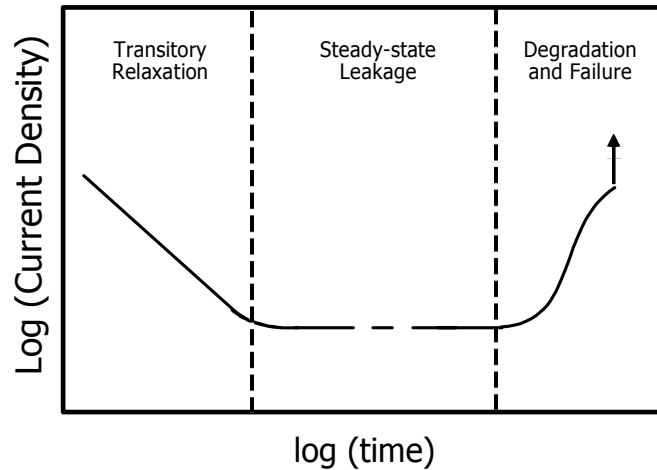


Figure 2.10: Current-time schematic showing the three main regimes[112].

### 2.2.3: AC Stress

Some earlier reports suggest that AC stress may be important[126, 166]. As there was not an available system capable of performing the necessary measurements, one was constructed. The difficulty of AC reliability testing is that the Keithley 617, used to measure current, would be damaged by the AC signal necessary to stress the BST. This problem was overcome by using Two solid state relays to alternately stress and measure the films. The SSRs were used because standard relays do not provide sufficient resistance in the off state. The SSRs are actually composed of two separate circuits, as can be seen in Figure 2.11. When a +25 V bias is applied across the terminals, the resistance of the relay drops from 5 G $\Omega$  to 25  $\Omega$ . A negative bias has no effect.

The HP4192A was used as the voltage source, with the SSRs wired oppositely, so that when a positive bias was applied, one SSR was on, and the Keithley 617 was connected to the test fixture for measurement. When a negative bias was applied, the other SSR turned on, and the HP33120A function generator was connected to the test fixture for electrical stress.

The AC test procedure is as follows: (1) Make a 10 sec. J-t measurement via the Keithley 617, (2) Electrically isolate the Keithley, (3) Stress the sample at a given field, frequency, and time with a function generator, (4) Electrically isolate the function generator. It was verified that the length of time of the J-t measurement does not significantly affect the time to failure in the when the measurement takes from approx. 5 sec. to 2 min. This is due to the nature of traps in BST films and is contrary to what was seen by Baumart *et al.*[116], but consistent with the results of Resinger, *et al.*[126], which is a better comparison because of the similarity of the deposition system.

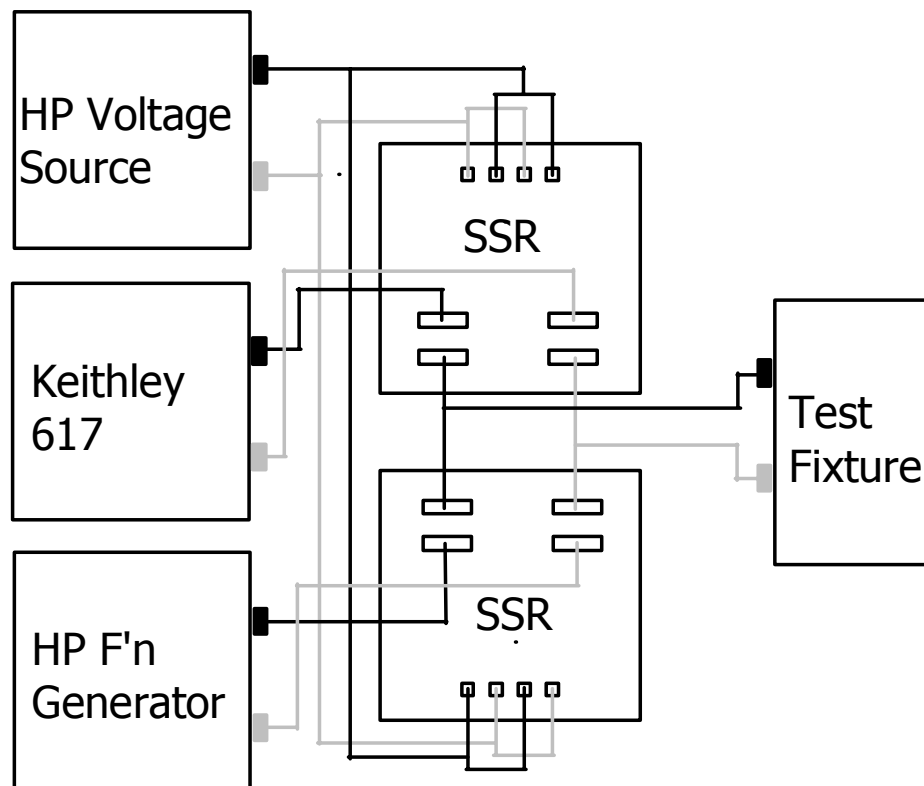


Figure 2.11: Schematic of AC degradation system.

## 2.3: X-Ray Analysis

X-ray diffraction measurements were taken with a Bruker D-5000 using a HighStar wide area detector. The x-ray source was Cu-K $\alpha$  radiation generated at 40 kV and 30 mA. The detector is capable of measuring about 35° 2 $\theta$  and 45°  $\chi$  simultaneously. This system is well-suited to measuring textured thin films, as the diffraction intensity is spread over many more degrees than for single crystal materials. A screenshot of the XRD is shown in Figure 2.12.

While the XRD was used for phase identification and texture analysis, the primary use was making precision out-of-plane lattice parameter measurements to quantify the strain relief in the sample.

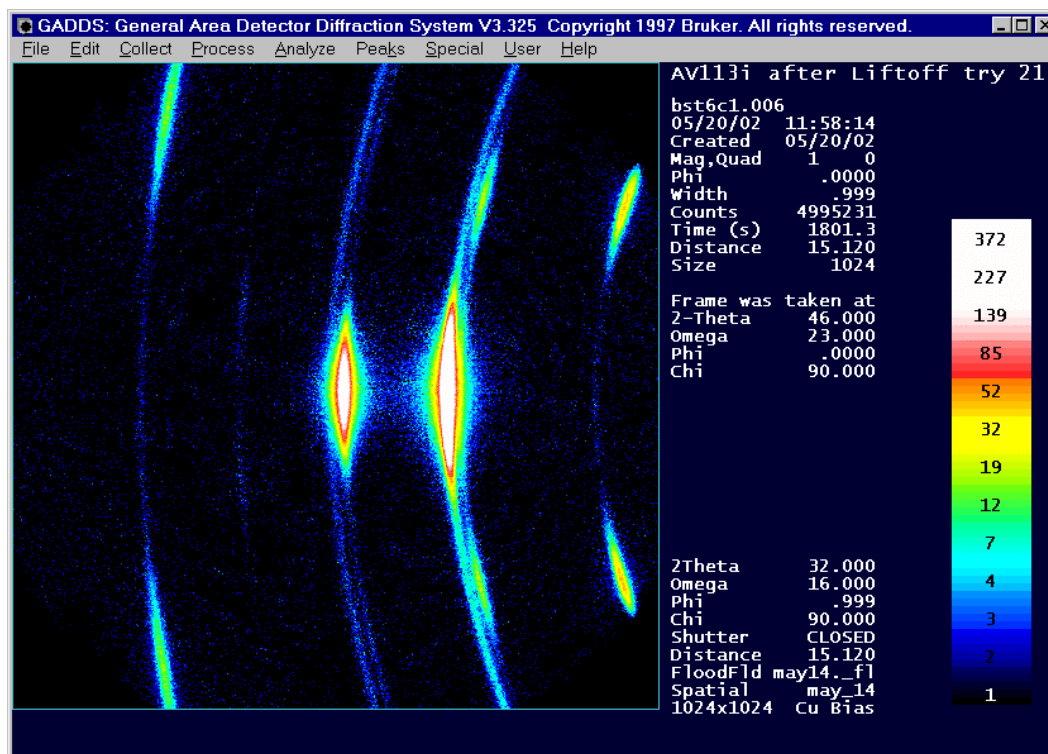


Figure 2.12: Screen capture from XRD system

## 2.4: Temperature Measurement

The temperature measurements were made with an MMR temperature stage and temperature controller, shown in Figure 2.13. The system consists of a source of high pressure nitrogen gas, a combination hydrocarbon filter and dryer, a refrigerator, a vacuum pump, a temperature controller, and a computer. The cold stage uses the Joule-Thompson effect to cool the stage and a resistive heater to heat it, with a nominal range of 77 to 580 K and a functional range of 85 to 580 K. The Joule-Thomson effect occurs when a non-ideal gas, typically an inert gas such as nitrogen or argon, expands from high to low pressure in an adiabatic system. The system provides a cooling capacity of 250 mW at 85 K.

The cold stage is in a vacuum chamber that is evacuated to 5 mtorr, to decrease heat transfer. UHP Nitrogen flows in through a filter designed to trap hydrocarbons and water, the main contaminants of nitrogen gas. The initial nitrogen pressure is 1800 psi, expands to atmospheric pressure and cools, then flows out through a heat exchanger to pre-cool the incoming gas. The system cools to 85 K in approximately 15 min. One advantage of Joule-Thompson cooling is that the system is relatively free from mechanical, acoustic, and electrical noise. Temperature sensing is done with a Pt RTD. The system is accurate to  $\pm 0.05$  K at steady state and  $\pm 1$  K during a temperature ramp. The maximum allowable temperature ramp rate is 1 K/sec.

Eight electrical feed-throughs provide access to the interior of the vacuum chamber. This is enough for all eight lines, four shield and four signal, of the HP4192A test fixture. The shielding provided by the vacuum chamber provides a low noise environment. To minimize heat flow into the temperature stage, the following sample

preparation technique was used. The samples were mounted in a 16-pin ceramic dual inline package ceramic. The pins were removed from the chip carrier and the bottom was sanded with diamond sand paper until smooth, to ensure good thermal transfer. The chip carrier was mounted using standard zinc oxide thermal grease. The samples were attached to the carrier by a silver epoxy, with the entire bottom of the sample coated, again to ensure good thermal transfer. Contact was made to the electrodes on the sample by wirebonding. Single strands of a fine gauge copper wire were soldered to the chip carrier using a high melting point lead/tin/silver solder. These strands were then soldered to the test fixtures. The effect of the single strand of copper wire was to decrease the minimum attainable temperature from 110 K to 85 K. The addition of a peltier cooler and heatsink to the vacuum chamber system served to cool the entire chamber and further reduced the attainable temperature from 85 K to the limit for a nitrogen system, 77 K.

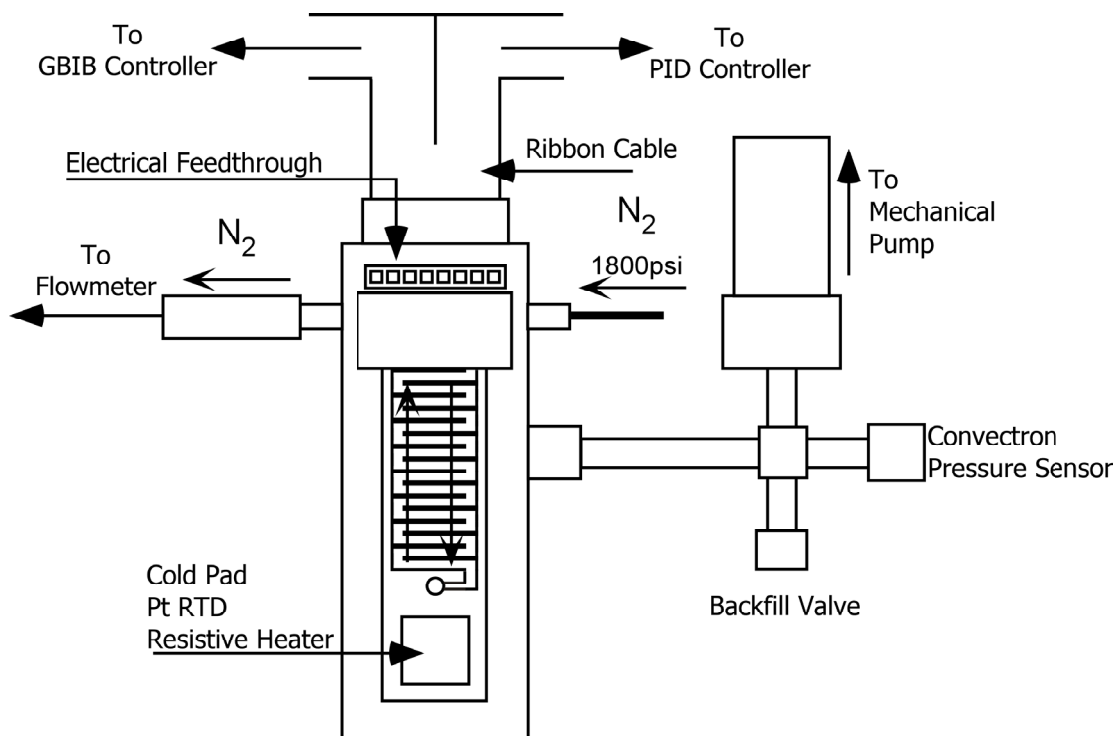


Figure 2.13: Schematic of the temperature stage.

There is a temperature difference between the stage RTD and the surface of the sample in the chip carrier. A separate Pt RTD was used to calibrate the system, using the HP4192A to make a four-point impedance measurement. It is not possible to measure the temperature with the second RTD and measure a BST capacitor, so a series of calibration curves were taken to allow the stage RTD reading to be translated to the sample temperature. An example is given in Figure 2.14 of a 10 K per minute temperature ramp from 85 K to 580 K. Each ramp rate was calibrated so that the temperature can be known at all times. It should be noted that the heating rate is more controlled than the cooling rate, so measurements were always made with increasing temperature.

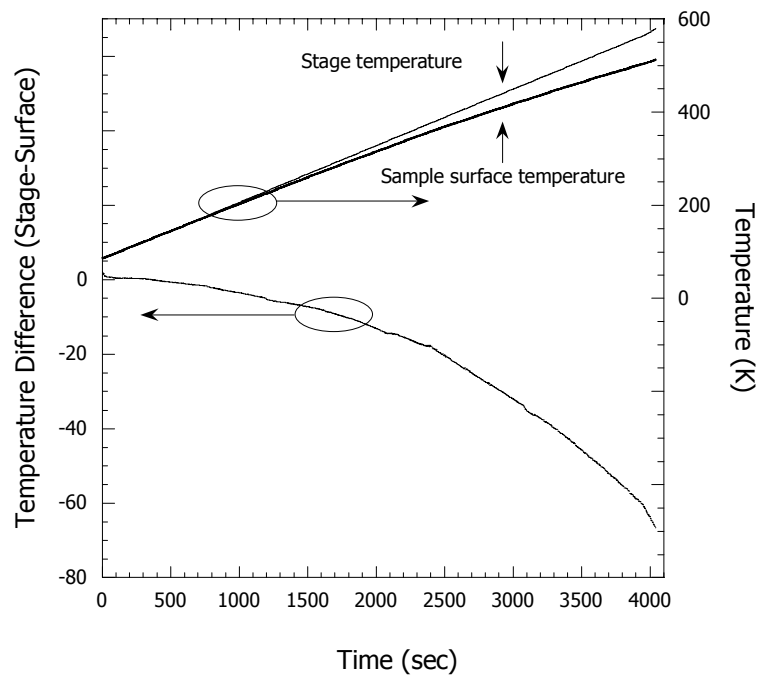


Figure 2.14: 10 K per minute temperature ramp showing the stage temperature and sample surface temperature.

It was verified that 300 seconds was sufficient to achieve steady state conditions. As some high temperature measurements were taken in air, both air and vacuum data were collected. This data is presented in Figure 2.15.

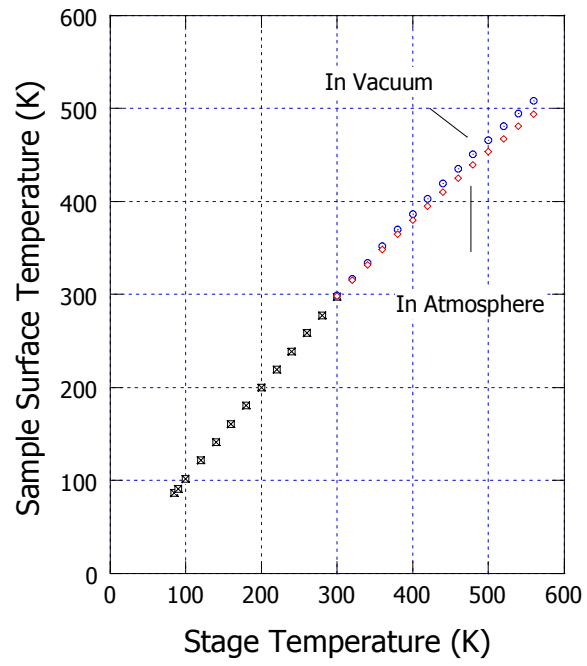


Figure 2.15: Steady-state temperature calibration data for cold stage from 85 K to 580 K.

## 2.5: Film Lift Off

The Pt/SiO<sub>2</sub> interface has poor adhesion. Efforts have been made to improve the adhesion properties by adding additional layers between the Pt bottom electrode and the SiO<sub>2</sub>, such as titania or zirconia. However, this poor adhesion was used advantageously to estimate the effect of strain on the dielectric properties of the BST films. Strain is an important boundary condition in the measurement of size effects and this procedure allows relatively direct measurement.

The lift off process is straightforward. If the samples are submerged in acetone, the films separate at the Pt/SiO<sub>2</sub> interface. The films float off the substrate and then as the acetone evaporates, the films come to rest on the substrate. After lift off, the films are not under the biaxial strain caused by the thermal expansion mismatch with the substrate. The films shrink slightly after liftoff, indicating that the strain is tensile, as can be seen in Figure 2.16.

The films are thought to be free of thermal mismatch strain for two reasons. First, the bottom Pt is a blanket layer and the top is not, so if there were residual strain, the BST/Pt films would curl up. Second, the thermal expansion coefficient for BST is close to that of Pt.

It difficult to make electrical contact to films after they have been lifted off the substrate. Additionally, the films do not delaminate uniformly and simultaneously. Rather, it is like an interface moving across the film. The films tend to break apart due to the large amount of strain in the film. Both problems were solved by mounting the films in the chip carriers and wire bonding all possible top electrodes. Structural support was

provided by the wire bonds and electrical contact had already been made. A top electrode with an attached wire bond can be seen in Figure 2.17.

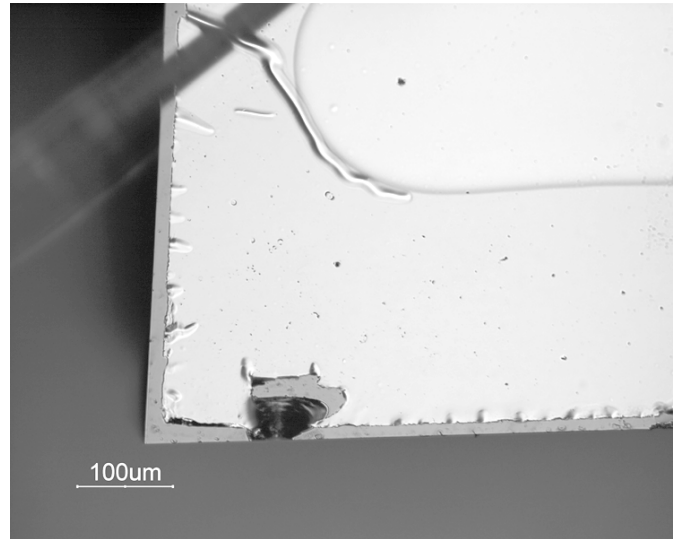


Figure 2.16: Pt/BST/Pt film after liftoff and redeposition on the substrate.

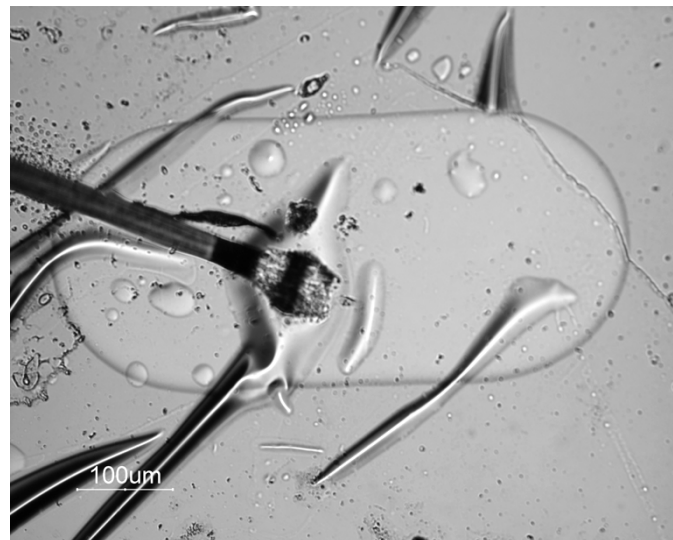


Figure 2.17: Wire bond attached to a top electrode on a lifted off BST film.

# Chapter 3: SIZE EFFECTS

The experimental results are presented in the first section, followed by fitting the results to the two main models, dead layer theory and finite size scaling. The two models are then summarized and the implications for BST as a DRAM dielectric are discussed.

## 3.1: Thickness Dependent Properties

The experimental results are presented in the following five subsections, each addresses a component necessary to evaluate the two competing theories.

### 3.1.1: Temperature dependence of the dielectric response

The main data is the temperature dependence of the dielectric constant. The dielectric response of six films, with thicknesses from 15 to 581 nm, is measured from 85 to 520 K. The films were then lifted off the substrate and measured again. The on substrate/lifted off pairs are shown in Figure 3.29 through Figure 3.34. In some cases it was possible to measure the same electrode both before and after liftoff. Several trends are

apparent. With increasing thickness, the permittivity increases, the range of the permittivity increases, and the temperature of the peak permittivity increases.

The effect of substrate removal is not constant as a function of thickness. The effect for thinner films is more pronounced. For thicker films the permittivity difference is only significant near the transition temperature. The permittivity converges above and below  $T_{\max}$ . The two films are closer in permittivity further from the phase transition. This is expected, as near the phase transition, ferroelectrics are more sensitive to changes in condition. Further from the transition, the dielectric response is more based upon the ionic polarizability.

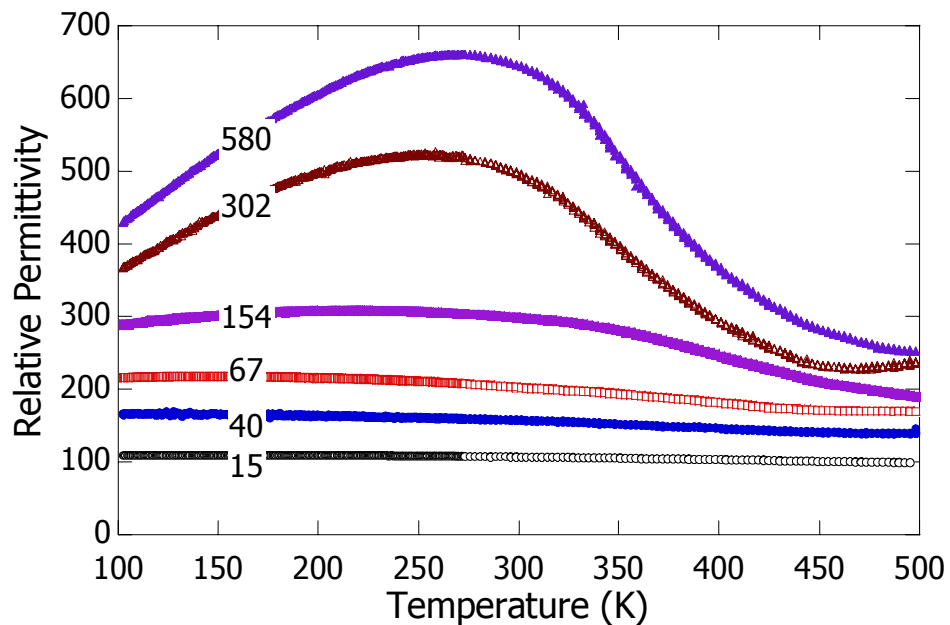


Figure 3.1: Relative permittivity as a function of temperature for various thicknesses, given in nm, on the substrate.

Figure 3.1 shows the relative permittivity for all six of the films before removal from the substrate. Above about 450 K, the permittivity for some of the films, most notably the 302 nm film, deviates from the trend by turning upwards. This is likely due to the effect of space charge being generated from the exposure to vacuum at higher

temperature. The curves are not symmetric because below the first transition, there are other transitions. The paraelectric/ferroelectric transition is the largest in magnitude; subsequent lower-temperature ferroelectric phases have a smaller dielectric anomaly. The first transition is largely suppressed, the lower temperature phases are more so. Distinct peaks are not seen, but rather a diffuse increase in the permittivity, thus the asymmetry.

The lifted off films are shown in Figure 3.2. It is largely similar in form to the films in Figure 3.1. The permittivity is higher in the lifted off films. The transition temperature is also higher. The permittivity peaks are slightly less diffuse. The permittivity of the 302 nm film is close to the 581 nm film. There may be a limit to the property changes with increasing thickness. There are several possible explanations for this behavior; two of the more likely are microstructure and film quality. First, grains or sub-grains may nucleate when the films reach a certain thickness. Instead of the film being a single, columnar grain it is composed of two or more grains. Second, even thick films of MOCVD BST are not as good as poor ceramic samples. The nearest-neighbor and next-nearest-neighbor disorder, because of low temperature processing, may be overwhelming the effects of strain relief or crystal size.

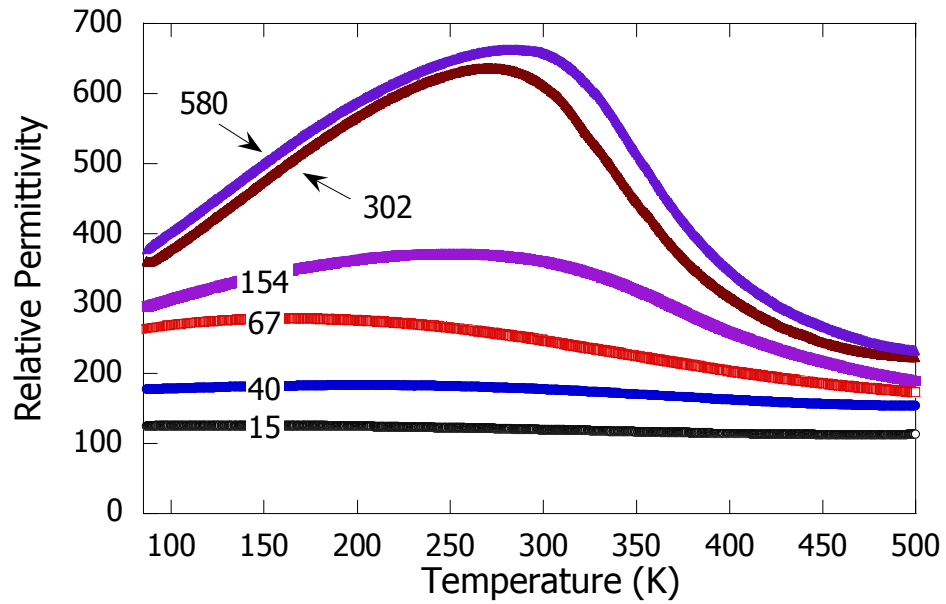


Figure 3.2 Relative permittivity as a function of temperature for various thicknesses, given in nm, after being lifted off the substrate.

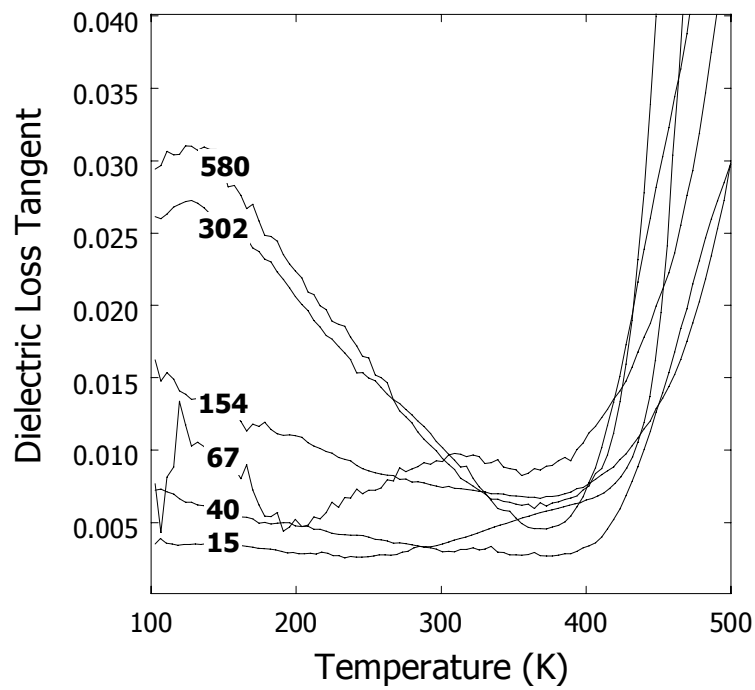


Figure 3.3: The dielectric loss tangent BST films as a function of temperature, on the substrate. Thicknesses are given in nm.

The dielectric loss tangent for the films is given in Figure 3.3 and Figure 3.4. The former is the dielectric loss tangent of the films on the substrate and the latter lifted off

the substrate. The films display the expected relationship between temperature, thickness, and dielectric loss. In a sense, the more ferroelectric films have higher loss tangents. If the loss tangent increases were caused by some other thickness dependent property, the loss would not have a strong temperature dependence. The dielectric loss tangent at 300 K is less than 1%, which indicates the high quality of the films.

The low-temperature peak in the loss, which is more pronounced in the 302 and 581 nm samples, is evidence of the low temperature phases discussed above. This effect is more pronounced in the lifted off films. For instance, the low temperature peak in the 581 nm sample increases from about 3.2% for the sample on the substrate to 3.7% for the lifted off sample, though the minimum value actually falls from 0.6% to 0.3%, respectively.

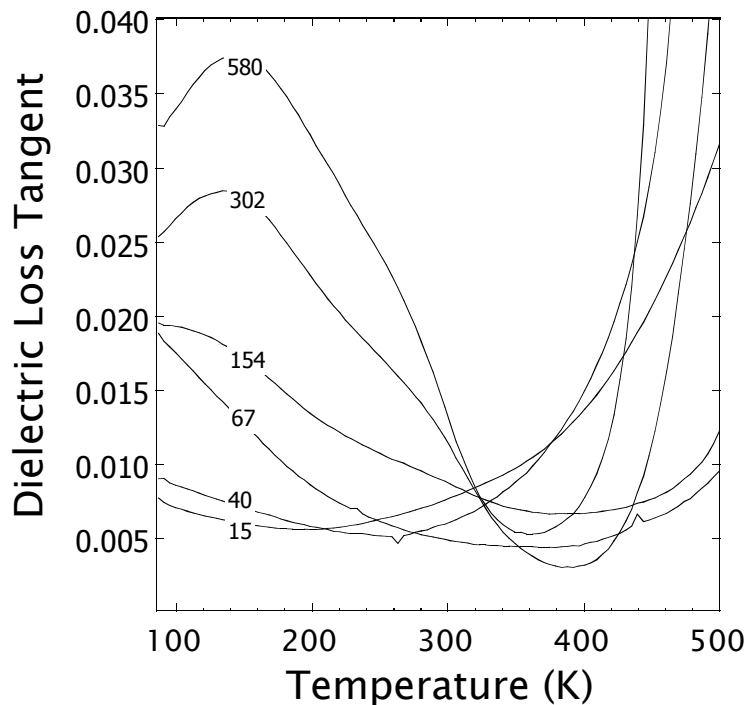


Figure 3.4: The dielectric loss tangent BST films as a function of temperature, after being lifted off the substrate. Thicknesses are given in nm.

### 3.1.2: Electric field dependence of the dielectric response

The dielectric response as a function of field for the six films is given in Figure 3.5 through Figure 3.10. The relative permittivity and dielectric loss tangent are plotted on the left and right axes, respectively. The permittivity peak in Pt/BST/Pt films has a voltage offset of about 0.2 V, independent of the field applied across the film. This offset was also noted by Basceri[112]. The effect is consequently larger for thinner films.

The dielectric loss tangent is largely flat as a function of field, especially for the thinner samples. The low-field values are reasonably good, below 0.5% for the two thinner films and 1% for all but the thickest. The dramatic increases in the dielectric loss tangent with increasing field is due to leakage current. This current is related to the electrodes. The Schottky barriers at the electrode are voltage, not field, dependent. This is why dramatic  $\tan(\delta)$  increases are not observed in the thinner samples. For instance, 500 kV/cm corresponds to 29 V for the 581 nm film. The peak in the dielectric loss tangent for 3 thickest films is due to a contribution from the ferroelectric domain wall motion.

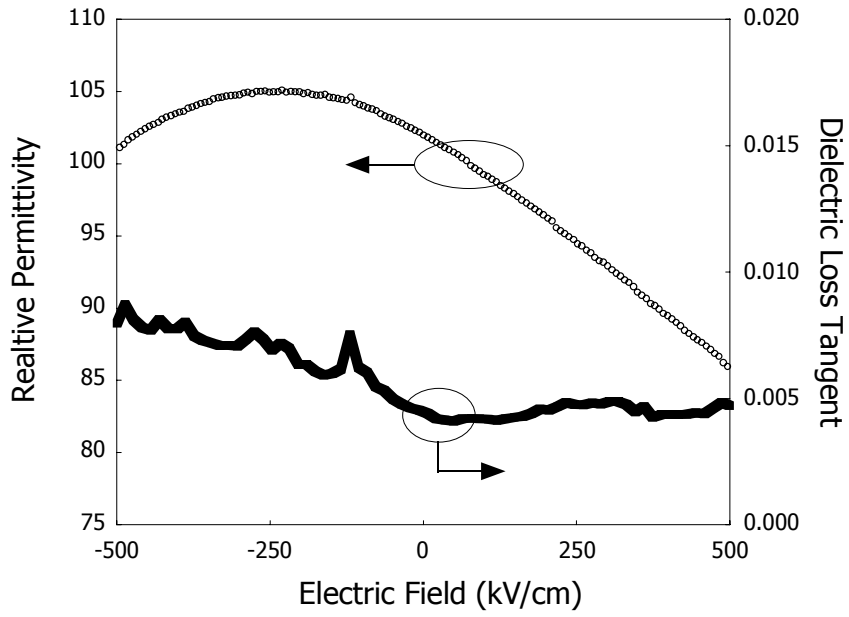


Figure 3.5: Relative permittivity and dielectric loss tangent as a function of electric field for a 15 nm BST film.

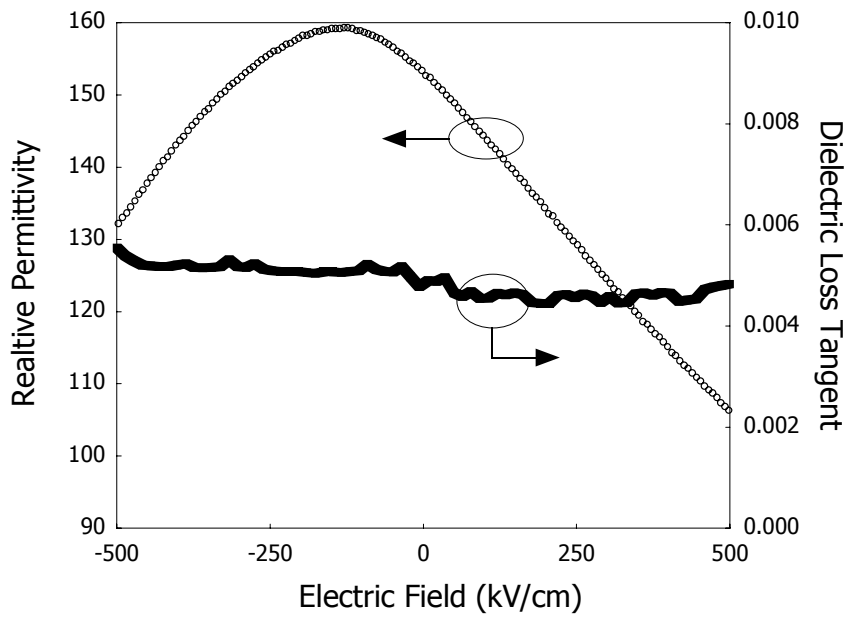


Figure 3.6: Relative permittivity and dielectric loss tangent as a function of electric field for a 40 nm BST film.

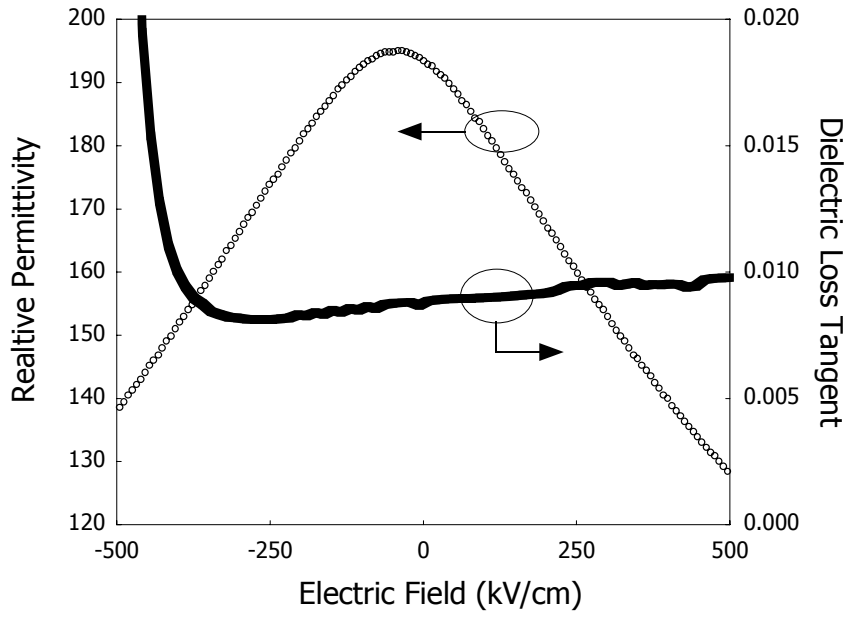


Figure 3.7: Relative permittivity and dielectric loss tangent as a function of electric field for a 67 nm BST film.

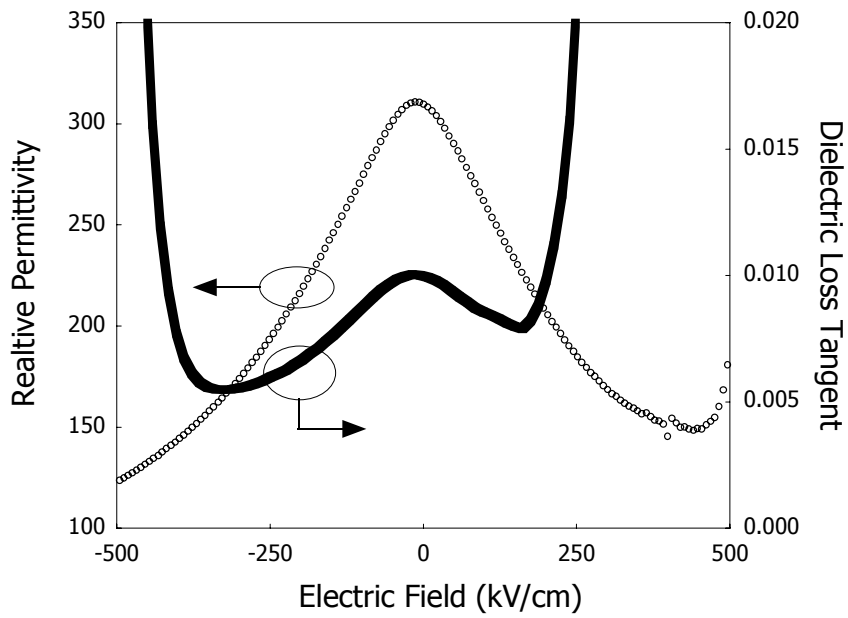


Figure 3.8: Relative permittivity and dielectric loss tangent as a function of electric field for a 154 nm BST film.

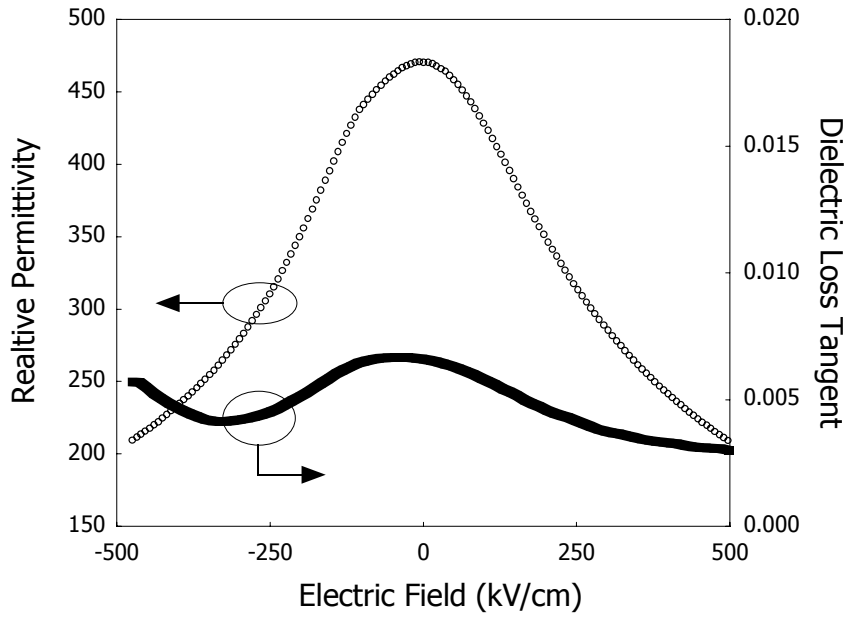


Figure 3.9: Relative permittivity and dielectric loss tangent as a function of electric field for a 302 nm BST film.

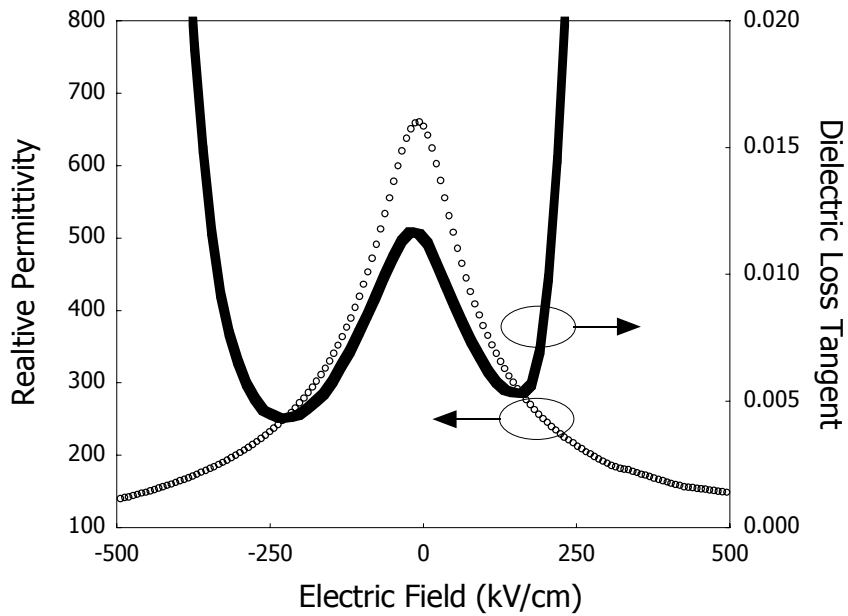


Figure 3.10: Relative permittivity and dielectric loss tangent as a function of electric field for a 581 nm BST film.

All of the relative permittivities are shown in Figure 3.11. The zero bias permittivity increases as a function of thickness, but the curves converge at high field.

This behavior is well explained by the LGD formalism[4, 5]. Permittivity is a measure of the effect that an electric field has on the dipole response, similar to the mass on a spring. A large response to a small mass means that the spring has a low stiffness. At low fields, the ferroelectric has a low dielectric stiffness. Under large fields, the ferroelectric has a much higher dielectric stiffness. The physical analog is a spring that become stiffer the more it is stretched.

The increase in the dielectric stiffness is dramatic. Figure 3.12 shows high- and low-field permittivity data for the 581 nm film, taken from a series of C-V curves as a function of temperature. The high-field permittivity is close to the zero-field permittivity of the 15 nm film, which is also shown.

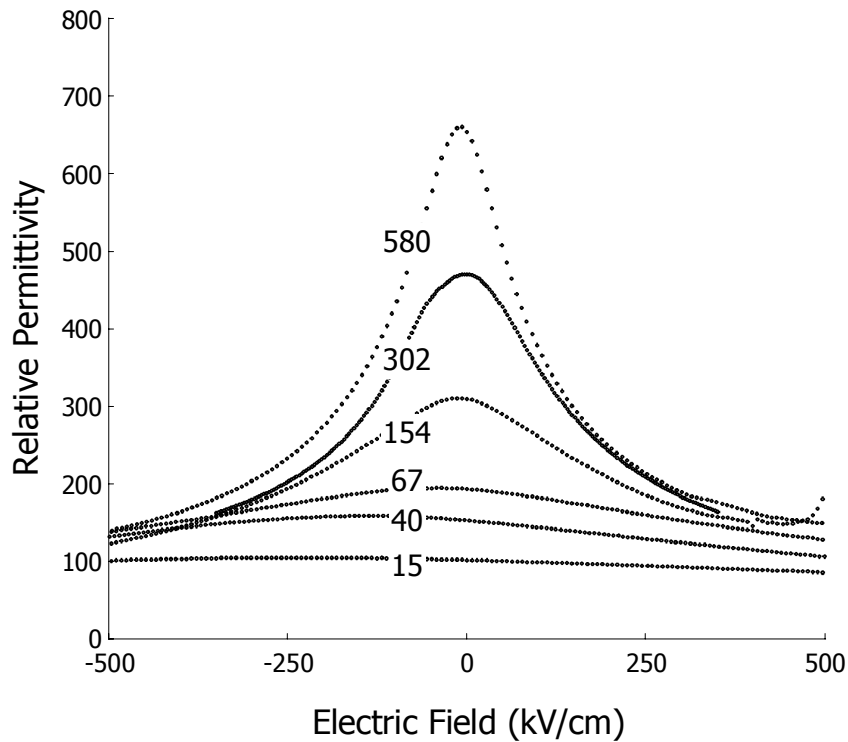


Figure 3.11: The relative permittivity as a function of electric field for various BST film thicknesses, given in nm.

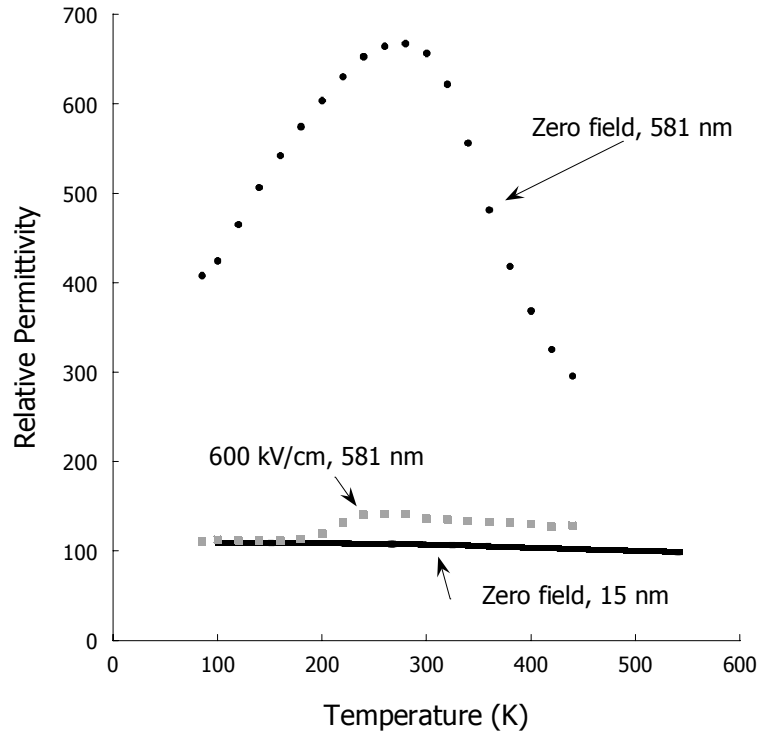


Figure 3.12: The effect of field on the permittivity of a 581 nm BST film as a function of temperature, with a 15 nm film for comparison.

### 3.1.3: Frequency dependence of the dielectric response

The equation used to quantify the diffuseness of the phase transition was suggested by Uchino and Namura[67] and is given as

$$\frac{1}{\epsilon} = \frac{1}{\epsilon_{Max}} + \frac{(T - T_{Max})}{2\epsilon_{Max}\delta^2}$$

where  $T$  is temperature,  $\epsilon$  is permittivity and  $\delta$  is the diffuseness. One of the origins of a diffuse phase transition is relaxor-like behavior. An example of relaxor behavior is shown in Figure 3.13. The  $\text{Pb}(\text{Li}_{1/4}\text{Fe}_{1/4}\text{W}_{1/2})\text{O}_3$  ceramic was measured as a function of test frequency and shows the expected response[167]. A similar response is seen in the dielectric loss tangent. A series of permittivity-temperature curves for BST films were taken as a function of frequency to investigate the possibility of relaxor-like behavior. As

can be seen from Figure 3.14, neither the transition temperature nor the relative permittivity are strong functions of frequency. The same data as Figure 3.14 is plotted on a full scale in Figure 3.15, in order to show that the variation seen in the former figure is relatively small.

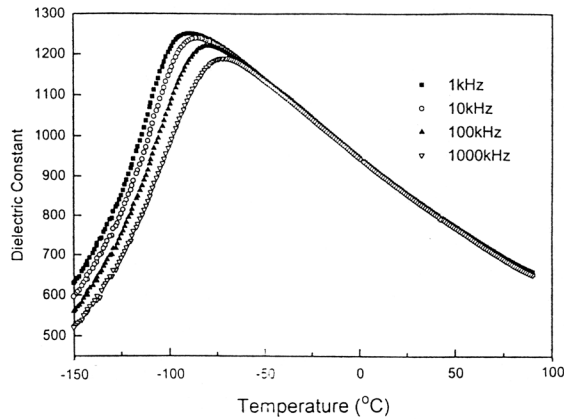


Figure 3.13: Dielectric response of a  $\text{Pb}(\text{Li}_{1/4}\text{Fe}_{1/4}\text{W}_{1/2})\text{O}_3$  ceramic as a function of temperature for various frequencies, from Lu *et al*[167].

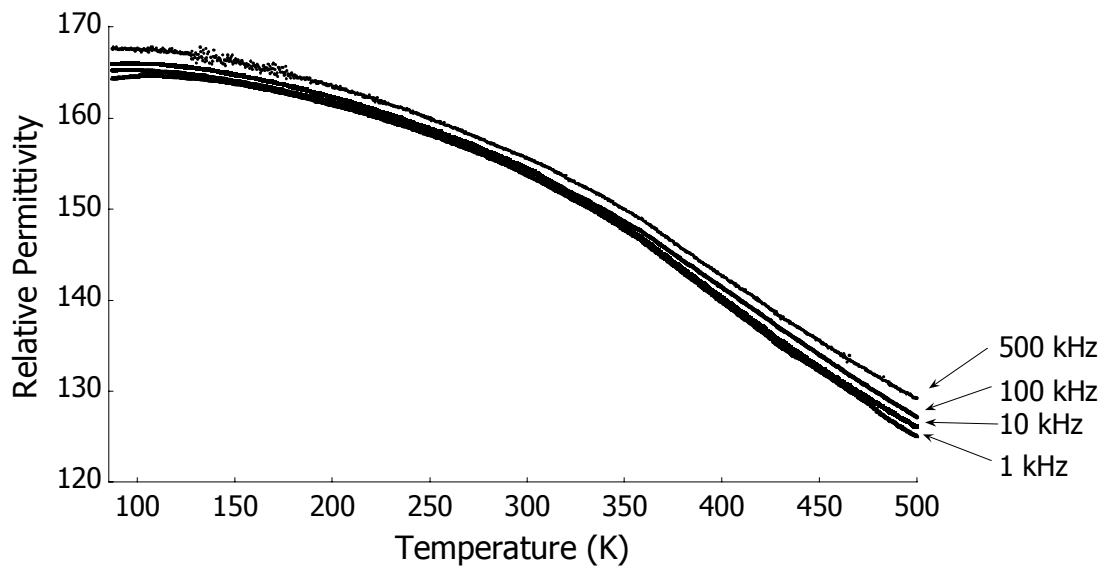


Figure 3.14: Relative permittivity versus temperature for a 53.1% Ti, 40 nm BST film for a number of frequencies.

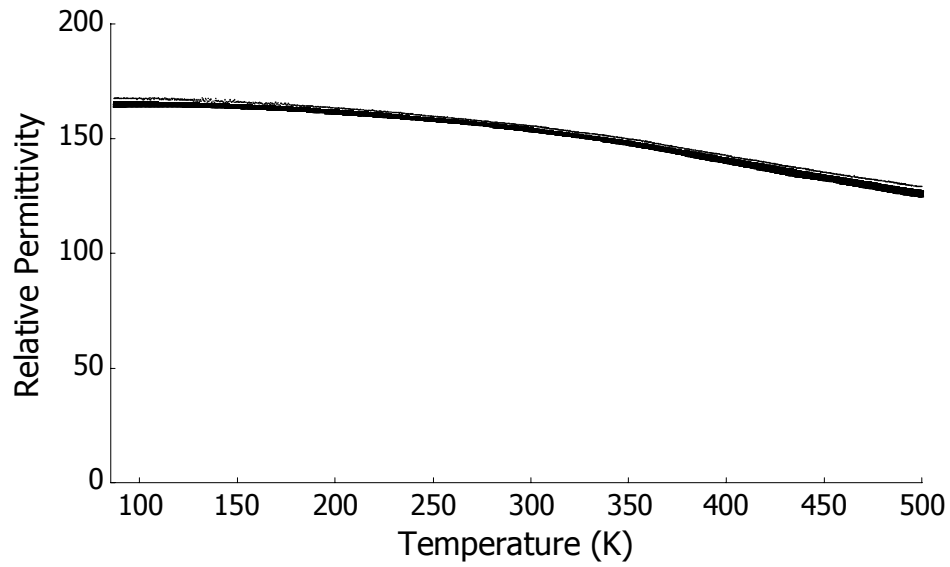


Figure 3.15: Relative permittivity versus temperature for a 53.1% Ti, 40 nm BST film for a number of frequencies, ordinate shown from origin.

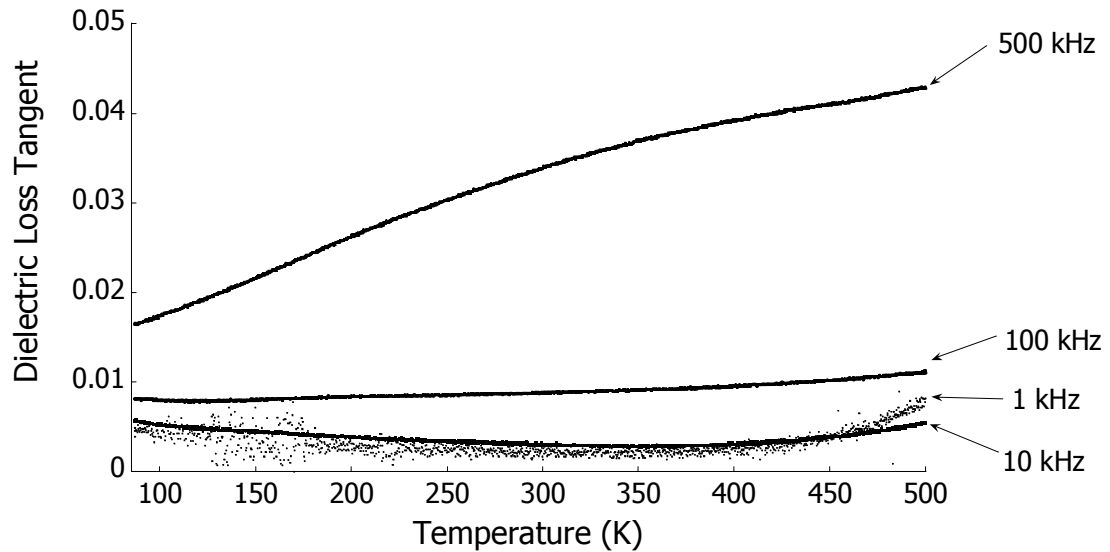


Figure 3.16: Dielectric loss tangent versus temperature for a 53.1% Ti, 40 nm BST film for a number of frequencies.

The dielectric loss tangent is shown in Figure 3.16. The variation does not show a relaxor-type response. It does show some of the limitations of the test fixture. The 1 kHz data is noisy. The 100 kHz data is beginning to show the influence of the test fixture impedance, while the 500 kHz data is strongly affected by the lead inductance.

### 3.1.4: Hysteresis as a function of temperature

The BST films should be ferroelectric at temperatures below  $T_{\max}$ . The hysteretic electrical properties could complicate the size effects analysis, so C-V curves were taken as a function of temperature to determine its relative importance. This analysis is only performed on the thickest film, as it is the most likely to show hysteresis. The resultant relative permittivity-electric field curves are shown in Figure 3.17. Ferroelectricity would cause the peaks of the curves to separate, giving a “butterfly” appearance. The 300 K curves show no switching, which is expected, as it is above the transition temperature. Figure 3.34 shows that the 85 K curves are well below the transition temperature. There is some peak splitting, but it is not well developed.

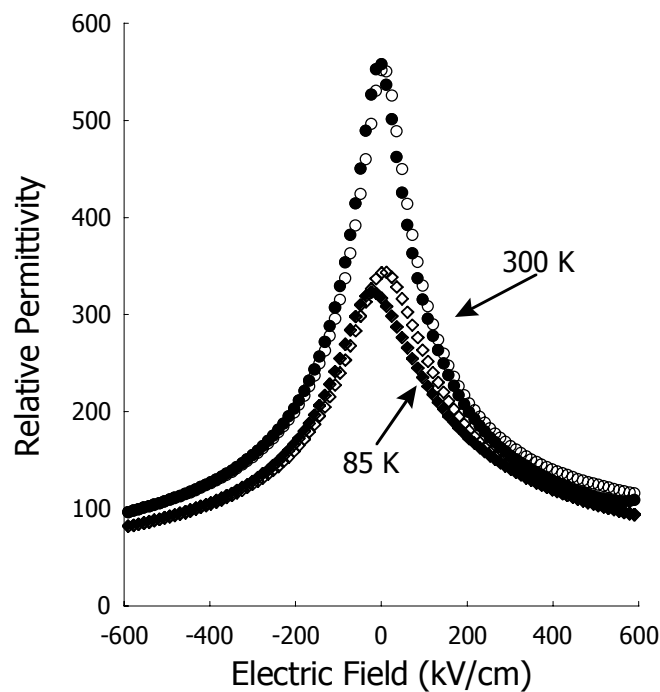


Figure 3.17: Relative permittivity as a function of electric field, at 85 and 300 K, for a 581 nm BST film. Open symbols indicate negative to positive sweep, closed symbols the opposite.

The dielectric loss tangent shows similar behavior to the permittivity, as shown in Figure 3.18. The dielectric loss tangent has a peak at zero field because the domain

contribution. The 300 K curves do not show splitting. At 85 K, there is some evidence of switching. The high-field dielectric loss tangent is largely a result of leakage currents. At lower temperatures, the Schottky barrier is higher, so the leakage is low and the high-field dielectric loss tangent is correspondingly low. At higher temperatures, the opposite occurs.

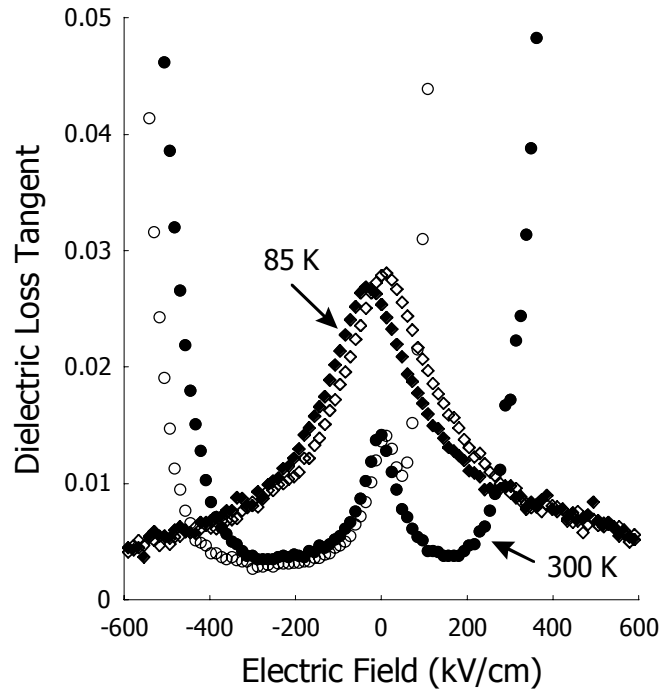


Figure 3.18: Dielectric loss tangent as a function of electric field, at 85 and 300 K, for a 581 nm BST film. Open symbols indicate negative to positive sweep, closed symbols the opposite.

### 3.1.5: X-ray estimation of strain

BST films on Si substrates are under the influence of appreciable strains resulting from thermal expansion mismatch between dielectric and substrate. Since BST films are ferroelectric, they will also be ferroelastic, *viz.*, the electrical properties depend strongly on the applied strain. Consequently, it is important that we understand the degree to which the residual strain from the thermal expansion mismatch strain influences BST film

properties if thickness effects are to be fully characterized. To quantify strain effects, the ideal approach is to measure properties both in the presence and absence of strain. This has been accomplished by developing the technique of substrate removal described in the experimental section. In this section, the amount of strain relief from substrate removal is measured directly by XRD and its impact on temperature-dependent dielectric properties. The strain effects of the Pt bottom electrode are neglected for three reasons. First, a 100-200 nm film of Pt cannot have a significant strain gradient. Second, Pt is unlikely to have significant strain itself, as the films are annealed at 550 °C for 30 min following top electrode deposition and Pt begins to relax at 500 °C. Third, after the solvent evaporates, the films lie relatively flat. The bottom electrode is blanket Pt and the top is not, so if there were a significant stress mismatch in the two layers, BST and Pt, the films would tend to curl up.

To characterize the amount of strain relieved by substrate removal, x-ray diffraction and the Nelson-Riley approach was used. In this approach, a family of reflections are measured and the peak positions are plotted using the Nelson-Riley function[168], given as

$$\frac{\Delta d}{d} = K \left( \frac{\cos^2 \theta}{\sin(\theta)} + \frac{\theta}{\cos^2 \theta} \right)$$

where K is a sample-specific fitting parameter. This treatment minimizes two sources of error, sample height adjustment error and x-ray absorption error. Sample height adjustment error is more important for thin films. The N-R approach is only sensitive to coherent strain. Incoherent strains stemming from stress gradients or extended defect populations are not visible. Only coherent strains are expected from the presence of a macroscopic equi-biaxial strain resulting from the thermal expansion mismatch between dielectric and substrate.

ted in Table 3.1. By using a number of peaks, the error of the lattice constant measurement can be reduced.

Table 3.1: Approximate positions for (0 0  $\ell$ ) family of planes in BST

	Index		d-spacing	2 $\theta$
$h$	$k$	$l$		
1	0	0	3.92	22.663
2	0	0	1.96	46.278
3	0	0	1.31	72.236
4	0	0	0.981	103.614

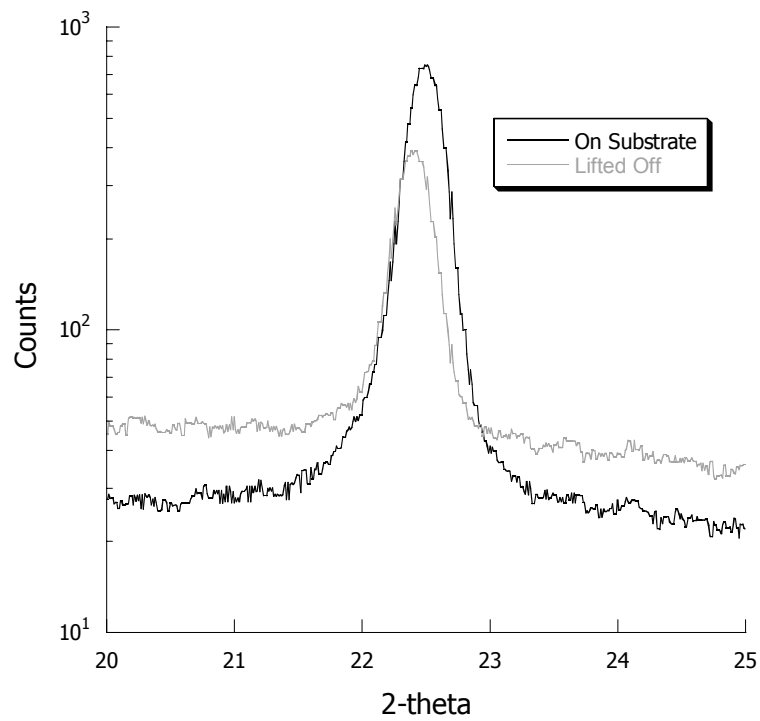


Figure 3.19: (001) peak of a 40 nm BST film both on the substrate and lifted off.

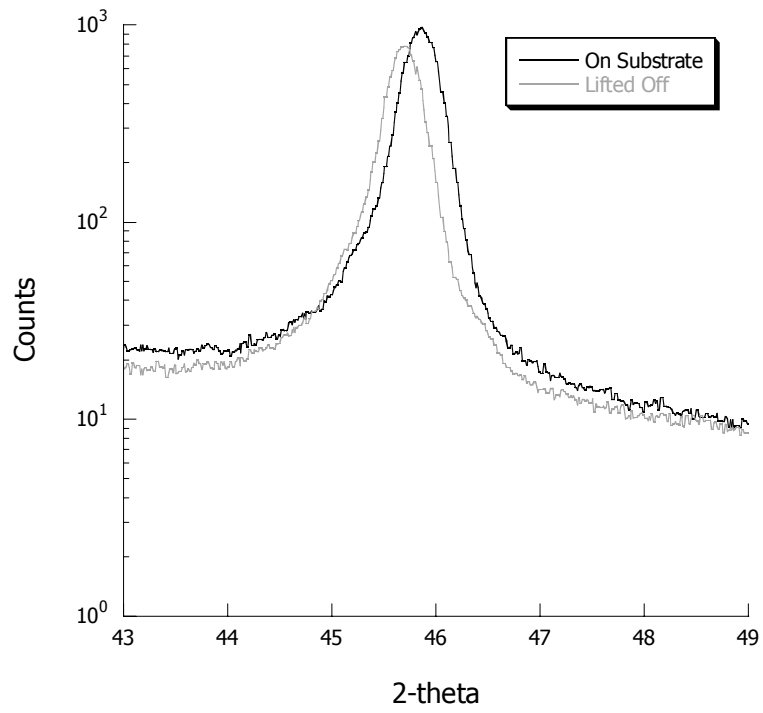


Figure 3.20: (002) peak of a 40 nm BST film both on the substrate and lifted off.

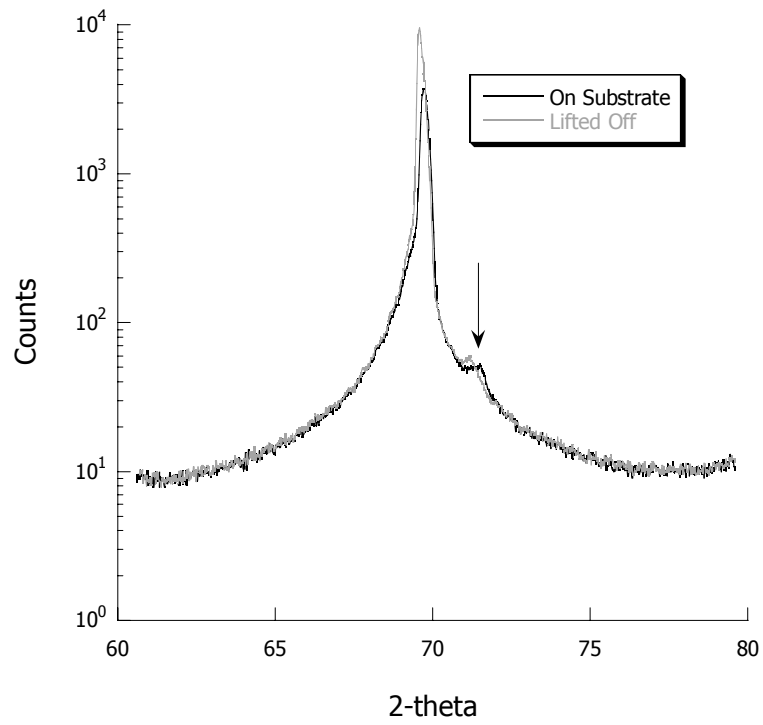


Figure 3.21: (003) peak of a 40 nm BST film both on the substrate and lifted off.

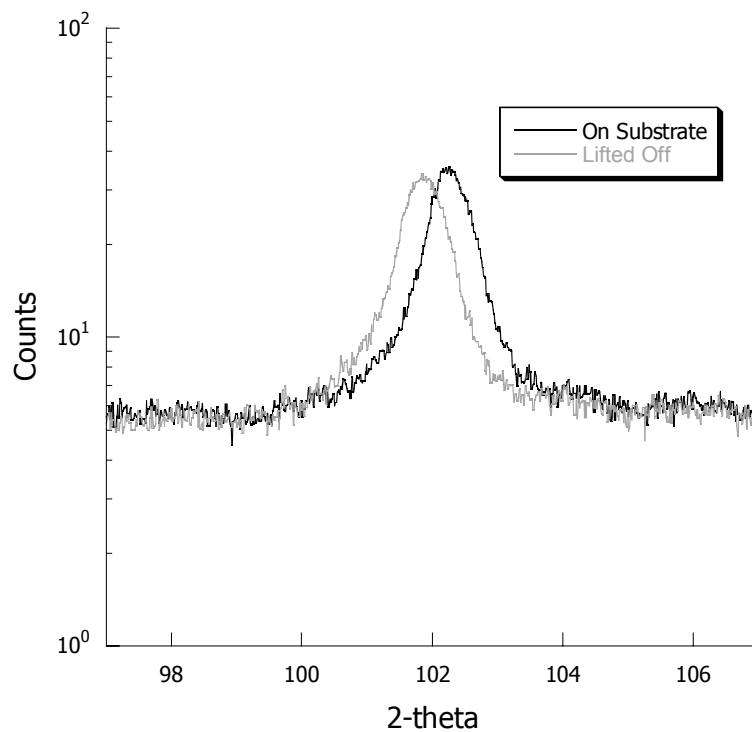


Figure 3.22: (004) peak of a 40 nm BST film both on the substrate and lifted off.

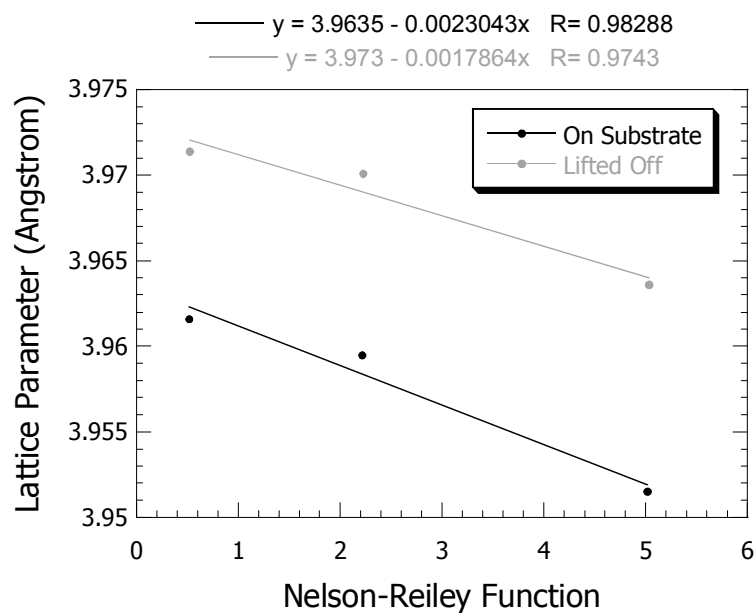


Figure 3.23: Lattice parameter versus the Nelson-Riley function for a 40 nm film, both on and lifted off the substrate.

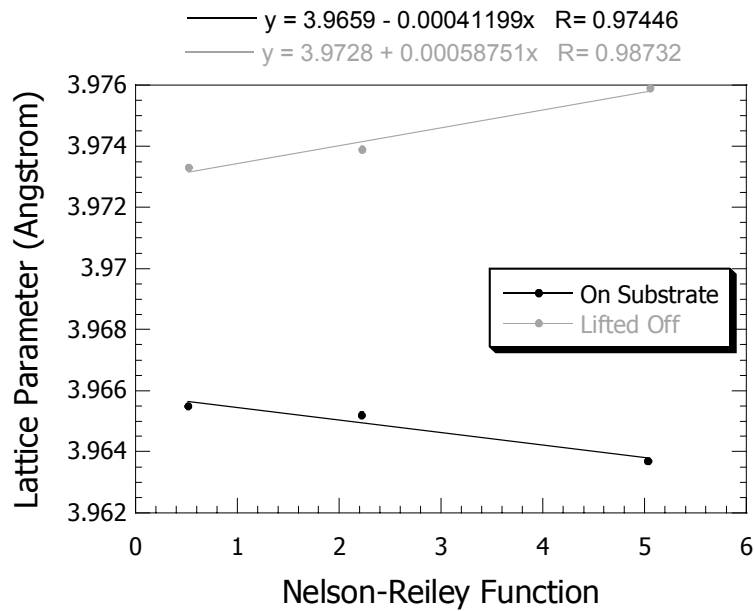


Figure 3.24: Lattice parameter versus the Nelson-Reiley function for a 150 nm film, both on and lifted off the substrate.

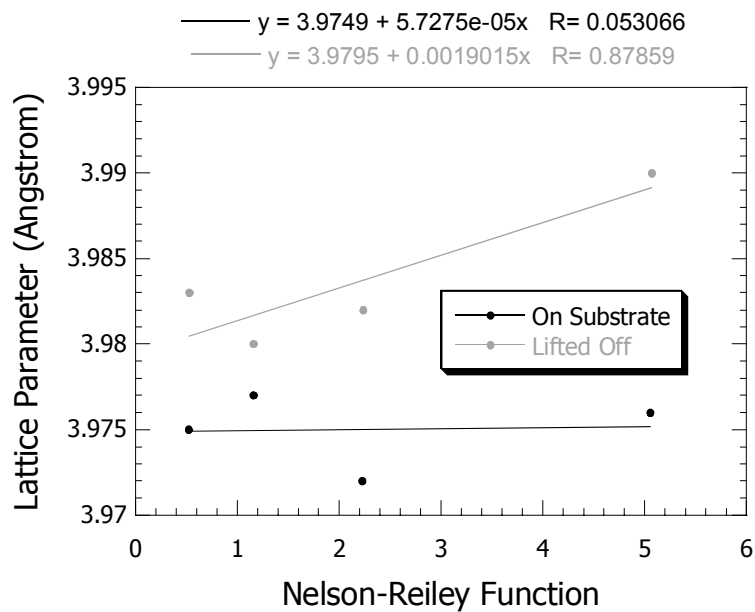


Figure 3.25: Lattice parameter versus the Nelson-Reiley function for a 580 nm film, both on and lifted off the substrate.

Table 3.2: Results of x-ray estimation of strain

Film Thickness (nm)	Lattice Parameter (Å)		Strain (%) (out of plane)	Strain (%) (in plane)
	On Substrate	Lifted Off		
40	3.964	3.967	0.1	0.2
150	3.968	3.972	0.1	0.2
600	3.975	3.979	0.1	0.2

Results of the measurement are shown in Table 3.2. Three thicknesses were measured. 0.1% out-of-plane strain is relieved by the lift off process. The in-plane value can be calculated from Poisson's ratio, assuming that it is an ideal material, i.e., a value of 0.33. This value is consistent with laser wafer curvature measurements by Shaw *et al*[169]. A strain of 0.1% is the fracture strain of the material, so the values are within the upper bound of the range.

The effect of the strain relief on the electrical properties are shown in Figure 3.29 through Figure 3.34. The general trends are these. As film's strain is relieved, the transition temperature increases, the diffuseness decreases, and the peak permittivity increases. The effect of the liftoff is greater for thinner films. Summary plots are shown for the three quantities in Figure 3.26 through Figure 3.28. The trend for maximum permittivity is less clear than the transition temperature and diffuseness because the transition temperature and diffuseness are calculated from the change in permittivity over many degrees. The absolute permittivity has the largest error of the three quantities.

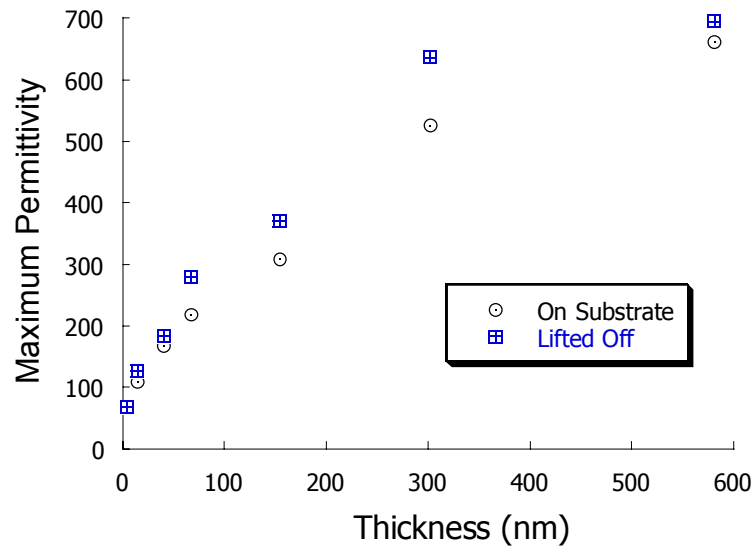


Figure 3.26: Maximum Permittivity on and lifted off the substrate.

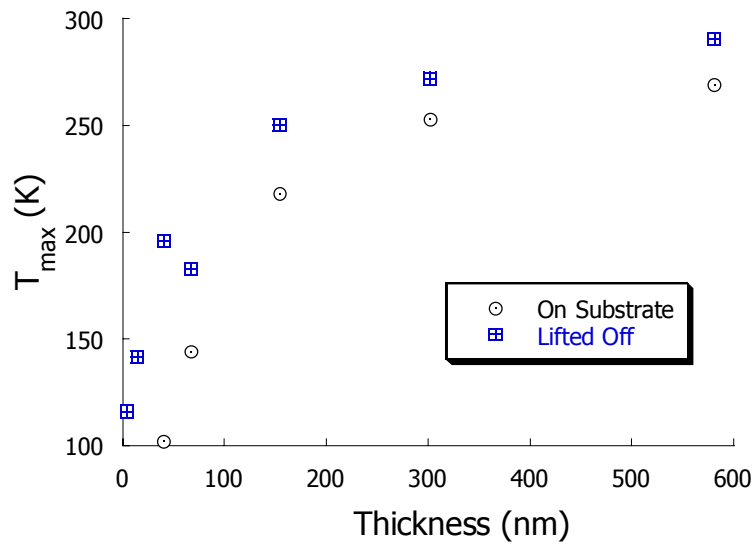


Figure 3.27: Transition temperature on and lifted off the substrate.

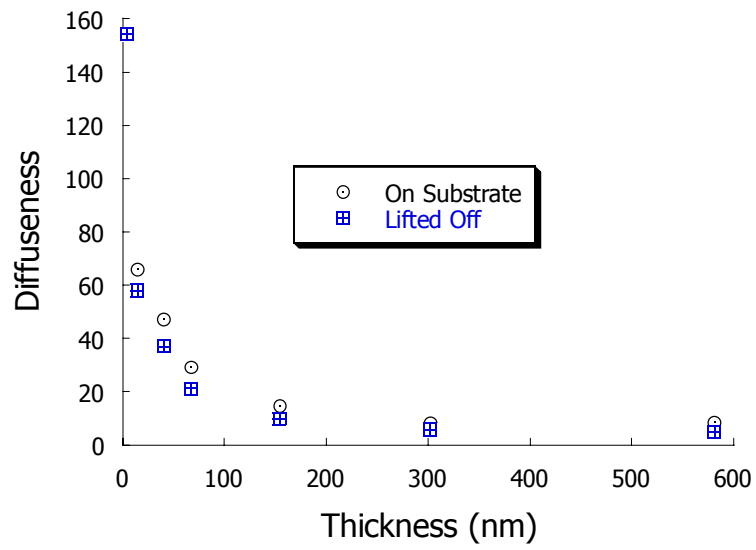


Figure 3.28: Diffuseness on and lifted off the substrate.

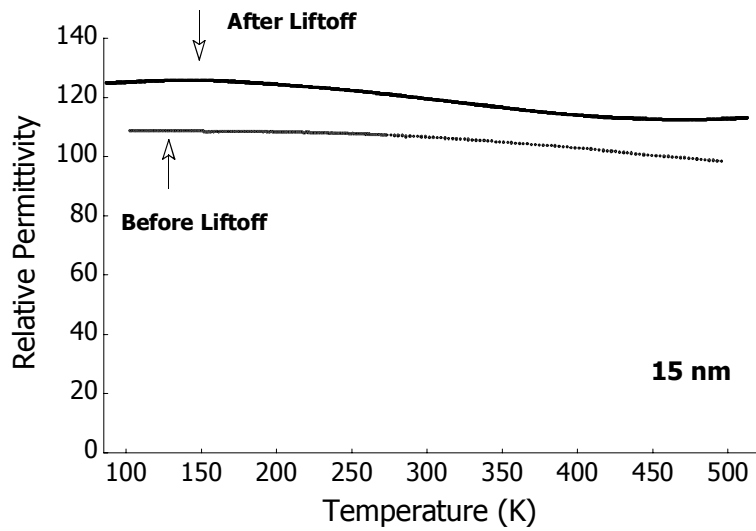


Figure 3.29: The relative permittivity of a 15 nm, 53.1% Ti BST film, before and after removal from substrate.

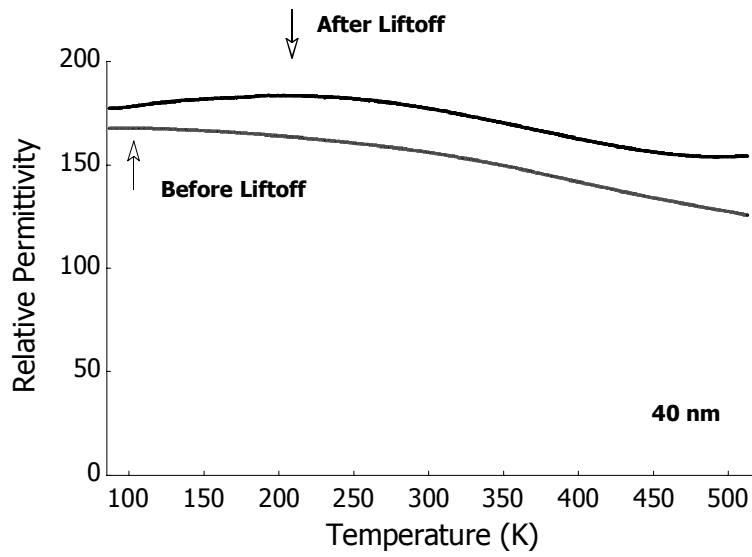


Figure 3.30: The relative permittivity of a 40 nm, 53.1% Ti BST film, before and after removal from substrate

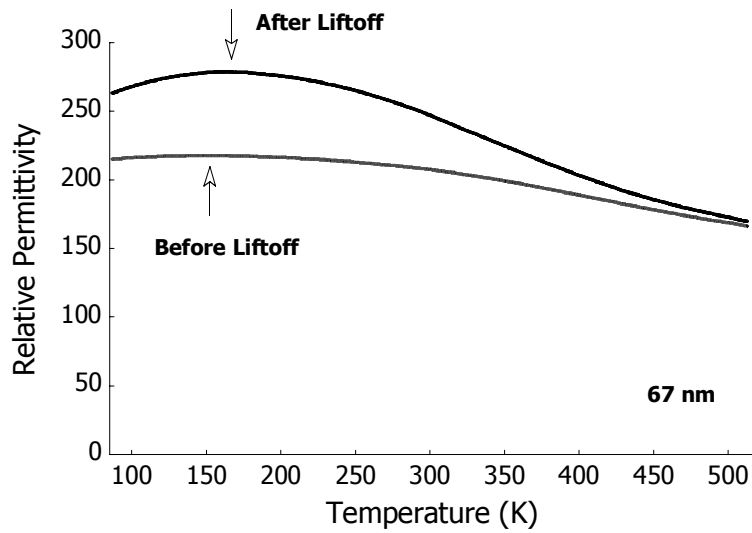


Figure 3.31: The relative permittivity of a 67 nm, 53.1% Ti BST film, before and after removal from substrate.

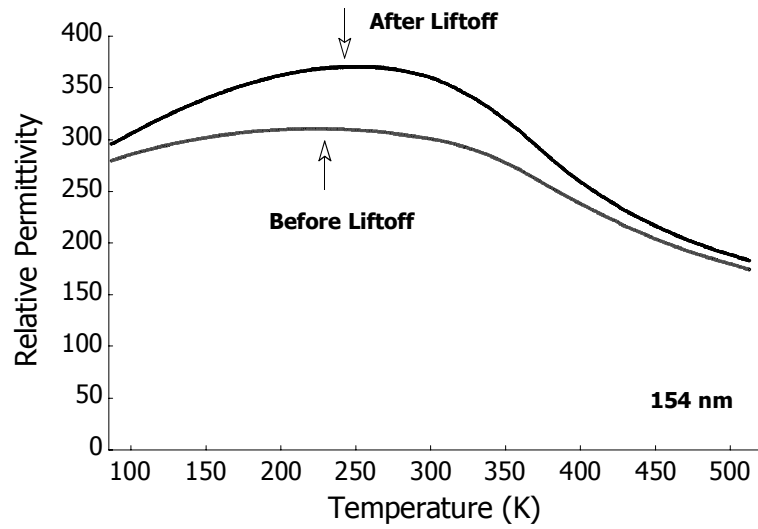


Figure 3.32: The relative permittivity of a 154 nm, 53.1% BST film, before and after removal from substrate.

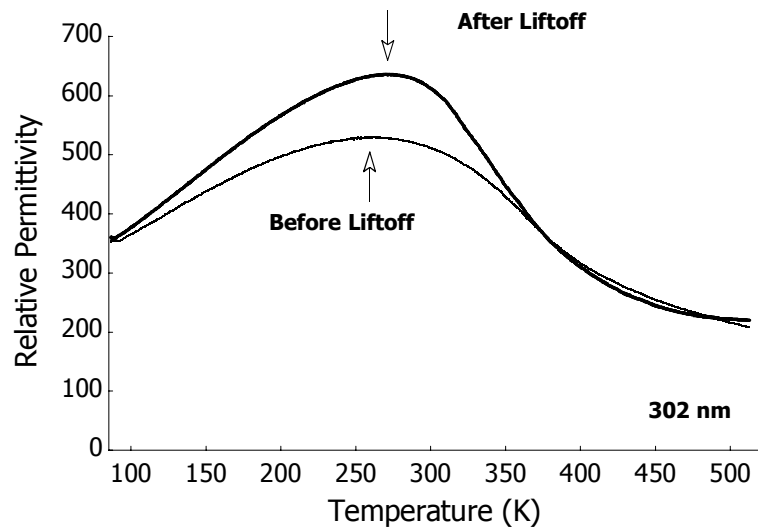


Figure 3.33: The relative permittivity of a 302 nm, 53.1% Ti BST film, before and after removal from substrate.

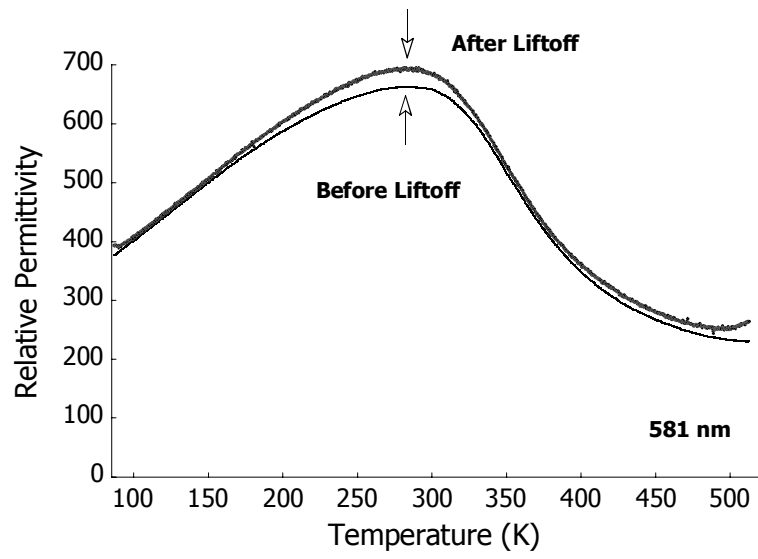


Figure 3.34: The relative permittivity of a 581 nm, 53.1% Ti BST film, before and after removal from substrate.

## 3.2: Modeling Thickness Dependant Properties With the “Dead” Layer Concept

As discussed in the literature survey, the dead layer model has been widely used to describe thickness-dependent properties in ferroelectric thin films. The dead layer model predicts a linear relationship between the capacitance density and film thickness,

$$\frac{A}{C} = \frac{t - 2\delta}{\epsilon_b} - \frac{2\delta}{\epsilon_o}$$

where  $A$  is the capacitor area,  $C$  is the capacitance,  $t$  is film thickness,  $\delta$  is the dead layer thickness,  $\epsilon_b$  is the bulk permittivity, and  $\epsilon_o$  is the dead layer permittivity. The individual components are summarized in Figure 3.35. The important interpretation of the dead layer model is that the film interior behaves as a ferroelectric, whereas the surface, or dead layer, has non-ferroelectric behavior, *i.e.*, a linear dielectric. Furthermore, as a function of thickness, the characteristics of both components remain constant, only the relative volume fraction changes.

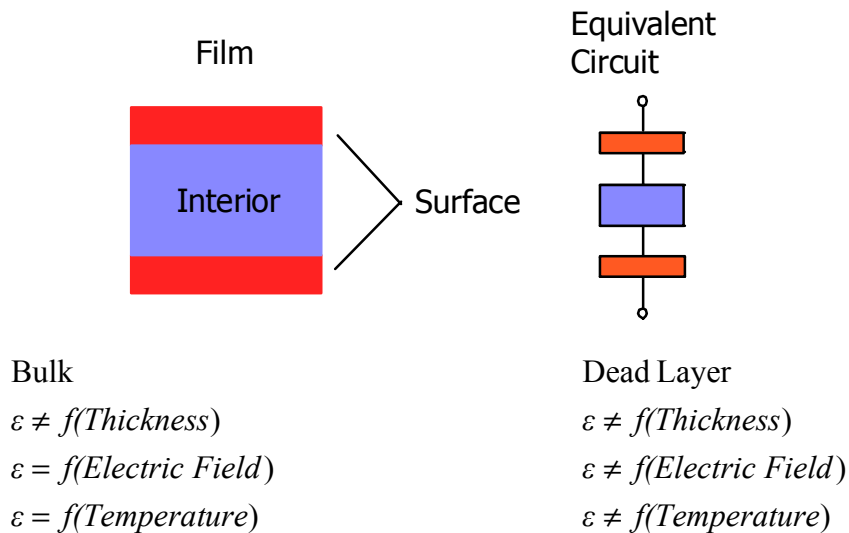


Figure 3.35: Schematic of capacitor circuit with dead layer approximation, composed of bulk and interface capacitors, dependencies of components are detailed. The equivalent circuit is shown on the right.

The dead layer model uses a plot of inverse capacitance density versus thickness to extract the components of the model. An example of this treatment is given in Figure 3.36. The interfacial component only gives the ratio of thickness to permittivity; the actual thickness of the dead layer cannot be extracted from the model.

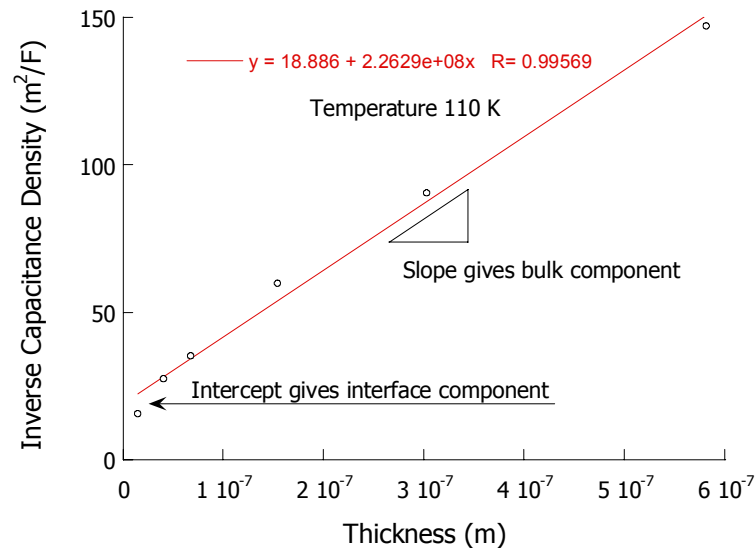


Figure 3.36: Dead layer treatment of inverse capacitance density as a function of thickness.

The relative permittivity data given on pages 184 through 187 was fit using the dead layer treatment. This corresponds to about 1500 lines fit for the combined on substrate and lifted off films. The slopes are shown in Figure 3.37 and the intercepts in Figure 3.38. The intercept indicates the interfacial capacitance and the slope indicates “bulk” permittivity. Comparing Figure 3.35 and Figure 3.38 highlights some of the inconsistencies in the model. Since the intercept corresponds to the capacitance originating from the non-ferroelectric interface, its temperature dependence should only arise from the temperature dependence of the ionic and electric polarizability the volume thermal expansion. There should be no extrema within any temperature range. The intercept should be constant with temperature. It is not. The exact form of the interfacial capacitance density is not important. What is important is that it varies with

temperature. It is not possible to determine whether it is the thickness, the permittivity, or both that vary, but neither should.

The temperature dependant slope data can be used to calculate the thickness-independent “bulk” permittivity, shown in Figure 3.39. The bulk permittivity data is more difficult to interpret. Although it is below the ceramic or single crystal values, it is possible that the difference is due to the quality of the dielectric and no film, however thick, will reach the values seen in the ceramic. Not only is it difficult to know the magnitude of the permittivity, it is also difficult to know the temperature dependence of the bulk permittivity.

In Figure 3.39, the bulk permittivity was calculated using films with three thickness ranges: 40 to 154 nm, 40 to 302 nm, and 40 to 581 nm. The resulting bulk permittivities are different. The magnitude of the relative permittivity is dependant upon the range of thicknesses used to calculate it. It varies from 920 for the largest range to 461 for the smallest range. The transition temperature varies from 272 for the largest range to 238 for the smallest range. Finally, the shapes of the curves are different. The bulk permittivity values predicted by the dead layer treatment are not the true bulk permittivity, but are an extrapolation based on the measured permittivities.

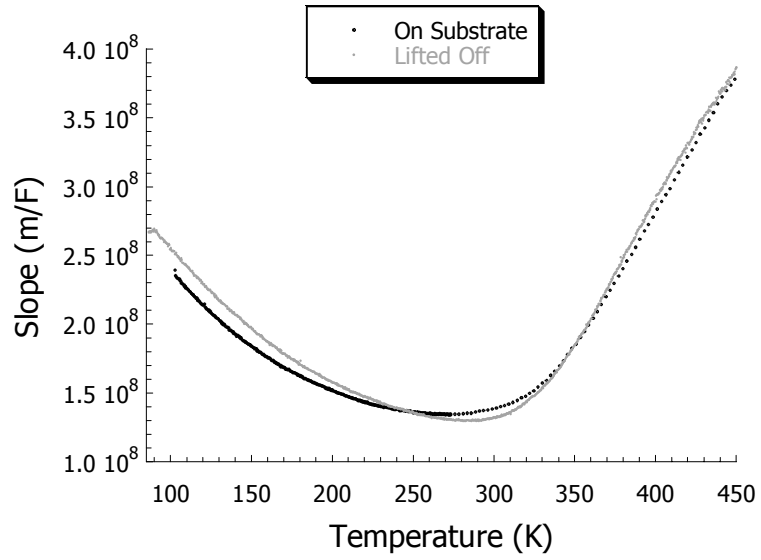


Figure 3.37: Slopes calculated from the dead layer treatment as a function of temperature.

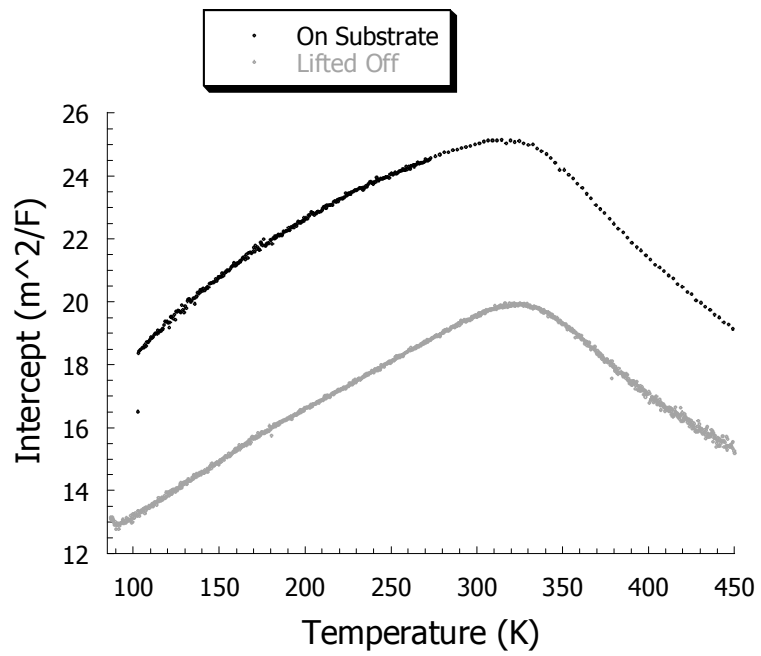


Figure 3.38: Intercepts calculated from the dead layer treatment as a function of temperature.

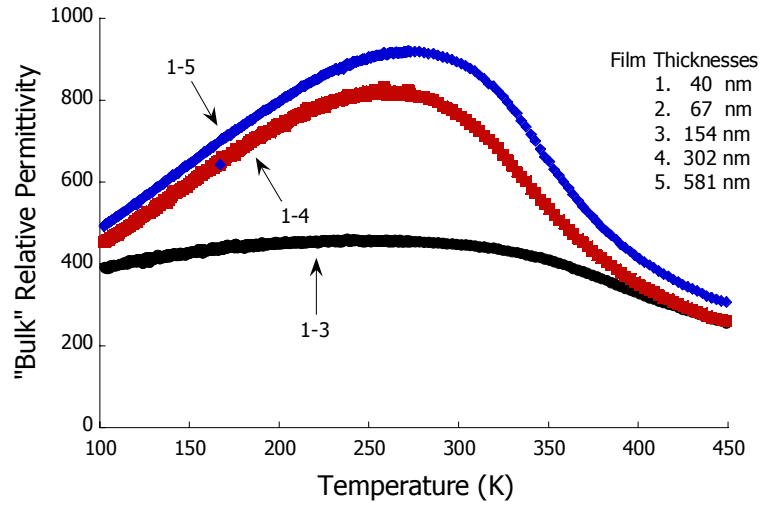


Figure 3.39: "Bulk" relative permittivities calculated from the dead layer treatment.

The dead layer model also predicts that the presence of the dead layer will affect the Curie-Weiss temperature, but not the Curie constant[14]. Discussed in more detail previously, the Curie-Weiss equation is given as

$$\frac{1}{\epsilon(T)} = \frac{(T - T_c)}{C'}$$

Curie-Weiss plots were constructed for both the on substrate and lifted off data, shown in Figure 3.40 and Figure 3.41, respectively. The dead layer model predicts the following relationship between the Curie temperature and film thickness

$$T_c^{eff} = T_c - \frac{2\delta}{d\epsilon_0} T_1$$

where  $T_c$  is the bulk Curie temperature,  $T_1$  is a model parameter  $\delta$  is the dead layer thickness,  $d$  is the film thickness, and  $\epsilon_0$  is the dead layer permittivity. Lines were fit to Curie temperature versus inverse film thickness and the agreement is good, as can be seen in Figure 3.42.

However, the dead layer theory predicts that with decreasing thickness, only  $T_c$  will shift,  $C'$  will remain constant. It specifically predicts that any change in the Curie

constant as a function of temperature is extraneous to the theory. The change in Curie constant with temperature is shown in Figure 3.43. Also shown in Figure 3.43 are the Curie temperatures. The trend as a function of thickness is similar in form. While the relationship between the Curie-Weiss temperature and film thickness is a predictive success, the similarity between the Curie temperature and constant suggest a common origin and is a difficulty that is unexplained.

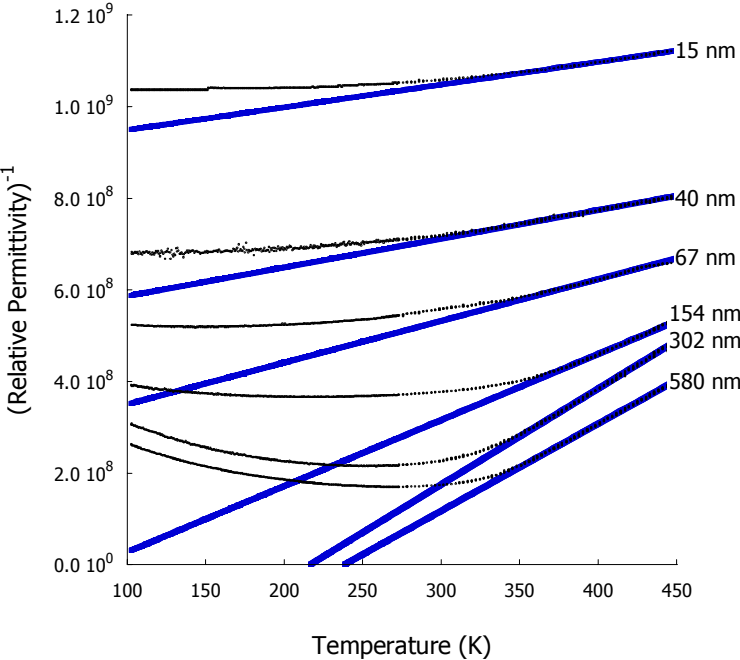


Figure 3.40: Curie-Weiss plot of inverse permittivity as a function of temperature, for various thicknesses, BST films on the substrate.

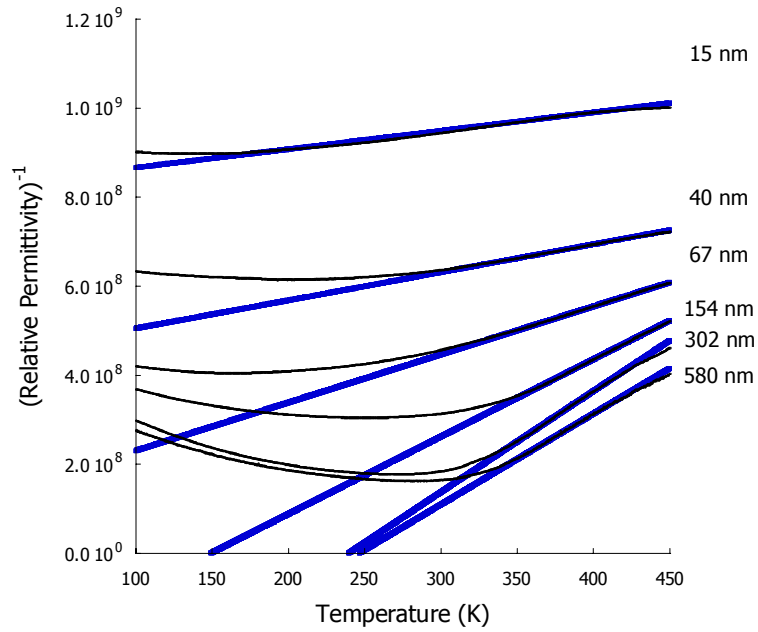


Figure 3.41: Curie-Weiss plot of inverse permittivity as a function of temperature, for various thicknesses, BST films lifted off the substrate.

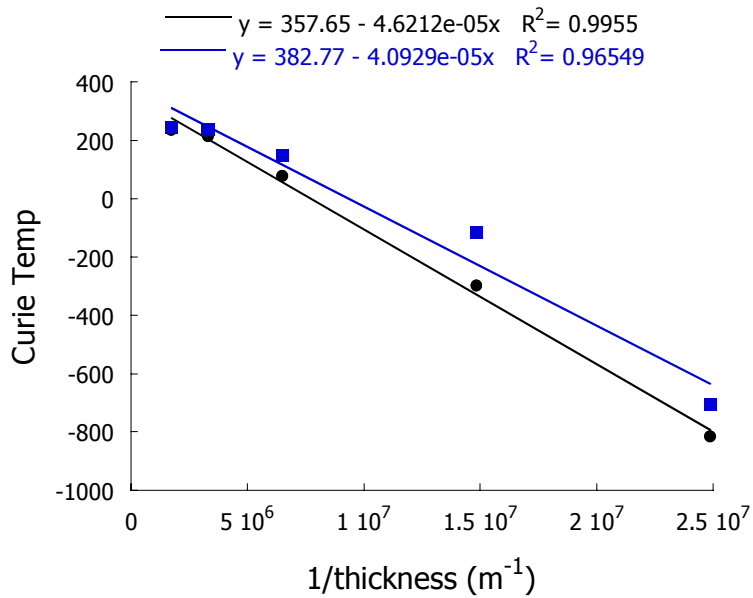


Figure 3.42: Curie temperatures from the Curie-Weiss plots shown in Figure 3.40 and Figure 3.41, as a function of inverse thickness.

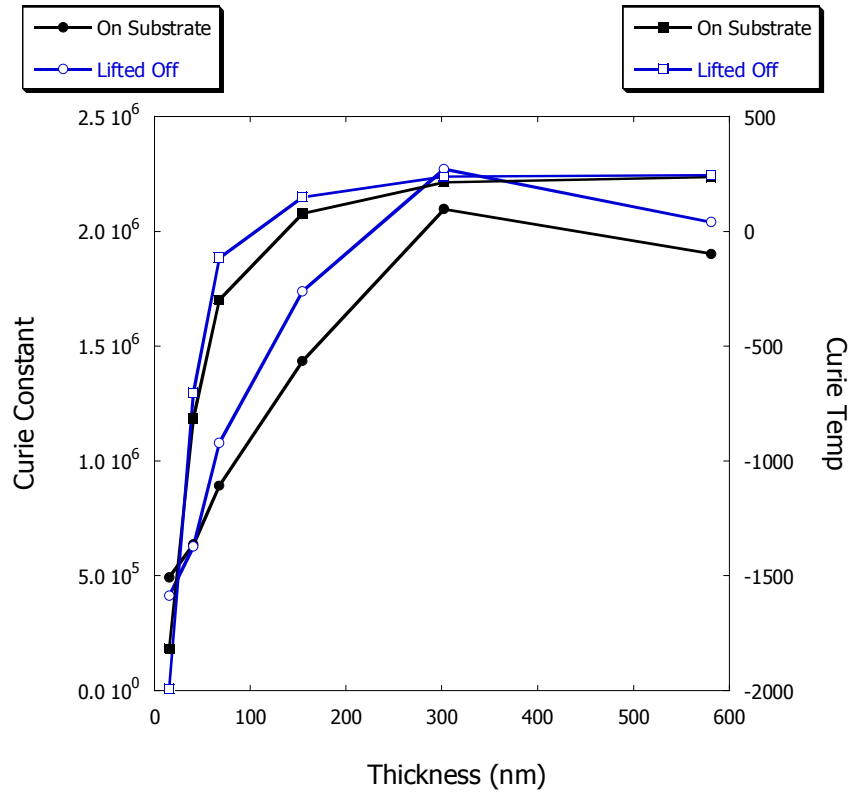


Figure 3.43: Curie constants and temperatures from the Curie-Weiss plots shown in Figure 3.40 and Figure 3.41, as a function of thickness.

The conclusion drawn from the calculated “bulk” permittivities, the variation of the interfacial capacitance, and the form of the Curie constant as a function of thickness is that ferroelectric thin films cannot be represented as nonferroelectric surfaces with a ferroelectric bulk. The dead layer plot, which seems reasonable upon first consideration, is obviously nonphysical upon further investigation. The permittivity-temperature data is shown in part a of Figure 3.44. The dead layer plot chooses a single temperature, indicated by a vertical line. But the different film thicknesses are different distances from the transition temperature. Moreover, different film thicknesses can be thought of a different dielectrics. The phase transition is the important characteristic of a ferroelectric and the transition changes as a function of thickness. Part b of Figure 3.44 shows a schematic of the required permittivity-thickness-temperature data for the dead layer model to be appropriate.

It should be emphasized that the difficulty of the dead layer model is only apparent when the dielectric response is examined as a function of temperature. Otherwise the differences in the transitions are not seen.

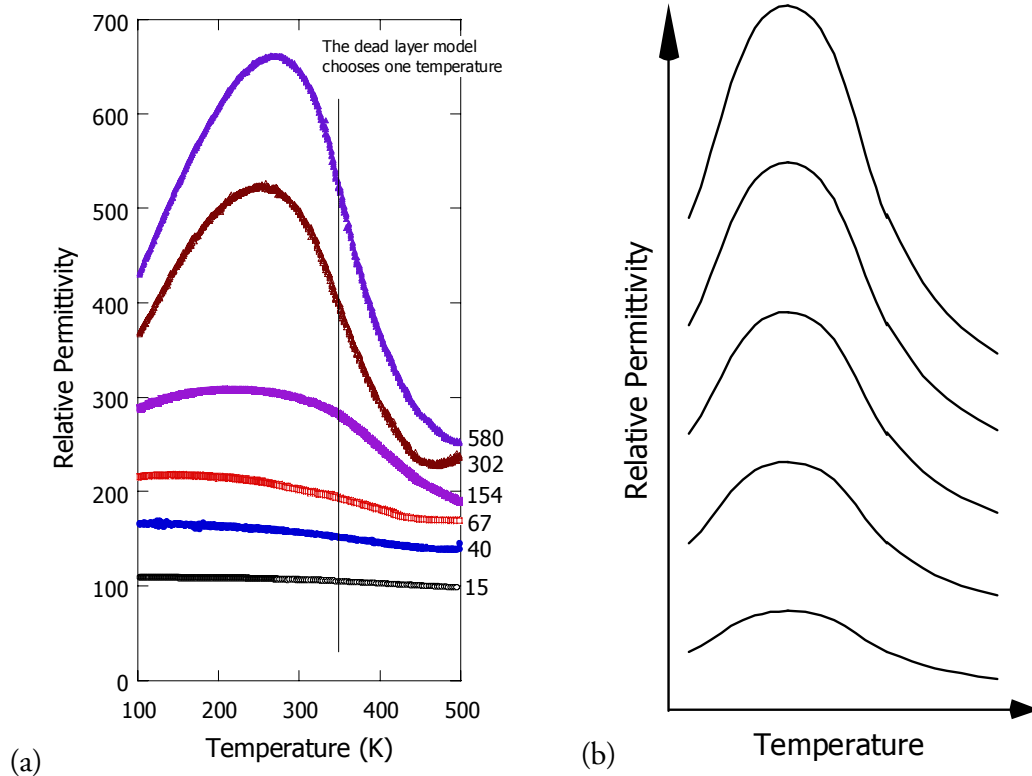


Figure 3.44: The dead layer plot chooses one temperature for the analysis, as shown in part a with the measured permittivities. But the curves would require the form in part b for the analysis to yield the proffered interpretation.

### 3.3: Modeling Thickness Dependant Properties With the Scaling Laws

A second common approach to modeling crystal size effects in many systems, including ferroelectric systems, is based on scaling laws. These approaches are applied to the current data set, assess the appropriateness of fit, and the appropriateness of associated physical phenomena.

Following the concepts of finite size scaling as applied to ferroelectric crystals, the primary outcomes are predicted with decreasing physical dimension.

- Permittivity should decrease.
- The temperature of the ferroelectric/paraelectric phase transition should decrease.
- The character of the transition should change from ideal second order at infinite size to infinitely diffuse in the limit.

The equation used to quantify the broadening or rounding of thermodynamic property anomalies should following this form

$$\Delta T_{rounding} \propto N^{\frac{-\theta}{D}}$$

where  $\theta$  is the rounding exponent,  $D$  is the dimensionality of the system, and  $N$  is the number of units cells. The equation used to quantify the  $\Delta T_{rounding}$  of the the phase transition was suggested by Uchino and Namura for relaxor ferroelectrics, as discussed above, and is given as

$$\frac{1}{\varepsilon} = \frac{1}{\varepsilon_{Max}} + \frac{(T - T_{Max})}{2\varepsilon_{Max}\delta^2}$$

where  $T$  is temperature,  $\varepsilon$  is permittivity and  $\delta$  is the diffuseness[67].

The shift in  $T_c$ , with decreasing crystal dimension, follows the equation

$$T_c(N) - T_c(\infty) \approx N^{\frac{-\gamma}{D}}$$

where  $\gamma$  is the shift exponent. Finally, the reduction in the magnitude of the properties, such as maximum permittivity, follows

$$K_{Max} = L^{\frac{\nu}{D}}$$

where  $\gamma$  is the dielectric constant critical exponent,  $\nu$  is the correlation length critical exponent, and  $L$  is the linear dimension of crystal, typically in unit cells[12].

Using these three functions, the fit of the scaling model to the experimental data set can be assessed. For each film thickness, broadening, transition temperature, and maximum permittivity were either measured or calculated. The thickness dependence of these data were compared to the predictions of scaling theory. The plots do show the correct relationships, but the *gestalt* of the data is not obvious. Following each of the three plots are more accessible plots of the data.

Figure 3.45 and Figure 3.46 show the diffuseness coefficients plotted as a function of film thickness on logarithmic and linear scales, respectively. Data for the film lifted from the substrate is also included. The logarithmic plot clearly shows a power-law dependence that is predicted by scaling theory. The effect of lifting the sample off the substrate was to decrease the diffuseness by a small amount. It is not clearly known why release from the substrate should change the diffuseness of the transition. The lifted off

films are strain relieved and while strain can affect the transition temperature, in only a few special circumstances is strain predicted to affect the diffuseness[58]. In any case, the degree to which the diffuseness is affected by strain release is negligible compared to the diffuseness of both cases compared to that of a standard ceramic sample.

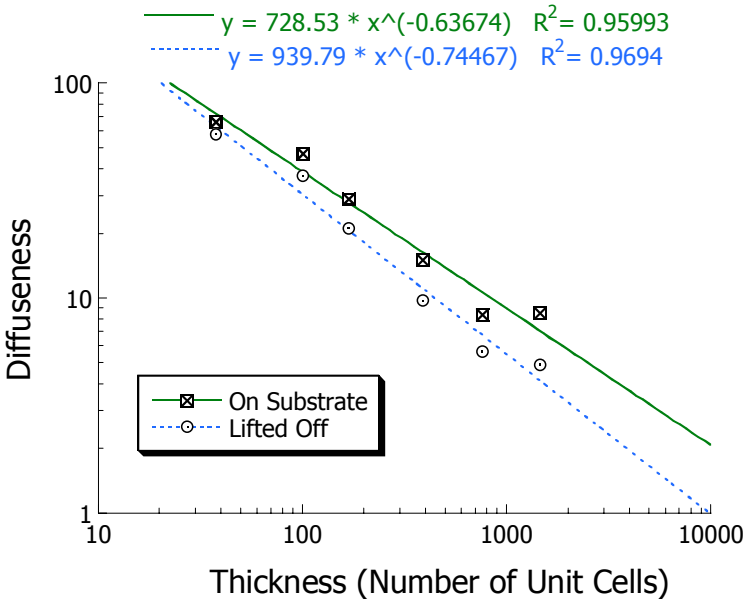


Figure 3.45: Log-log plot of transition diffuseness as a function of thicknesses, given in number of unit cells.

The diffuseness data are plotted on a linear scale in Figure 3.46. Thinner films have a more diffuse transition until at zero thickness the transition is infinitely diffuse.

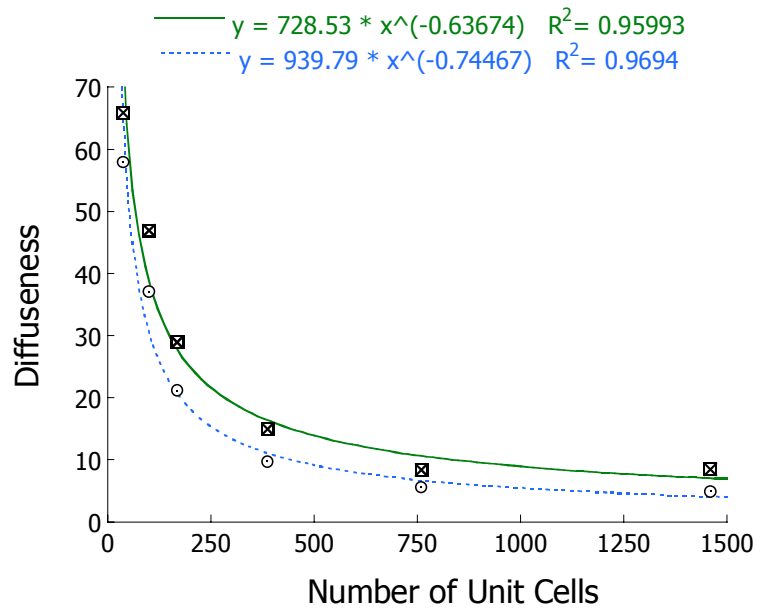


Figure 3.46: Transition diffuseness as a function of thicknesses, given in number of unit cells.

The maximum relative permittivity is presented as a function of thickness in Figure 3.47 and Figure 3.48. The permittivity data plotted on a log-log scale shows the power-law relationship between permittivity and sample size predicted by finite size scaling. The effect of lifting the sample off the substrate was to increase the permittivity. The percentage increase was approximately the same across the film thicknesses, as indicated by the line of fits having a different intercept, but approximately the same slope.

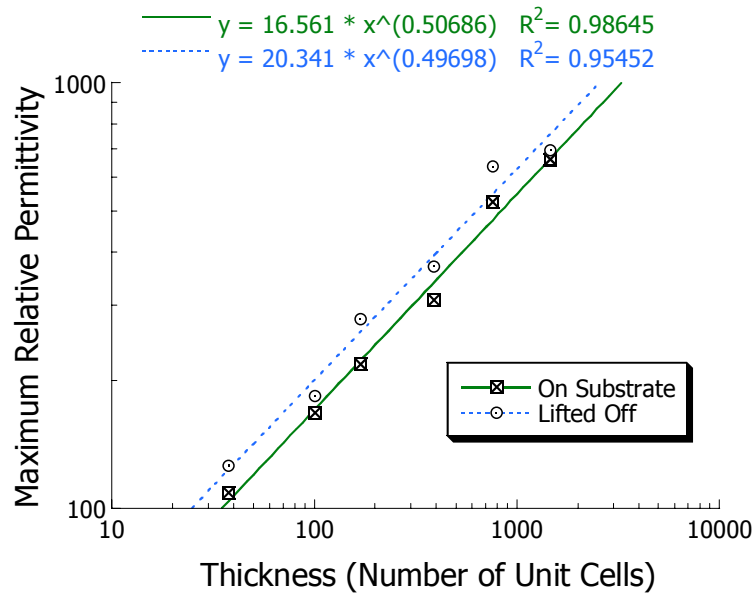


Figure 3.47: Log-log plot of maximum permittivity as a function of thicknesses, given in number of unit cells.

Figure 3.48 shows the peak permittivity data on a larger scale. Extrapolation to zero thickness is a potentially errant exercise, but the result confirms both Finite Size Scaling and the intuition about relative permittivity of an infinitely thin dielectric. The prediction is that thinner films have a lower permittivity peak, until at zero thickness, the relative permittivity is 1.

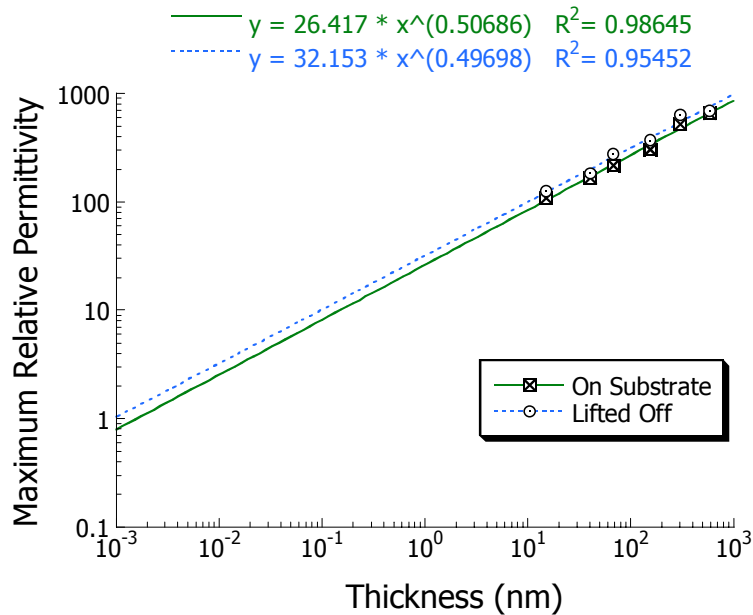


Figure 3.48: Log-log plot of maximum permittivity as a function of thicknesses, given in nm.

It is difficult to make predictions about the values of the power-law exponents. While the overall relationship is understood, the specifics of a system are more difficult to predict. Often the results of finite scaling theory are unmeasurable quantities, such as polarization profiles within materials. However, the final of the three predictions does have a predicted exponent. If the ratio of  $\Delta T_{\text{shift}}/T_{\text{bulk}}$  is plotted as a function of number of units cells, the slope of a power law fit should be  $-0.7$ [53]. This relationship was derived for ferromagnetic transitions, but should also hold for ferroelectric transitions. Figure 3.49 shows that the expected relationship is seen for both films on the substrate and lifted off the substrate. The exact predicted exponent is observed. The effect of lifting the films off the substrate is again a shift in the intercept, but not in the slope, of the fit.

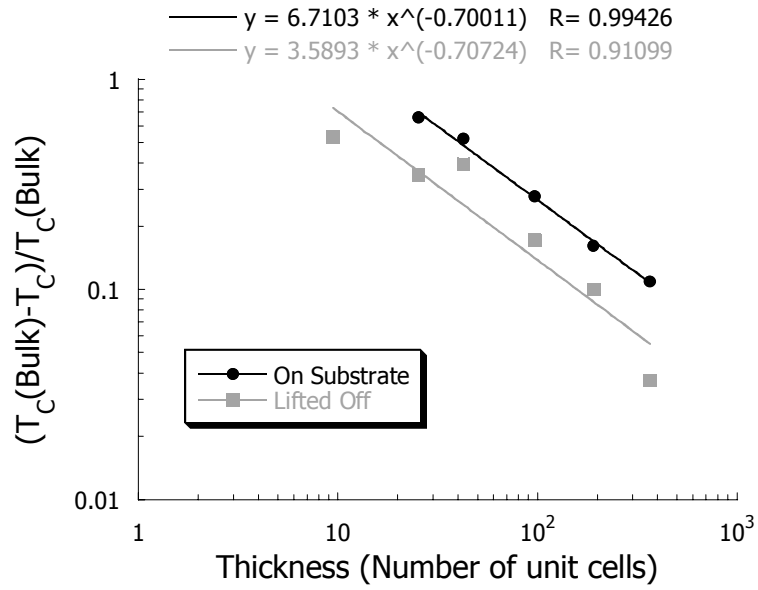


Figure 3.49: Log-log plot of transition temperature shift as a function of thicknesses, given in number of unit cells.

Figure 3.50 shows that the sense of the data is correct. Recall that the bulk transition temperature is about 300 K. Thinner films have a lower transition temperature, so the transition temperature shifts so that close to zero thickness, the transition temperature is 0 K.

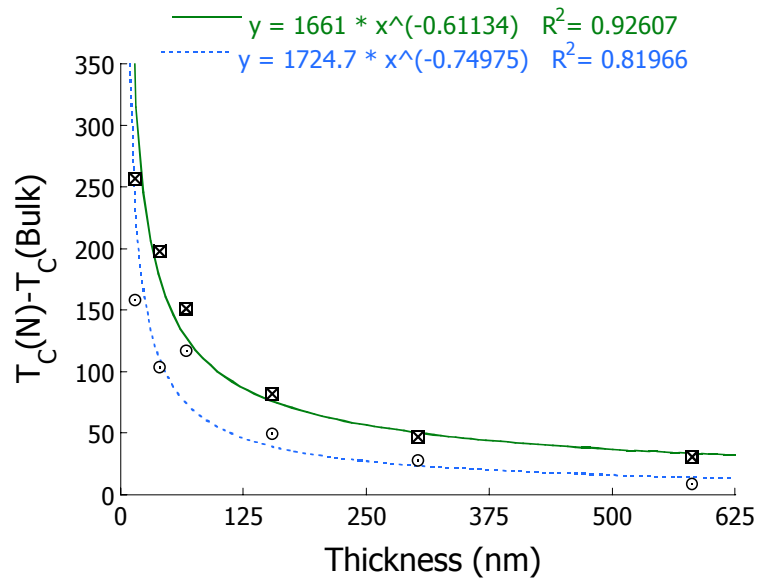
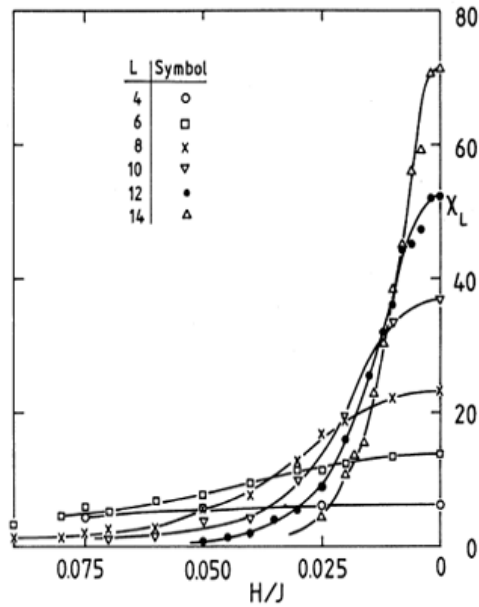


Figure 3.50: Transition temperature shift as a function of thicknesses, given in nm.

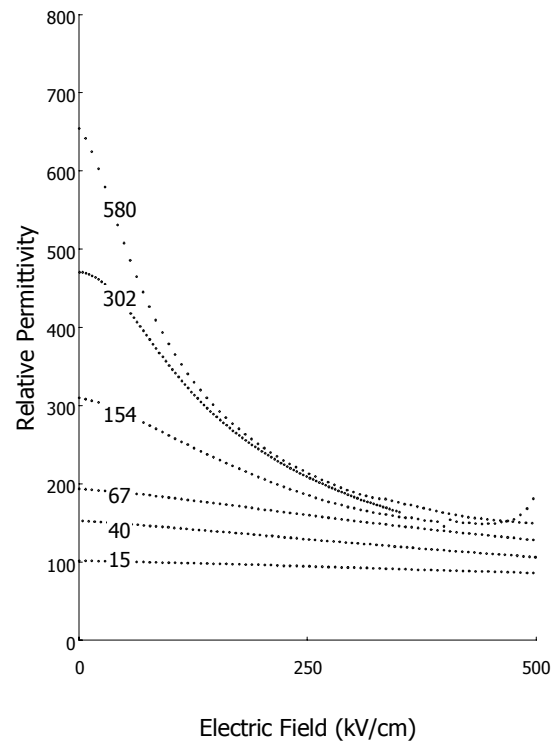
The final observation about finite size scaling is the behavior of susceptibility as a function of field. Susceptibility,  $\chi$ , be it magnetic or electric, is related to permittivity,  $\epsilon$ , by the following relation

$$\chi = \epsilon - 1$$

so for high  $\epsilon$  materials, they are practically indistinguishable. Figure 3.51 shows the similarity between the effect of thickness on the field dependence of the Ising model Binder and Hohenburg use to model ferromagnetics and the field dependence of the permittivity data presented in Figure 3.11. While the range of thicknesses is not the same, the overall form is quite similar. This resemblance is an example of how changes in sample dimension can affect dissimilar materials in a common way and how scaling theory can be used to explain properties observed in seemingly unrelated materials.



(a)



(b)

Figure 3.51: (a) Magnetic Susceptibility as a function of field for various thicknesses, given in number of unit cells, from Binder and Hohenburg[53] (b) Relative permittivity as a function of electric field for a number of thicknesses, given in nm.

## 3.4: Confounding Factors

The experimental and theoretical difficulties of size effects investigation were detailed in the literature review. The major considerations are depolarization fields in the ferroelectric, polarization screening in the electrode, strain, incomplete carrier depletion, domain patterns, and grain size. Strain was addressed previously.

### 3.4.1: Depolarization Fields in the Ferroelectric

The effect of depolarization fields is to reduce the polarization in the ferroelectric by creating a field in the opposite direction to the ferroelectric polarization near the sample interfaces. The dead layer theory does not account for the effects of depolarization fields, while finite size scaling does. The differences should be small, because of the sample configuration. The single grains are well compensated at the interface by the electrodes. More importantly, the materials are in the paraelectric state, so there is no ferroelectric polarization to compensate. Depolarization fields are a more significant difficulty for ceramic ferroelectrics, or ferroelectric particles in a non-conducting matrix.

### 3.4.2: Electrode Effects

#### *3.4.2.1: Polarization Screening in the Electrode*

The possibility was raised by Black *et al.* that the polarization screening length might be important to film properties. Central to the argument was that metal electrodes have a much lower static dielectric constant than perovskite electrodes and that the screening length should be correspondingly much longer in the metal electrodes. The

data used in the paper for SRO were assumed, so the results were not useful for evaluating the argument. To estimate the order of the effect, better numbers for SRO were used.

From Kittel[59], as discussed previously, recall that

$$\frac{1}{k_s} = \text{Thomas Fermi Screening Length}$$

and

$$k_s^2 = \frac{6\pi z n_0 e^2}{\mathcal{E}_F}$$

where  $z$  is the valency,  $n_0$  is the carrier concentration,  $e^2$  is the charge on the electron, and  $\mathcal{E}_F$  is the Fermi energy. This means that the screening length is proportional to

$$\sqrt{\frac{\mathcal{E}_F}{n_0}}$$

Using literature values, Table 3.3 contains the necessary information to estimate the ratio upon which the screening length calculation is based. This ratio is  $9.6 \cdot 10^{-12}$  for Au and  $1.2 \cdot 10^{-11}$  for SrRuO<sub>3</sub>. The direction of the shift is the opposite of the Black estimate, suggesting that the overall effect of depolarization fields is not consistent with the Black model.

Table 3.3: Material parameters for Au and SrRuO<sub>3</sub> used in the calculation of the Thomas-Fermi screening length.

Material	Au[59]	SrRuO <sub>3</sub>
Valence	1	1[170]
Carrier Density (#/cm <sup>3</sup> )	$5.9 \cdot 10^{22}$	$1.72 \cdot 10^{22}$ [170]
Fermi energy (eV)	5.51	2.2-2.5[171]
Ratio	$9.6 \cdot 10^{-12}$	$1.2 \cdot 10^{-11}$

The other main approach was taken by Batra, Wurfel, and Silverman[23-26]. Their calculations suggest that the effects of finite screening length in metal electrodes will

be small until films are less than 4 nm. Thus the effects of polarization screening, although not zero, are small enough to be neglected for the purposes of this study.

#### *3.4.2.2: Perovskite electrodes.*

It has been suggested that ferroelectrics with perovskite electrodes have larger permittivities than those on metal electrodes. Unfortunately, a pure comparison of different top electrodes is not available in the literature. The films would have to be grown on the same substrate, with the same bottom electrodes, by the same process. The different top electrodes would then need to be deposited, being careful that the ferroelectric is exposed to the same conditions.

It has been argued that the reason for the difference is that the polarization is somehow “frozen” on the ferroelectric/electrode interface[75, 76, 79, 80]. This is unlikely. Polarization can be communicated in two ways. The first is the charge generated by the ferroelectric polarization. Electrostatic charge is not frozen on the electrode, but is screened by the electrode. This reasoning was addressed in the previous section and is not significant.

The second way is by the soft mode. It is the case that the soft mode is altered near the interface, as there is no longer translational invariance. Since the soft mode is related to the crystallographic structure, perovskite electrodes should allow a larger dielectric constant, if it is assumed that the lattice vibrations can extend into the electrode. However, the soft mode frequency of a ferroelectric decreases as the transition temperature is approached, as can be seen from Figure 3.52[20]. Non-ferroelectric perovskites, such as  $\text{SrRuO}_3$ , do not experience a strong variation in phonon mode with temperature. Thus, if coupling to the soft mode occurred, at some temperature, the soft mode frequency would

correspond to the lowest phonon mode in the electrode and the dielectric constant would increase dramatically. This is not seen.

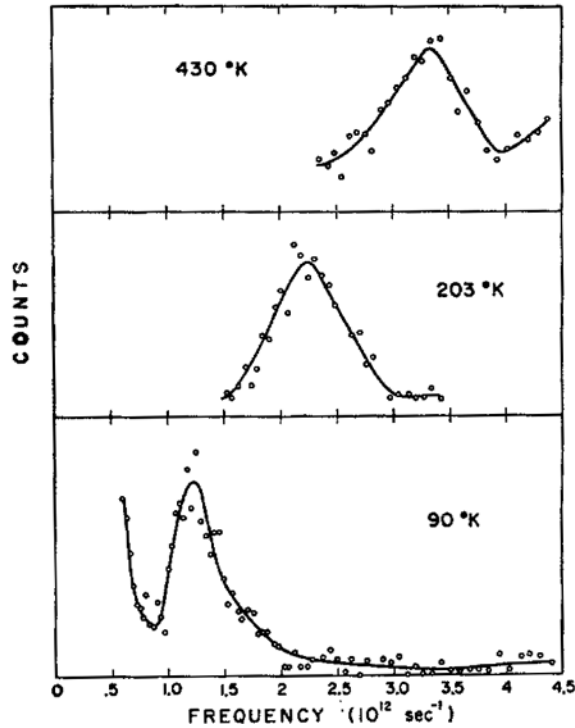


Figure 3.52: Variation of the soft mode in SrTiO<sub>3</sub> for various temperatures, from Cowley[20].

Nevertheless, there is some evidence that materials with perovskite electrodes have properties more similar to bulk crystals. There are several possible origins of the difference. One possibility is that perovskites such as SrRuO<sub>3</sub> are almost ideal growth surfaces. Xi *et al.* examined the effect of various perovskites growth surfaces on the properties of SrTiO<sub>3</sub>. Films of YBCO, GBCO, SmBCO, Y<sub>0.3</sub>P<sub>0.6</sub>BCO, and SRO were deposited on LaAlO<sub>3</sub> substrates. Top electrodes of gold were deposited by thermal evaporation. To the extent that atomic registry was the isolated control variable, which is difficult at best, it was found that the differences in lattice matching do not have a strong effect on the permittivity, loss tangent, or temperature of maximum permittivity, excepting the film with an SRO growth surface, which displayed a low loss tangent,

0.0016. Also, different materials certainly have different phonon mode frequencies, which is further evidence against the soft mode matching argument[172].

### 3.4.3: Ferroelectric not Fully Depleted

A study of photoemission spectroscopy on BST indicates that the depletion induced by the Schottky barrier is on the order of 70 nm, so for films less than 140 nm, the films are completely depleted. However, the consequences of incomplete depletion are not clear. The incomplete depletion does not have a tremendous effect on the dielectric response in this case, as the polynomial fit to permittivity indicates in the next section.

### 3.4.4: Domain Patterns

The effects of domain patterns are not clear in this study. The difficulty in this regard stems from the inability to observe ferroelectric switching. The origin of this effect is not understood, but some speculations regarding likely possibilities can be made. One possible origin is the growth of the film itself. The fiber-textured growth may result in a defect or composition distribution in the film that creates a preferred direction for the polarization. This may be the origin of the frustrated transition seen in BST. There are two pieces of evidence for the frustrated transition. The first is the lack of switching in the low temperature C-V curves in Figure 3.17. The second is that the phase diagram in Figure 1.26 shows that there should be an in-plane phase transition due to the strain, calculated by Streiffer *et al.* to be at about 380 K[8]. However, examination of this permittivity-temperature data shows no such transition. In neither case is switching seen. Domain walls separate regions with different polarization vectors, so there may be no

domain walls, or more likely, there are no switchable domain walls. In this data set, little is known regarding the presence or specific behavior of ferroelectric domains. However, what evidence exists suggests that thickness does not play a prominent role in what influences domain formation or behavior.

#### 3.4.5: Grain Size

The effects of grain size can be neglected for the purposes of this study because the grains are strongly columnar. An increase in film thickness does not result in a significant increase in column diameter, but rather in a heightening of the column, which makes the comparison of grain size more straightforward. This study is different from the investigation of Frey and Payne[91] on BaTiO<sub>3</sub>. The grain size required modeling and the microstructure required careful characterization, to account for twinning. These difficulties are not present in the for the BST films studied, again because of the relatively straightforward microstructure.

### 3.5: Polynomial Fit of Permittivity

The polynomial fit of permittivity arose out of two needs, the first was to compare the films grown with two slightly different processes and the second was to make quantification of the dielectric response more accessible. Two thickness series were compared, the first series was used in this study and is shown in Figure 3.53. The second series was deposited through the U.S. DRAM consortium, and is given in Figure 3.54.

The permittivity-field data was fit to the following equation

$$E = \beta_0 + \beta_1 P + \beta_2 P^3 + \beta_3 P^5$$

where  $E$  is the electric field,  $P$  is the permittivity and the  $\beta$ s are the fitting coefficients. The fits were good, which is to be expected, as a relatively large number of terms are used to model a smooth curve. The fits are shown as the solid lines in Figure 3.53 and Figure 3.54.

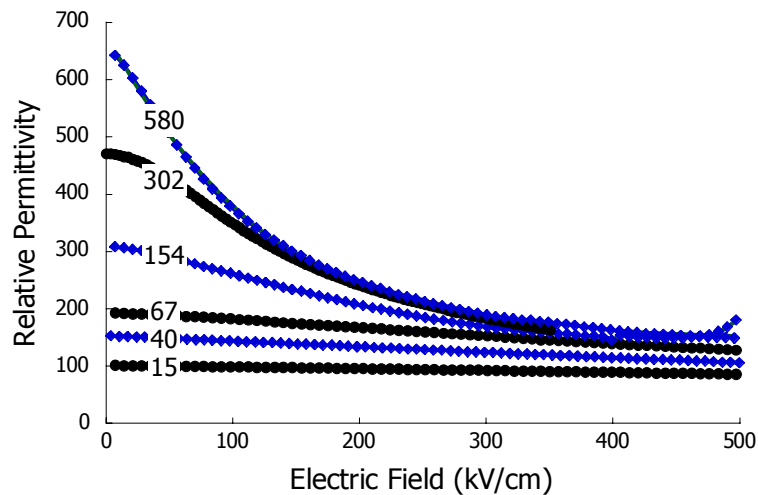


Figure 3.53: The relative permittivity as a function of electric field for various BST films, from the US DRAM consortium, used in this study; thicknesses given in nm.

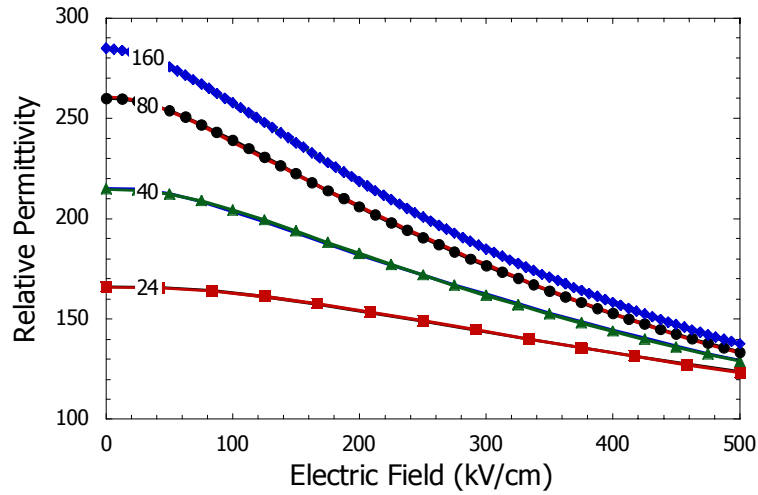


Figure 3.54: The relative permittivity as a function of electric field for various BST films; thicknesses given in nm.

The three main fits of data of this form are  $1/x$ ,  $\ln(x)$ , and  $x^\beta$ . All three fits are shown in Figure 3.55. The power law fit is the best in every case, as seen in Table 3.4. All four parameters are shown in Figure 3.55 to Figure 3.58. The fits yield one curve for each parameter as a function of thickness, indicating that the sets of films are very similar in their room temperature behavior. More significantly, the power law nature of the fits suggests that scaling is responsible for the thickness effects in all cases.

The remarkable consistency of the parameters as a function of thickness can be used as a test for theories of size effects. If the behavior does not explain the dielectric response over a wide range of thicknesses, then it is incomplete. For instance, the incomplete depletion of the films would be expected to affect films of greater than 140 nm thickness, but there is no kink in the curve that indicates that the behavior is changing. Likewise, if the dead layer model were correct, the parameters would fit a  $1/x$  relationship, as series of capacitors add in inverse. No such relationship is seen.

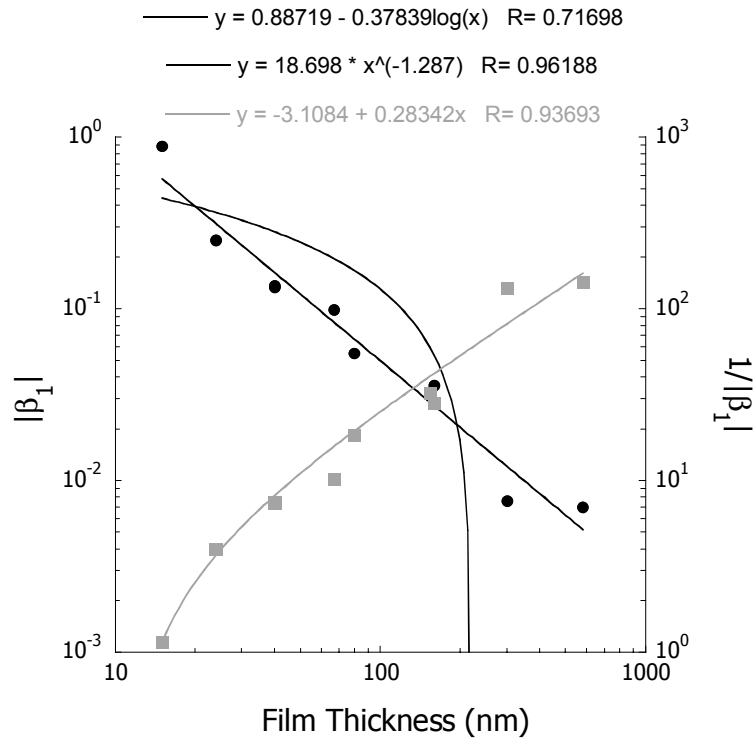


Figure 3.55: Linear terms of polynomial fit to electric field-permittivity curves, as a function of thickness.

Table 3.4:  $R^2$  values for the fitting parameters.

Parameter	$1/x$	$\ln(x)$	$x^\beta$
$\beta_0$	0.780	0.798	0.937
$\beta_1$	.878	.0515	0.926
$\beta_2$	.0970	0.610	0.971
$\beta_3$	0.928	0.315	0.966

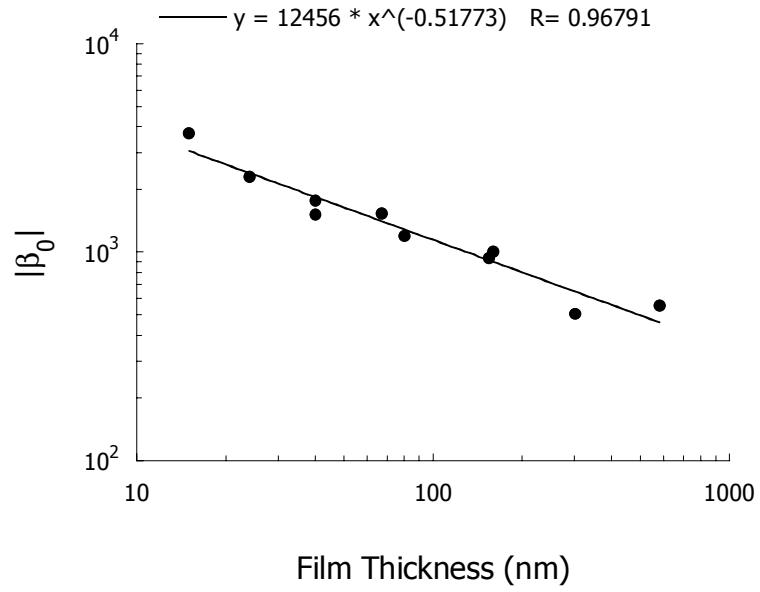


Figure 3.56: Mean terms of polynomial fit to electric field-permittivity curves, as a function of thickness.

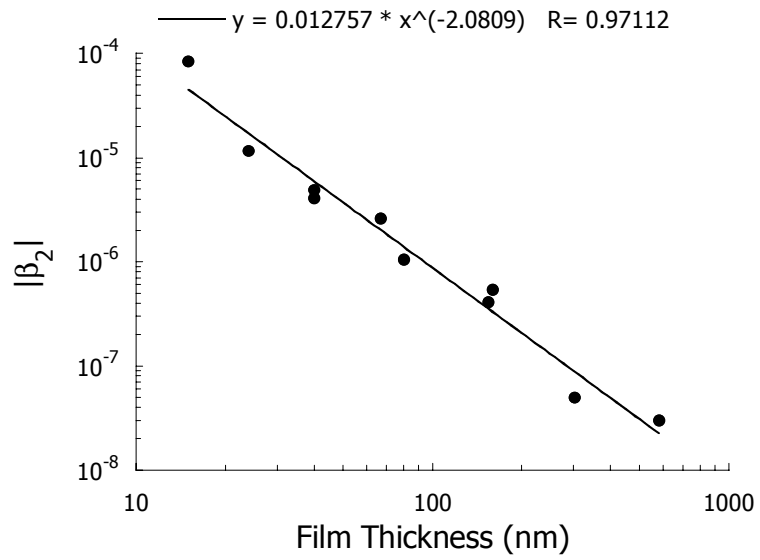


Figure 3.57: Quadratic terms of polynomial fit to electric field-permittivity curves, as a function of thickness.

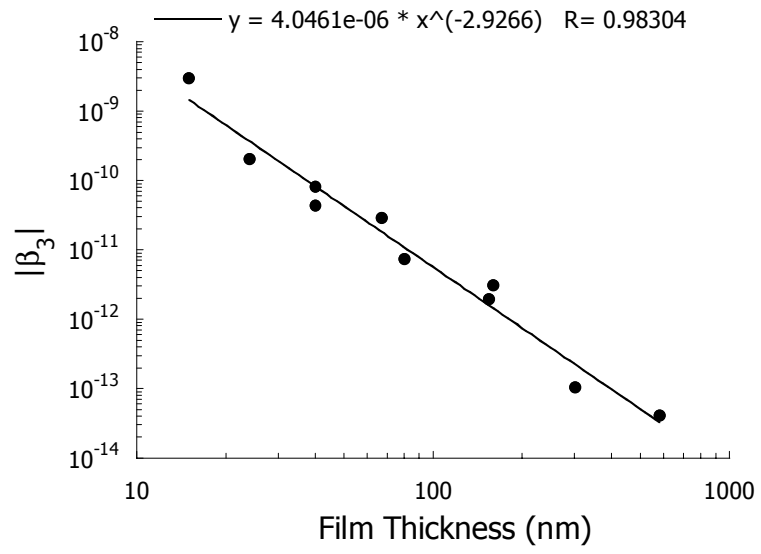


Figure 3.58: Third-order terms of polynomial fit to electric field-permittivity curves, as a function of thickness.

### 3.6: Summary of Size Effects Models

Two models were evaluated, the dead layer model and the finite size scaling model. The models are similar in many ways. Both predict that  $T_0$  will decrease as a function of film thickness. Both predict that the permittivity will decrease near the surface of the film. The permittivity versus thickness at a given temperature has a similar form. Both approaches start with a lattice of points with a vibrational frequency and a long-range interaction; the dead layer model uses the Thomas theory and the finite size scaling model uses the 3D Ising model. These model Hamiltonians are then manipulated to make them compatible with the LGD formalism. The size effects are largely corrections to the LGD model.

The dead layer model has several successes. It explains the approximately linear relationship between inverse capacitance density and thickness. It models correctly the observed shift in Curie temperature. The approximately linear relationship between the first term of the LGD model is observed. Finally, the fundamental physical insight is correct: the soft mode does change near the interface, if for no other reason than the break in translational invariance caused by the interface.

But there are many failures as well. First, the change in the Curie constant with temperature is not explained, but is of the same form as the shift in the Curie temperature. Second, the properties of the modeled interface layers are temperature dependent, *i.e.*, the dead layer is not dead. Third, the extracted “bulk film” properties are dependant upon the total film thickness, which should not be the case. Finally, it is concerning that a model specifically derived for ferroelectric films is weakest when the films are the most ferroelectric, as indicated by the  $R^2$  plot.

The reason that the dead layer model fails is that it must make strong assumptions in order to produce an analytically tractable equation. The permittivity profile is taken to be a step function at the dead layer/film interface, which is a simplification. The treatment makes the mean field assumption that the order parameter takes the average value throughout the film, when it is the case that the polarization drops near the surface. The result of this assumption is that the correlation length is constant as a function of temperature. The expansion of the correlation length is inseparable from the phase transformation itself. The behavior of the correlation length is likely why the model is progressively less accurate as the phase transition temperature is approached from either side.

Finite size scaling has several successes as well. The prediction of the shift in transition temperature, diffuseness, and maximum permittivity fit the power law treatment well. The correct form of the permittivity is given and instead of being a step function it is approximately exponential. The surface region is less ferroelectric, so it still can have a temperature dependence. The bulk value, *i.e.*, the value at the center of the film, is a function of thickness, which accounts better for the observed properties. Although the calculations were for magnetic materials, susceptibility versus field has the correct form. The theory accounts for the presence of depolarization fields and domain patterns.

In the finite size scaling model, the transition from the Hamiltonian to LGD form was done considering the theory of critical phenomena. This approach obviates many of the shortcomings of mean field theory. The correlation length diverges correctly as a function of temperature. This leads to the model providing the correct polarization profile as the transition temperature is approached; it is not less accurate near the transition temperature.

The failures of the finite size scaling model are largely related to its lack of specificity. While the correct relationships are predicted, the exponents of the model are rarely predicted. Only a few cases are solvable and many of those are uncertain. Additionally, they are difficult to measure. Few are experimentally accessible. Most of the supporting “data” is in the form of Monte Carlo trials, which have improved in the past decade, but are still short of being able to fully simulate macroscopic systems. The power law relationships that are the central idea of scaling theory are theoretically well-developed, but experimentally wanting.

It is the author’s opinion that the strongest argument for the finite size scaling theory is also the most inexact. The thinking is as follows.

Early in the investigation of ferroelectricity, it was generally believed that ferroelectricity was quite rare. The theories that were developed tended to be material-specific, such as the Slater theory of  $\text{BaTiO}_3$ , or the Valasek theory of KDP. Gradually, it was discovered that a wide range of materials displayed ferroelectric properties. The theories shifted to explaining ferroelectrics generally. At about the same time, Landau formulated a theory that describes second order and, to a lesser extent, first order phase transformations generally. All phase transformations could be more or less represented by the same set of equations.

Similarly, there are various descriptions of size effects in ferroelectrics: modifications of phenomenological theory; consideration of electrode effects, such as Black *et al.*; particle theories; and the dead layer. All theories provide some insight. Those theories designed for specific physical systems yield accurate, but limited, predictions. The attraction of finite size scaling is not that it captures the most minute detail, rather that critical phenomena describes, and describes well, not only ferroelectrics, but

ferromagnets, and superfluid He, and other systems that have nothing in common but the symmetry of their Hamiltonian. It provides a single answer to the question of why large systems behave differently than small ones.

### 3.7: Implications of Finite Size Scaling Model

The finite size scaling model was used to estimate the permittivity of BST. BST experiences Volmer-Weber growth, marked by the coalescence of nuclei. The thinnest continuous film of BST is approximately 4.5 nm[123]. The properties of this thickness of BST were estimated by the finite size scaling model and are listed in Table 3.5. It should be possible to engineer films that have an optimized strain condition, so both the “on substrate” and “lifted off” models were evaluated.

Table 3.5: Properties of 4.5 nm BST film based on finite size scaling extrapolation.

Property	On Substrate	Lifted Off
Maximum permittivity	56	68
Transition temperature	69	116
Diffuseness	156	154

These quantities were then used in the relaxor equation, given as

$$\frac{1}{\epsilon} = \frac{1}{\epsilon_{Max}} + \frac{(T - T_{Max})}{2\epsilon_{Max}\delta^2},$$

to model the temperature behavior. It was flat within experimental resolution and so is not shown. The room temperature permittivity was used to calculate the equivalent oxide thickness,

$$t_{eq} = t_x \frac{\epsilon_x}{\epsilon_{SiO_2}}$$

where  $t_x$  is the physical thickness of the BST,  $\epsilon_x$  the relative permittivity, and  $\epsilon_{SiO_2}$  is 3.9.  $t_{eq}$  for the “on substrate” film is 0.31 nm and for the “lifted off” film is 0.26.

The capacitance density was calculated as

$$\frac{C}{A} = \frac{\epsilon_0 \epsilon_r}{d}$$

where  $\epsilon_0$  is the permittivity of free space,  $\epsilon_r$  is the relative permittivity, and  $d$  is the film thickness. The value of the capacitance density for the “on substrate” film is  $111.4 \text{ fF}/\mu\text{m}^2$  and for the “lifted off” film is  $133.7 \text{ fF}/\mu\text{m}^2$ . The capacitance density data can be used to evaluate the applicability of BST for use as the dielectric in a DRAM capacitor. This analysis was adapted from an analysis of Summerfelt, also for BST[173].

Consider an  $8F^2$  cell with vertical sidewalls and rounded corners. The dimensions are shown in Figure 3.59. Assuming the requirement for  $30 \text{ fF}/\mu\text{m}^2$ , three different values for  $F$  were evaluated. The only parameter is cell height,  $H$ .

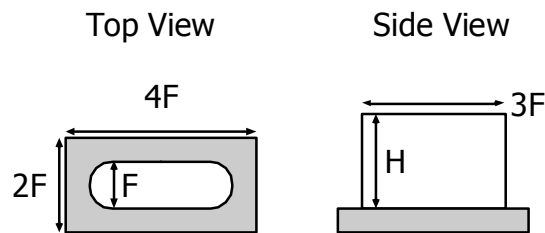


Figure 3.59: Schematic of a BST DRAM cell.

Figure 3.60 shows a plot of capacitance density versus cell height with the  $30 \text{ fF}$  curves, one for each  $F$ . The “on substrate” and “lifted off” films are indicated. Even for the  $0.25 \mu\text{m}$  generation, the capacitance density of the “lifted off” film is insufficient for a planar capacitor, i.e., a height of 0. BST provides acceptable capacitance density to the  $0.13 \mu\text{m}$  generation.

One of the benefits of BST or other high- $k$  dielectric is the elimination of process steps. At the  $0.13 \mu\text{m}$  generation, the  $0.2 \mu\text{m}$  height requires an etch angle of  $80^\circ$  for the Pt bottom electrode. This is considered to be the upper limit of etch selectivity of Pt[173]. The required capacitance density for this criterion is  $117 \text{ fF}/\mu\text{m}^2$ . Neither film meets the required capacitance density, although the “lifted off” film is close.

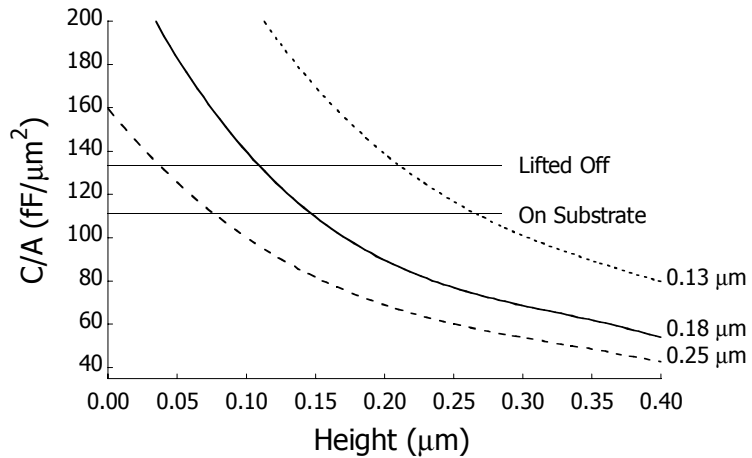


Figure 3.60: Curves of capacitance density versus DRAM cell height for various design rules, adapted from Summerfelt[173].

A second consideration is the spacing of the DRAM cells. A schematic of two cells is shown in Figure 3.61. Twice the thickness of the BST films plus the top electrode metallization must fit in the space between the capacitors. If the gap length is  $F$  and the Pt requires  $0.5F$ , then the maximum BST thickness is  $0.25F$ . For the  $0.25 \mu\text{m}$ ,  $0.18 \mu\text{m}$ , and  $0.13 \mu\text{m}$  generations the maximum is  $63 \text{ nm}$ ,  $45 \text{ nm}$ , and  $30 \text{ nm}$ , respectively. The BST is well within these thicknesses.

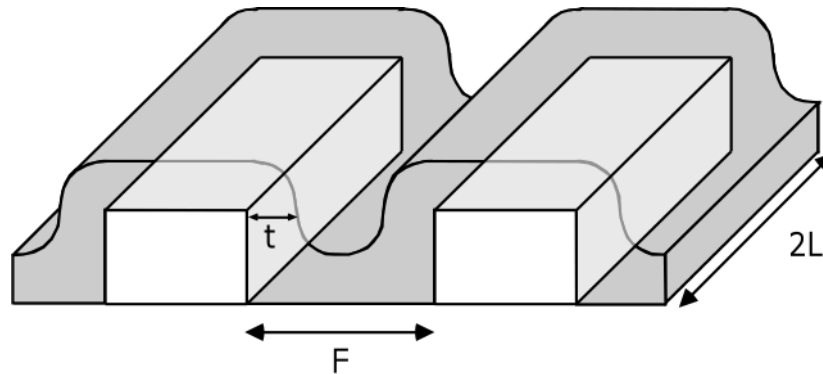


Figure 3.61: Schematic of conformal BST on Pt bottom electrodes showing geometric limitations of the plug type capacitor. Adapted from Summerfelt[173].

## 3.8: Conclusions

The dielectric response of a series of BST films with thicknesses from 15 to 580 nm was measured from 85 to 580 K. The thickness series was extensively characterized. Factors that might confound the analysis of the thickness effects were investigated. Processing effects were evaluated, including thermal mismatch strain, grain size and morphology, compositional control, and electrode material. Considerations specific to ferroelectric and high-k materials that were evaluated are depolarization fields in the ferroelectric, finite screening length in the electrode, electrode material, and ferroelectric domain structure. It was concluded that the resulting data are a good attempt at eliminating experimental artifacts and observing crystal size effects directly.

Many theories of size effects exist. A criteria that was used to refine the set of theories to be investigated is that a given theory must start with a statistical basis. The model Hamiltonian should be evaluated in the continuum limit and be expressed as a phenomenological theory that can be used to evaluate the experimental data. Two theories provide such an explanation, the dead layer theory and finite size scaling. The data was used to evaluate these two theories. It was found that finite size scaling fit the data more completely. The theory predicted the power law relationship between the following three quantities and film thickness: transition temperature shift, diffuseness of transition, and maximum permittivity.

The effect of strain was investigated by measuring the dielectric response as a function of temperature for the thickness series. This is the first direct measurement of strain in a thin film ferroelectric. The films were removed from the substrate and measured again as a function of temperature, thus relieving the thermal mismatch strain

imposed by the Si substrate. The out-of-plane strain was calculated to be 0.1%, regardless of film thickness. It was found that strain relief served to shift the transition temperature closer to the bulk value and increase the maximum permittivity, with the effect being greater for thinner films.

The empirical power law exponents were used to predict the properties of BST at the estimated ultimate thinness for a continuous film, 4.5 nm. The relative permittivity of the on-substrate film was 56 and the lifted-off film was 68. The required capacitance density for a capacitor using a 0.13  $\mu\text{m}$  design rule is 117  $\text{fF}/\mu\text{m}^2$ . The extrapolated capacitance densities for the on-substrate and lifted-off films are 111.4  $\text{fF}/\mu\text{m}^2$  and 133.7  $\text{fF}/\mu\text{m}^2$ , respectively. BST is suitable for the 0.13  $\mu\text{m}$  design rule, but only if the strain conditions are correct.

## Chapter 4: RELIABILITY

Investigations of reliability in BST and the end member of the solid solution, BaTiO<sub>3</sub> and SrTiO<sub>3</sub>, largely mainly examined the role and mechanism of resistance degradation on the predicted lifetime. These experiments have typically been carried out at higher temperatures and under DC electrical stress, as shown in quadrant I in Figure 4.1 [161] [144, 154, 155]. However, this condition is only a small subset of experimental space. Figure 4.1 shows the convention used in this work. High field is above the operating voltage of 1.6 V, or 3.2 V<sub>pp</sub> for AC stress. High temperature is above 80 °C. This work will extend the understanding of failure into quadrants II and IV, in order to make a better estimation of failure modes operating in quadrant III.

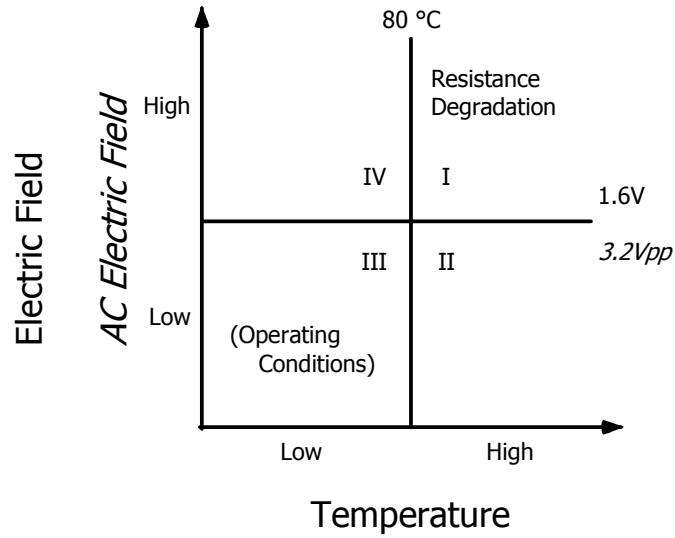


Figure 4.1: Most investigations of failure in BST have been conducted in quadrant I, where resistance degradation dominates. This dissertation will extend the investigation of failure to II and IV.

The main test parameters that may influence BST reliability are stress frequency, electric field, and temperature. Other experimental parameters include film composition, electrode material, film thickness, and processing conditions. The ultimate objective of the reliability work is to find the dominant failure mode at operating conditions and characterize it. To do that, the failure framework must be determined. The framework is a map of what failure modes occur in each quadrant, the mechanistic origins, and a determination of the dominant mode in each quadrant.

The number of parameters greatly increases the data requirements of a comprehensive investigation, but would not lead to a concomitant increase in understanding of the overall failure framework. As discussed in the literature review, predicting reliability requires estimating failure distributions of competing failure modes. Estimating a distribution is resource consuming; it requires 25-100 observations from each failure mode at each combination of parameters, such as field, composition, film thickness, temperature, *etc.*

The approach taken is to minimize the parameter variation in order to get a clearer picture of the failure modes that are operative in each quadrant, rather than investigate the effect of film parameters on lifetime. Unless otherwise noted, the reliability measurements were made of capacitors with Pt electrodes. The top electrodes were 190  $\mu\text{m}$  in diameter. The BST film was 40 nm thick and the composition was 51 at.% Ti. The DC voltage was +5 V (1250 kV/cm), applied at 25 °C. AC measurements were made at 10  $V_{pp}$ .

The chapter has two main parts. The first, sections 4.1 through 4.5, seeks to extend the understanding of BST failure into the low temperature, high field regime and the high temperature, low field regime to determine the failure mode that is most likely to limit device lifetime. This part also to evaluate the effects of AC stress to determine whether the AC failure mechanisms differ from DC failure. The four main types of DC failure that are considered are time dependent dielectric breakdown (tddb), noisy breakdown, stress induced leakage current (SILC), and resistance degradation. The second part, section 4.6, extrapolates the dominant failure modes from quadrants I and IV to operating conditions and makes specific predictions about device lifetime.

## 4.1: Low Temperature, High Field DC Failure

A large number of low temperature, high field measurements were taken. Three DC failure modes were seen. Typical examples of the different types of failure are shown in Figure 4.2 through Figure 4.4. Figure 4.2 shows tddb failure, with a continuous decrease in current until failure occurs suddenly and irreversibly. This is the most common type of failure under these test conditions. It has the same form as tddb failure in  $\text{SiO}_2$ . Figure 4.3 starts as tddb, but instead of failure in a single step, there are a series of discharges that are progressively higher current and noisier as time proceeds. A similar phenomenon, called soft breakdown, has been observed in very thin  $\text{SiO}_2$ , where a series of small failures occur before tddb. However, in the case of  $\text{SiO}_2$ , the statistical distribution of soft breakdown is the same as hard breakdown, which may not be the case for BST. To prevent confusion with the  $\text{SiO}_2$  analogue, this failure mode will be called noisy breakdown. Early in the investigation of PZT, it was found that biasing the sample after top electrode deposition gave better leakage characteristics. The initial current was large and noisy initially and transitioned into steady-state leakage. This procedure gave way to a furnace anneal. There may be a relationship between the phenomena in PZT and BST. An example of this “voltage annealing” is given in Figure 4.32.

Finally, Figure 4.4 shows resistance degradation. It is plotted on a linear scale for comparison with the other failure modes instead of the log-log plots that are more common, to be comparable with the other two failure modes. Perhaps the best understood of the three failure modes, resistance degradation is a monotonic increase of the leakage current under a constant applied electric field over time. It is believed to be caused by the motion of oxygen vacancies toward the cathode. Resistance degradation has

been investigated as a function of composition, film thickness, temperature, and Ti%. It is most dominant in the high temperature, high field regime[144].

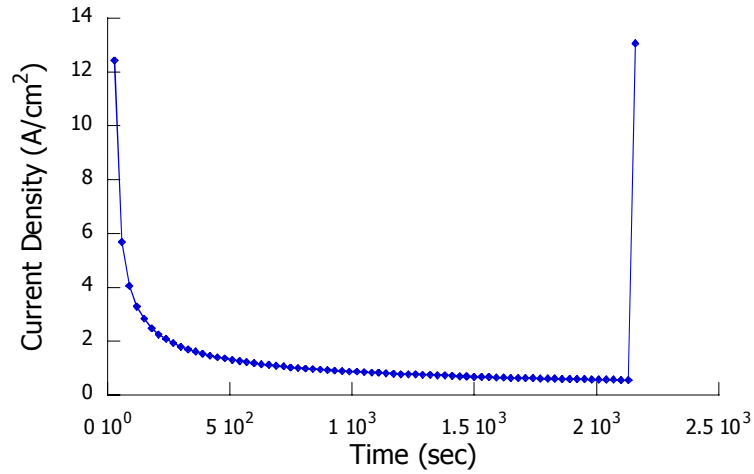


Figure 4.2: Typical tddb failure, shown for a 51% Ti, 40 nm BST sample stressed at 1250 kV/cm at 25 °C.

The relaxation current dominates at short times, followed by a sudden, catastrophic failure

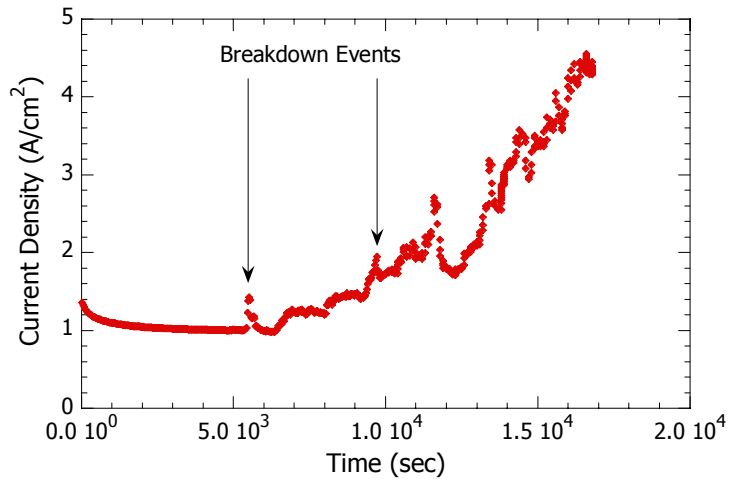


Figure 4.3: Typical noisy breakdown failure, shown for a 51% Ti, 40 nm BST sample stressed at 1250 kV/cm at 25 °C.

The relaxation current dominates at short times, followed by discharges, and failure in steps

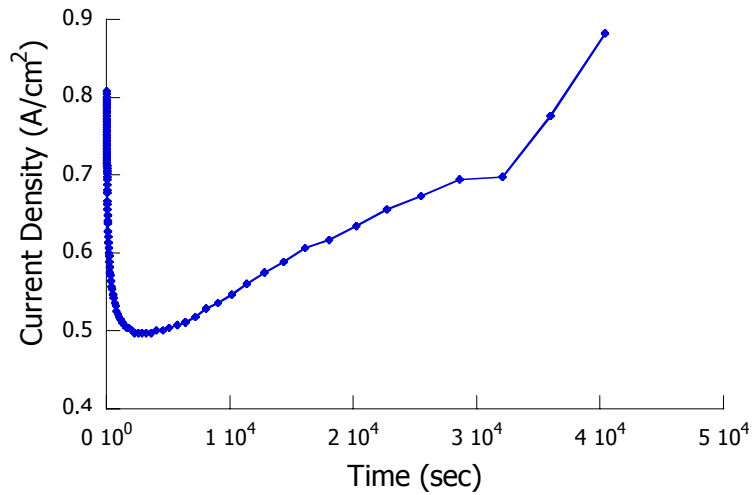


Figure 4.4: Typical resistance degradation failure, shown for a 51% Ti, 40 nm BST sample stressed at 1250 kV/cm at 25 °C.

The relaxation current dominates at short times, followed by a slow increase in leakage current

#### 4.1.1: Tddb and Noisy Breakdown

Tddb and noisy breakdown are the most common failure modes at low temperature, so they will be considered first. The resistance degradation that is seen at high temperature and high field can be modeled by least squares because it displays constant, lognormal variance in the underlying failure distribution. This is not the case for low temperature failure. The process is statistical in nature, with competing defects, each with its own distribution. In some cases, nonparametric (distributionless) tests were used to evaluate the effect of some experimental changes, to avoid the data requirements of estimating a distribution. To determine if tddb and noisy breakdown are two different failure modes, a Weibull plot was employed. It is important to distinguish failure modes and mechanisms. In SiO<sub>2</sub>, tddb and soft breakdown are caused by the same mechanism, i.e., by the same defect. However, the failure modes are different. Tddb fails in a single, catastrophic breakdown and soft breakdown fails in a series of steps.

Plotting the failure data on a Weibull plot is standard methodology for discerning separate failure modes. In Figure 4.5, the data are plotted as  $\log(-\log(\text{Surv}))$  versus logarithmic time. *Surv* is the same as 1-Cumulative percent failed. The plot groups together the tddb and noisy breakdown failures. There are clearly two failure distributions. Different failure distributions suggest different failure modes and perhaps different mechanisms. The tddb failures have a larger spread of the breakdown times and a shorter median  $t_{BD}$ . It is easier to see the difference in the distributions of failure times from the combined plot, but for completeness they are shown separated in Figure 4.6. The tddb failure to the left of the soft breakdown failures. The corresponding Weibull fits are shown in Table 4.1. The two Weibull parameters are  $\alpha$ , the time at which 63.2 percent have failed, and  $\beta$ , the slope of the line. The values confirm what was evident by inspection. The soft breakdown distribution has a larger  $\alpha$ , indicating a longer time to failure, and a larger  $\beta$ , indicating a tighter distribution of values.

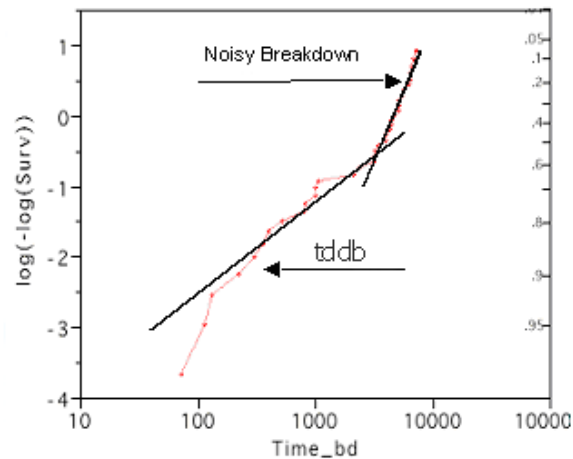


Figure 4.5: Weibull plot of tddb and noisy breakdown failures together for 51.0% Ti, 40nm, 1250 kV/cm DC stress.

The lines are a guide to the eye.

Table 4.1: Weibull parameter estimates for tddb and soft breakdown distributions

Failure Mode	$\alpha$	$\beta$
Noisy bd	8097.50	1.20637
tddb	1569.33	0.85887

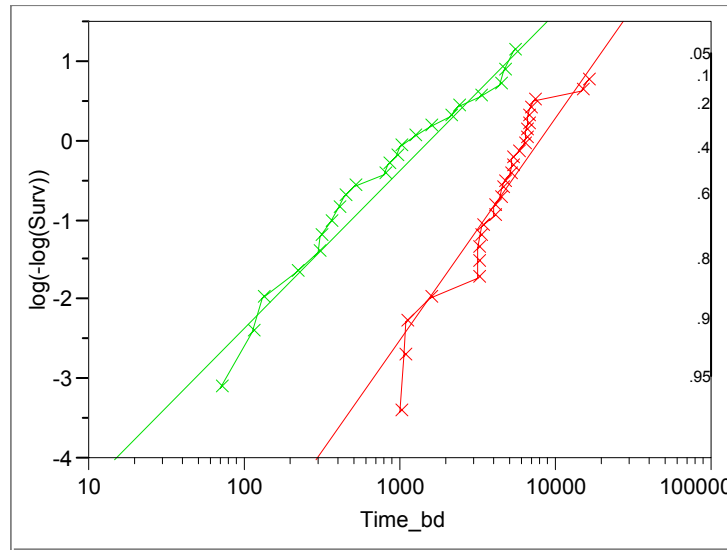


Figure 4.6: Weibull plots of tddb and noisy breakdown failures for 51.0% Ti, 40nm, 1250 kV/cm DC stress.

The leftmost curve is the tddb distribution and the rightmost the noisy breakdown distribution.

It is possible that the Weibull distribution is not the correct distribution, although it is the most likely and is widely used for microelectronic failure. Weibull plots are augmented by the appropriate nonparametric tests. The two used in this case are the Log-rank and Wilcoxon signed rank. The tests have slightly different emphases. The Log-Rank test places more weight on larger survival times and is best if the hazard function of the two groups is about the same. The Wilcoxon test places more weight on short survival times and can accommodate largely different hazard functions. The Prob>ChiSq column indicates the probability of obtaining by chance alone a Chi Square value greater than the one computed if the survival functions are the same for both distributions. The

result for this case is that both tests indicate that the distributions have a greater than a 99.99% chance of being different.

Table 4.2: Nonparametric tests for soft breakdown and tddb distributions

Test	ChiSquare	Prob>ChiSq
Log-Rank	23.8407	<.0001
Wilcoxon	28.0290	<.0001

Several sample sets, each with more than 30 failed capacitors, were examined by SEM, for evidence of catastrophic failure. Specifically, the top electrodes of capacitors that failed by noisy breakdown and by tddb were examined. The first image is shown in Figure 4.7. The dark circles seen in the image were common on the tddb capacitors, but were not seen on the noisy breakdown capacitors. It was not possible to exhaustively examine the soft breakdown top electrodes, but the available data suggests that the breakdown mechanisms are different. The dark circles appeared to be holes, as if some of the electrode is evaporated. Recall the percolation model for  $\text{SiO}_2$  has a failure region that spreads across the sample. It is possible that the multiple failure points are the result of a similar process in BST. As the failure spreads, the weak areas on the top electrode undergo some breakdown, possibly evaporation, resulting in the image in Figure 4.7.



Figure 4.7: Top electrode of a capacitor that failed from tddb. The areas of failure can be seen as dark circles in the image.

The next two images form a pair. The first, Figure 4.8, shows the scratch the probe made on the top electrode of a sample that underwent noisy breakdown. While the probe has scratched the top electrode, there is not a hole in the electrode near the probe scratch. This is in contrast to Figure 4.9, which underwent tddb failure. There is a similar scratch, but also near the point of contact is a hole in the electrode that is likely a result of tddb failure. Over 20 soft breakdown probe scratches were examined, none had the hole near the probe tip. About half of the tddb top electrodes did.

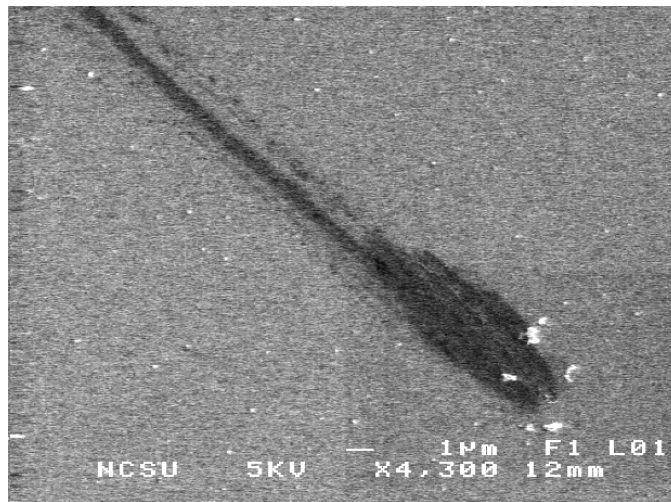


Figure 4.8: Scratch made by probe on the top electrode of a sample that failed from noisy breakdown.



Figure 4.9: Scratch made by probe on the top electrode and a nearby hole in the electrode of a sample that failed from tddb.

Occasionally, the point of failure on the top electrode is much more dramatic than a small dark circle. An example is shown in Figure 4.10. The top electrode was melted, with Pt splattered across the film surface.

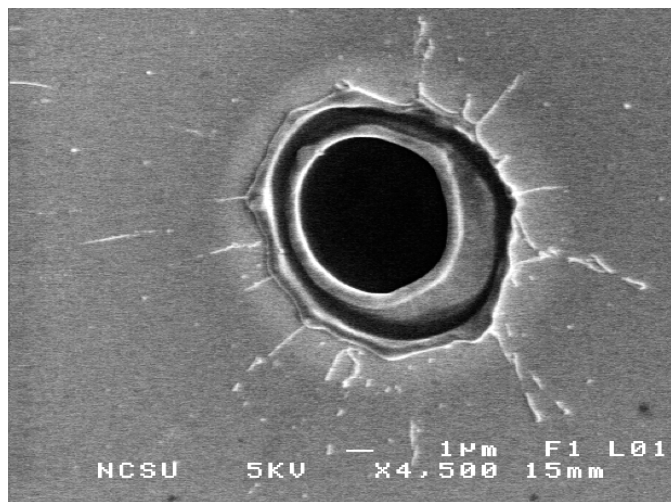


Figure 4.10: Top electrode of a capacitor that failed from tddb showing catastrophic failure.

It was hypothesized that tddb and noisy breakdown are caused by different mechanisms based on the SEM data. Noisy breakdown and tddb failures have different distributions and are thus different failure modes. It is desirable to see if different defects

are causing the failures. To do this, the area dependence of the failure modes was examined. Different area dependences suggest different mechanisms. Extrinsic, or processing, defects are assumed to be randomly scattered across the film. Thus, a larger capacitor would have a higher probability of having an extrinsic defect. Intrinsic defects are area independent. This possibility was investigated by testing 30 larger capacitors and comparing those measurements with the measurements made on smaller capacitors. The fraction of capacitors that fail from tddb almost doubles from a 190  $\mu\text{m}$  diameter to a 612  $\mu\text{m}$  diameter capacitor (an area ratio of 1:10.4), as can be seen in Table 4.3.

Table 4.3: Percentage of failures from noisy breakdown and tddb for capacitors of two sizes

	Small (%)	Large (%)
noisy bd	64.29	33.33
tddb	35.71	66.67

The significance of the difference was examined using a contingency table analysis, as the responses are categorical rather than continuous. The Pearson  $\chi^2$  is a nonparametric test of the hypothesis that the response rates, *i.e.*, frequency of soft breakdown and tddb, are the same across both categories, *i.e.*, large and small capacitors. It is calculated by summing the squares of the differences between observed and expected counts and calculating the probability of obtaining the observed  $\chi^2$  value from chance alone to see if the difference is significant. The  $\chi^2$  value calculated was 3.657, which gives a 1-0.0558 or 94.4% chance that the difference is real. Thus, it is reasonable to conclude that soft breakdown and tddb are caused by different mechanisms. Tddb is caused by an extrinsic defect. Noisy breakdown does not have a strong area dependence. The interrelationship of tddb and noisy breakdown is discussed in section 4.5.

#### 4.1.2: Stress Induced Leakage Currents

A failure mechanism that must be investigated differently than either tddb or noisy breakdown is stress induced leakage current (SILC). SILC does not cause breakdown, though it may cause failure. It is leakage caused by damage to the oxide during stress. As the damage proceeds, the current becomes unacceptably large. It is difficult to measure SILC in BST. The high field is needed to damage the capacitor and induce SILC, but a measurement of the leakage at the higher voltages will not give a reasonable estimate of SILC. The stress voltage must be different than the measurement voltage.

A brief explanation of the dielectric relaxation of BST and the resulting trade-offs inherent in SILC measurements follows. The charging current that flows into the capacitor falls into one of three categories. The first is steady-state leakage, which is current flow across the capacitor. The second is polarization, which is the storage of charge in the system. Polarization is manifested by positive potential building up on one electrode and negative potential building up on the other, but it appears macroscopically like a current flowing across the capacitor. The third is traps, which impede the flow of current by capturing electrons or holes. When the voltage is stepped to zero, the steady-state leakage stops immediately, the polarization component discharges, resulting in the bulk of the discharging current, and the electrons or holes de-trap.

MOCVD BST deposited using the ATMI process is of high quality, so trapping is not normally a large component. The importance of separating the other two components, leakage and polarization, was discussed by Kingon *et al*[174]. A BST capacitor was charged at two different fields and then discharged. Figure 4.11 shows the resulting current-time measurements. At lower fields, the charging and discharging

currents are almost the same. This indicates that the majority of the charge is going to polarization of the dielectric and thus the current measured is due to dielectric relaxation. At higher fields, there is a large difference between the charging and discharging currents. The discharging currents are only dielectric relaxation, but the charging currents are dielectric relaxation plus steady-state leakage.

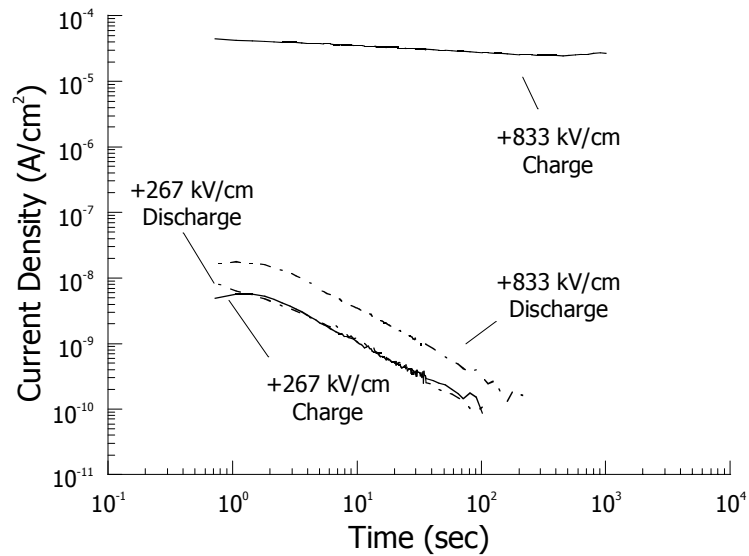


Figure 4.11: Charging and discharging measurements showing separation of polarization and true leakage currents for a 52.0 at% Ti 60 nm BST film at 25 °C. Adapted from Kingon *et al*[174].

For stresses large enough to cause trap formation or electrode damage, both possible causes of SILC, the situation is more complicated than charging and discharging a capacitor. The time dependence of the current depends on the traps and dielectric relaxation. Additionally, neither polarization nor filling of existing traps causes damage. The competing considerations for measuring SILC in BST are as follows.

- (1) Damage is only caused by stressing long enough to have leakage currents dominate, which happens after traps and polarization are satisfied. This time is about  $10^{-2}$  sec[174]. This criterion is not important to the DC case, but has ramifications for AC measurements.

(2) BST requires about 10x the stress time to for the sample to return to equilibrium conditions after being stressed.

(3) Measurement and stress conditions are different enough to require observation of item 2 for accurate measurement of SILC.

(4) Stress intervals that are too large will lead to leave alone rather than SILC. Stress intervals that are too small will lead to extremely long test times, where the BST will be subject to environmental exposure and SILC will not be correctly measured.

The important thing about SILC is how it relates to tddb, if it has a longer lifetime, it need not be characterized further. Two approaches were taken. The first was to take an accurate measurement of leakage, with sufficient time between stress intervals for depolarization to occur. A stress of +18 V (2 MV/cm) was applied to a BST film. The stress was applied for a number of seconds, the sample was allowed to depolarize, and a J-t measurement taken to determine if SILC had been caused by the stress.

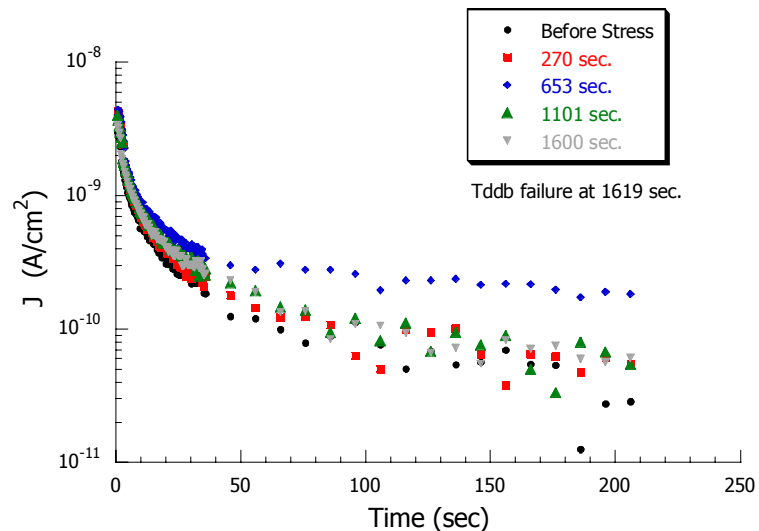


Figure 4.12: Current-time of a 52.0 at% Ti, 90 nm film at 25 °C, for various stress times.

Even at times close to failure, specifically 1600 of 1619 seconds, the J-t curve shows no evidence of SILC. Additionally, even at short times, the leakage current is below  $10^{-8}$  A/cm<sup>2</sup>, which is considered the upper limit of acceptable leakage. A number of measurements were taken; none resulted in a change in the leakage before breakdown.

The second approach was to push the sample more slowly toward failure and not allow it to relax properly between measurements. Two types of measurements were made, the first measured the discharge currents and the second took a J-V curve. The former indicates dielectric damage and the latter indicates interfacial damage. These combined with the J-t curves taken during the stresses give a good picture of the way that electrical stress causes SILC in BST. Most of the samples that were tested failed quickly from tddb. Only a few survived long enough to produce the discharge and J-V data. Because of this survival bias, the data are not generalizable, but should nevertheless give insight into the nature of SILC.

The discharge J-t plots are shown in Figure 4.13. The lines fit to the plots are power-law fits consistent with the Curie-von Schweidler fit. The data are only shown for the first second, before the currents descend uninterestingly into noise. The number indicates the number of 1800 second stress cycles that the sample has undergone. As it was not possible to make capacitance measurements between stresses, the discharge data gives insight into the polarization component of the relaxation currents. Even near breakdown, after 10.5 hours of stress, the dielectric relaxation is unchanged. This indicates that whatever damage the stress is causing; it does not affect charge storage in the capacitor.

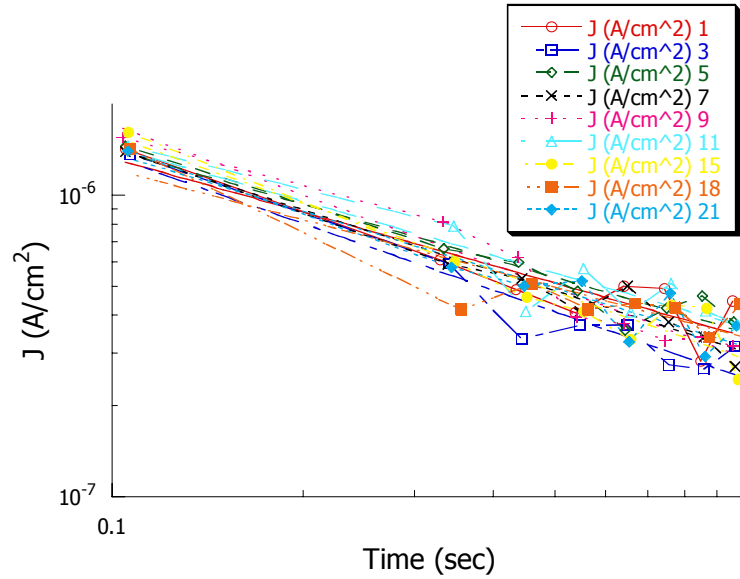


Figure 4.13: Discharge current-time data for a 51.0 at% Ti, 40nm BST film, lines indicate power-law fit.

The J-V curves taken on another capacitor are shown full scale in Figure 4.14. The effect of the double Schottky barriers of the Pt/BST/Pt system can be seen in the plot, following the form shown in Figure 2.8. At low fields, dielectric relaxation dominates, seen in the relatively flat portion of the J-V curve. It is not until the potential barrier of the Schottky barrier is exceeded that the leakage increases considerably. Although not individually labeled, the data is of 15 stress cycles of 1800 sec. at 6 V, followed by taking a  $\pm 4V$  J-V curve.

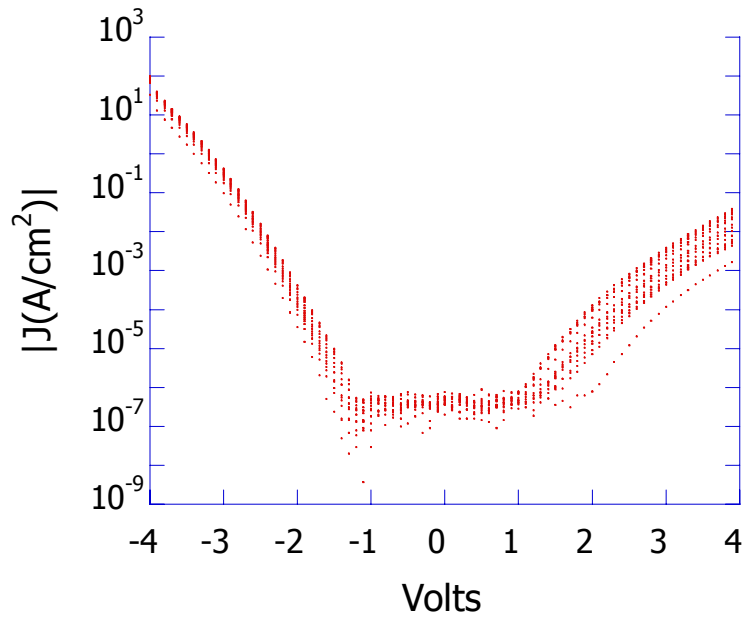


Figure 4.14: Log current versus voltage for a 51.0 at% Ti, 40nm BST film, for various stress cycles.

More interesting is a closer view of the positive voltage region where the current begins to increase. The positive and negative sides are approximately the same, but the positive side degrades more as the stress proceeds, so that side is the one that will be examined. The odd numbered J-V curves are shown in the range of 0 to 2 V in Figure 4.15. The voltage where the leakage shifts from being dominated by dielectric relaxation to Schottky emission steadily decreases as the number of stress cycles increase. This stress suggests that the SILC damage is occurring at the Pt/BST interface. The result of the damage is to lower the Schottky barrier height.

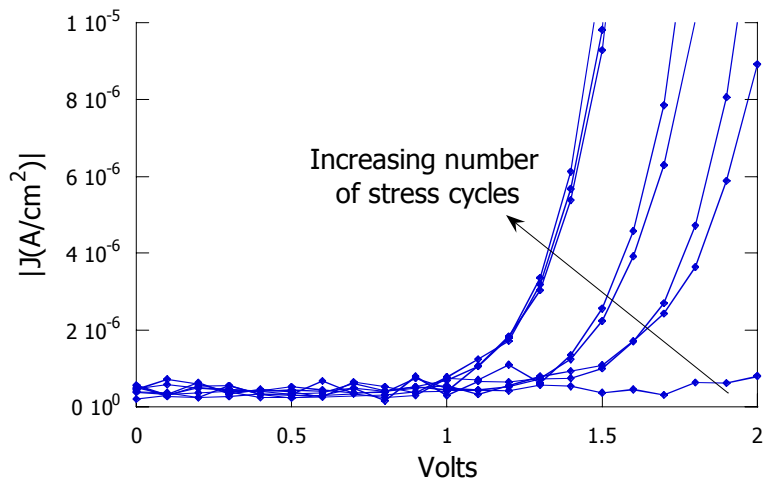


Figure 4.15: Current versus voltage for a 51.0 at% Ti, 40nm BST film, for various stress cycles.

SILC is not the lifetime-limiting failure mechanism at low temperature and high field. Both soft breakdown and tddb failure have shorter lifetimes. The J-V data, combined with the discharge data, are strong indications that SILC damage caused by electrical stress is mainly to the Schottky barrier and not to the film. There are two implications. First, the SILC is likely not a concern at all. DRAM and tunable dielectric applications will work either at high frequencies or at a sufficiently low voltage that other failure mechanisms will dominate. Second, if it is later shown to be lifetime-limiting, the electrode material and processing can be changed to achieve a larger Schottky barrier.

The main conclusion from the low temperature, high field investigation is that tddb is the limiting failure mechanism in quadrant IV. Tddb is caused by an extrinsic defect and is manifested as a sudden change in conduction mechanism. The origin of noisy breakdown may be similar to that seen previously in the BST system.

## 4.2: High Temperature, Low Field DC Failure

Failure was not seen in this regime at test times up to 48 hours. DC measurements were made at  $\pm 1.6$  V at temperatures up to 275 °C. This results is not unexpected based on the understanding of both tddb and resistance degradation. The damage process that occurs in tddb is likely trap creation from current across the capacitor. Figure 4.15 shows the initial J-V curve and the current is negligible up to 2 V. The process that creates traps and leads to tddb failure does not operate fast enough at low voltages. Resistance degradation is a diffusional process. Zafar *et al.* have found that the electrical driving force that causes defect migration is opposed by the concentration gradient that is established over time[154, 155]. Thus, for low enough voltages, there is an insufficient driving force for the segregation of defects to cause thermal runaway, which is the underlying failure mechanism of resistance degradation.

### 4.3: High Temperature, High Field

Resistance degradation is the dominant failure mode in this quadrant. Tddb failures are seen, but are as rare as resistance degradation in quadrant IV. A large amount of resistance degradation data is available[112, 144, 153]. The work on resistance degradation has examined the effects of film thickness, composition, and temperature, field, and polarity. However, the data has never been fit to a multiple regression model that considers the interaction of the variables, *e.g.*, the composition was fit separately for each field.

Basceri *et al.* have used the following form to model resistance degradation

$$t_d = t_0[V^{-n}]\exp\left[\frac{Q_T(V)}{kT}\right].$$

The voltage is modeled by a power law and the temperature by an Arrhenius relationship[144]. However, the point was made that it was not easy to distinguish between exponential and power law forms. Other investigators, such as Baumert *et al.*, have chosen to model both components as an exponential[116]. Additionally, field scaling for SiO<sub>2</sub> is either exponential or inverse exponential in form. Thus, the form for all experimental variables is chosen to be exponential.

The exponential form is convenient because exponential models are intrinsically linear. A natural log transformation allows the model to be treated by standard linear regression techniques. The model was constructed by considering the primary experimental variables, or effects. They are field, temperature, composition, and thickness. The first order interactions and second order effects were initially added in the screening phase. Those with Prob>|t| more than 0.05 were removed from the model.

The primary experimental variables were centered at their respective means when used in interaction terms. Centering produces better estimates by preventing the multicollinearity problems that arise from having continuous primary experimental parameters and continuous interaction terms. The centers of the terms are listed in Table 4.4 and the main equation of fit and implicitly included throughout.

Table 4.4: Means of primary experimental variables.

Effect	Center of Polynomial
Field	760.649
Thickness	54.4536
1000/T	2.01337
Ti%	52.1289

The equation of fit is

$$\begin{aligned}
 \ln(t_{BD}) = & \beta_0 + \beta_1 \cdot Field + \beta_2 \cdot Thickness + \beta_3 \cdot \frac{1000}{T} + \beta_4 \cdot Ti\% \\
 & + \beta_5 \cdot (Field - 760.6) \cdot (Thickness - 54.45) + \beta_6 (Field - 760.6) \cdot \left( \frac{1000}{T} - 2.013 \right) \\
 & + \beta_7 \cdot (Thickness - 54.45) \cdot \left( \frac{1000}{T} - 2.013 \right) + \beta_8 (Field - 760.6) \cdot (Ti\% - 52.13) \\
 & + \beta_9 \cdot (Thickness - 54.45) \cdot (Ti\% - 52.13) + \beta_{10} \left( \frac{1000}{T} - 2.013 \right) \cdot (Ti\% - 52.13) \\
 & + \beta_{11} \cdot (Thickness - 54.45) \cdot \left( \frac{1000}{T} - 2.013 \right) + \beta_{12} \cdot (Ti\% - 52.13) \cdot \left( \frac{1000}{T} - 2.013 \right)
 \end{aligned}$$

where the  $\beta_i$  are the parameters, given in Table 4.5. The overall model was evaluated by the adjusted  $R^2$ , discussed previously. The adjusted  $R^2$  value is 0.961. The model was graphically evaluated by a leverage plot and a whole-model residual plot.

Table 4.5: Parameter estimates for the effects in the resistance degradation model.

Term	Estimate	Std Error	t Ratio	Prob> t	VIF
Intercept	-64.93905	2.696704	-24.08	<.0001	.
Field	-0.011087	0.000288	-38.47	<.0001	3.58
Thickness	-0.056186	0.002921	-19.24	<.0001	12.34
Field*Thickness	-0.000025	0.000008	-2.92	0.0045	10.56
1000/T	14.217893	0.556074	25.57	<.0001	1.08
Field*1000/T	-0.014155	0.004221	-3.35	0.0012	2.06
Thickness*1000/T	-0.052093	0.016888	-3.08	0.0028	1.41
Ti%	1.0710907	0.050803	21.08	<.0001	9.27
Field*Ti%	0.002331	0.000281	8.31	<.0001	3.41
Thickness*Ti%	0.0178289	0.001562	11.41	<.0001	2.47
1000/T*Ti%	2.6244583	0.657532	3.99	0.0001	2.78
Thickness*Thickness	0.0002984	0.000037	8.17	<.0001	3.98
Ti%*Ti%	-1.5373	0.08098	-18.98	<.0001	1.64

The leverage plot is a generalization of the partial-regression residual leverage plot and is a way to graphically represent fits of high-dimensionality data[175]. Testing for the significance of an effect is done by comparing the sum of squared residuals with and without the effect. If the residuals are sufficiently smaller, the effect is significant. The leverage plot shows each point with and without the effect in the model. Figure 4.16 shows a schematic of a leverage plot. The distance from the point to the line of fit is the residual with the effect, the horizontal line is the residual without the effect, *i.e.*, the  $\beta$  associated with that variable is zero. For a model with a single slope and intercept, the points correspond to the data points, but for multiple regression, the points correspond to the residual with all other effects included. Similarly, if the effect tested is not a main effect, but is more complex, such as a nominal effect or interaction, the x-values are scaled. This is the advantage of the leverage plot. The same intuition that is applied to simple linear models, *i.e.*, whether the model is a better fit than just the mean value, can be applied to complex multilinear regressions to graphically show whether the model is better or worse without a given effect. Typically leverage plots are shown with 95% model confidence intervals. The leverage plot is read by seeing if the confidence interval contains the horizontal line. If so, the effect is insignificant.

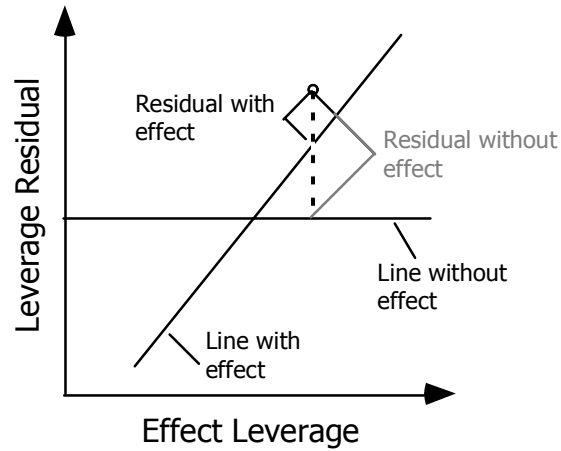


Figure 4.16: Schematic of a leverage plot.

A special case of the leverage plot is the whole model leverage plot. In this case, the horizontal line is the average of the data and the line of fit is the model with all effects included. The leverage plot for the resistance degradation model is shown in Figure 4.17. The plot shows the overall model to be quite good. The data are close to the equation of fit; there are small residuals and no extreme outliers.

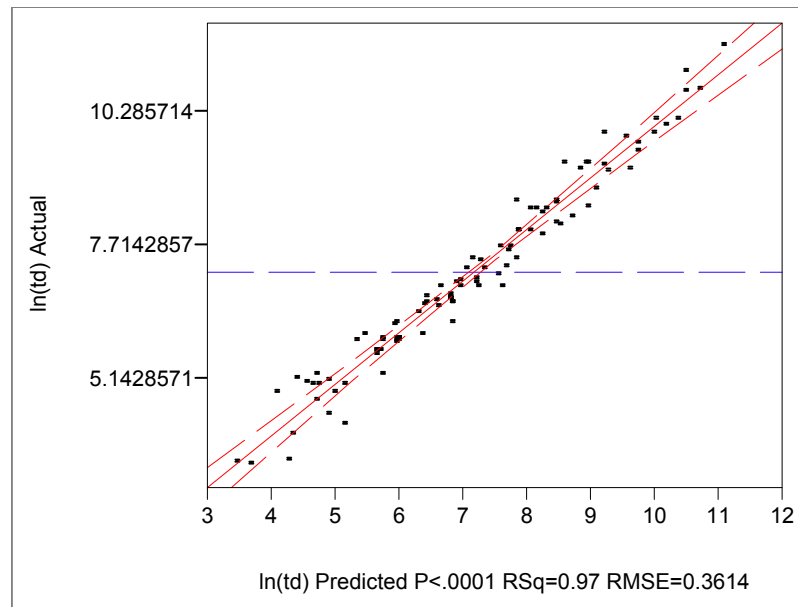


Figure 4.17: Whole model leverage plot for resistance degradation model.

A residual for an observation is calculated as (measured value-predicted value). The residual plot, shown in Figure 4.18, shows residuals that are consistent with the use

of least squares fitting. Additionally, there is no pattern to the residuals, which suggests that there is neither autocorrelation nor missing effects.

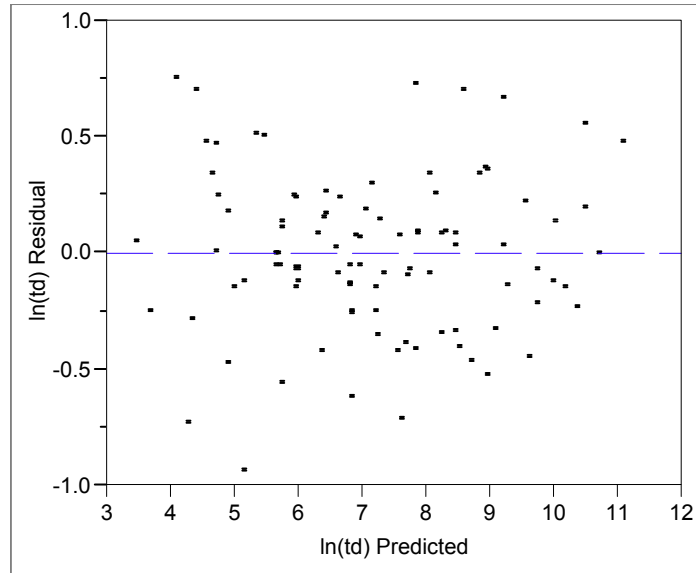


Figure 4.18: Plot of model residuals for the resistance degradation model.

The individual leverage plots are shown in Figure 4.21 through Figure 4.31. The individual leverage plots do not require comment, but a few general notes are as follows. First, the primary effects, *i.e.*, field, temperature, thickness, and composition, are all significant and the associated  $\beta$ s are large in magnitude. The second order effects and interactions are generally smaller in magnitude and the insignificant parameters were excluded in the screening process.

Second, the origin of the significance of a particular parameter can be supposed, but it is a question rather than an answer. For instance, other things being equal, thicker films have shorter lifetimes. It is possible that there is a composition gradient, or thicker films are rougher. The same question about origins is applies to interactions. For instance, there is an interaction between field and thickness, thicker films have shorter lifetimes as a function of field than thinner films. This is consistent with thicker films

being rougher. The field concentration effects from a rough interface would be stronger in thicker films.

Third, the clustering of data seen toward the center of some of the leverage plots, such as in Figure 4.29, is due to collinearity between effects, *i.e.*, a relationship, especially a linear relationship between effects. A metric for the degree of collinearity is the variance inflation factor. It is calculated from the inverse of the correlation matrix. Values below 10 are considered good. Table 4.5 lists the calculated VIF values for the model parameters. The numbers, especially for thickness and related interactions, are borderline. It is possible to remove some of the interactions to lower the VIF values overall, but the explanatory power of the model would decrease, so it is a matter of preference.

To illustrate the advantage of leverage plots, the measured and predicted time to breakdown is plotted as a function of electric field. Figure 4.19 shows a conventional plot. It is difficult, by inspection, to evaluate the goodness of fit. Contrast this to Figure 4.20. It is possible to see how significant the effect is.

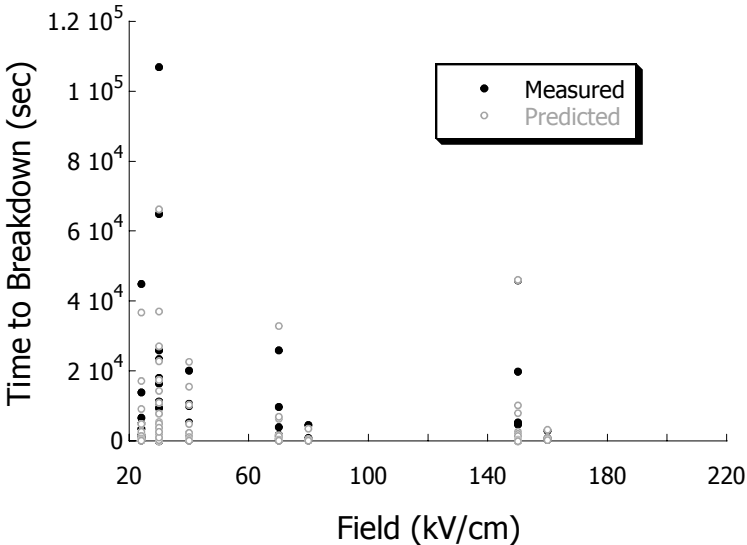


Figure 4.19: Time to breakdown as a function of field with measured and predicted values.

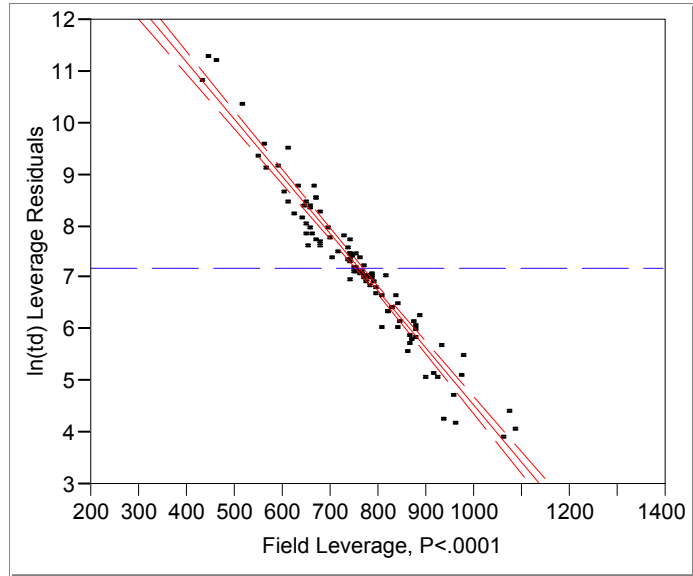


Figure 4.20: Leverage plot for field.

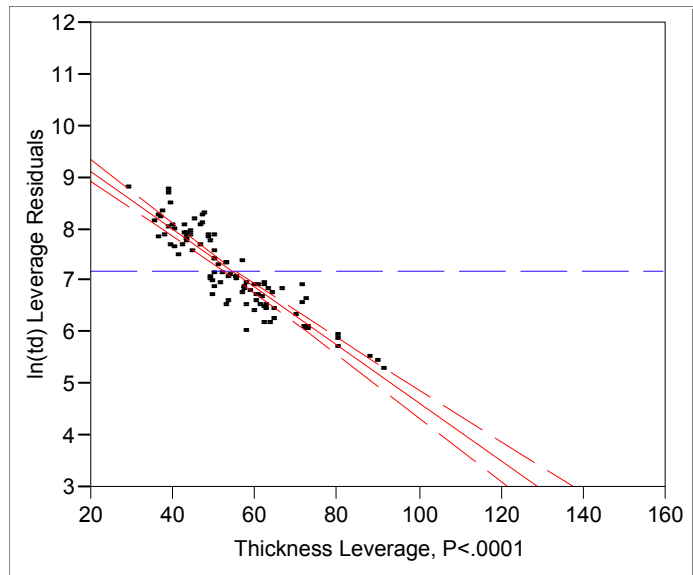


Figure 4.21: Leverage plot for thickness.

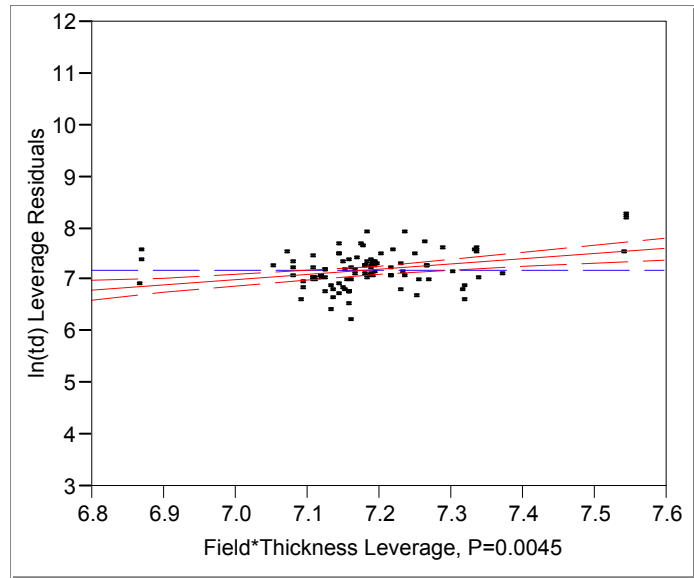


Figure 4.22: Leverage plot for interaction of field and thickness.

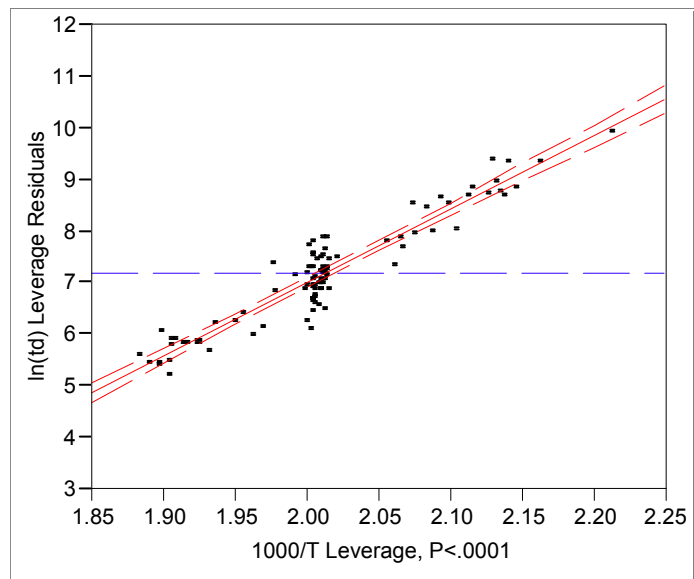


Figure 4.23: Leverage plot for temperature, on an Arrhenius scale.

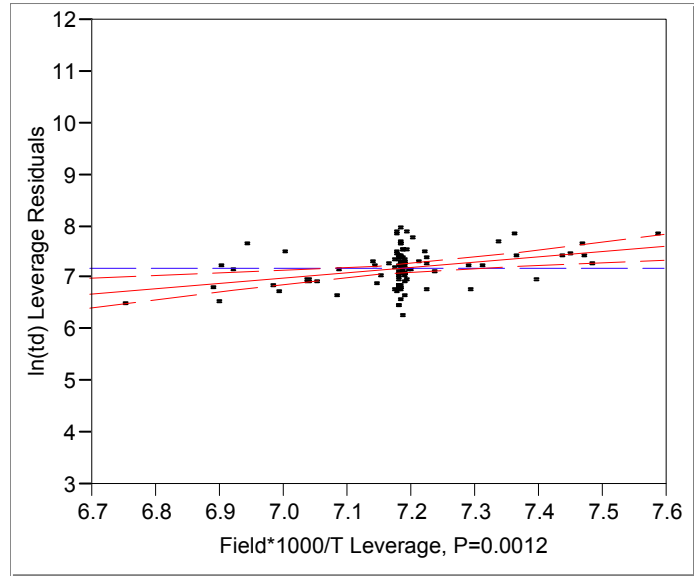


Figure 4.24: Leverage plot for the interaction of field and temperature.

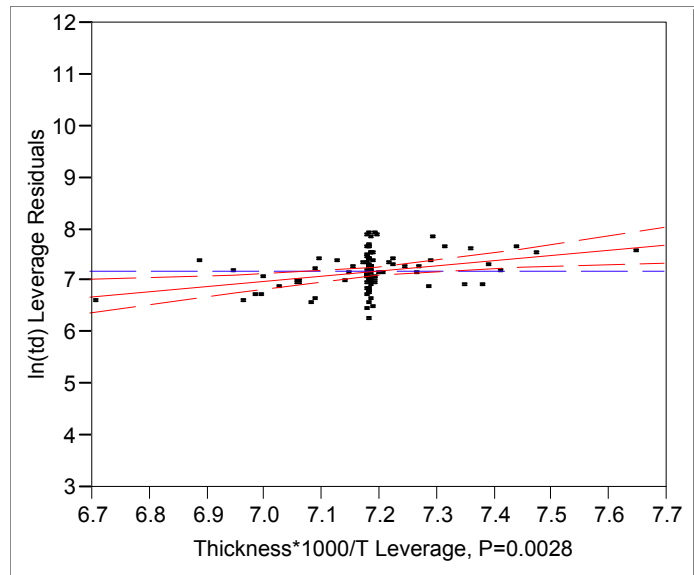


Figure 4.25: Leverage plot for the interaction of thickness and temperature.

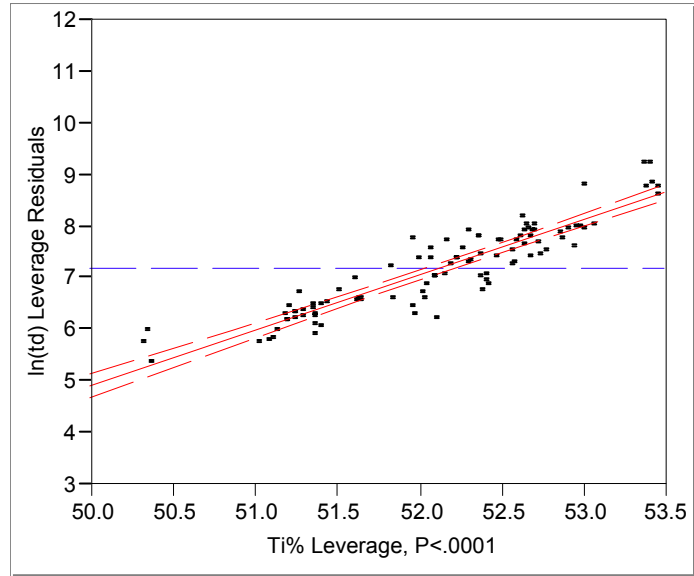


Figure 4.26: Leverage plot for composition.

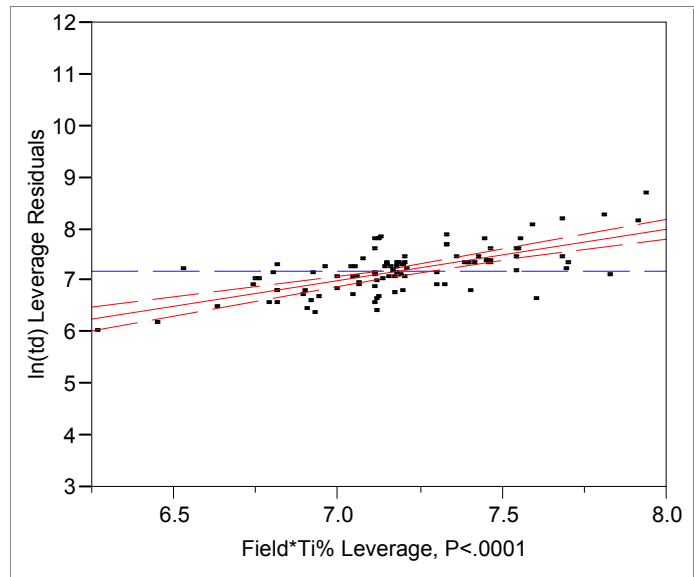


Figure 4.27: Leverage plot for the interaction of field and composition.

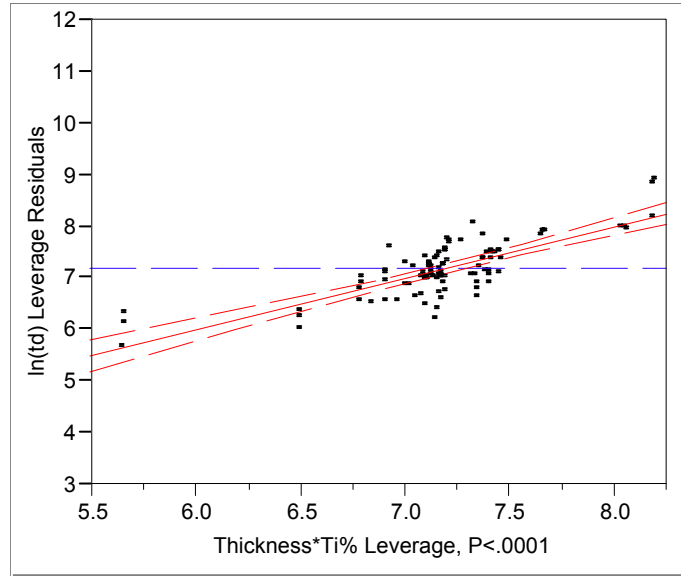


Figure 4.28: Leverage plot for the interaction of thickness and composition.

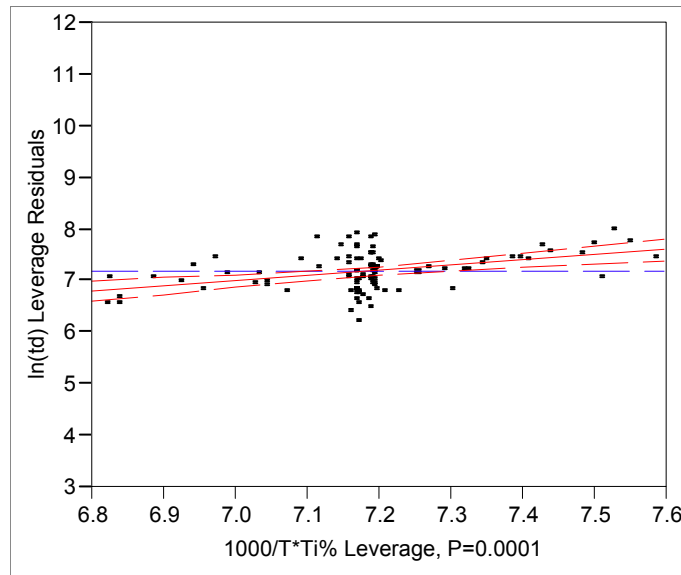


Figure 4.29: Leverage plot for the interaction of temperature and composition.

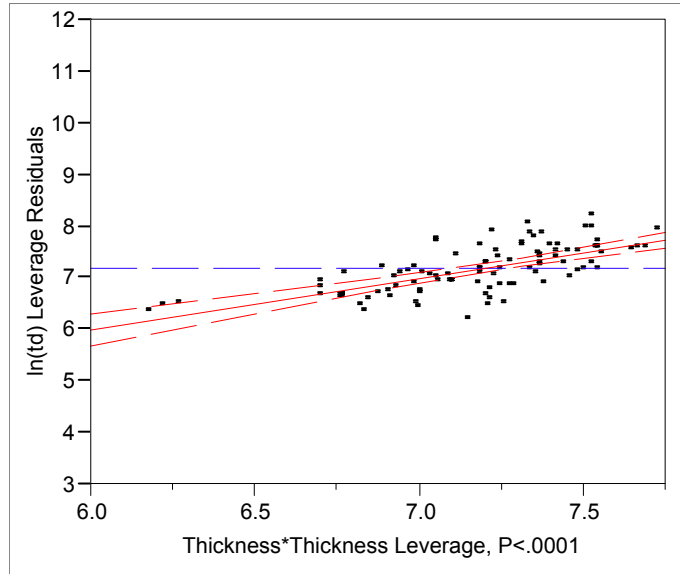


Figure 4.30: Leverage plot for second order thickness effect.

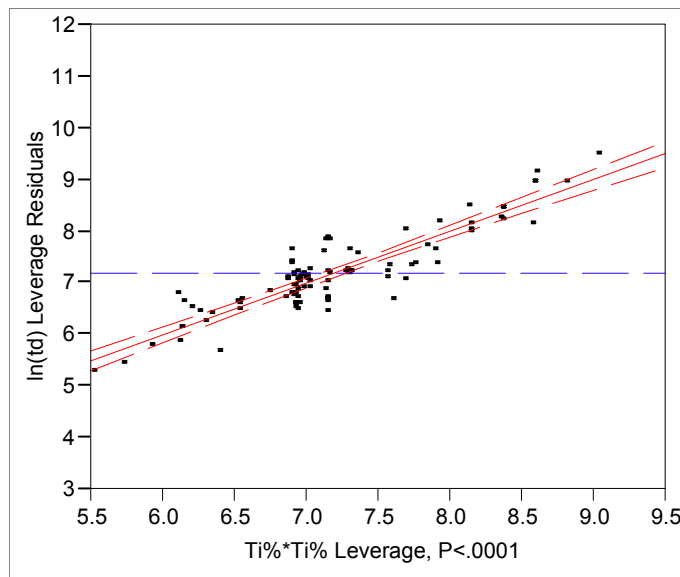


Figure 4.31: Leverage plot for second order composition effect.

Resistance degradation is well understood, being well characterized and modeled. The data are consistent with a diffusional process, not a statistical process. The errors for a diffusional process are typically normal or lognormal distributed. The errors for a statistical processes, such as  $tddb$ , are Weibull or gamma distributed. In a diffusional

process, the errors are not because of an underlying statistical failure mode, but because of standard measurement errors: capacitor size, BST film thickness, temperature, *etc.* The exponential relationship is reasonable to model resistance degradation. Finally, resistance degradation is the dominant failure mode in quadrant I.

## 4.4: AC Failure

BST is used in the paraelectric phase, so the fatigue and imprint problems that result from AC stress in ferroelectrics are not as important. The AC failure investigation seeks to determine whether AC failure occurs more quickly than DC failure and if different failure mechanisms manifest themselves in the AC regime. The testing was via two routes. The first stressed the samples at different temperatures and number of stress cycles and allowed them to relax completely before J-t curves were taken to determine the conditions for AC failure. Similar to the SILC investigation, this gives the most accurate determination of whether the sample has failed. Second, the samples were stressed and given insufficient time to relax, in order to cause failure in a reasonable period of time.

A curious result is shown in Figure 4.32. A number of different films were stressed. All had similar leakage characteristics, the result is repeatable. The leakage is better after the stress than before the stress. A possible explanation has been mentioned previously. BST and related ferroelectrics such as PZT require electrode anneals for low leakage. It was found that the same effect could be produced by electrical stress.

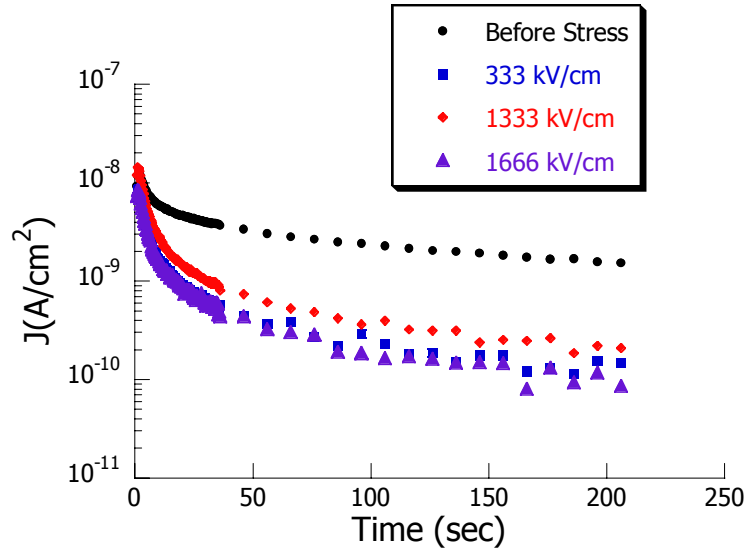


Figure 4.32: Log Current versus time for several 51.0 at% Ti 40 nm BST films, stressed at 1 kHz for  $10^9$  cycles at various stress levels.

The AC stress device described in the experimental procedure was used to drive BST films to failure. A typical result for AC stress is shown in Figure 4.33. As for SILC, one possible source of experimental error is an effect based upon depolarization and detrapping of the sample between stress periods. This effect was investigated, as discussed in the experimental methods section and was not found to be significant in the range of 5 seconds to 2 minutes. The data density was limited by the time needed for the circuit transients to die out. It should be noted that work by Chen, *et al.*, for SrTiO<sub>3</sub> has not found a similar independence of time to failure and duty cycle, but the dependence is process-specific[163].

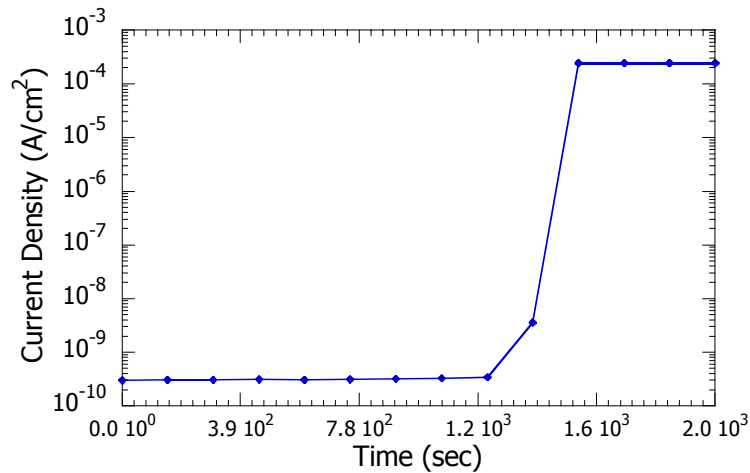


Figure 4.33: Log current versus time for a 51.0 at% Ti, 40 nm sample stressed at 10 Vpp and 1 MHz.

The form of AC failure is similar to the tddb case. A Weibull plot of the two types of failure is shown in Figure 4.34. As the model parameters show in Table 4.6, the failure distributions are quite similar. The same nonparametric tests were employed comparing tddb versus soft breakdown and are shown in Table 4.7. Both tests indicate that it is unlikely that there is a real difference in the failure times. Combining the similar failure distributions from the Weibull plot and the results of the nonparametric tests suggest that there exists a common defect causing the AC and DC tddb failure.

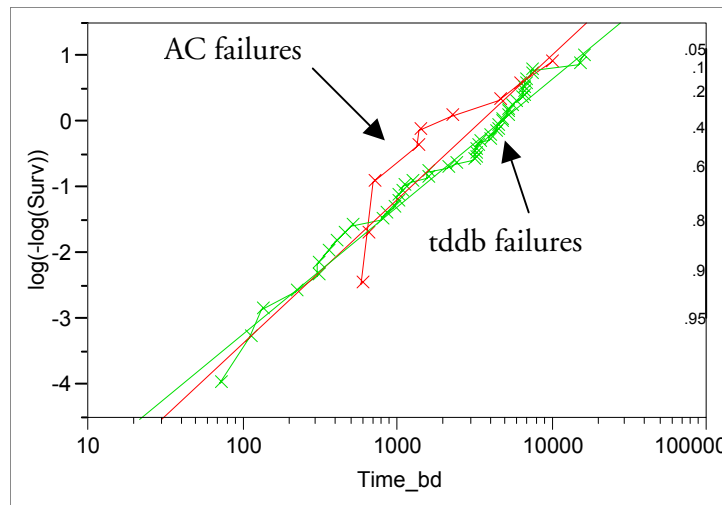


Figure 4.34: Weibull plot of AC failure times and DC tddb failure times.

Table 4.6: Weibull Parameter Estimates for Figure 4.34.

Test	$\alpha$	$\beta$
AC	3496.45	0.946537
DC	4694.57	0.837013

Table 4.7: Significance of the difference in lifetime between low temperature ac and dc tddb failure using nonparametric tests.

Test	Chi-Square	Prob>ChiSq
Log-Rank	1.1355	0.2866
Wilcoxon	0.7282	0.3935

The effect of higher stress frequency is inconclusive, as can be seen in Figure 4.35. There appears to be a downward trend to the data, but this trend is not significant given the noise in the data. More investigation is needed to confirm this trend. A comprehensive examination was done by Reisinger, *et al*[126]. Approximately 25 samples were used to calculate the median time to failure for films at each frequency. Samples were tested in the range of 0.01 to 1kHz. In the range of 1 to 100 Hz, the lifetimes were lower than the dc lifetime and decreased with increasing frequency. From 100 Hz to 1 kHz, the lifetime increased to the DC lifetime. This effect was attributed to a trapping-detrapping process[126]. This agrees with the above AC and DC comparison, as the AC data was taken at 1 kHz.

The result is consistent with the understanding of leakage current in BST. At low frequency, there is enough time for traps to fill and empty with each cycle, which acts to impede the current. As the frequency increases, the traps do not have enough time to fill and the effect diminishes. Dielectric relaxation accounts for almost all of the charging current before  $10^{-5}$  sec and is small fraction by  $10^{-2}$  sec[174]. Polarization currents also impede the flow of leakage current across the capacitor. Leakage is likely the source of the damage. This effect would start at about 100 Hz and increase, reaching its maximum value at about 10 kHz.

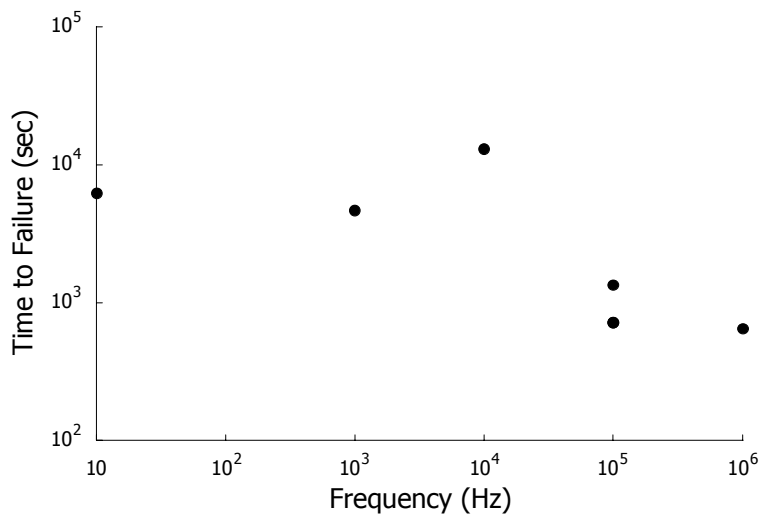


Figure 4.35: Time to failure for 51.0 at% Ti, 40 nm samples as a functions of frequency.

The effect of nonstoichiometric Ti was investigated. Excluding the 53.0% Ti composition, the lifetime is relatively independent of Ti%, as can be seen in Figure 4.36. As discussed in the literature review, rougher films tend to yield shorter tddb lifetimes. If AC stress is operating upon the same interface features as the tddb failures, then smoother films should have a longer lifetime. A second phase is not observed in by EXFAS at or below 52.5% Ti [107]. Ti excess above this point causes mechanism of accommodation seems to change from accommodation in the grain to segregation at the grain boundaries. The segregation may be the reason that BST becomes smoother at high excess Ti%, thus leading to the longer AC lifetimes.

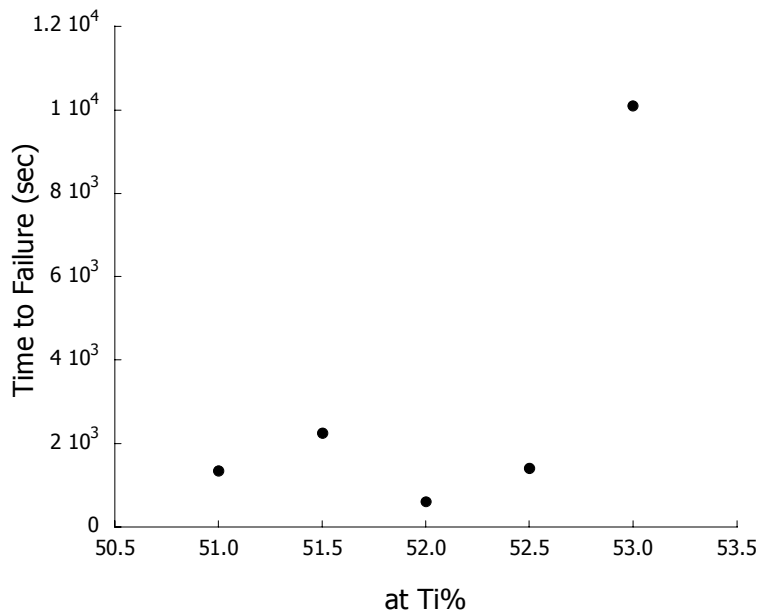


Figure 4.36: Time to failure of various compositions of 40 nm BST films.

The case of high temperature AC failure should be different than under DC stress. In resistance degradation, it is believed that the failure mechanism is migration of charge carriers, most likely oxygen vacancies, toward the cathode. No net motion of any species should occur under bipolar stress in the bulk of the film, so presumably the damage is being done at the interfaces, either by defect motion or trap creation. Several measurements were made to investigate the interaction of temperature and AC stress. The first, shown in Figure 4.37, used several capacitors and applied a 100 kHz stress of 6 V<sub>pp</sub> at several temperatures. The J-t curves before the stress were similar; one is given as an example. After the stress, the samples were cooled to 25 °C and allowed to return to equilibrium. The effect of the 25 °C stress was the same as in Figure 4.32. At higher temperatures, the same stress caused more damage. The dielectric relaxation was not affected, as the current at short times was about the same, but the steady-state leakage value increased for higher-temperature stress. This leads to the same conclusion as for SILC. The combination of temperature and AC stress damages the Schottky barrier.

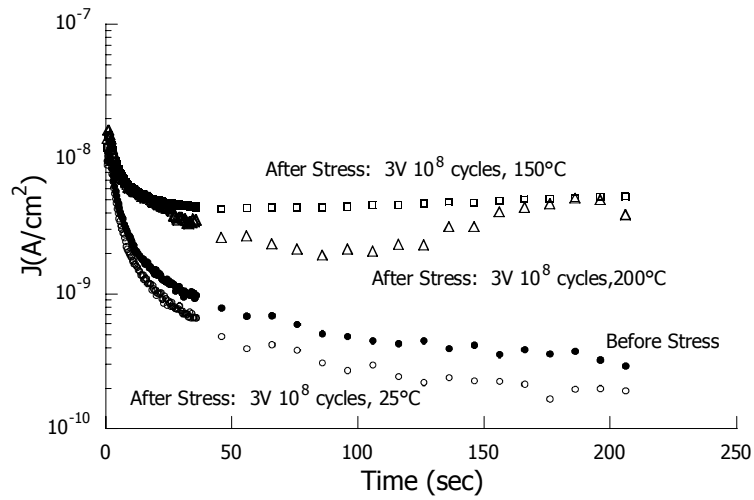


Figure 4.37: Log current density versus time for a 52.0 % Ti, 40 nm BST sample, for various stress conditions.

Another series of tests were performed at 150 °C, using the same procedure as for the previous measurements, but here the number of stress cycles was varied. As the number of cycles increases from  $10^8$  to  $10^9$ , the steady-state leakage increases. It is not until  $10^9$  cycles are reached that initial current is affected.

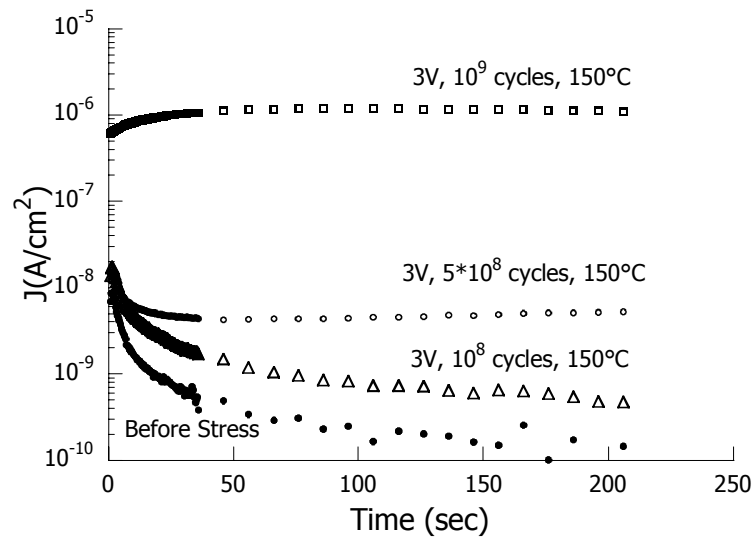


Figure 4.38: Log current density versus time for a 52.0 % Ti, 40 nm BST sample, stressed at  $\pm 3$  V and 1 kHz, for various numbers of cycles.

Finally, to determine if this high temperature damage would cause breakdown or just failure, a 40nm, 51.0% Ti sample was heated to 230°C and a current-voltage

measurement taken from -1.5 V to 1.5 V both before and after the applied stress. The capacitors which experienced an AC stress fail quickly, *i.e.*, the leakage currents become unacceptably large. However, the current reaches a plateau and does not worsen to catastrophic levels, unlike the other types of failure, namely tddb and resistance degradation. The J-V plot gives additional evidence that high temperature AC failure alters the Schottky barrier. Before the stress, the form of the J-V plot has the expected form: low currents in the dielectric relaxation regime and increasing currents at the onset of Schottky emission. Once the sample fails from ac stress, it exhibits a linear behavior about 0 Volts which appears ohmic in nature. This suggests that ac stress at elevated temperature causes damage to the interface, lowering the barrier.

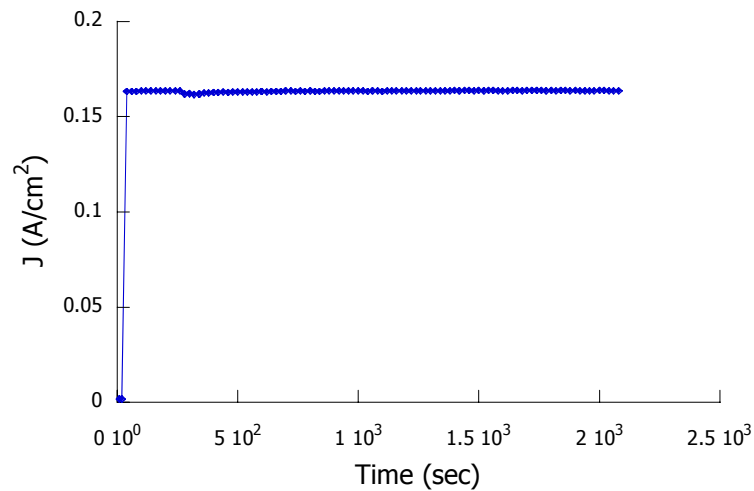


Figure 4.39: Current density versus time for a 40nm, 51.0% Ti sample stressed of  $\pm 3V$  at 1 kHz.

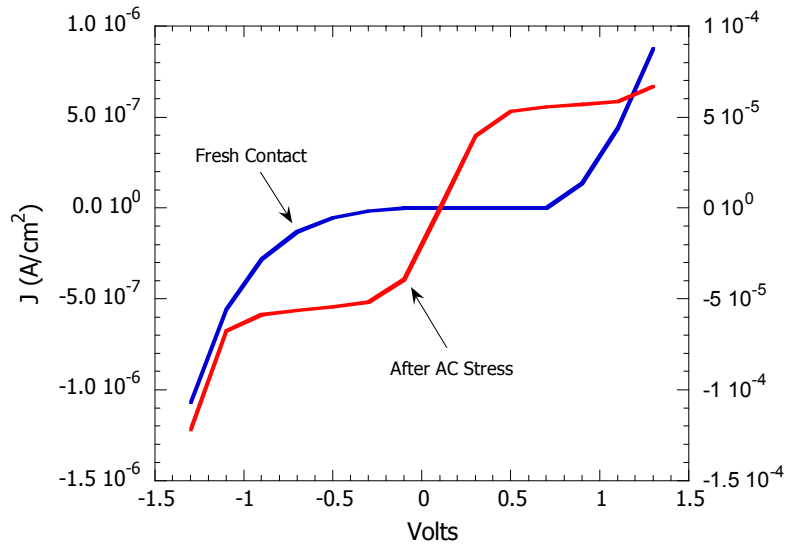


Figure 4.40: Current density versus voltage for a 40nm, 51.0% Ti sample before and after stress.

Leakage across the film causes damage. There is a critical frequency range where damage occurs more quickly than the DC case because of the relationship between polarization, trap filling, and leakage. Low temperature AC and DC failure at seems to be caused by the same failure mechanism, *i.e.*, indistinguishable  $t_r$ . At high temperature, breakdown does not occur, but failure occurs quickly. It is not known what causes AC failure at high temperature, but it damages the interface, rather than operating in the bulk of the film.

## 4.5: General Failure Model

The general failure model attempts to provide a framework for BST failure, starting with a subset of failure modes, breakdown modes, and how the failure modes are related to failure mechanisms. As Figure 4.41 illustrates, breakdown in BST can be divided into two categories: intrinsic and extrinsic. The extrinsic branch is on the left, the intrinsic branch is on the right. The two schemas agree on the place of resistance degradation and tddb, but differ on the classification of noisy breakdown.

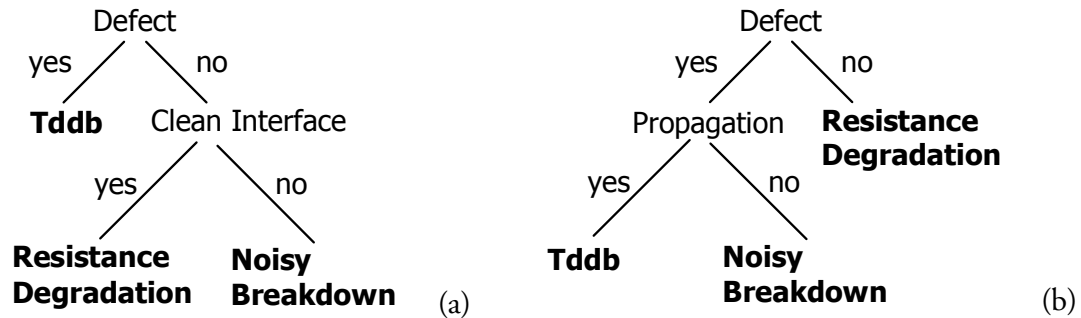


Figure 4.41: Two schemas for classification of BST failure modes (a) attributes soft breakdown to interfacial contamination and (b) attributes soft breakdown to the same mechanism, expressed in a different mode.

The intrinsic breakdown mode is resistance degradation. It is due to oxygen vacancy motion, specifically transport to the interface, that lowers the Schottky barrier height. It is modeled via an exponential relationship. As it is a diffusional process, resistance degradation is prominent at high temperatures. The mechanism operates at low fields and causes failure at high fields. It might be controlled by decreasing the concentration of oxygen vacancies through doping, annealing, changing electrode type, or other experimental parameter, but it is unlikely to be eliminated. The resistance degradation lifetime is the ultimate available lifetime of BST.

An extrinsic defect is seen in  $t_{ddb}$ . It is likely to be strongly process dependent. The defect is described via a Weibull distribution. It operates under both AC and DC stress and is the dominant defect at low temperatures and high fields. The defect is correlated to interfacial roughness. It is not known if interfacial roughness influences the defect directly, *e.g.*, by changing the concentration, or if it is through field enhancement. The same type of effect is exhibited in the polarity dependence of  $\text{SiO}_2$   $t_{ddb}$ , where oxide damage, as measured by  $D_{it}$ , occurs more quickly from gate electron injection than from substrate injection because poly-Si grain boundaries locally enhance current injection, versus the single crystal Si substrate[176]. Tsai, *et al.*, compared the lifetime of BST deposited on several bottom electrode materials: Pt, Ir,  $\text{IrO}_2/\text{Ir}$ , Ru, and  $\text{RuO}_2/\text{Ru}$  and found that increasing bottom electrode roughness was correlated with shorter  $t_{ddb}$  lifetime[160]. Noma and Ueda measured only one trap via DLTS. This suggests that  $t_{ddb}$  is caused by a single defect[161].

Noisy breakdown begins much like  $t_{ddb}$ , but instead of failing in one step, degrades in a series of steps. This is similar in form to the soft degradation in the  $\text{SiO}_2$  literature discussed earlier. The difference between the two schemas is the classification of soft breakdown.

In schema a, if the capacitor does not have the extrinsic defect and the interfaces are contaminated, it undergoes soft breakdown. This agrees with two pieces of data. The first is that a Weibull plot clearly shows two populations of defects, *i.e.*, two different distributions. The second is difference in the area dependencies. Typically, different area dependencies means that the mechanisms are different. The area scaling of the  $t_{ddb}$  defect demonstrates that it is an extrinsic defect, whereas soft breakdown and resistance degradation are intrinsic. A possible mechanism is as follows. Impurities and defects at the electrode/BST interface lower the Schottky barrier. Localized barrier lowering results

in local leakage increasing. These areas self-heal by thermal annealing, explaining the short increase in leakage current. Earlier work on voltage burn-in of BST films is consistent with this healing process.

The schema b is more consistent with the percolation model of  $\text{SiO}_2$  failure. Noisy breakdown would thus have the same defect as tddb. The percolation modes suggests that accumulation of defects leads to the creation of a conductive pathway. When a conductive pathway is created through the dielectric, there is a capacitive discharge. Sometimes this discharge propagates through the material oxide, leading to tddb. The balance of the time there is only a local discharge that causes an increase in current, but does not propagate through the material. An illustration of the two cases is given in Figure 1.76. This explanation is consistent with the form of the BST tddb data. Second, the discharges tend to occur in the later portion of the failure test, rather than the earlier portion. This is also consistent with a percolation model.

The two additional failure modes are AC failure and SILC. The effect of AC stress is likely interfacial rather than a bulk effect, both at low and high temperatures. The low temperature ac failure resembles tddb breakdown. It is reasonable to suppose that it is tddb for two reasons. First, the distributions for AC failure and tddb are statistically indistinguishable. Second, the AC failure lifetime is significantly longer in films that are smoother as a result Ti nonstoichiometry. Tddb lifetime also longer for smoother films.

High temperature ac failure causes damage to the Schottky barriers at the electrodes, which results in the J-V behavior becoming more ohmic. The nature of the damage is not known. Resistance degradation, from DC stress, is known to lower the barrier height in one direction. This lowering is attributed to oxygen vacancy transport to

the interface. There should be little net charge motion at the interface, as the motion of oxygen vacancies is slow. Even under low frequency stress there is insufficient time for the resistance degradation mechanism to operate. Some other phenomena is occurring.

SILC is difficult to measure directly because of BST's dielectric response. The J-t curves taken between stresses indicate that the dielectric relaxation, evidenced by the short-time currents, does not appreciably change, which suggests that the dielectric is not being damaged. The J-V curves show that the voltage at which the leakage changes from dielectric relaxation to Schottky emission decreases as a function of voltage, suggesting further that the nature of the damage is interfacial.

The two failure modes most likely to cause failure are tddb and resistance degradation. A further investigation was done of tddb failure. The results were compared to the extrapolation from resistance degradation model to determine the most likely failure mode at operating conditions.

## 4.6: Further Investigation of Tddb

The screening experiments revealed that tddb is the most likely failure mode in quadrant IV and resistance degradation is the most likely failure mode in quadrant I. While sufficient data exists for resistance degradation to extrapolate from the high temperature direction, additional data was necessary to extrapolate tddb lifetime from the low temperature direction. The following aspects of tddb were investigated: effect of capacitor size, field dependence, and finally whether the pre-stress leakage is correlated to time to tddb. The films that were measured were 40 nm, 51.0 at.% Ti. The thickness was constant, so electric field will be given in volts. 7 V corresponds to 1750 kV/cm, 8 V corresponds to 2000 kV/cm, and 9 V to 2250 kV/cm. The reason for using only a positive voltage is shown in the TEM of BST in Figure 4.42. The bottom BST/Pt interface is different than the top Pt/BST interface. The bottom interface is much smoother than the top interface. Additionally, the bottom film/electrode interface should be much cleaner than the top, as the top electrode is often deposited several weeks after the BST is deposited. If the electrode/film interface is contaminated, the Schottky barrier will be damaged. This will lead to larger leakage and might bias the results. This circumstance is unlikely for real devices. As a result, electron emission from the bottom interface will likely give a better estimate of reliability of real devices than electron emission from the top electrode.

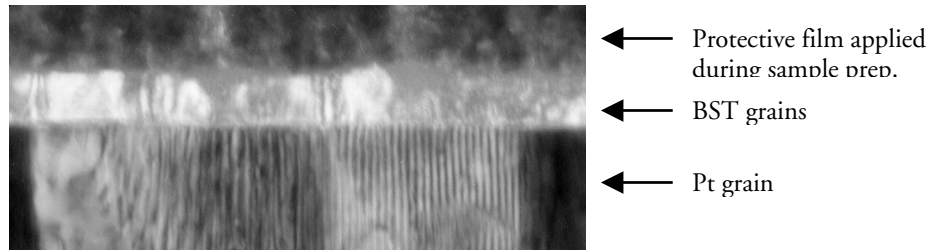


Figure 4.42: Dark field image of Pt/BST/Pt.

The effect of capacitor size was investigated by testing capacitors of three nominal diameters:  $50 \mu\text{m}^2$ ,  $200 \mu\text{m}^2$ , and  $500 \mu\text{m}^2$ . The capacitors were tested at  $1750 \text{ kV/cm}$ . It has been noted that there may be a relationship between the time to failure and capacitor size, with larger capacitors failing in a shorter time[126]. This could arise from a distribution of defects, with any one capable of causing failure. The probability of having a worse defect would then increase with oxide area.

The results are shown in Figure 4.43, with the Weibull fits given in Table 4.8. There is no trend across an order of magnitude of capacitor size. This indicates that the defect that is responsible for  $t_{ddb}$  is, over the area tested, relatively narrow and monodispersed. The results eliminate the possibility that there are several defects responsible for  $t_{ddb}$ .

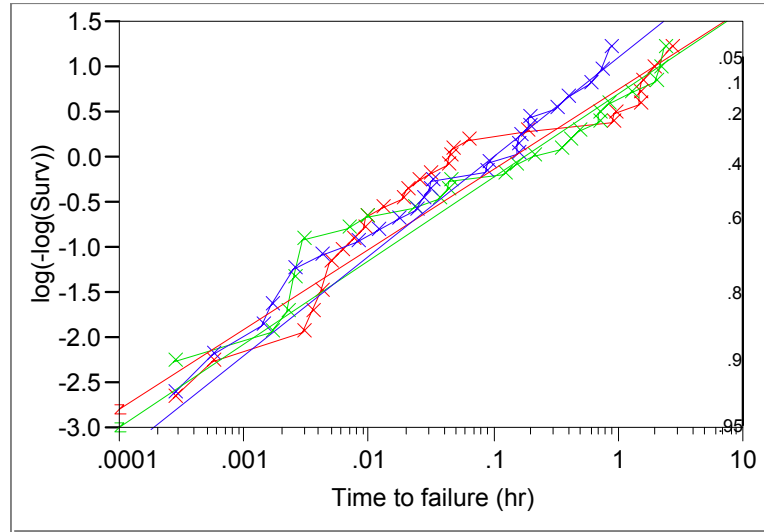


Figure 4.43: Weibull plot for three capacitor sizes: the red line indicates  $50 \mu\text{m}^2$  capacitors, the green line  $200 \mu\text{m}^2$ , and the blue  $500 \mu\text{m}^2$ .

Table 4.8: Weibull parameter estimates for curves shown in Figure 4.43.

Contact Size	Alpha	Beta
$50 \mu\text{m}^2$	0.145768	0.382533
$200 \mu\text{m}^2$	0.177880	0.400061
$500 \mu\text{m}^2$	0.100465	0.476507

The second aspect of the investigation is the influence of pre-stress leakage as an indicator of tddb lifetime. Before stress, both positive and negative J-t measurement were taken at a field of 400 kV/cm for 100 seconds. The steady-state leakage values were extracted. This data was collected on the contact size and the field data. The results were used in a parametric regression, which fits a survival distribution to a linear model using maximum likelihood estimation. The survival distribution was chosen to be Weibull.

The details of the whole model test is given in Table 4.9. The result can be understood as follows. The model is fit twice. The first time uses the parameter estimates calculated from the fitting. The second time assumes that the parameter estimates are zero. Twice the difference in loglikelihood between the two cases happens to have a chi-

square distribution, so that test is used to determine if the difference in loglikelihood is significant. In this case, it is highly significant.

Table 4.9: Whole model test for pre-stress leakage model.

Model	-LogLikelihood	ChiSquare	DF	Prob>Chisq
Difference	26.3596875	52.7194	5	<.0001
Full	189.174329			
Reduced	215.534017			

The significance of the parameter estimates is given in Table 4.10. The positive pre-test leakage is more significant, >98%, than the negative pre-test leakage, >94%, but both are significant.

Table 4.10: Effect likelihood ratio tests, indicating significance, for pre-stress leakage model

Source	Nparm	DF	L-R ChiSquare	Prob>ChiSq
Positive leakage (A/cm <sup>2</sup> )	1	1	6.27430644	0.0123
Negative leakage (A/cm <sup>2</sup> )	1	1	3.62406234	0.0569
Voltage	1	1	48.2331966	0.0000
Contact Size	1	1	0.00210329	0.9634

The parameter estimates are the linear slopes fit to the model. Table 4.11 shows the values of the estimates. The positive values for both the positive and negative pre-test leakage suggest that leakier films have longer lifetimes. It is not clear why this should be the case. [unfinished]

Table 4.11: Parameter estimates for pre-stress leakage model.

Term	Estimate	Std Error
Intercept	14.1725473	1.9415159
Positive leakage (A/cm <sup>2</sup> )	595103.621	237551.33
Negative leakage (A/cm <sup>2</sup> )	38.4918935	15.92329
Voltage	-2.0612999	0.247367
Contact Size	-0.0059872	0.1305661

The final aspect of tddb investigated was the field dependence. Three voltages were measured and the Weibull statistics generated for each. The tests were conducted at 25 °C, as Reisinger found that the tddb lifetime was worse at that temperature than at the operating temperature, 80 °C. The Weibull plot of the data is shown in Figure 4.44. Some of the values in the plot are right censored, so the shape of the curves, particularly the 7 V curve, may not appear to correspond to the data.

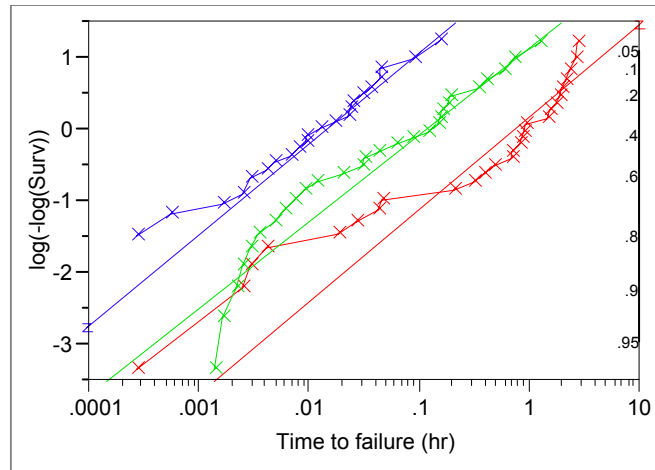


Figure 4.44: Weibull plot for stress voltages: the red line indicates 7 V stress, the green line 8 V stress, and the blue line 9 V stress.

The values of the Weibull fit are given in Table 4.12. The  $\beta$  values, the Weibull slope, are constant with voltage. The  $\alpha$ , or characteristic values, show the time where the Weibull cdf fulfills the condition  $1-1/e$ . This value was extrapolated assuming an inverse exponential dependence of field on tddb lifetime.

Table 4.12: Weibull parameter estimates for curves shown in Figure 4.44.

Voltage	Alpha	Beta
7	0.729	0.560
8	0.115	0.525
9	0.0148	0.553

Three main insights were gained from the investigation of tddb. The first is that tddb appears to be caused by one defect and not a distribution of defects. Calculated

distributions from a large range of capacitor sizes shows no trend with area. Second, the failure distribution is modeled by the Weibull distribution. Field scaling has an inverse exponential form for the  $\alpha$ , or characteristic values. The  $\beta$  values do not change with field scaling. Finally, time to tddb failure is longer for capacitors that are leakier. The origin of this dependence is unknown.

## 4.7: Extrapolation of Tddb and Resistance Degradation Lifetimes

Three quadrants were examined and the dominant failure mode was determined. From the high temperature, high field quadrant, resistance degradation was found to be the dominant failure mechanism. From the low temperature, high field quadrant, tddb was found to be the dominant failure mechanism. The high temperature, low field regime did not show failure in a reasonable time. Determining the dominant failure mode at operating conditions is accomplished by extrapolating resistance degradation from the high temperature direction and tddb from the low temperature direction.

The resistance degradation lifetimes were calculated for the same composition and thickness that are used in the tddb field extrapolation, in order to compare the resistance degradation lifetime to the tddb lifetime at the operating conditions. The results are summarized in Table 4.13. It was discussed previously that predicting reliability required predicting the first 1% of failures. Since the failure distribution of resistance degradation is lognormal, the standard confidence intervals provide an estimate of the distribution. was not collected such that the projection can be made. The 99% confidence intervals for the model and for the individual observations were calculated. The distribution is slightly skewed so the values are not symmetric. The model confidence reflects the uncertainty in the values calculated for the parameters. The individual confidence reflects the underlying failure distribution.

Table 4.13: Lower and upper confidence intervals for the model and for individual observations, for various fields, for a 51.0% Ti, 40 nm film at 85 °C. Values are in seconds.

	Field (kV/cm)		
	250	400	500
Lifetime	$1.2167 \times 10^{12}$	$3.1389 \times 10^{10}$	$2.7405 \times 10^9$
L99 Model	$1.6351 \times 10^{10}$	$1.3176 \times 10^9$	$2.2235 \times 10^8$
U99 Model	$9.0537 \times 10^{13}$	$7.4775 \times 10^{11}$	$3.3778 \times 10^{10}$
L99 Individual	$1.4736 \times 10^{10}$	$1.1455 \times 10^9$	$1.8673 \times 10^8$
U99 Individual	$1.0046 \times 10^{14}$	$8.6012 \times 10^{11}$	$4.0220 \times 10^{10}$

The lower 99% confidence interval for the individual observations is the number that will give the best estimate of the resistance degradation lifetime of BST at various fields. As can be seen from Table 4.14, BST will offer acceptable reliability at 1.6 V and below, but not at 2 V.

Table 4.14: Extrapolated resistance degradation lifetime for a 51.0% Ti, 40 nm film at 85 °C.

Volts	Field (kV/cm)	L99 Indv. (sec)	Lifetime (years)
1	250	$1.4736 \times 10^{10}$	467.0
1.6	400	$1.1455 \times 10^9$	36.3
2	500	$1.8673 \times 10^8$	5.92

The tddb lifetime is extrapolated using the Weibull plot-based procedure outlined in the literature review. The cdf of the failure distribution at operating voltages will be calculated based on the extrapolation of the distributions taken at higher voltages. A Weibull plot will be constructed of this data along with an AFR based on the calculated chip size and the area tested. If the extrapolated distribution falls in the forbidden region of the plot, as shown in Figure 1.71, the AFR is too high.

The values of the Weibull fit are given in Table 4.15. The  $\beta$  values, the Weibull slope, are constant with voltage, so the average value will be used for the extrapolation. The  $\alpha$ , or characteristic, values show the time where the Weibull cdf fulfills the condition  $1-1/e$ . This value was best fit with an inverse exponential dependence of field on tddb lifetime.

Table 4.15: Weibull parameter estimates for curves shown in Figure 4.44.

Voltage	Alpha	Beta
7	0.729	0.560
8	0.115	0.525
9	0.0148	0.553

The voltage scaling extrapolated the Weibull distribution parameters and used those parameters to construct a distribution at various stress levels. The voltages calculated were 1 V, 2 V, and 4 V. The plot uses  $\log_{10}$  rather than natural log because the axes are more intuitive.

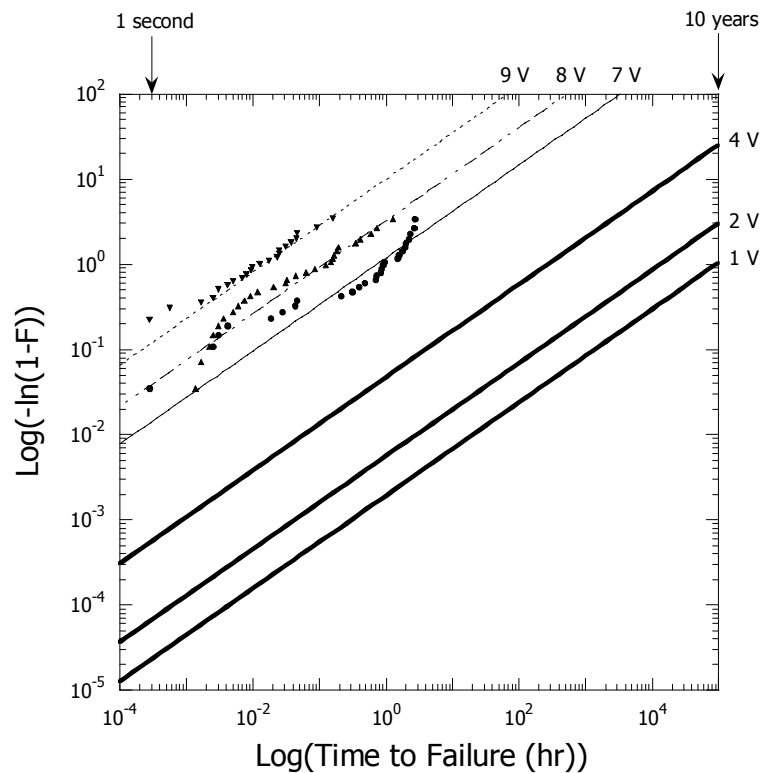


Figure 4.45: Weibull plot of the three voltages, tested at 25 °C, their associated lines of fit, and the extrapolated failure distributions for various voltages.

The data was taken at 25 °C, but the operating conditions are at 80 °C. Reisinger *et al.* carefully investigated the temperature dependence of tddb in BST and found that the lifetime shifted the distribution 1.5 orders of magnitude[126]. So a temperature

extrapolation was carried out, using a value of 1.5 orders of magnitude. The resulting plot is shown in Figure 4.46. This data represents a better case and it will be determine if the reliability is sufficient at 80 °C.

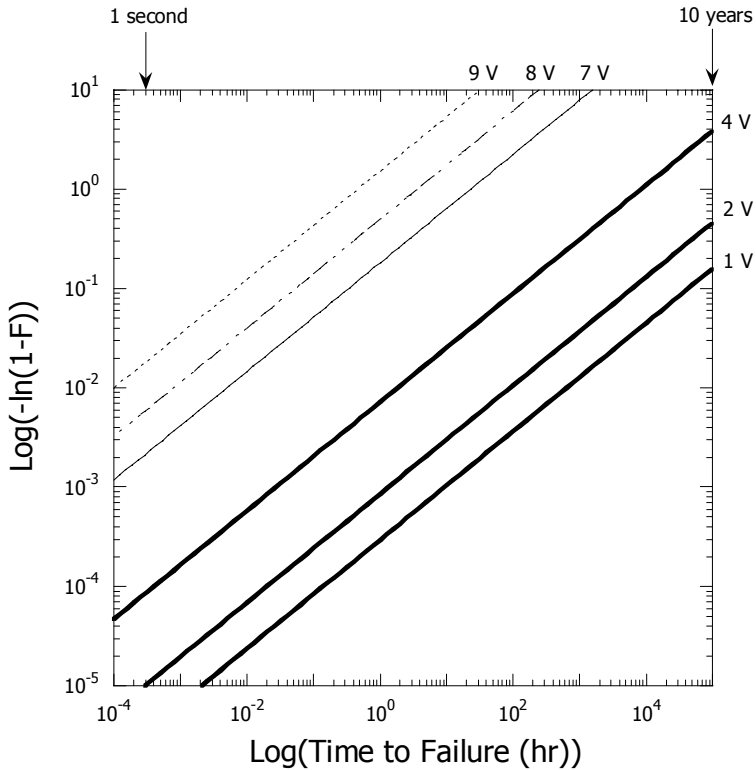


Figure 4.46: Weibull plot of the three voltages, at 80 °C, extrapolated using the Resinger temperature data, their associated lines of fit, and the extrapolated failure distributions for various voltages.

The final correction is area scaling. The area tested does not correspond to the area of a chip, so the area must be scaled. Area scaling requires estimation of the area of the chip. The BST relative permittivity is 310. To obtain 30 fF/cell, the minimum for reliable operation of a DRAM cell, an individual device must have a certain size. Assuming that the device is planar, to simplify the calculations, the size will be  $0.4367 \mu\text{m}^2$ . For a 1 Gbit device, this corresponds to a capacitor area of  $4.37 \text{ cm}^2$ . As is typical, the total tested area is smaller, at  $0.2558 \text{ cm}^2$ . Area scaling is straightforward on a Weibull plot. The relationship is given as

$$-\ln(1 - F_{chip}) = -\ln(1 - F_{test}) \left( \frac{A_{chip}}{A_{test}} \right)$$

for this case, the area ratio is  $5.855 \cdot 10^{-3}$ . Thus the AFR required for 1 FIT is  $5.85 \cdot 10^{-12}$  and for 10 FIT it is  $5.85 \cdot 10^{-11}$ .

The reliability of BST is insufficient for 1 V operation either at 25 °C or 85 °C, as can be seen in Figure 4.47. Two 10 FIT lines are shown, one for the chip, with an AFR of  $10^{-8} \text{ hr}^{-1}$ , and one for the experimental data with area scaling, with an AFR of  $5.85 \cdot 10^{-11} \text{ hr}^{-1}$ .

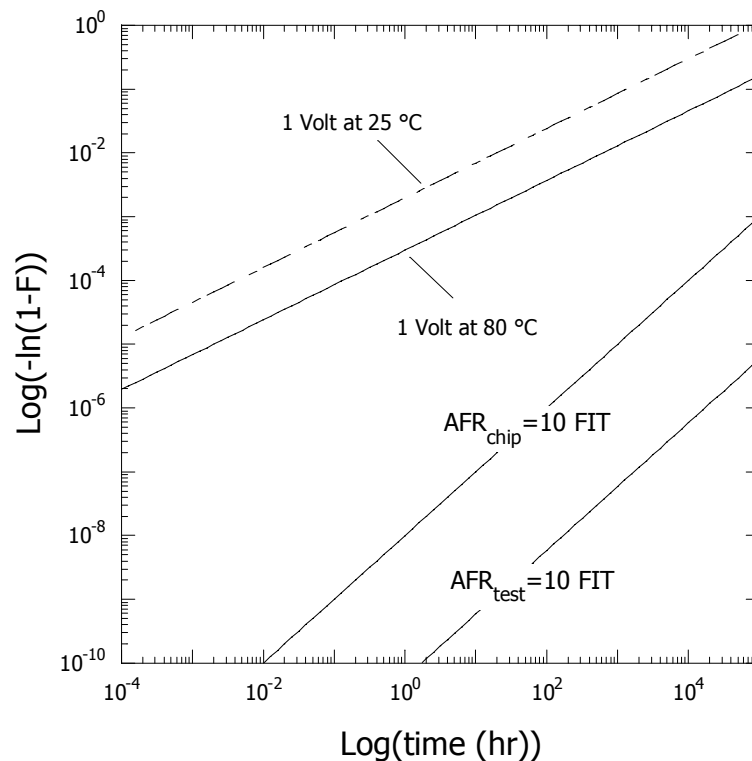


Figure 4.47: Weibull plot showing extrapolated BST failure distributions as well as the 10 FIT lines for the device and tested area.

The results of the tddb investigation suggest that the Pt/BST/Pt system is not currently suited for use as DRAM. The defect that is causing the tddb failures is likely a

processing defect, so an investigation of BST processing parameters, or a general improvement in film quality, is necessary.

## 4.8: Conclusions

The failure of BST capacitors was investigated in order to understand the failure modes operating at different combinations of stress conditions, especially temperature and electric field. While the BST system was not exhaustively characterized, careful comparisons were made to elucidate the main relationships. The low temperature, high field regime was emphasized to complement the previous body of work on BST reliability. The framework for BST failure is as follows.

Failure in BST can be divided into two categories: intrinsic and extrinsic. The intrinsic failure mode is resistance degradation. It is a materials property and is believed to be due to oxygen vacancy transport to the interface that lowers the Schottky barrier height. It can be modeled via an exponential relationship. Resistance breakdown lifetime should be considered the ultimate available lifetime. Resistance degradation is prominent at high temperatures, although it can occur at low temperatures.

The extrinsic failure mode is a defect that is strongly process dependent and is described via a Weibull distribution. It is manifested in AC and DC tddb. Occurrence of defect-related failure increases at low temperature. This extrinsic defect is related to interfacial roughness between the BST and Pt. This defect causes the shortest lifetime.

Sometimes noisy breakdown is seen. Noisy breakdown begins much like tddb, but instead of failing in one step, the capacitor degrades in a series of steps. The origin of noisy breakdown is not clear, but a possible mechanism is as follows. Impurities and defects at the Pt/BST interface lower the Schottky barrier. Localized barrier lowering results in local thermal leakage increases. These self-heal by thermal annealing. This

explains the short increase in leakage current. Earlier work on voltage “burn-in” of BST films is consistent with this “healing” process.

The conclusion from the framework is that the most common failure mode in the high temperature, high field regime is resistance degradation. The most common failure mode in the low temperature, high field regime is tddb. Extrapolation of the resistance degradation lifetime to operating conditions shows that it will likely limit device lifetime. However, extrapolation of the resistance degradation lifetime to operating conditions shows that the tddb will be lifetime limiting.

## Chapter 5: FUTURE WORK

The results of the size effects investigation show that size effects in BST are best explained by Finite Size Scaling. However, the application of the model to BST capacitors is not ideal. The model parameters of Finite Size Scaling are empirically measured, rather than calculated. The proper boundary conditions are essential to the proper application of the model, but the boundary conditions must be considered within the larger model and not as ends in themselves. For example, the work of Black and Welsler on the effect of screening in the electrodes attributed the thickness dependence of the permittivity of BST entirely to the electrode effect, leaving nothing for strain, compositional variation, or Finite Size Scaling itself. All of the relevant boundary conditions must be reformulated along with Finite Size Scaling as a coherent whole before the understanding of size effects in thin film ferroelectrics can advance.

The investigation of failure in BST shows that tddb failure is the lifetime-limiting failure mode at operating conditions. The defect causing the failure mode must be found so that processing changes can be implemented to reduce the prevalence of the defect. Alternately, an empirical optimization can be performed on factors known to be correlated with the defect, such as interfacial roughness, to reduce the prevalence of the

defect. It is important that one of the two paths be taken in order for BST to be attractive as the capacitor dielectric in DRAM.

## Chapter 6: BIBLIOGRAPHY

1. Valasek, J., *Physical Review*, 1921. 17: p. 475.
2. Xu, Y., *Ferroelectric Materials and Their Applications*. 1991, New York, NY: Elsevier Science Publishing Company.
3. Megaw, H.D., *Ferroelectricity in Crystals*. 1956, London, UK: Methuen & Co.
4. Devonshire, A.F., *Theory of Barium Titanate--Part 1*. *Philosophical Magazine*, 1949. 40(309): p. 1040-1063.
5. Devonshire, A.F., *Theory of Ferroelectrics*. *Advances in Physics*, 1954. 3(10): p. 85-130.
6. Nye, J.F., *Physical Properties of Crystals*. 1985, New York, NY: Oxford University Press.
7. Basceri, C., et al., *The Dielectric Response as a function of Temperature and Film Thickness of Fiber-Textured (Ba,Sr)TiO<sub>3</sub> Thin Films Grown by Chemical Vapor Deposition*. *Journal of Applied Physics*, 1997. 82(5): p. 2497-2504.

8. Streiffer, S.K., et al., *Ferroelectricity in Thin Films: The Dielectric Response of Fiber-Textured  $(\text{Ba}_x\text{Sr}_{1-x})\text{Ti}_{1+y}\text{O}_{3+z}$  Thin Films Grown by Chemical Vapor Deposition*. Journal of Applied Physics, 1999. **86**(8): p. 4565-4575.
9. Strukov, B.A. and A.P. Levanyuk, *Ferroelectric Phenomena in Crystals: Physical Foundations*. 1998, Heidelberg: Springer Verlag. 213.
10. Wang, Y.G., W.L. Zhong, and P.L. Zhang, *Surface Effects and Size Effects on Ferroelectrics with a First-Order Transition*. Physical Review B, 1996. **53**(17): p. 11439-11443.
11. Wang, C.L., et al., *Size Effects of Ferroelectric Particles Described by the Transverse Ising Model*. Physical Review B, 2000. **62**(17): p. 11423-11427.
12. Binder, K., *Finite Size Effects on Phase Transitions*. Ferroelectrics, 1987. **73**: p. 43-67.
13. McCauley, D., R.E. Newnham, and C.A. Randall, *Intrinsic Size Effects in a Barium Titanate Glass-Ceramic*. Journal of the American Ceramic Society, 1998. **81**(4): p. 979-987.
14. Zhou, C. and D.M. Newns, *Intrinsic Dead Layer Effect and the Performance of Ferroelectric Thin Film Capacitors*. Journal of Applied Physics, 1997. **82**: p. 3081-3088.
15. Zhou, C. and D.M. Newns, *Is There an Intrinsic Dead Layer Effect at Ferroelectric Surfaces?* Superlattices and Microstructures, 1998. **23**(3-4): p. 539-545.
16. Binder, K., *Surface Effects on Phase Transitions in Ferroelectrics and Antiferroelectrics*. Ferroelectrics, 1981. **35**: p. 99-104.

17. Binder, K. and P.C. Hohenberg, *Phase Transitions and Static Spin Correlations in Ising Models with Free Surfaces*. Physical Review B, 1972. **6**(9): p. 3461-3487.
18. Kretschmer, R. and K. Binder, *Surface Effects on Phase Transitions and Dipolar Magnets*. Physical Review B, 1979. **20**(3): p. 1065-1076.
19. Selke, W. and K. Binder, *Ising Models for Ferroelectric and Ferromagnetic Transitions*. Ferroelectrics, 1984. **53**: p. 7-13.
20. Cowley, R.A., *Lattice Dynamics and Phase Transitions of Strontium Titanate*. Physical Review A, 1964. **134**(4A): p. A981-A997.
21. Sinnamon, L.J., R.M. Bowman, and J.M. Gregg, *Investigation of Dead-Layer Thickness in SrRuO<sub>3</sub>/Ba<sub>(0.5)</sub>Sr<sub>(0.5)</sub>TiO<sub>3</sub>/Au Thin-Film Capacitors*. Applied Physics Letters, 2001. **78**(12): p. 1724-1726.
22. Bhide, V.G., R.T. Gonhalekar, and S.N. Shringi, *Surface Layers on BaTiO<sub>3</sub> Crystals*. Journal of Applied Physics, 1965. **36**(12): p. 3825.
23. Batra, I.P. and B.D. Silverman, *Thermodynamic Stability of Thin Ferroelectric Films*. Solid State Communications, 1972. **11**: p. 291-294.
24. Batra, I.P., P. Wurfel, and B.D. Silverman, *Phase Transition, Stability, and Depolarization Field in Ferroelectric Thin Films*. Physical Review B, 1973. **8**(7): p. 3257-3265.
25. Batra, I.P., P. Wurfel, and B.D. Silverman, *Depolarization Field and Stability Considerations in Thin Ferroelectric Films*. Journal of Vacuum Science and Technology, 1973. **10**(5): p. 687-692.

26. Wurfel, P. and I.P. Batra, *Depolarization-Field-Induced Instability in Thin Ferroelectric Films--Experiment and Theory*. Physical Review B, 1973. **8**(11): p. 5126-5133.
27. Teowee, G., et al., *Effect of Top Metallization on the Fatigue And Retention Properties of Sol-Gel Pzt Thin-Films*. Integrated Ferroelectrics, 1995. 7(1-4): p. 149-160.
28. Lee, B.T. and C.-S. Hwang, *Influences of Interfacial Intrinsic Low-Dielectric Layers on the Dielectric Properties of Sputtered (Ba,Sr)TiO<sub>3</sub> Thin Films*. Applied Physics Letters, 2000. 77(1): p. 124-126.
29. Choi, D.K., et al., *Evaluation of Tailored Electrode (Ba,Sr)RuO<sub>3</sub> for (Ba,Sr)TiO<sub>3</sub>*. Journal of Applied Physics, 1999. **86**(6): p. 3347-3351.
30. Stolichnov, I., et al., *Control of Leakage Conduction of High-Fatigue-Endurance (Pb, La)(Zr, Ti)O<sub>3</sub> Film Ferroelectric Capacitors with Pt/SrRuO<sub>3</sub> Electrodes*. Applied Physics Letters, 1999. 75(12): p. 1790-1792.
31. Li, H.C., et al., *Thickness Dependence of Dielectric Loss in SrTiO<sub>3</sub> Thin Films*. Applied Physics Letters, 1998. 73(4): p. 464-466.
32. Ley-Koo, M. and M.S. Green, *Revised and Extended Scaling for Coexisting Densities of SF<sub>6</sub>*. Physical Review A, 1977. **16**: p. 2483-2487.
33. Pittman, C., T. Doiron, and H. Meyer, *Equation of State and Critical Exponents of <sup>3</sup>He and a <sup>3</sup>He-<sup>4</sup>He Mixture Near Their Liquid-Vapor Critical Point*. Physical Review B, 1979. **20**(9): p. 3678-3689.

34. Holmes, L.M., L.G. van Uitert, and G.W. Hull, *Magnetoelectric Effect and Critical Behavior in the Ising-Like Antiferromagnet, DyAlO<sub>3</sub>*, Solid State Communications, 1971. 9(16): p. 1373-1376.
35. Clarke, R. and A.M. Glazer, *The Observation of Critical Behaviour in the Thermal Expansion of Pb(Zr<sub>0.9</sub>Ti<sub>0.1</sub>)O<sub>3</sub>*, Journal of Physics C Solid State Physics, 1974. 7(12): p. 2147-2156.
36. Lines, M.E. and A.M. Glass, *Principles and Applications of Ferroelectrics and Related Materials*. 1977, Oxford, England: Clarendon Press. 680.
37. Goldenfeld, N., *Lectures on Phase Transformations and the Renormalization Group*. Frontiers in Physics. 1992, Reading, Massachusetts: Perseus Publishing. 394.
38. Frowein, R. and J. Kotzler, *Direct Observation of the Logarithmic Correction to Landau's Equation of State at Marginal Dimension*. Physical Review B, 1982. 25(5): p. 3292-3297.
39. Goodstein, D.L., *States of Matter*. 1985, Toronto, Canada: Dover Publications. 491.
40. Wilson, K.G., *Renormalization Group and Critical Phenomena. I. Renormalization Group and the Kadanoff Scaling Picture*. Physical Review B, 1971. 4(9): p. 3174-3183.
41. Wilson, K.G., *Renormalization Group and Critical Phenomena. II. Phase-Space Cell Analysis of Critical Behavior*. Physical Review B, 1971. 4(9): p. 3184-3205.
42. Aharony, A., *Critical Behavior of Magnets with Lattice Coupling*. Physical Review B, 1973. 8(9): p. 4314-4273.

43. Aharony, A., *Critical Behavior of Anisotropic Cubic Systems*. Physical Review B, 1973. **8**(9): p. 4270-4273.
44. Aharony, A. and M.E. Fisher, *Critical Behavior of Magnets with Dipolar Interactions, I. Renormalization Group Near Four Dimensions*. Physical Review B, 1973. **8**(7): p. 3323-3341.
45. Aharony, A. and M.E. Fisher, *Critical Behavior of Magnets with Dipolar Interactions, II. Feynman-Graph Expansion for Ferromagnets Near Four Dimensions*. Physical Review B, 1973. **8**(7): p. 3342-3348.
46. Aharony, A. and M.E. Fisher, *Critical Behavior of Magnets with Dipolar Interactions, III. Antiferromagnets*. Physical Review B, 1973. **8**(7): p. 3349-3357.
47. Aharony, A. and M.E. Fisher, *Critical Behavior of Magnets with Dipolar Interactions, IV. Anisotropy*. Physical Review B, 1973. **8**(7): p. 3358-3362.
48. Aharony, A. and M.E. Fisher, *Critical Behavior of Magnets with Dipolar Interactions, V. Uniaxial Magnets in  $d$  Dimensions*. Physical Review B, 1973. **8**(7): p. 3363-3370.
49. Fisher, M.E., *Critical Phenomena in Films and Surfaces*. Journal of Vacuum Science and Technology, 1973. **10**(5): p. 665-673.
50. Binder, K., *Statistical Mechanics Of Finite 3-Dimensional Ising Models*. Physica, 1972. **62**: p. 508.
51. Weber, H., D. Marx, and K. Binder, *Melting Transition in Two Dimensions: A Finite-size Scaling Analysis of Bond-Orientational Order in Hard Disks*. Physical Review B, 1995. **51**(20): p. 14636-14651.

52. Landau, D.P. and K. Binder, *Critical Behavior of the Surface-Layer Magnetization at the Extraordinary Transition in the Three-dimensional Ising Model*. Physical Review B, 1990. **41**(7): p. 4786-4788.
53. Binder, K. and P.C. Hohenberg, *Surface Effects on Magnetic Phase Transitions*. Physical Review B, 1974. **9**(5): p. 2194-2214.
54. Binder, K. and D.P. Landau, *Finite-Size Scaling at First-Order Transitions*. Physical Review B, 1984. **30**(3): p. 1477-1485.
55. Black, C.T. and J.J. Welser, *Electric-Field Penetration Into Metals: Consequences for High-Dielectric-Constant Capacitors*. IEEE Transactions on Electron Devices, 1999. **46**(4): p. 776-780.
56. Natori, K., D. Otani, and N. Sano, *Thickness Dependence of the Effective Dielectric Constant in a Thin Film Capacitor*. Applied Physics Letters, 1998. **73**(5): p. 632-634.
57. Pertsev, N.A., A.G. Zembilgotov, and A.K. Tagantsev, *Effect of Mechanical Boundary Conditions on Phase Diagrams of Epitaxial Ferroelectric Thin Films*. Physical Review Letters, 1998. **80**(9): p. 1988-1991.
58. Tagantsev, A.K., et al., *Strain-Induced Diffuse Dielectric Anomaly and Critical Point in Perovskite Ferroelectric Thin Films*. Physical Review B, 2001. **65**: p. 12104.
59. Kittel, C., *Introduction to Solid State Physics*. 7 ed. 1996, New York: John Wiley & Sons. 673.

60. Watanabe, Y., *Theoretical Investigation of the Thickness Effect of Ferroelectric Incorporating Semiconducting Properties*. Applied Surface Science, 1998. **130-132**: p. 610-615.
61. Watanabe, Y., *Theoretical Stability of the Polarization in a Thin Semiconducting Ferroelectric*. Physical Review B, 1998. **57(2)**: p. 789-804.
62. Watanabe, Y., *Theoretical Stability of the Polarization in Insulating Ferroelectric/Semiconducting Structures*. Journal of Applied Physics, 1998. **83(4)**: p. 2179-2193.
63. Pertsev, N.A., et al., *Ferroelectric Thin Films Grown on Tensile Substrates: Renormalization of the Curie-Weiss and Apparent Absence of Ferroelectricity*. Journal of Applied Physics, 1999. **85(3)**: p. 1698-1701.
64. Forsbergh, P.W., *Effect of a Two-Dimensional Pressure on the Curie Point of Barium Titanate*. Physical Review, 1954. **93(4)**: p. 686-692.
65. Samara, G.A., *Pressure and Temperature Dependence of the Dielectric Properties of the Perovskites  $BaTiO_3$  and  $SrTiO_3$* . Physical Review, 1966. **151(2)**: p. 378-386.
66. Yasuda, N., S. Fujimoto, and K. Tanaka, *Dielectric Properties of  $Pb(Fe_{(2/3)}W_{(1/3)})O_3$  Under Pressure*. Journal of Physics D: Applied Physics, 1985. **18**: p. 1909-1917.
67. Uchino, K. and S. Nomura, *Critical Exponents of the Dielectric Constants in Diffused-Phase-Transition Crystals*. Ferroelectrics Letters, 1982. **44**: p. 55-61.
68. Roth, P., et al., *Deviations from Curie-Weiss Behavior of  $(Ba_{0.06}Sr_{0.94})TiO_3$  Caused by High Hydrostatic Pressure Due to Quantum Effects*. Ferroelectrics, 1987. **74**: p. 331-337.

69. Muller, K.A. and H. Burkhead, *SrTiO<sub>3</sub>: An Intrinsic Quantum Paraelectric Below 4K*. Physical Review B, 1979. **19**(7): p. 3593-3602.
70. Ishibashi, Y., H. Orihara, and D.R. Tilley, *Thickness Transitions of Ferroelectricity in Thin Films*. Journal of the Physical Society of Japan, 1998. **67**(9): p. 3292-3297.
71. Tilley, D.R. and B. Zeks, *Landau Theory of Phase Transitions in Thick Films*. Solid State Communications, 1984. **49**(8): p. 823-827.
72. Zhong, W.L., et al., *Thickness Dependence of the Dielectric Susceptibility of Ferroelectric Thin Films*. Physical Review B, 1994. **50**(17): p. 12375-12380.
73. Wang, Y.G., W.L. Zhong, and P.L. Zhang, *Lateral Size Effects on Cells in Ferroelectric Films*. Physical Review B, 1995. **51**(23): p. 17235-17238.
74. Park, Y., *Surface Effect and Phase Transitions in Ferroelectric Thin Films*. Solid State Communications, 1999. **112**: p. 167-171.
75. Vendik, O.G. and L.T. Ter-Martirosyan, *Size Effect in Layered Structures: Ferroelectric/Normal Metal and Ferroelectric/High T<sub>C</sub> Superconductor*. Physics of the Solid State, 1994. **36**(11): p. 1778-1781.
76. Vendik, O.G. and S.P. Zubko, *Modeling the Dielectric Response of Incipient Ferroelectrics*. Journal of Applied Physics, 1997. **9**: p. 4475-4483.
77. Vendik, O.G. and S.P. Zubko, *Ferroelectric Phase Transition and Maximum Dielectric Permittivity of Displacement Type Ferroelectrics (Ba<sub>(x)</sub>Sr<sub>(1-x)</sub>TiO<sub>3</sub>)*. Journal of Applied Physics, 2000. **88**(9): p. 5343-5350.

78. Vendik, O.G., S.P. Zubko, and M.A. Nikol'skii, *Modeling and Calculation of the Capacitance of a Planar Capacitor Containing a Ferroelectric Thin Film*. Technical Physics, 1999. **44**(4): p. 349-355.
79. Vendik, O.G., S.P. Zubko, and L.T. Ter-Martirosayn, *Correlation Effects in a Thin-Film Capacitor*. Physics of the Solid State, 1996. **38**(12): p. 1991-1995.
80. Vendik, O.G., S.P. Zubko, and L.T. Ter-Martirosayn, *Experimental Evidence of the Size Effect in Thin Ferroelectric Films*. Applied Physics Letters, 1998. **73**(1): p. 37-39.
81. Vendik, O.G., I.G. Mironenko, and L.T. Ter-Martirosayn, *Size Effects in Dynamic Polarization in Displacive Ferroelectric Films*. Soviet Physics of the Solid State, 1984. **26**(10): p. 1864-1867.
82. Shaoping, L., et al., *Dimension and Size Effects in Ferroelectrics*. Japanese Journal of Applied Physics, 1997. **36**: p. 5169-5174.
83. Shaoping, L., et al., *Size Effects in Nanostructured Ferroelectrics*. Physics Letters A, 1996. **212**: p. 341-346.
84. Ishikawa, K., K. Yoshikawa, and N. Okada, *Size Effect on the Ferroelectric Phase Transition in  $PbTiO_3$  Ultrafine Particles*. Physical Review B, 1998. **37**(10): p. 5852-5855.
85. Zhong, W.L., et al., *Phenomenological Study of the Size Effect on Phase Transitions in Ferroelectric Particles*. Physical Review B, 1994. **50**(2): p. 698-703.
86. Wang, Y.G., W.L. Zhong, and P.L. Zhang, *Size Effects on the Curie Temperature of Ferroelectric Particles*. Solid State Communications, 1994. **92**(6): p. 519-523.

87. Jiang, B. and L.A. Bursill, *Phenomenological Theory of Size Effects in Ultrafine Ferroelectric Particles of Lead Titanate*. Physical Review B, 1999. **60**(14): p. 9978-9982.
88. Zhang, L., W.L. Zhong, and J.-F. Hu, *Dielectric Behavior and Correlation Length of Ferroelectric Particles in the Paraelectric Phase*. Solid State Communications, 2000. **116**: p. 349-354.
89. Randall, C.A., D. McCauley, and D.P. Cann, *Finite Size Effects in a BaTiO<sub>3</sub> Ferroelectric Glass Ceramic*. Ferroelectrics, 1998. **206-207**(1-4, 1-2): p. 325-335.
90. Frey, M.H., et al., *The Role of Interfaces on an Apparent Grain Size Effect on the Dielectric Properties for Ferroelectric Barium Titanate Ceramics*. Ferroelectrics, 1998. **206-207**(337-353).
91. Frey, M.H. and D.A. Payne, *Grain-Size Effect on Structure and Phase Transformations for Barium Titanate*. Physical Review B, 1996. **54**(5): p. 3158-3168.
92. Zhang, L., et al., *Finite-Size Effects in Ferroelectric Solid Solution Ba<sub>(x)</sub>Sr<sub>(1-x)</sub>TiO<sub>3</sub>*. Journal of Physics D: Applied Physics, 1999. **32**: p. 546-551.
93. Song, T.K., J. Kim, and S.-I. Kwun, *Size Effects on the Quantum Paraelectric SrTiO<sub>3</sub> Nanocrystals*. Solid State Communications, 1996. **97**(2): p. 143-147.
94. Ishikawa, K. and T. Uemori, *Surface Relaxation in Ferroelectric Particles*. Physical Review B, 1999. **60**(17): p. 11841-11845.
95. Chattopadhyay, S., et al., *Finite-Size Effects in Antiferroelectric PbZrO<sub>3</sub> Nanoparticles*. Journal of Physics: Condensed Matter, 1997. **9**: p. 8135-8145.

96. Park, Y., K.M. Knowles, and K. Cho, *Particle-Size Effect on the Ferroelectric Phase Transition in  $PbSc_{(1/2)}Ta_{(1/2)}O_3$  Ceramics*. Journal of Applied Physics, 1998. **83**(11): p. 5702-5708.
97. Paek, S.-H., et al., *Electrical and Microstructural Degradation with Decreasing Thickness of  $(Ba, Sr)TiO_3$  Thin Films Deposited by RF Magnetron Sputtering*. Japanese Journal of Applied Physics, 1996. **35**: p. 5757-5762.
98. Larsen, P.K., et al., *Ferroelectric Properties and Fatigue of  $Pb_{(0.51)}Ti_{(0.49)}O_3$* . Journal of Applied Physics, 1994. **76**(4): p. 2405-2412.
99. Tsai, F. and J.M. Cowley, *Thickness Dependence of Ferroelectric Domains in Thin Crystalline Films*. Applied Physics Letters, 1994. **65**(15): p. 1906-1908.
100. Wu, D.W., et al., *Characterization of Metalorganic Decomposition-Derived  $SrBi_{(2)}Ta_{(2)}O_{(9)}$  Thin Films with Different Thicknesses*. Journal of Applied Physics, 2000. **87**(4): p. 1795-1800.
101. Bharadwaja, S.S. and S.B. Krupanidhi, *Dielectric Relaxation in Antiferroelectric Multigrain  $PbZrO_3$  Thin Films*. Materials Science and Engineering B, 2000. **78**: p. 75-83.
102. Lee, J.J., C.L. Thio, and S.B. Desu, *Electrode Contacts on Ferroelectric  $Pb(Zr_{(x)}Ti_{(1-x)})O_3$  and  $SrBi_{(2)}Ta_{(2)}O_3$  Thin Films and Their Influence on Fatigue Properties*. Journal of Applied Physics, 1995. **78**(8): p. 5073-5078.
103. Shaw, T.M., S. Trolrier-McKinstry, and P.C. McIntyre, *The Properties of Ferroelectric Films at Small Dimensions*. Annual Review of Materials Science, 2000. **30**: p. 263–98.

104. Werner, M.C., et al., *Microstructure of (Ba,Sr)TiO<sub>3</sub> Thin Films Deposited by Physical Vapor Deposition at 480 °C and Its Influence on the Dielectric Properties*. Applied Physics Letters, 2000. 77(8): p. 1208-1211.
105. Horikawa, T., et al., *Dielectric Properties of (Ba,Sr)TiO<sub>3</sub> Thin-Films Deposited by rf-Sputtering*. Japanese Journal of Applied Physics, 1993. 32(9B): p. 4126-4130.
106. Bethe, K. and F. Welz, *Preparation and Properties of (Ba,Sr)TiO<sub>3</sub> Single Crystals*. Materials Research Bulletin, 1971. 6(4): p. 209-217.
107. Stemmer, S., et al., *Accommodation of Nonstoichiometry in (100) Fiber-Textured (Ba<sub>(x)</sub>Sr<sub>(1-x)</sub>)Ti<sub>(1-y)</sub>O<sub>(3+z)</sub> Thin Films Grown by Chemical Vapor Deposition*. Applied Physics Letters, 1999. 74(17): p. 2432-2434.
108. Smyth, D.M., Y.H. Hu, and M.P. Harmer, *Solubility of BaO in BaTiO<sub>3</sub>*. Journal of the American Ceramic Society, 1985. 68(7): p. 376-379.
109. Yamamichi, S., et al., *(Ba+Sr)/Ti Ratio Dependence of the Dielectric Properties for (Ba<sub>0.5</sub>Sr<sub>0.5</sub>)TiO<sub>3</sub> Thin Films Prepared by Ion Beam Sputtering*. Applied Physics Letters, 1994. 64(13): p. 1644-1646.
110. Hench, L.L. and J.K. West, *Principles of Electronic Ceramics*. 1990, New York: Wiley. 546.
111. Horikawa, T., et al., *Effects of Post-Annealing on Dielectric Properties of (Ba,Sr)TiO<sub>3</sub> Thin Films Prepared by Liquid Source Chemical Vapor Deposition*. IEICE Transactions on Electronics, 1998. E81-C(4): p. 497-504.

112. Basceri, C., *Electrical And Dielectric Properties Of (Ba,Sr)TiO<sub>3</sub> Thin Film Capacitors For Ultra-High Density Dynamic Random Access Memories*, in *Department of Materials Science and Engineering*. 1997, North Carolina State University: Raleigh.
113. Noh, D.Y., et al., *Crystallization of Amorphous (Ba, Sr)TiO<sub>3</sub>/MgO(001) Thin Films*. *Applied Physics Letters*, 1998. 72(22): p. 2823-2825.
114. Lee, W.J., et al., *Japanese Journal of Applied Physics*, 1995. 34: p. 196.
115. Lee, W.-J., H.G. Kim, and S.-G. Yoon, *Microstructure Dependence of Electrical Properties of (Ba<sub>0.5</sub>Sr<sub>0.5</sub>)TiO<sub>3</sub> Thin Films Deposited on Pt/SiO<sub>2</sub>/Si*. *Journal of Applied Physics*, 1996. 80(10): p. 5891-5894.
116. Baumert, B.A., et al., *Characterization of Sputtered Barium Strontium Titanate and Strontium Titanate-Thin Films*. *Journal of Applied Physics*, 1997. 82(5): p. 2558-2566.
117. Taguchi, M., et al. *Dielectrically Encapsulated Trench Capacitor Cell*. in *International Electron Devices Meeting 1986*. 1986: IEEE.
118. Saha, S. and S.B. Krupanidhi, *Study of the Electrical Properties of Pulsed Laser Ablated (Ba<sub>0.5</sub>Sr<sub>0.5</sub>)TiO<sub>3</sub> Thin Films*. *Materials Science and Engineering B*, 1999. 57(2): p. 135-146.
119. Ezhilvalavan, S. and T.-Y. Tseng, *Progress in the Developments of (Ba,Sr)TiO<sub>3</sub> (BST) Thin Films for Gigabit Era DRAMs*. *Materials Chemistry and Physics*, 2000. 65(3): p. 227–248.

120. Yamamichi, S., et al., *A Stacked Capacitor Technology With ECR Plasma MOCVD (Ba,Sr)TiO<sub>3</sub> and RuO<sub>2</sub>/Ru/Tin/TiSi<sub>x</sub> Storage Nodes For Gb-Scale Drams*. IEEE Transactions on Electron Devices, 1997. **44**(7): p. 1076-1083.
121. Kawahara, T., et al., *Step Coverage and Electrical Properties of (Ba,Sr)TiO<sub>3</sub> Films Prepared by Liquid Source Chemical Vapor Deposition Using TiO(DPM)<sub>2</sub>*. Japanese Journal of Applied Physics, 1994. **33**(9B): p. 5129-5134.
122. Kotecki, D.E., et al., *(Ba,Sr)TiO<sub>3</sub> Dielectrics for Future Stacked Capacitor DRAM*. IBM Journal of Research and Development, 1999. **43**(3): p. 367-382.
123. Lash, S.E., *Growth and Properties of MOCVD (Ba,Sr)TiO<sub>3</sub> Thin Film Capacitors*, in *Department of Materials Science and Engineering*. 1999, North Carolina State University: Raleigh.
124. Tsai, M.S., S.C. Sun, and T.-Y. Tseng, *Effect of Bottom Electrode Materials and Annealing Treatments on the Electrical Characteristics of Ba<sub>0.47</sub>Sr<sub>0.53</sub>TiO<sub>3</sub> Film Capacitors*. Journal of the American Ceramic Society, 1999. **82**(2): p. 351-358.
125. Hilton, A.D. and B.W. Ricketts, *Dielectric Properties of Ba<sub>1-x</sub>Sr<sub>x</sub>TiO<sub>3</sub> Ceramics*. Journal of Physics D: Applied Physics, 1996. **29**(5): p. 1321-1325.
126. Reisinger, H., et al. *Dielectric Breakdown, Reliability, and Defect Density of (Ba<sub>0.7</sub>Sr<sub>0.3</sub>)TiO<sub>3</sub> (BST)*. in *1998 Symposium on VLSI Technology*. 1998: IEEE, New York, NY.
127. Degraeve, R., et al., *A New Statistical Model for Fitting Bimodal Oxide Breakdown Distributions at Different Field Conditions*. Microelectronics Reliability, 1996. **36**(11-12): p. 1651-4.

128. Ross, R.J., C. Boit, and D. Staab, eds. *Microelectronic Failure Analysis*. 1999, ASM International: Materials Park, OH.
129. Hunter, W.R. *The Analysis of Oxide Reliability Data*. in *IRW Final Report*. 1998.
130. Nelson, W., *Accelerated Testing: Statistical Models, Test Plans, and Data Analyses*. 1 ed. 1990, New York, NY: Wiley-Interscience. 601.
131. Lawless, J.F., *Statistical Models and Methods for Lifetime Data*. 1982, New York, NY: John Wiley and Sons. 580.
132. Yamamichi, S., et al., *Impact of Time Dependent Dielectric Breakdown and Stress-Induced Leakage Current on the Reliability of High Dielectric Constant (Ba,Sr)TiO<sub>3</sub> Thin-Film Capacitors for Gbit-Scale Drams*. IEEE Transactions on Electron Devices, 1999. **46**(2): p. 342-7.
133. Devore, J.L., *Probability and Statistics for Engineering and the Sciences*. 1991, Belmont, CA: Duxbury Press.
134. Stathis, J.H., *Physical and Predictive Models of Ultrathin Oxide Reliability in CMOS Devices and Circuits*. IEEE Transactions on Device and Materials Reliability, 2001. **1**(1): p. 43-59.
135. Nafria, M., J. Sune, and X. Aymerich, *Breakdown of Thin Gate Silicon Dioxide Films -- A Review*. Microelectronics Reliability, 1996. **36**(7/8): p. 871-905.
136. Nigam, T., et al. *Constant Current Charge-to-Breakdown: Still a Valid Tool To Study the Reliability of MOS Structures?* in *36th Annual International Reliability Physics Symposium*. 1998. Reno, Nevada.

137. Prendergast, J., N. Finucane, and J. Suehle. *Investigation of the Intrinsic SiO<sub>2</sub> Area Dependence Using Tddb testing*. in *1997 International Integrated Reliability Workshop*. 1997. S. Lake Tahoe, CA.
138. Kotov, A.E. *Reliability Aspects of Thin Dielectric Films Used in NVM ICs*. in *Materials Research Society Proceedings*. 1995. San Francisco, CA: Materials Research Society.
139. Depas, M., T. Nigam, and M.H. Heyns, *Soft Breakdown of Ultra-Thin Gate Oxide Layers*. IEEE Transactions on Electron Devices, 1996. 43(9): p. 1499-1504.
140. Degraeve, R., et al., *New Insights in the Relation Between Electron Trap Generation and the Stastical Properties of Oxide Breakdown*. IEEE Transactions on Electron Devices, 1998. 45(4): p. 904-911.
141. Wu, E.Y., J.H. Stathis, and L.-K. Han, *Ultra-Thin Oxide Reliability for ULSI Applications*. Semiconductor Science and Technology, 2000. 15: p. 425-435.
142. Sune, J., G. Mura, and E. Miranda, *Are Soft Breakdown and Hard Breakdown of Ultrathin Gate Oxides Actually Different Failure Mechanisms?* IEEE Electron Device Letters, 2000. 21(4): p. 167-169.
143. Satake, H. and A. Toriumi, *Dielectric Breakdown Mechanism of Thin-SiO<sub>2</sub> Studied by the Post-Breakdown Resistance Statistics*. IEEE Transactions on Electron Devices, 2000. 47(4): p. 741-745.
144. Basceri, C., et al. *An Important Failure Mechanism in MOCVD (Ba,Sr)TiO<sub>3</sub> Thin Films: Resistance Degradation*. in *Ferroelectric Thin Films VI*. 1998. Boston, MA: Materials Research Society, Warrendale, PA, USA.

145. Bunting, E.N., et al., *Properties of Beryllium-Barium Titanate Dielectrics*. Journal of Research of the National Bureau of Standards, 1951. 47(1): p. 15-24.
146. Neumann, H. and G. Arlt, *Maxwell-Wagner Relaxation and Degradation of SrTiO<sub>3</sub> and BaTiO<sub>3</sub> Ceramics*. Ferroelectrics, 1986. 69: p. 179-186.
147. Waser, R., T. Baiatu, and K.-H. Hardtl, *dc Electrical Degradation of Perovskite-Type Titanates:I Ceramics*. Journal of the American Ceramic Society, 1990. 73(6): p. 1645-1653.
148. Waser, R., T. Baiatu, and K.-H. Hardtl, *dc Electrical Degradation of Perovskite-Type Titanates:II, Single Crystals*. Journal of the American Ceramic Society, 1990. 73(6): p. 1654-1662.
149. Waser, R., T. Baiatu, and K.-H. Hardtl, *dc Electrical Degradation of Perovskite-Type Titanates:III, A Model of the Mechanism*. Journal of the American Ceramic Society, 1990. 73(6): p. 1663-73.
150. Warren, W.L., et al., *Oxygen Vacancy Motion in Perovskite Oxides*. J. Am. Ceram. Soc., 1996. 79(2): p. 536.
151. Numata, K., et al., *Analysis of Resistance Degradation of SrTiO<sub>3</sub> and Ba<sub>(x)</sub>Sr<sub>(1-x)</sub>TiO<sub>3</sub> Thin Films*. Japanese Journal of Applied Physics, 1995. 34(9B): p. 5245-5249.
152. Grossmann, M., et al., *Resistance Degradation Behavior of Ba<sub>0.7</sub>Sr<sub>0.3</sub>TiO<sub>3</sub> Thin Films Compared to Mechanisms Found in Titanate Ceramics and Single Crystals*. Integrated Ferroelectrics, 1998. 1-4: p. 603-614.

153. Basceri, C. *Resistance Degradation of CVD (Ba,Sr)TiO<sub>3</sub> Thin Films for DRAMs and Integrated Capacitors*. in *Proceedings of the 8th International Symposium on Integrated Ferroelectrics*. 1996.
154. Zafar, S., et al., *Oxygen Vacancy Mobility Determined From Current Measurements in Thin Ba<sub>0.5</sub>Sr<sub>0.5</sub>TiO<sub>3</sub> Films*. Applied Physics Letters, 1998. 73(2): p. 175-177.
155. Zafar, S., et al., *Resistance Degradation in Barium Strontium Titanate Thin Films*. Journal of Applied Physics, 1999. 86(7): p. 3890-3894.
156. Tsai, M.S. and T.Y. Tseng, *Effect of Bottom Electrodes on Resistance Degradation and Breakdown of (Ba,Sr)TiO<sub>3</sub> Thin Films*. IEEE Transactions on Components and Packaging Technology, 2000. 23(1): p. 128-135.
157. van Buskirk, P.C., J.F. Roeder, and S. Bilodeau, *Manufacturing of Perovskite Thin Films Using Liquid Delivery MOCVD*. Integrated Ferroelectrics, 1995. 10(1-4): p. 9-22.
158. Scott, J.F., et al., *Dielectric Breakdown in High-ε Films for ULSI DRAMs: II. Barium-Strontium Titanate Ceramics*. Integrated Ferroelectrics, 1994. 4: p. 61-84.
159. Huang, S.-C., et al., *Time Dependent Dielectric Breakdown of Paraelectric Barium-Strontium-Titanate Thin Film Capacitors for Memory Device Applications*. Journal of Applied Physics, 1998. 84(9): p. 5155-7.
160. Tsai, M.S., S.C. Sun, and T.-Y. Tseng, *Effect of Bottom Electrode Materials on the Electrical and Reliability Characteristics of (Ba, Sr)TiO<sub>3</sub> Capacitors*. IEEE Transactions On Electron Devices, 1999. 46(9): p. 1829-1839.

161. Noma, A. and D. Ueda, *Reliability study on BST capacitors for GaAs MMIC*. Integrated-Ferroelectrics, 1997. 15(1-4): p. 69-78.
162. Yamamichi, S., et al. *Impact of Time Dependent Dielectric Breakdown and Stress Induced Leakage Current on the Reliability of (Ba,Sr)TiO<sub>3</sub> Thin Film Capacitors for Gbit-Scale DRAMs*. in *International Electron Devices Meeting 1997*. 1997. Washington, D.C.: Institute of Electrical & Electronics Engineers.
163. Chen, T.-S., et al. *Dynamic Stressing Effects on Reliability of Strontium Titanate (SrTiO<sub>3</sub>) Thin Film Capacitors for High-density Memory Applications*. in *1998 Symposium on VLSI Technology Digest of Technical Papers*. 1998. Honolulu, HI: IEEE ; Tokyo.
164. Bilodeau, S., et al., *MOCVD BaSrTiO<sub>3</sub> for >=1-Gbit DRAMs*. Solid State Technology, 1997. 40(7): p. 235.
165. Honda, M., *The Impedance Measurement Handbook*. 1989.
166. Horikawa, T., et al. *Degradation in (Ba,Sr)TiO<sub>3</sub> Thin Films Under DC and Dynamic Stress Conditions*. in *IEEE Reliability Physics Symposium*. 1997. Denver, Colorado.
167. Lu, C.-H. and W.-S. Hwang, *Formation Mechanism and Relaxor Ferroelectric Properties of Lead Lithium Iron Tungstate Ceramics*. Journal of Materials Research, 1995. 10(11): p. 2755-2763.
168. Cullity, B.D., *Elements of X-ray Diffraction*. 2 ed. Vol. 1. 1978, Reading, Massachusetts: Addison-Wesley. 555.

169. Shaw, T.M., et al., *The Effect of Stress on the Dielectric Properties of Barium Strontium Titanate Thin Films*. Applied Physics Letters, 1999. 75(14): p. 2129-2131.
170. Cox, P.A., et al., *The Metal-To-Semiconductor Ternary Ruthenium (IV) Oxides: A Study by Electron Spectroscopy*. Journal of Physics C-Solid State Physics, 1983. 16(32): p. 6221-6239.
171. Allen, P.B., et al., *Transport properties, Thermodynamic Properties, and Electronic Structure of SrRuO<sub>3</sub>*. Physical Review B, 1996. 53(8): p. 4393-4398.
172. Li, H.C., et al., *Dielectric Properties of SrTiO<sub>3</sub> Thin Films Grown on Various Perovskite Electrodes by Pulsed Laser Deposition*. Materials Science and Engineering B, 1998. 56: p. 218-222.
173. Summerfelt, S.R., *(Ba,Sr)TiO<sub>3</sub> Thin Films for DRAMs*, in *Thin Film Ferroelectric Materials and Devices*, R. Ramesh, Editor. 1997, Kluwer Academic Publishers: Norwell, Massachusetts. p. 249.
174. Kingon, A.I., et al., *Leakage and Relaxation Behavior in Ferroelectric Films*. US-Japan, 1995: p. 32-35.
175. Sall, J.P., *Leverage Plots for General Linear Hypotheses*. American Statistician, 1990. 44(4): p. 303-315.
176. Apte, P.P. and K.C. Saraswat, *SiO<sub>2</sub> Degradation with Charge Injection Polarity*. IEEE Electron Device Letters, 1993. 14(11): p. 512.